Deposition and Characterisation of RF Magnetron Sputtered Phosphate Based Glasses

Bryan W. Stuart

Thesis submitted to the University of Nottingham for the degree of Doctor of Philosophy

October 2016

Declaration

I, Bryan W. Stuart, herby certify that this thesis has been composed by myself and that it is a record of my own work over the period from October 2013 to October 2016.

Except where specific reference is made to other sources or collaborators, the work presented in this thesis is the original work of the author. It has not been submitted, in whole or in part, for any other degree.

Bryan W. Stuart

Acknowledgements

I would like to acknowledge the EPSRC Centre for Innovative Manufacturing in Medical Devices (MeDe Innovation)* for funding my PhD and would like to express my appreciation to Prof. David Grant, Dr. Ifty Ahmed, Dr. Joel Segal and Dr. Miquel Gimeno-Fabra for their ongoing supervision and support during the course of this project.

I would like to thank all members of the Wolfson technical team, in particular Nigel Neate and Martin Roe for their assistance in microscopy and materials characterisation techniques. Characterisation of NMR and Helium Pycnometry were carried out by Prof. Jeremy J. Titman and Dr. Lee Stevens respectively. Rietveld Refinement was conducted with assistance from Zdenek Pala. Cell culture laboratory work was undertaken by undergraduate students, Samuel Evans, Kathryn Thomas and Elana Super, under the supervision of Dr. Colin Scotchford.

Finally I would like to thank all friends and family, in particular my girlfriend Natasha Pettit for their support over the last three years.

*This work was funded through MeDe Innovation, the EPSRC Centre for Innovative Manufacturing in Medical Devices, under grant number EP/K029592/1.

Abstract

Phosphate based glasses are emerging in the field of biomaterials for their potential to resorb in biological environments, fulfilling applications from the fibre reinforcement of resorbable polymeric matrices to carriers for therapeutic drug delivery.

Here we show the optimisation and characterisation of thin film glasses deposited by RF magnetron sputtering onto medical implant materials such as Ti6Al4V to function as ion leaching coatings to promote osseointegration or inhibit bacterial attachment.

Vaporisation of the target preform occurs by momentum exchange interactions leading to non-stoichiometric transfer to the condensed coating. Elements were found to sputter in the order Na > Mg > Ca > Fe > P, corresponding to dissociation energies of 257, 788, 928, 818 or 1227 and 2983 kJ mol^{-1} and masses of 23.0, 24.3, 40.1, 55.9 and 31.0 g mol^{-1} for Na^{+}, Mg^{2+}, Ca^{2+}, Fe^{2+} or $^{3+}$ and P^{5+} respectively.

Structural analyses revealed short-range variation between compositionally equivalent glasses such that coatings with 32.5, 34 and 37 mol% P_2O_5 showed bulk polymerisation increasing in Q^2 species by (23% to 45%) versus (9% to 32%) in quenched glasses. P-O-P bridging oxygens on the surface of coatings remained consistent at (34% to 35%) forming $(PO_3)^-$ metaphosphates (Q^2), compared to the increase from (12% to 18%) forming majority $(PO_4)^{3-}$ orthophosphates (Q^0) and $(P_2O_7)^{4-}$ pyrophosphates (Q^1) in quenched glasses.

Quinternary coatings of up to 2.67 μm, containing Fe^{3+} and Ti^{4+} intermediate and cross linking elements were degraded in distilled water and phosphate buffered saline. Fe_2O_3 was increased from 4 to 8 mol% to stabilise dissolution, however an observed increase was attributed to variable condensation energies leading to inequivalent enthalpy and internal stress states. A comparison of a compositionally equivalent

condensed and quenched glass suggested that the surface ratios of P-O-P to (P=O and PO^-) were 34.2% to 65.8% versus 20.5% to 79.5% respectively leading to more soluble coating surfaces, exhibiting an exponential degradation dependence in the first 2 h in distilled water, followed by a linear profile. Incongruent degradation caused pitting whilst in PBS, a stable, adherent layer precipitated within 12 h of submersion.

Post deposition heat treatments at 500, 550 and 610 °C were employed to stabilise dissolution and to tailor mechanical properties. All phosphate glass coatings showed interfacial tensile adhesion in excess of 73.6 MPa; surpassing ISO and FDA requirements for HA coatings. Scratch testing revealed brittle failure modes, whilst interfacial failure occurred from 2.3 to 5.0 N. Coatings on sandblasted substrates did not suffer from tensile cracking or trackside delamination showing interfacial improvements to between 8.6 to 11.3 N. The initial exponential degradation from 0-2 h was stabilised via heat treatment. From 2-24 h coatings exhibited linear ion release rates ordering P > Na > Mg > Ca > Fe whilst dissolution rates reduced by factors of 2.44 to 4.55, attributed the formation of crystals and the depletion of hydrophilic P-O-P bonds within the surface layer.

Phosphate glasses submerged in SBF showed no signs of apatite formation over 28 d. In contrast a 490 nm silicate glass coating precipitated an apatite layer within 7 d of submersion. SBF was deemed an inconsistent method for testing bioactivity pending *in vitro or in vivo* testing.

Vapour deposition has shown its ability to condense tailorable compositions of glasses, maintaining their amorphous tetrahedral structures whilst demonstrating exceptional adhesion to Ti6Al4V substrates. Coatings have demonstrated linear ion release capabilities and the ability to accommodate a vast array of potentially therapeutic ions to promote osteogenic or antimicrobial capabilities.

Table of Contents

List of Abbreviations and Sample Nomenclature

ACP	Amorphous Calcium Phosphate
AD	As Deposited
AFM	Atomic Force Microscopy
ATR	Attenuated Total Reflectance
BG 45S5	Bioglass 45S5
BO	Bridging Oxygen
Ca:P	Calcium Phosphate
CB	Cortical Bone
CAP	Carbonated Apatite
CHA	Carbonated Hydroxyapatite
DC	Direct Current
deiH_2O	Ultra-Pure Deionised Water
dH_2O	Distilled Water
DMEM	Dulbecco's Modified Eagle's Medium
DTA	Differential Thermal Analysis
ECM	Extra Cellular Matrix
EDX	Energy Dispersive X-ray Spectroscopy
EPD	Electrophoretic Deposition
FDA	Food and Drug Administration
FIB-SEM	Focussed Ion Beam Scanning Electron Microscopy
FTIR	Fourier Transform Infrared Spectroscopy
FWHM	Full Width at Half Maximum
HA	Hydroxyapatite
HOB	Human Osteoblast Cells
HT	Heat Treated
ICP	Inductively Coupled Plasma
MAS-NMR	Magic Angle Spinning - Nuclear Magnetic Resonance
MHRA	Medicines & Healthcare Products Regulatory Agency
MQG	Melt Quenched Glass
NBO	Non Bridging Oxygen
PBG	Phosphate Based Glass

PBS	Phosphate Buffered Saline
PLA	Poly Lactic Acid
PMMA	Polymethyl Methacrylate
PPM	Parts Per Million
PVD	Physical Vapour Deposition
RF	Radio Frequency 13.56 MHz
RFMS	Radio Frequency Magnetron Sputtering
SBF	Simulated Body Fluid
SBG	Silicate Based Glass
SEM	Scanning Electron Microscopy
TB	Trabecular Bone
T_c	Crystallisation Temperature
TCP	Tri Calcium Phosphate
TEC	Thermal Expansion Coefficient
T_g	Glass Transition Temperature
T_m	Melting Temperature
TMA	Thermo Mechanical Analysis
TRIS	Tri Buffer Solution
XPS	X-ray Photoelectron Spectroscopy
XRD	X-ray Diffraction

Sample Nomenclature: Targets, Coatings and Heat Treated Coatings

Target glass is labelled (TxU or TxT to denote either the UoN PVD or TEER UDP 650 rigs respectively, where x, from 1-9 represents the target number. Similarly melt quenched glasses are labelled as (MQx) and coatings as (CxU or CxT). The codes in text are followed by the samples P_2O_5 and the dopant oxide mol%, of Fe_2O_3, TiO_2 or CuO, forming an overall example code of T6U: P51.5 Fe5, See *Table 3.2*.

Heat treated samples are denoted by the original coating code, limited to CxU, followed by the heat treatment temperature in °C and the dwell time in minutes (eg. C7U-500°-30) to denote heat treatment of C7U: P40 Fe4 as shown in *Table 3.4*

.

List of Figures

List of Tables

1. Introduction

Advancements have been made in orthopaedic fixation methods from the bioinert acrylic cements first used by Charnley to modern day bioactive ceramic coatings in the form of hydroxyapatite (HA), however large scope for improvement still remains [1].

Between 2003 and 2014 a total of 708,311 hip procedures were conducted in the United Kingdom, of which 93% were the result of osteoarthritis [1]. The number of primary revisions totalled 17,916. Aseptic loosening occurred in 4,376 cases and was the biggest cause of implant failure, accounting for ~24% of revisions [1]. Implant fixation methods have shifted from bone cement, decreasing from 60.4 to 31.8% between 2003-2014 [1]. During this period infection accounted for 2,443 revisions.

Zhang *et al.* describes a Biomaterial as a "material intended to interface with biological systems to evaluate, treat, augment, or replace any tissue, organ, or function of the body" [2]. In particular, the evolution of biomedical hip implants began with an ivory implant in 1890 followed by the transition to metals and polymers in the 1960s [2]. These materials were anchored to the body via cement, with integration enhanced by surface topographical modifications such as voids. These modifications would increase the adhesion and prolong implant/bone bonding without biological resorption as the new bone formation would anchor within [2]. The emphasis is now on tissue engineering as Ca:P based materials have proved clinically successful in promoting osteogenesis. However, osteogenic capabilities can be further enhanced by delivering therapeutic ions or by exploration of bioactive glasses for soft and hard tissue repair. Silicate bio glasses are capable of forming bonds with host tissue and in the case of phosphate glasses, can fully resorb into their environment, limiting foreign body inflammation with resorption time [2].

Implant devices are designed from combinations of ceramics, polymers and metals. The chosen implant should endure the mechanical stresses imposed by the user, based on the age and the mobility of the patient.

In the case of the total hip prosthesis, the acetabular cup; processed from either ceramic or metal is fixated into the pelvis. A polyethylene acetabular lining provides a low friction self-lubricating surface between the femoral head and the acetabular cup [3]. This junction provides rotational motion of the joint. The early femoral stems were made from stainless steel and Co-Cr alloys, however recent research and improvements in biomaterials is fuelling the shift towards titanium alloy implants, which have inherent resistance to corrosion and superior biocompatibility [3].

Fixation methods and implant design vary in affordability and practicality as longevity and durability differ from person to person. Fixation mechanisms in the form of bioinert cements and HA coatings may be applied to load bearing implants as anchoring layers to the surviving skeleton [2]. A hip replacement in particular is fixated to the surviving bone via the acetabular cup and the femoral stem therefore the designed coatings are for application at these locations.

Fully resorbable coatings and partially degradable bioactive materials have applications for a variety of orthopaedic implants and could potentially be advantageous in the fixation of dental implants, bone fracture plates and cranial reconstructions. Such coatings may promote cellular activity leading to enhanced attachment, proliferation and differentiation of human osteoblast cells for bone regeneration [2].

By 2016 the push for innovation in medical devices has led to developments in additive manufacturing, implant customisation, and more reliable applications. The

objective of the EPSRC Centre for Innovative Manufacturing in Medical Devices is to produce fully customised implants, manufactured at the point of need. Processing precision and ease of surgical implantation may lead to a single day clinical service. The potential for stratified design of orthopaedic coatings by therapeutic ion inclusions is therefore under investigation. Ultimately thin film resorbable coatings presented here may prove useful for a variety of applications ranging from hard tissue fixation and soft tissue integration to the delivery of therapeutic ions to an implantation site to promote osteogenesis, treat degenerative diseases or prevent infection.

1.1 Generations of Medical Implants

The early generation implants were designed to match the mechanical properties of the bones they replaced whilst limiting biological impact. Considerations such as fibrous encapsulation were poorly understood [4]. Materials included ceramics such as alumina and zirconia, polymers such as polyethylene and metal implants made from stainless steel [2]. Many of these implants were cytotoxic, resulting in infection, limiting the longevity of the implant device to a few years, or resulting in necessary revision surgery to prevent inflammation and further infection [2]. To fix the implants in place the use of acrylic cement was common practice.

John Charnley pioneered the first large scale hip prosthesis in the late 1950s using stainless steel, fixated via an acrylic cement to fill a hollowed out cavity within the femur [5]. The prosthetic was then aggressively pressed into the cement, creating adhesion by filling the voids within the cavity [5].

The next generation of bioceramics are those which facilitate interfacial bonding between the host tissue and the implant by allowing hard tissue formation on to the

surface of the implant [2]. HA first surfaced as an osteoconductive orthopaedic coating for implant osseointegration in the 1980's [4]. Larry Hench was the first to develop bioactive glass, labelled 45S5 Bioglass in 1969, which during its dissolution forms a carbonated HA (CHA) surface layer [2].

The latest generation of implant devices can be classified as those which are both resorbable in the body and are involved in the process of repairing the surrounding tissue by activating a controlled cellular response [4].

1.2 Bone Morphology, Osseointegration and Hydroxyapatite

Human bone undergoes remodelling through resorption, remineralisation and regeneration [6, 7]. The skeleton provides a framework for the muscular system to protect the organs and to function as an interconnected cellular network. The 213 bones present in the human body require variable mechanical properties to reinforce the skeletal structure [7]. On average the outer dense layer of cortical bone (CB) makes up 20% of the bone volume and 80% of the density. The remaining is the inner trabecular bone (TB) and porous layer. Porosity increases with age as bone remodelling accelerates such that resorption exceeds regeneration, leading to osteoporosis [6-8]. Precise ratios of CB:TB are based on bone function and therefore vary considerably throughout the skeletal structure. For example the ratio of the femoral head is closer to 50:50% [7]. CB is composed mainly of Ca:P, ideally in the ratio of 1.67, however, deficiencies in either of these elements is common, leading to abnormalities in bone density and sustainability. The CB has an average porosity of <5% and is similar in composition to HA [7, 9]. The mineral HA ($Ca_{10}(PO_4)_6(OH)_2$) constitutes the majority of the human bone with trace additions of ions and compounds, including Mg and Carbonate. According to Clarke *et al.* HA crystals within the bone are of an approximate size of 20 nm which lend themselves to

resorption within the body [7]. A biologically favoured cellular response is induced by bone like coating layers such as plasma sprayed HA, which facilitate protein attachment and lead to activation of the osteoblast cells necessary for bone growth [6, 7, 9].

During bone remodelling osteoclast cells release H^+ ions to lower the local pH surrounding the resorption region, which is followed by the breakdown of the extracellular matrix [7, 10]. Variation in strain gradients within the resorbing bone area are followed by further osteoclast or subsequent osteoblast activation [7]. Collagen protein fibrils are the main organic component found in bone and are laid down by osteoblast cells along the bone surface, facilitating regeneration from the creation of a extracellular matrix (ECM) [7]. Ca and P within the formed net of the ECM, given the correct proportions, nucleation points, and protein involvement will mineralise the ECM into crystallised bone in the form of HA. A schematic of bone remodelling can be found in *Figure 1.1*.

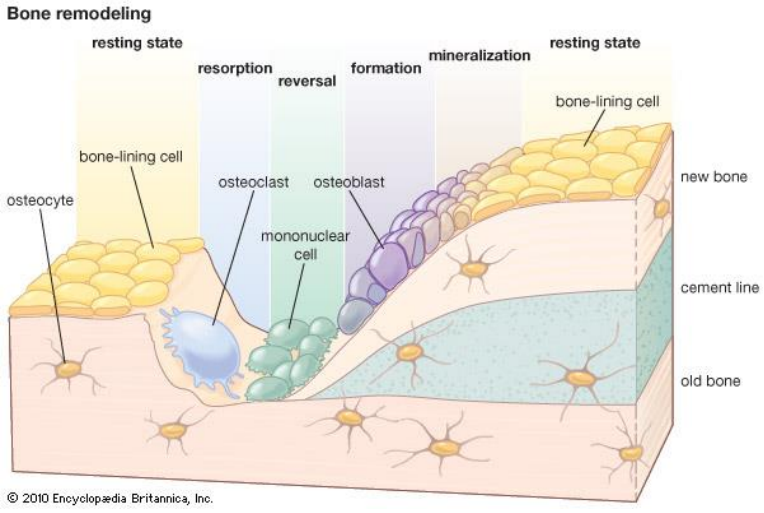

Figure 1.1: Bone remodelling showing the initial resorption by osteoclasts followed by the secretion of collagen fibrils, the formation of an ECM and eventual mineralisation of healthy bone. The cement line is a boundary between old and newly formed bone [11].

A key factor for bioactivity is the stimulation of osteoblasts for collagen secretion and subsequent mineralisation of bone material, which may be assisted by creating an environment for osteoconduction at the surface of the implant device [8]. Osteoblast and osteoclast cells are responsible for bone mineralisation and resorption respectively [9]. Surface modification can be useful in maintaining the mechanical properties whilst enhancing the materials ability to form a bone bonding apatite layer [8]. Clarke *et al.* suggested an approximate time of 4-6 months to undergo the full remodelling process. Ion release and mineral homeostasis is then maintained by the intercellular network of healthy bone.

- **Osteoclasts:** Responsible for the resorption of unhealthy or damaged bone. Excessive osteoclast activity can result in osteoporosis [7, 10].
- **Osteoblasts:** Secrete collagen fibrils and develop an ECM, further mineralised into new bone formation [7].
- **Collagen:** Protein secreted by osteoblasts. Responsible for Ca uptake [10].
- **Osteocalcin:** Considered as an indicator of bone remodelling as it is generally proficient during the resorption of the ECM and differentiation of osteoblast cells. Non-collagenous proteins assist in the upregulation of Ca and P towards the formation of HA [7].

The application of HA for osseointegration is commonly discussed in relation to the hip stem and acetabular cup; however, HA is widely used to induce osseointegration in dental implants *Figure 1.2A* [12], fracture plates, fixation screws, bone anchored hearing aids, and can stretch to custom orthopaedic usages including the bone anchoring in a full maxillofacial reconstruction or limb prosthesis as shown in *Figure 1.2B* and *C* [13].

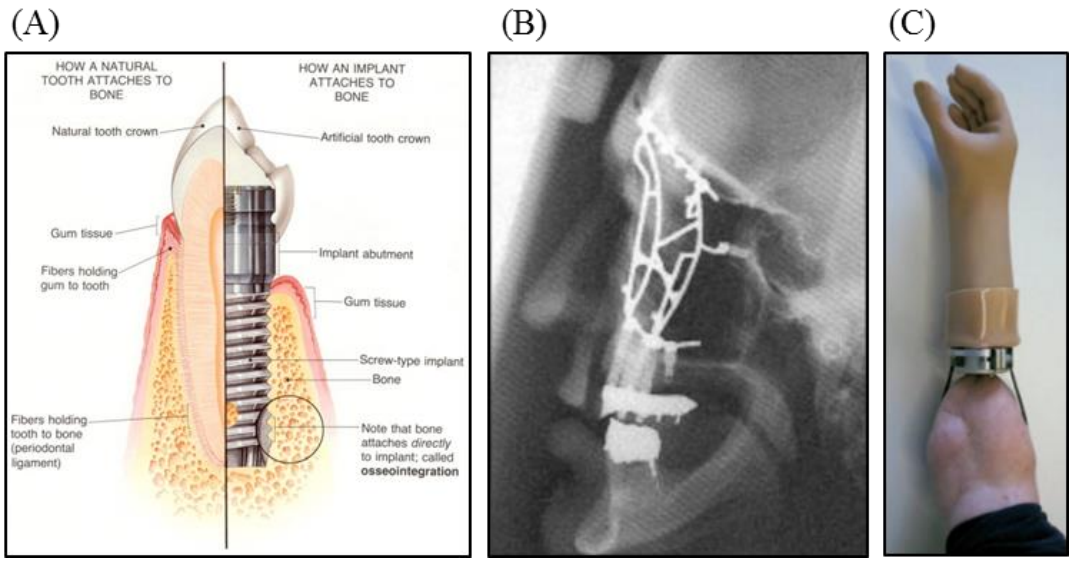

Figure 1.2: Applications of bone bonding coatings (A) dental implant (B) anchorage of a maxillofacial reconstruction. (C) Full limb prostheses integrated to the surviving bone [13].

Such applications fit into a category of integrating medical devices [14]. Dental implants contain intricate features such as threads, which may not be entirely suitable for the splat method of plasma spray deposition and can, similarly to HA coatings on hip prostheses, delaminate from the implant interface [12]. The surface of a dental implant requires roughening to induce adhesion between plasma sprayed HA, which can assist in creating nucleation sites for biomimetically formed Ca:P layers [12].

The current industrial standard for coating implants for bone integration utilises thick (>50 μm) HA, applied via plasma spraying, a process, which injects powdered ceramics into a high temperature energy source [2, 15]. The thermal process can cause decomposition to phases such as tricalcium-phosphate and lamellar discontinuities within the microstructure as processing temperatures of the particles can exceed 2000 °C [2, 15, 16]. The HA ejected is molten, or partially molten particles, which are cooled on the substrate [15]. The characteristics of the as-deposited coatings are widely dependent upon the processing parameters and can lead to large variations in adhesion, porosity and crystallinity [2, 15]. *Figure 1.3A and B* show the variation in

morphology within a plasma sprayed HA coating [15]. *(C)* shows an HA cross section, displaying the porosity associated with plasma sprayed coatings [17].

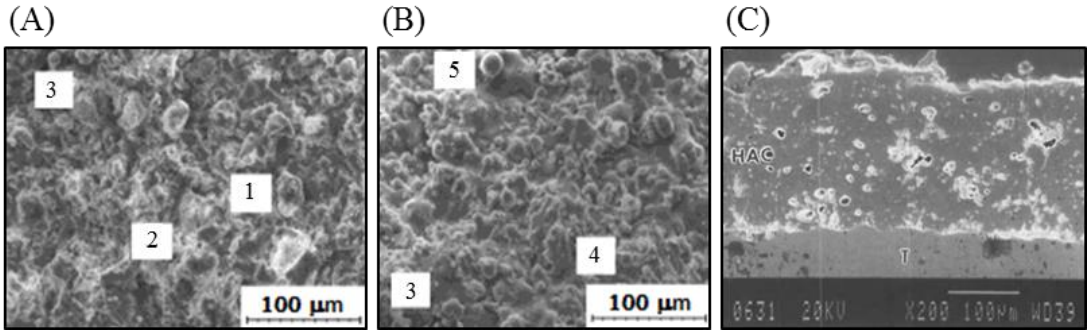

Figure 1.3: (A) and (B)"Surface morphology of plasma sprayed HA coatings. (1) Partially melted large particles, (2) Partially melted fine particles (3) Flattened splat, (4) Accumulated splats, (5) Spheroidised particles" [15]. (C) Cross Sectional view of a plasma sprayed HA coating [17].

In practice, HA coatings approved for use *in vivo* must adhere to the regulations dictated by authorities such as the FDA and MHRA [18]. The draft guidance for submissions for orthopaedic and dental endosseuous implants outline the general requirements for HA coatings based on those, which have been deemed substantially equivalent to existing approved coatings (*Table 1.1*) [19]. Additionally the ASTM standard for "Calcium Phosphate Coatings for Implantable Materials" outlines the necessary experimental processes necessary for confirming the structure and mechanical properties of the deposited coatings by multiple deposition methods, including sputtering [20].

Table 1.1: FDA requirements for HA coatings based on substantially equivalent coatings [19].

Specification	Acceptable Range
Ca:P Ratio	1.67-1.76
Density	2.98 g/cm^2
Tensile Strength	>50.8 MPa
Shear Strength	>22.0 MPa
Phase purity	>95% for a single powder phase
Thickness and roughness	Not specified

Recent studies into deposition of HA have shown that in order to induce full osseintegration by osteoconduction, the coating layer may be in the range of tens of

nanometres rather than hundreds of microns [21]. Plasma sprayed HA coatings were tested on dental implants in dogs to observe the difference in osseointregration with variation in coating thickness. Thicknesses of 1, 5 and 15 μm showed that early osseointegration at 3 weeks was improved [21]. However, no significant difference in bone formation for the HA coated implants 12 week post implementation existed. The uncoated control implant showed a significant lack of bone formation and incomplete osseointegration, supporting the use of HA for osteoconduction [21].

1.3 Implant Failures in Total Hip Prostheses and Dental Implants

Aseptic loosening and delamination of the implant/bone interface in both cemented and uncemented prosthesis may occur by osteolysis caused by wear of the acetabular cup [22].

With reference to aseptic loosening, research conducted over 170,413 operations showed that cemented acetabular cups required fewer revisions than their uncemented counterparts [23]. Cemented implants are more commonly used in older patients whom do not outlive the life of the implant, leading to few revisions. However, uncemented stems out-performed cemented stems in terms of longevity and gradual improvements in acetabular cup design have resulted in a levelling out of revision risk for uncemented and cemented components. The results collected referred to a range of fixation designs including the use of HA coatings [23].

Wear induced osteolysis is bone resorption as a consequence of phagocytosis of polyethylene wear particles, which stimulate macrophages at the implant site [22]. The polyethylene acetabular cup is worn away by the rotation of the femoral head. As wear particles deposit around the implant site, macrophages accumulate and encapsulate the foreign bodies leading to bone resorption as locational pathological

changes activate osteoclast cells. Osteolysis may be accelerated by apoptosis and bacteria which attract macrophages [22, 24].

As wear particles may be produced between any two contact surfaces under relative motion, accelerated by increased activity and cyclic loading. Behaviour of coatings in particular is highly dependent upon material properties such as surface roughness, hardness and abrasive characteristics [25]. HA coatings have been shown to increase abrasion, leading to particulate spallation. Ultimately, macrophage activation increases with size of wear particles and varies depending on patient lifestyle and nature of the implant device [26]. Research conducted by Lee *et al.* tested the size of the debris particles based on implant material of failed implants and concluded that the metallic debris sizes were similar for Ti-alloy, stainless steel and Co-Cr alloys [27]. The polyethylene particles were found to be greater in Ti-alloy implants thus leading to a greater abundance of Ti-alloy implant failure from wear induced osteolysis [27].

HA coated implants are initially press fit to accommodate fixation and may cause delamination of the coating and spallation into the surroundings leading to aseptic loosening [28, 29]. A study by Bloebaum *et al.* found particles of HA up to 75 μm, and metal particles due to wear of the underlying metallic components embedded in the acetabular cup. The HA layer has been known to delaminate entirely at the interface, preventing complete osseointegration via the coating layer or causing integration directly with the implant surface [28].

Investigations of plasma sprayed HA thicknesses suggest that thinner layers have improved stability [17, 24, 30]. Wang *et al.* found that by increasing HA thickness from 50 to 200 μm, the shear strength 12 weeks post implantation in canine femurs reduced from 13.97 ± 3.11 to 9.24 ± 1.61 MPa respectively. Failures occurred at the

Ti/coating interface as well as the coating/bone interface for the thicker layer [17]. Failure mode at the Ti/coating interface may be perpetuated due to residual stresses within the layer during cooling, which are believed to increase with thickness [30]. Bauer *et al.* suggested that coating thickness remain under 100 μm to prevent fatigue failures of the HA layer [24].

Many authors suggest that significant resorption of HA *in vivo* over years of implantation may lead to implant loosening however clinical data both supports and refutes these claims [24, 31, 32]. A clinical report of the effectiveness of plasma sprayed HA on dental implants tested in 65 patients with a combined total of 325 implants, placed in 4 locations of the maxilla and mandible showed no significant difference in failure based on the presence of HA coatings. Jones *et al.* did however conclude that HA was responsible for early stage integration whilst 9/15 failures were from non-HA coated implants in the posterior mandible [33].

Grit blasted Ti acetabular cups, plasma sprayed with 155 ± 35 μm of HA were tested. Coatings typically failed by delamination or resorption, followed by fretting between the implants surface and bone. As bone integration reduces with coating delamination and subsequent osteolysis, the implant was susceptible to accelerated loosening. It is suggested that the HA layer be porous to improve fixation by bone ingrowth [31].

1.4 Aim and Objectives

The clinical performance over the last 30 years of HA has proven adequate, however with an ageing population and demand for implants to outlast the life of the patient, third generation biomaterials must be explored to provide not only fixation at the bone interface but the inclusion of therapeutic ions to tailor to specific bone defects, potentially enhancing the rate of fixation and improving the durability through optimisation and regeneration of the tissue surrounding the implantation site.

Magnetron sputtering is a suitable method of producing thin films of glass and may be suitable for low temperature applications, therefore permitting coatings onto a range of materials from polymers to ceramics. By understanding the manufacturing process of magnetron sputtering, coating morphologies, compositions and microstructures may be optimised for implant use.

The aim of this project was to develop phosphate based glass (PBG) coatings, which can be readily applied to a range of implant devices including hip stems, acetabular cups, dental implants or bone fracture plates, to act as a controlled ion release mechanism whilst bone remodelling is in progress.

The objectives of the work presented here are to:

1. Apply and investigate the behaviour of various melt quenched glass systems under ion bombardment to subsequently determine the optimal processing parameters to obtain dense customised compositions of nano and micro thick coatings of PBG.
2. Determine the structural properties and similarity of vapour deposited glasses and melt quenched glasses of compositional equivalence.

3. Assess the dissolution properties of thin film glass coatings in water and physiological media and by the addition of cross linking elements explore and tailor dissolution rates.
4. Explore post processing heat treatments for stabilisation of degradation, assessing the dissolution dependence upon structural differences. Determine the mechanical properties of glass coatings.
5. Determine the potential bioactivity in simulated body fluids of various glass coating compositions.

The following *Section 2* is a detailed literature review covering melt quenched (MQ) bio-active glasses, coatings for orthopaedic applications, and the utilisation of magnetron sputtering for the deposition of thin films.

2. Literature Review

PBGs have the ability to fully resorb in aqueous solution and leach ionic by-products [34]. For biomedical applications these glasses have been used for tissue engineering scaffolds and to produce glass fibres as reinforcement materials for biodegradable polymer composites [35-38]. This potential in the field of biomaterials may be expanded to bioactive coatings. The following section reviews the literature pertaining to, glass structure/formation (*Sections 2.1 and 2.2*), degradation and *in vitro* bioactivity (*Sections 2.3 and 2.4*), anti-infection devices (*Section 2.5*), coating methods for glasses and orthopaedic applications (*Section 2.6*), RF sputtering of Ca:P and glasses, mechanical properties of sputtered films, cell culture of melt quenched and sputtered coatings (*Section 2.7*), and processing associated with sputtered coatings (*Section 2.8*).

2.1 Glass Formation and Structures via Conventional Melt Quenching

Thermodynamically, a structure will attempt to reach its lowest energy state upon cooling from liquid to solid, and in doing so the structure may begin to orientate to form crystals. Glasses have a near random molecular alignment termed “amorphous”, which is created by rapidly cooling a liquid network former to below or near to the T_g, such that the structure has insufficient time for alignment, leading to high entropy and enthalpy states (*Figure 2.1*) [39]. Whilst glasses lack long-range order associated with crystalline materials they maintain short-range order; geometric relation of the elements to their first or second nearest neighbours [40]. Elements capable of operating as network formers include Si, P, B and less common backbone materials such as Ge or As [36]. PBGs are less common due to their resorbable properties. This, however, makes them desirable in the biomaterials industry for delivery of therapeutic ions and resorbable composites [36].

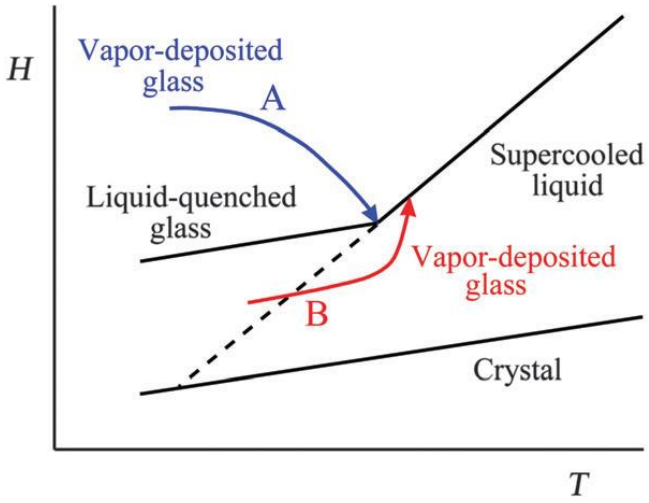

Figure 2.1: Enthalpy dependence with temperature of a super cooled liquid. Below the T_g quenched glasses freeze in a high enthalpy stressed state. Vapour deposition can surpass such states to create molecularly relaxed structures due to atomic relaxation during deposition [41].

Vitreous P_2O_5 glasses; those entirely composed of the network forming backbone are hydrophilic in nature and will readily resorb in the atmosphere. Additionally, they are difficult to manufacture due to their tendency to crystallise. Network modifier ions such as Ca, Mg or Na are added to the glass structure by ionic bonds to oxygens. Modifying the glasses composition and structure can affect the thermal properties and dissolution rates, and can provide preferable ions for controlled leaching into the environment (*Figure 2.1*) [36, 42].

The melting temperatures for Si glass can reach as high as 1450 °C [39] whilst PBGs melt between 900-1200 °C [39]. The poor thermal conductivity of glass, results in uneven cooling leading to variation in volume during conventional glass formation. This variation can form large residual stresses within the glass. The thermal conductivity of ordinary window glass is 0.8 $Wm^{-1}K^{-1}$ compared to Al: 205 $Wm^{-1}K^{-1}$ or Cu: 385 $Wm^{-1}K^{-1}$ [43]. To release these stresses, the glass can be heated above the T_g to allow for molecular mobility; a process known as annealing [39]. In transparent optical applications nanophase glass-ceramics <100 nm (crystal size) can be designed

to reduce the thermal expansion coefficient (TEC) and prevent crack propagation [44].

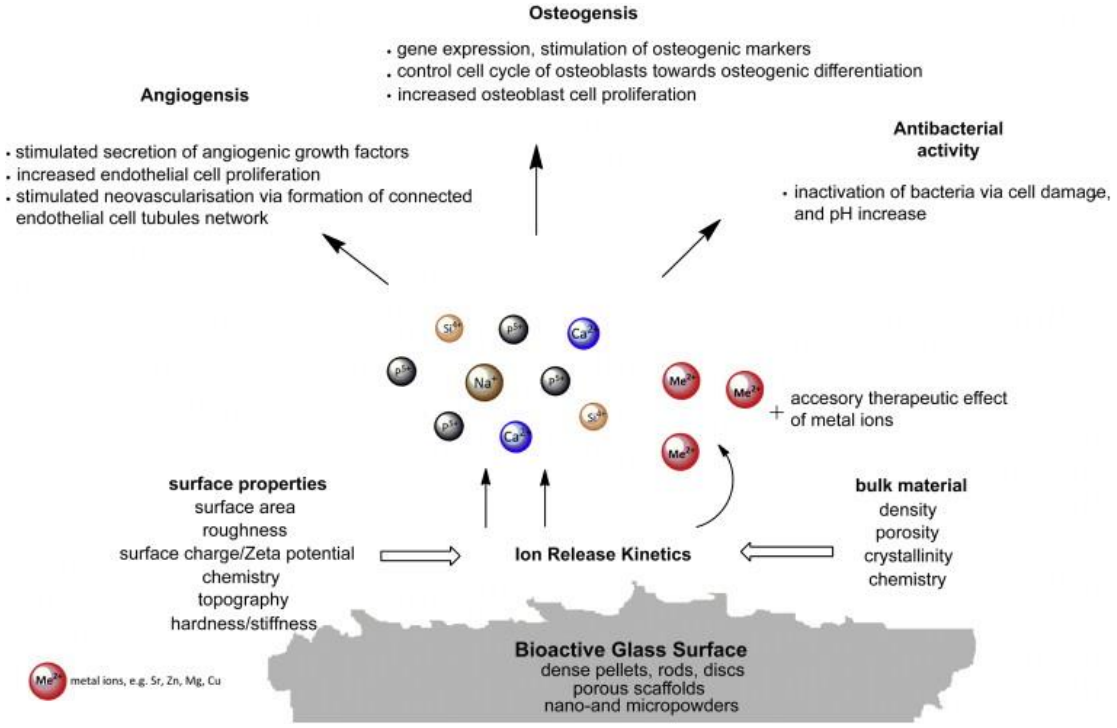

Figure 2.2: Ionic release dependence from bioactive glass and their potential orthopaedic applications [42].

Larry Hench engineered the first bioactive glass termed "Bioglass" in 1969, when he formulated "45S5" 46.1-SiO_2 24.35-Na_2O 26.91-CaO 2.60-P_2O_5 mol%, a glass capable of eliciting advantageous biological responses, specifically the formation of CHA upon dissolution within the body. Since then, formulations have been explored to release therapeutic ions and to improve the rate of osseoconduction [45]. Although bioactive, the structure may only partially breakdown, leaving behind a silica gel layer [45, 46]. In order to achieve specific ion release profiles, glasses derived from PBG were developed [36]. Bunker *et al.* was the first to publish in 1984 on the degradation properties of PBG in distilled water, showing complete dissolution of ternary glass compositions at rates associated with their structural properties [34].

PBGs are less durable then their silicate counterparts, attributed to their structural arrangement and hydration ability. Both form tetrahedral structures however the Si and P have a charges of 4+ and 5+ respectively, leading to the formation of 4 single oxygen bonds or 3 single and 1 double bond, forming a terminal end unit (*Figure 2.3A*). The network is composed of bridging oxygens (BO) that connect the tetrahedral units through the backbone P-O-P structure. Non-bridging oxygens (NBO) are P=O and $P\text{-}O^-$ bonds where oxygens are terminated by an ionically bound "network modifier". Modifier ions change the properties of the glass due to their valences and atomic properties [34]. Examples include monovalent ions such a Na^+ which depolymerise the network whilst Ca^{2+}, Mg^{2+}, Ti^{4+} are examples which function as network cross linkers, linking together 2 or more tetrahedral units through ionic linkages. The ionic bond strength, whilst related to charge, is highly dependent upon the size, or radius of the atom such that the bonding strength is increased with charge/size ratio [39]. Terminal ionic species such as Na or K in the network lowers the network connectivity, reducing the chemical and thermal durability of the glass.

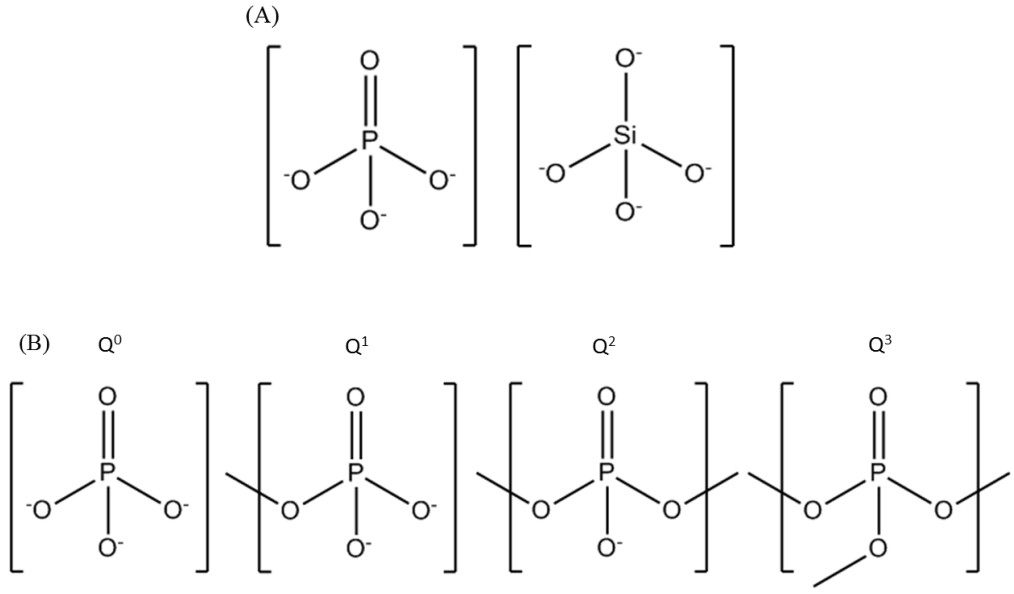

Figure 2.3: (A) Silicate and phosphate tetrahedra. (B) Structural units regarding the number of Bridging Oxygens per tetrahedra.

^{31}P MAS-NMR has provided further insight into the structure of the PBG network; by enabling analysis of tetrahedral bonding configurations (*Figure 2.3B*). The glass structure is described by its Q^n distribution where "n" denotes the number of BO per PO_4 tetrahedra unit. Ahmed *et al.* studied ternary Ca/Na/P glass compositions showing variation in connectivity of the glass network with various proportions of P_2O_5. The findings suggested that 45-P_2O_5 mol% compositions were made up of Q^1 and Q^2 species whilst 50 and 55-P_2O_5 mol% compositions were almost entirely Q^2 species, indicating a near infinite polymer-like chain of PO_4 tetrahedra. Imihezri *et al.* conducted NMR on a number of 40, 45 and 50 mol% P_2O_5 compositions, containing Fe and Ti, which showed a similar Q^2 increase with P_2O_5 content, however, variation due to network cross linking notably depolymerised the network due to Fe inclusion [47]. Compositions composed of Q^1 and Q^2 species are referred to as polyphosphate, entirely Q^2 as metaphosphate, and entirely Q^3 as ultraphosphates (*Figure 2.3B*) [48].

A third group of elements in glasses exists as intermediate oxides including Al, Ti, and Fe which fit into the glass network as either network formers or network modifier ions [36, 39].

The ionic inclusion of elements can assist in bone formation and function to deliver potentially therapeutic ions at the implantation site (*Figure 2.1*). The inclusion of Mg [49, 50], Ca [42, 51, 52], Sr [53, 54], F [55], have been used for bone tissue generation, Ti [52, 56, 57], Fe [58, 59] to improve durability, Cu [60] and Ag [61, 62] for their antibacterial properties. Ca is essential for the formation of, or in the case of glasses, the *in vivo* precipitation of HA as shown for BG 45S5 [46, 63]. It has been commonly included in PBG structures, functioning as a divalent cation leading to reduced solubility as compared to the Na^+ monovalent ion [64-66]. Owing to its structural similarities to Ca, Sr additions have been considered as a potential treatment

for osteoporosis for its ability to increase new bone formation and has been commercially used in "Strontium Renelate" [64, 67]. The substitution of Ca with Sr in silicate based glass (SBG) has shown to improve osteoblast proliferation and osteoclast suppression, enhancing bioactivity [64, 67], resulting from promotion of osteo precursor attachment [68]. Sr increases the network size via an increase in ionic radius, maintaining charge for an increase in glass solubility. This has been attributed to an increased rate of apatite formation [64, 67]. Sr additions in PBG have been explored, and has been suggested by Massera *et al.* to facilitate apatite formation of a PBG composition in Simulated Body Fluid (SBF) [53, 54]. The precipitated layer shown by cross sectional analysis was not confirmed by EDX or XRD and therefore may be misinterpreted as apatite. Abou Neel *et al.* showed that biocompatibility was improved with up to 5 mol% Sr substitution in comparison to Ca inclusion [53]. Whilst the addition of Ti was proven to further enhance activity of MG63 cells relating to network stability [69]. The greater density of Sr, and similar bone integration properties to Ca leads to a densified bone structure [53]. Sr on its own has been applied by magnetron sputtering for bone ingrowth and showed an increase in bone growth for coatings thickness up to 1 μm. *In vivo* tests in rats showed median bone formation of 53%, 4 weeks post implementation whilst the control showed 0%, Post 1000 nm cell proliferation decreased as inflammation occurred due to the formation of strontium hydroxide, raising the local pH, whilst pH of 8.5 was seen to be most effective for bone growth formation [70]. Sr has also been co-sputtered into an HA lattice via RF magnetron sputtering (RFMS) showing its potential inclusion for PBG coating structures [71].

MgO also fits into the glass structure as Mg^{2+} and improves durability of the structure when compared to Ca and Sr, leading to improved biocompatible performance [50].

Mg, however has been cited as an inhibitor to crystallisation of apatite during formation, leading to the stabilisation of an amorphous HA layer [72, 73]. For a significant variation in dissolution rates Fe and Ti have been incorporated in PBG structures. Fe_2O_3 up to 5 mol% in PBGs has slowed glass dissolution resulting from increasing cross linking between phosphate tetrahedra as Fe may exist in the oxidation state (III) [59]. Substitution of CaO with 4-5% Fe_2O_3 mol% was sufficient for cell attachment and differentiation as Fe increased chemical durability stabilising the biocompatibility of glass fibres [59]. Yu *et al.* showed durability of Fe_2O_3 containing glasses with 43 mol% to be 100 times greater than window glass, resulting from the formation of Fe within the back bone as P-O-Fe [58]. Metallic Ti implants have been utilised as structural implant materials, including dental screws and hip stems, whilst its inclusion within the glass structure leads to the formation of Ti^{4+} cross linkers and formation within the backbone as P-O-Ti, similarly to Fe, improving durability [56]. Ti in PBG has been suggested by Kasuga *et al.* to form Ti-OH^- nucleation points for the precipitation of the apatite [52]. Kasuga *et al.* prepared PBGs by bonding powdered glass to Ti29Nb13Ta4.6Zr alloys by heat treatment during which the oxide layer bonded to the glasses. The glass ceramic formed, contained crystals of TCP [74]. Abou Neel *et al.* demonstrated the ability of up to 10 mol% CuO within the structure of fibres to prevent bacterial attachment of Staphylococcus Epidermidis within 3 h [60]. Cu can function in the structure as either Cu^{2+} or Cu^+ as well as forming within the structure backbone as P-O-Cu [75-77]. Ag up to 5 mol% has functioned as Ag^+ within the PBG structure for its potent antibacterial properties [78].

2.2 Thermodynamics of PVD Glasses

PVD provides a means to condense PBGs below their T_g, enabling them to surpass the kinetic barriers associated with conventional quenching [79]. The stability of

inorganic PVD glasses has not been shown however the unusual stability of organic glasses such as ethylbenzene, PMMA and indomethacin has previously been compared to their super-cooled equivalents [41, 80-82]. Low enthalpy states, characteristic of ultra-stable glasses may be attained within such structures due to the PVD process aiding prolonged molecular mobility [41, 79, 82, 83]. In contrast, during quenching or super-cooling, amorphous structures freeze in high enthalpy, stressed states due to the near instantaneous cooling rates necessary to prevent crystallisation during formation (*Figure 2.1*) [84].

Relaxation is commonly facilitated via thermal aging, at temperatures in the vicinity of the T_g leading to the suggestion that relaxation of quenched glasses may require thousands of years of aging to obtain similar levels of relaxation produced during PVD [85]. Kearns *et al.* found that indomethacin required 7 months of aging to approach similar relaxation to a PVD structure, deposited over a period of 60 min [82]. As molecular relaxation occurs, glass systems produced by PVD may have additional implications on their short-range microstructures, leading to unique properties compared to compositionally similar melt quenched glass [41, 79].

2.3 Dissolution of Silicate Based Glass

Dissolution of SBG involves the hydration and hydrolysis reaction of the Si-O-Si bonds. This leaves behind a stable silica gel Si-OH layer, preventing complete dissolution in the media; enabling its function is its ability to form osteoconductive HA [39], which is a common *in vitro* assessment of bioactivity by submersion of the material in SBF to observe the potential growth of a biological like apatite in solution (ISO 23317:2014). SBF is supersaturated with respect to HA. With the inclusion of Ca^{2+} and PO_4^{3-}, precipitation of apatite has been known to form spontaneously in solution alone, given nucleation points within the fluid container [86]. In essence the

reliability of the test may be questionable and shall only be considered an initial, *in vitro* indication of suitability for bioactive reactions in the body pending further cell studies and *in vivo* testing. A series of characterisation techniques including, SEM, EDX, XRD, FTIR, and Raman can be used to assess the composition and structure of visibly apparent crystal formation prior to definitively determining the presence and growth of apatite [87]. *Figure 2.4* shows SEM micrographs of precipitated apatite layers by cross sections analysis of a glass ceramic apatite-wollastonite, and formation of apatite on a titania gel layer [86, 88].

In 2006 Kokubo *et al.* reported a revised SBF methodology and composition to produce media similar to human blood plasma which is most recently reflected in ISO 23317:2014. Kokubo had originally created SBF in 1980. Previous iterations, were found to be deficient in SO_2^{4+} whilst further iterations were rich in Cl^- ions leading to the improved formulation to account for each imbalance [86]. Specific SBF formulations can be found in the methodology *Section 3.24*.

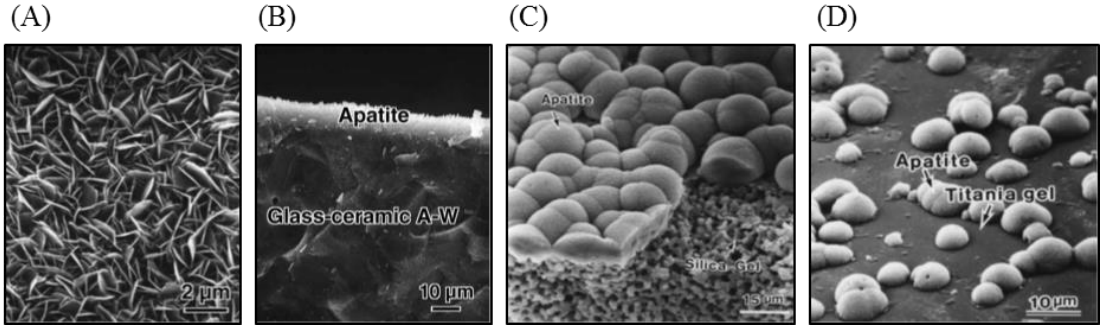

Figure 2.4: Apatite formation precipitated in SBF solution of an AW glass ceramic as shown by Kokubo et al. [86].

Hench's silicate Bioglass 45S5 (BG 45S5) has been known for decades to precipitate a CHA layer in solution [46]. The mechanism of apatite formation is a progressive process involving the leaching of network modifying ions, raising the local pH, and the loss of soluble silica in solution. A stabilised silica layer is formed and the pH rise leads to precipitation out of solution of Ca^{2+} reacted with PO_4^{3-}. As Ca ions continue

to leach the layer reorders to a crystalline HA. HA formation has been preceded by the formation of amorphous Calcium Phosphate, Brushite and Tricalcium Phosphate [89, 90]. Silica glass coatings prepared by sol gel on 316L stainless steel formed apatite on its surface [90]. Plewinski *et al.* showed crystallisation of 45S5 by heat treatment to stabilise the degradation profile, whilst exhibiting apatite formation [91].

The *in vitro* bioactivity following submersion in SBF solution leads to formation of a bone like CHA layer for compositions of silicate glass which are found to be within Hench's bioactivity triangle (*Figure 2.5*). The ability of a glass to form CHA has been suggested to be closely related to a compositions dissolution rate in media with glass containing greater than 60 mol% SiO_2 unable to show such formation as a result of their high durability. Furthermore the ability for a glass to readily release its cations is a critical occurrence for the creation of Si-OH nucleation groups [45].

From the dissolution of silicate glass to the formation of CHA a systematic process occurs [45].

1. Cation exchange of Ca^{2+} and Na^{+} with H^{+} to form Si-OH^{-} silanol groups.
2. pH increases as alkali ions release into the surrounding media and H^{+} are taken up by the glass. Hydroxyl OH^{-} degrades the silicate network forming $Si(OH)_4$ products in solution
3. A silica rich gel layer may recondense onto the surface.
4. Alkali Ca^{2+} and PO_4^{3-} are then believed to migrate to the surface through the silica gel layer.
5. Hydroxyl and CO_3 groups in solution lead to crystallisation of the formed layer.

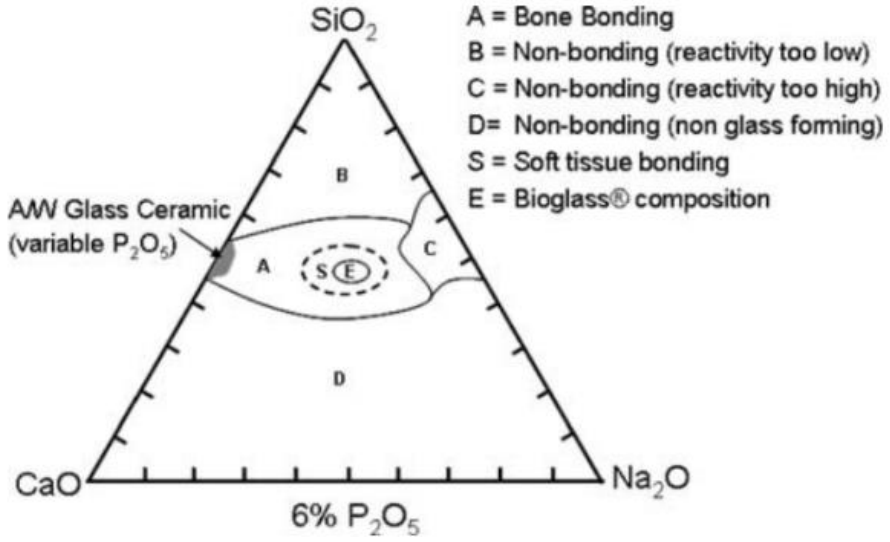

Figure 2.5: Hench's Bioactivity triangle. The assessment of composition within the glass structure to initiate the formation of apatite during dissolution in SBF [45].

Various authors have reported the formation of Ca:P apatite layer in phosphate containing saline solutions [72, 92-95]. Bioglass 45S5 and two other SBGs with SiO_2 content of 53 wt% and 68 wt% were submerged in SBF, Tri-buffer solution (TRIS), phosphate buffered saline (PBS) and osteoblast medium for up to two weeks to observe the surface reactions and potential *in vitro* bioactivity [94]. In TRIS, HA formation was observed during dissolution; however, as the layer formed further dissolution was inhibited as an effective diffusion barrier had been formed. The Ca ion released in PBS led to rapid formation of a Ca:P layer due to high concentrations of phosphates in solution which similarly prevented further dissolution through the newly formed diffusion barrier. ICP-AES of the solution showed an increase in Na and Si, a reduction in P and no change in Ca concentration, suggesting dissolution of the glass and consumption of the released Ca^{2+} ions in the form of precipitation. Cross sectional SEM micrographs of 45S5 immersed in PBS showed a Ca:P layer of ~1 μm similar in ratio to HA and a silicate rich layer of approximately 2.5 μm formed within 4 h of immersion. Both Ca:P and silicate layers were stabilised at the 4 h time point

and ceased to grow over the 2 week time point. In SBF, the Ca:P layer growth stopped after 72 h after growing to 3 μm whilst the silicate layers grew continuously to 32 μm over the 2 week period [94].

A review of 421 papers produced by Cuneyt Tas *et al.* concluded that Ca:P layers could be biomimetically synthesised at (37 °C - pH =7.4) in a range of aqueous saline solutions which specifically contained similar ionic concentrations as extracellular fluid (ECF). The review highlighted synthesis in Dulbecco's Modified Eagle's Medium (DMEM) and SBF whilst mentioning over a dozen solutions similar in composition to the ECF [92]. Particles were formed following Ca:P synthesis in DMEM solution and were found to be amorphous using X-ray diffraction. The coverage of precipitation was reported to increase and stabilise by 48 h on a glass slide test specimen [72, 92].

Varila *et al.* attempted to quantify dissolution through mass changes, however, this proved problematic as dissolution was coupled with Ca:P formation on the surface, thus the net mass change was equated as dissolution + layer formation. When 45S5 was submerged in PBS a net mass change of less than 0.2% over a 2 week test period was seen. The mass change was suggested by the author to be the result of counteracting reaction of dissolution and layer formation and therefore mass change was not indicative of the dissolution. In contrast, pH increased from 7.4 to 7.8 during degradation of BG 45S5, when submerged in PBS for 1 week, apparently stabilising after 72 h in solution utilising a Surace area:Volume ratio of 0.4 cm^{-1} [96].

Precipitation of apatite is uncommon in PBS, however it has been reported for SBG glasses within 3 d in solution for a Na-6, K-12, Mg-5, Ca-20, P-4, Si-53 wt% composition [97]. Reactivity of endodontic Ca:Si based cements tested in PBS showed precipitation of apatite with Ca:P ratio of 1.6 to 2.0. The Ca^{2+} release rates

were believed to be influential in producing biological like apatite in solution as Ca ions are especially reactive in phosphate containing solutions such as PBS [95, 96]. In fact it is recommended that phosphate containing physiological media should not be used for an accurate analysis of dissolution as HA commonly forms in solution. Fargerlund *et al.* recommended TRIS for dissolution analysis as HA can only form given leaching of Ca and P in the correct proportions [95]. The author also observed the formation of a biological Ca:P apatite ratio within 4 h of Bioglass submersion in PBS, greatly exceeding any rate of formation observed in SBF whilst no formation was observed in TRIS. This has been attributed to the abundance of phosphate in the PBS media in comparison to SBF [95].

2.4 Dissolution of Phosphate Based Glasses

Degradation studies on PBGs have frequently been conducted using deionised water (deiH_2O) and distilled water (dH_2O) [34, 38, 66, 98, 99]. More practical biomedical applications use *in vitro* media to mimic conditions within the body, with the solution of choice closely related to conditions at the point of use. For example SBF, Simulated Urine (SU), and PBS have been used as dissolution media [61, 86]. SBF and SU mimic ionic concentrations and chemical compositions of human blood plasma and urine respectively whilst PBS is one of many saline solutions which function as a buffering solution to recreate the pH conditions within the body [61, 86, 92]. Bunker *et al.* showed degradation of PBGs to be highly pH dependent, with increased degradation at lower pH [34]. PBS has been the media of choice to observe the *in vitro* dissolution kinetics of degradable polymers and PBGs as the solution buffers to a pH of 7.40 at 37 °C, similar to the physiological pH within the body [38, 100].

The degradation mechanism of melt quenched PBG is well understood, and dissolution rates of such systems have been shown to vary by orders of magnitude based on changes in glass compositions [34, 36, 66, 101]. For examples the range of dissolution based on composition in ternary systems varied from 10^{-4}-10^{-9} g $cm^{-2}min^{-1}$ [34]. PBG degrades in aqueous solution by reacting with H_2O molecules to break the P-O-P bonds and depolymerise the network [34, 99]. The process has been described in three stages for glass containing monovalent cations such as Na. First, the acid/base reaction during which the glass surface becomes saturated with acid H^+ or base OH^- ions, linearly increasing in time until no more uptake is possible (*Figure 2.6*) [34, 99]. Secondly, H_2O molecules hydrate the network by diffusion showing an exponential degradation profile of $t^{1/2}$ [34]. Bunker *et al.* described the third linear dissolution phase as a hydrolysis reaction upon which the polymeric chains began to disentangle and separate completely [34].

Bunker *et al.* were the first to publish on the dissolution mechanism of a ternary PBG system in dH_2O and showed that glasses doped with alkali ions of Na, Li or K reduced in durability with increasing alkali content such that elements with greater atomic radii added in the same proportions degraded faster. Interestingly the dissolution was uniform for the alkali ions present rather than pre-selective leaching of certain elements in both the $t^{1/2}$ and the linear phase. The stoichiometry therefore remained constant throughout degradation [34]. Degradation is function of pH, such that dissolution may be increased by up to 100 times in various solutions.

Bunker *et al.* tested the hypothesis that dissolution would stop when the glass became saturated in less soluble phases, finding that crystalline HA precipitated and did not dissolve. However, the remaining soluble species continued to dissolve in solution whilst the crystals continued to grow. Post-dissolution, the solution was saturated with

Ca and P ions, whilst no glass structure remained [34]. Haque *et al.* reported the peeling of 40-P_2O_5 24-MgO 16-CaO 16-Na_2O 4-Fe_2O_3 mol% fibres in dH_2O following 8 h degradation in water described as a form of pitting corrosion [102]. Degradation in PBS of boron containing PBGs showed similar flaking around the fibres [100]. Abou Neel *et al.* experienced a similar peeling effect for Fe containing fibres [98]. This peeling effect in fibres was suggested to be due to the differential hydration between surface and bulk layers leading to tensile forces and subsequent cracking [102, 103].

Comparisons of varying PBG compositions have been undertaken to explore the effects of structural changes in controlling degradation rates [104, 105]. Parsons *et al.* concluded that variation in phosphate content of the glass, relative to degradation and thermal properties were insignificant in comparison to the effects of cross linking in the systems. They attributed the overriding cause of changes in glass properties to the ionic linkages [104]. In addition results presented suggested that increased density played a significant role in reducing degradation rates [104]. However it is widely cited that comparative dissolution rates are primarily related to the network connectivity of the glass structure and are therefore dominated by the covalently bonded P_2O_5 (P-O-P) structure and by ionic cross linking [34, 50, 98, 101, 106].

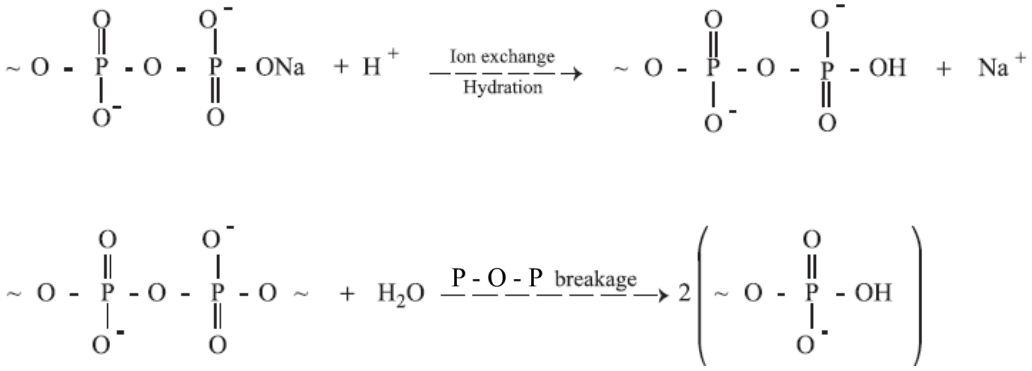

Figure 2.6: Primary acid/base reaction leading to hydration and subsequent chain hydrolysis. Taken from [99].

Various authors have shown the effects of substituting cations in ternary systems, concluding that increasing ionic cross linking decreases dissolution rates [34, 106-108]. Ahmed *et al.* maintained phosphate content at 50 mol% and substituted 0-50% Ca with Mg in a ternary glass structure, the degradation results showed variation in dissolution rates by up to four orders of magnitude. Christie *et al.* devised a simplistic model to predict dissolution with substitution of 5, 10, 15, 20, 25, and 30% Ca with Na, keeping network connectivity constant to conclude that Ca which cross-links two non-bridging oxygen's (NBOs) reduced glass solubility. Gao *et al.* suggested that this effect could partially be explained by inhibition of hydration from network cross linking [99].

Fe and Ti doping have been shown to improve durability [51, 58, 59, 109, 110]. For example certain compositions of binary Fe PBGs have exhibited durability 100 times greater than soda lime glass [58, 109]. It has been shown that Fe can exist in the phosphate structure as a network modifying ion or can be present in the phosphate backbone acting as a network former. In either case Fe can be found in either octahedral or tetrahedral coordination [109, 111]. This cross-linking in the backbone or between the phosphate chains is thought to be responsible for the greatly improved durability.

Ahmed *et al.* demonstrated that the cytocompatibility of quaternary Fe containing PBGs was improved with the inclusion of 4-5 mol% Fe_2O_3, finding that the least soluble glass formulation was the composition P_2O_5-50 CaO-40 Na_2O-5 Fe_2O_3-5 mol%. The degradation rate was 2.5 mg^{-7} mm^{-2} h^{-1} [59]. In an additional study Ahmed *et al.* considered the effect of substituting Ca^{2+} with Mg^{2+} suggesting that Mg^{2+} improved the cytocompatibility by further stabilising degradation and enabling initial cell attachment [50, 112]. Abou Neel *et al.* suggested that dissolution of the chains in

solution led to formation of phosphoric acid, lowering the pH of the media, leading to auto catalysis [98].

Contact angle values for distilled water on bulk PBGs reported by Abou Neel *et al.* varied from (13.2 ± 1.5°) to (26.4 ± 3.2°) for glasses containing 0-5% Fe [98]. Abou Neel *et al.* suggested the variation in polarity was due to P-O-P bonding in the wetted surface layer and in particular, due to the ease of chain hydration with less Fe to disrupt the P-O-P hydrophilic bonds [98].

Gao *et al.* suggested a model relating the distance of hydration into the glass surface, following initial exposure in a solution. They suggested that the rate of hydration is fastest during initial exposure and water diffusion decreased with thickness. This is followed by a steady state hydration rate during which degradation becomes linear. In a separate theory they proposed that the initial $t^{1/2}$ exponential stage could be related to pre-hydration of the P-O-P linkages due to atmospheric moisture during sample preparation [99].

The processing route also influences the degradation. For example thermally annealed glasses degraded at a slower rate to their melt quenched counterparts [113-115]. Cozien-Cazuc *et al.* showed annealing at 5 °C below the T_g for fibres, reduced dissolution by half and suggested that the significant difference in thermal history and equally the greater surface to volume ratio of fibres compared with melt quenched glasses would lead to more efficient annealing [114]. Annealing of glasses would allow the structure to re-orientate to its more thermodynamically stable position, consequently relieving internal stresses [114, 115].

Table 2.1 shows the variation that exists in literature within reported dissolution rates. Unfortunately the methodologies used varied considerably, specifically dissolution

times, medias and experimental methods, making systematic comparison difficulty. However within each publication the effects of independent variable such as Ca, Mg, Ti or Fe inclusion were assessed.

Uo *et al.* found a reduction in degradation rate for ternary glasses containing Na, Ca and P, degraded in SBF attributed to the presence of already soluble species in solution [105]. In contrast the behaviour of less soluble glasses in SBF were shown to precipitate apatite. The dissolution of the amorphous phase within Ca:P invert glasses and glass ceramics containing Na and Ti, specifically the composition 60-CaO 30-P_2O_5 3-TiO_2 7-Na_2O mol% have precipitated bone-like apatite phases of β-$Ca_3(PO_4)_2$ and β–TCP showing potential bioactivity of PBG. For a 10 d post submersion an apatite layer measuring 5 μm in thickness was observed by Kasuga *et al.* [52]. It has been suggested that for Ca:P glasses to exhibit bioactivity in SBF the glasses must release a considerable (unquantified) amount of Ca requiring the production of invert glasses as well as nucleation points such at Ti-OH groups for apatite formation [57].

Table 2.1: Degradation rates reported in literature for a range of glass compositions with modifying ions. A notable variation in measurement criteria and media specifications exists, increasing the complexity of cross analysis.

Formulation mol%	Degradation Rate	Substitution	Measurement Criteria and Media	Reference
50-P_2O_5 10-CaO 40-Na_2O	30.0 x 10^{-4} g cm^{-2} h^{-1}	Ca^{2+} for Na^{+}	Glass annealed deionised water 20 °C	[34]
50-P_2O_5 20-CaO 30-Na_2O	1.8 x 10^{-4} g cm^{-2} h^{-1}			
45-P_2O_5 30-CaO 25-Na_2O	12.7 x 10^{-4} mg cm^{-2} h^{-1}	Ca^{2+} for Na^{+} and variation from 45 to 55 P_2O_5	Glass annealed distilled water 37 °C	[66]
45-P_2O_5 40-CaO 15-Na_2O	1.6 x 10^{-4} mg cm^{-2} h^{-1}			
55-P_2O_5 30-CaO 15-Na_2O	3.5 x 10^{-4} mg cm^{-2} h^{-1}			
55-P_2O_5 40-CaO 5-Na_2O	3.1 x 10^{-4} mg cm^{-2} h^{-1}			
40-P_2O_5 25-CaO 35-Na_2O 0-MgO	1160.0 x 10^{-4} % weight loss h^{-1}	Mg^{2+} for Na^{+}	Deionised water adjusted to pH 7.4 for 700 h	[50]
40-P_2O_5 25-CaO 15-Na_2O 20-MgO	48.0 x 10^{-4} % weight loss h^{-1}			
50-P_2O_5 30-CaO 19-Na_2O 1-Fe_2O_3	4.6 x 10^{-4} mg cm^{-2} h^{-1}	$Fe^{2+/3+}$ Fe may fit into the backbone [58]	Glass fibres distilled water 37 °C	[59]
50-P_2O_5 30-CaO 15-Na_2O 5-Fe_2O_3	0.3 x 10^{-4} mg cm^{-2} h^{-1}			
50-P_2O_5 30-CaO 20-Na_2O	4.0 x 10^{-4} weight loss % mm^{-2} h^{-1}	Ti^{4+} for Na^{+} Ti may fit into the backbone [56]	Pure water adjusted to pH 7.0 37 °C 405 h	[116]
50-P_2O_5 30-CaO 15-Na_2O 5-TiO_2	1.0 10^{-5} weight loss % mm^{-2} h^{-1}			
45-P_2O_5 20-CaO 35-Na_2O	5.7 x 10^{-4} g cm^{-2} h^{-1}	Ag^{2+} and Cu^{2+} for Na^{+} Cu may fit into the backbone	Distilled water and artificial saliva ~175 h 5h	[117, 118]
	3.5 x 10^{-4} g cm^{-2} h^{-1}			
45-P_2O_5 20-CaO 30-Na_2O 5-AgO	3.9 x 10^{-4} g cm^{-2} h^{-1}			
	7.1 x 10^{-4} g cm^{-2} h^{-1}			
45-P_2O_5 20-CaO 30-Na_2O 5-CuO	4.4 x 10^{-4} g cm^{-2} h^{-1}			
	3.6 x 10^{-4} g cm^{-2} h^{-1}			
40-P_2O_5 24-MgO 16-Na_2O 20- Na_2O	0.10 x 10^{-4} g cm^{-2} h^{-1}	Bulk glass vs. fibres vs. annealed fibres and iron inclusion $Fe^{2+/3+}$ Fe may fit into the backbone	Glass annealed deionised water 37 °C	[114]
	0.10 x 10^{-4} g cm^{-2} h^{-1}		Fibres deionised water 37 °C 20h	
	0.07 x 10^{-4} g cm^{-2} h^{-1}		Fibres deionised water 37 °C annealed 40 h	
40-P_2O_5 24-MgO 16-Na_2O 16-CaO 4-Fe_2O_3	Ranged from 4.9 x 10^{-8} ,4.5 x 10^{-9} g cm^{-2} min^{-1} 8 x 10^{-10} g cm^{-2} min^{-1}		Fibres in deionised water pH 7.4 37 °C Measured from 72 h, 6 weeks through the origin and between 8-12 weeks.	[102]

2.6 Anti-Infection Devices

Bioactive glasses have been under investigation as antibacterial carriers similar in application to current non-degradable PMMA cements. Intravenous and surgically placed antibacterial agents in the event of bacterial infection can be costly and detrimental to the reconstruction of the implant location. There is the possibility for a bacterial film to attach and grow on the outer layers of these permanent materials, leading to secondary infection. Bacterial removal is nearly impossible without surgical intervention. Bioactive glasses were shown to carry antibacterial ions whilst the eventual result is the development of HA for osseoconductivity [119]. Similarly collagen sponge and polylactic acid (PLA) are biodegradable materials which may carry antibiotics; capable of rapid release of agents by breaking down into monomers within the first 2 h [119].

The concern with bioactive glasses is the potential change in local pH during the early stages of dissolution. The example given by Rahaman *et al.* is the change in local pH from 7.4 to 11.7 within 8 h for a bioactive glass in SBF [119].

Ferraris *et al.* experimented with Ti and Ti6Al4V implants that were acid etched in hydrofluoric acid to remove the TiO_2 oxide layer and treated in hydrogen peroxide containing Ag ions, leading to oxidation in solution and the embedding of nanoscale Ag ions into the substrate surface. Results suggested Ag leaching in solution in SBF and development of a Staphylococcus aureus inhibition zone. Similar tests in water showed no such antibacterial properties [120]. The cell data presented suggested cytotoxicity of Ti7A4V/Ag samples attributed to Ag ion release [120]. A study showing the effect of bioactive glass with Ag compared with Ti on its own showed that the infection rate was reduced from 100 to 70% after 6 weeks. This demonstrated a strong case for the use of bioactive glasses as antibacterial coatings. The inclusions

of both Ag and Cu in glasses have shown an ability to reduce bacterial attachment and may be included into the structure of sputtering compositions [121]. Ag may be more effective in fighting bacteria in comparison to Cu [60, 62].

2.7 Alternative Coating Methods for the Deposition of Glasses

Conventional plasma spraying remains the primary method of orthopaedic coating deposition; pre-existing and emerging technologies are demonstrating novel applications within the field. Lee *et al.* showed the successful plasma sprayed coating of Ti6Al4V substrates with amorphous Bioglass to a thickness of 50 μm [122]. Gomez-Vega *et al.* formed coatings 25-150 μm thick by an enamelling process by which a Ti6Al4V substrate was dipped into a molten glass mixture and removed to quench (*Figure 2.8B*) [123]. This method can alternatively be conducted by melting the glass into the substrate material [124]; however the thermal expansion mismatch usually leads to interfacial stresses and poor adhesion [123, 125]. Bolelli *et al.* suspended particles in an isopropanol and water mixture to deposit via suspension high velocity flame spraying (*Figure 2.7A and Figure 2.8A*) [126].

The inherent temperatures associated with thermal processes of plasma/flame spraying, or hot isostatic pressing, make the production of either adherent or amorphous glasses impractical without, delamination, cracking or crystallisation. The methods of Electrophoretic Deposition (EPD), Sol-gel, and Physical Vapour Deposition (PVD) may be more appropriate for the production of thin adherent amorphous glass coatings. Thin coatings in particular may be desired due to brittle failures associated with shear during implantation (see *Section 1.3*) for coating failure mechanisms.

SBG glasses and HA have been incorporated by EPD; a process by which suspended charged particles migrate to an electrically charged substrate material (*Figure 2.7B and Figure 2.8C*) [127]. HA deposition for 1 minute periods with various TiO_2 interlayers on Ti6Al4V substrates showed maximum shear adhesion properties of 21.0 MPa as shown by Albayrak *et al.* [128]. Improvements to 47.0 MPa was shown by Chen *et al.* on roughened substrates [129]. The benefit of this method is the ability to co-deposit in suspension. Coatings may be applied to 3D microstructures, with the capability of coating into porous materials [127]. Pishbin *et al.* co-deposited Bioactive glass, chitosan and Ag nano particles showing that they could inhibit bacterial growth and precipitate apatite *in vitro* [130].

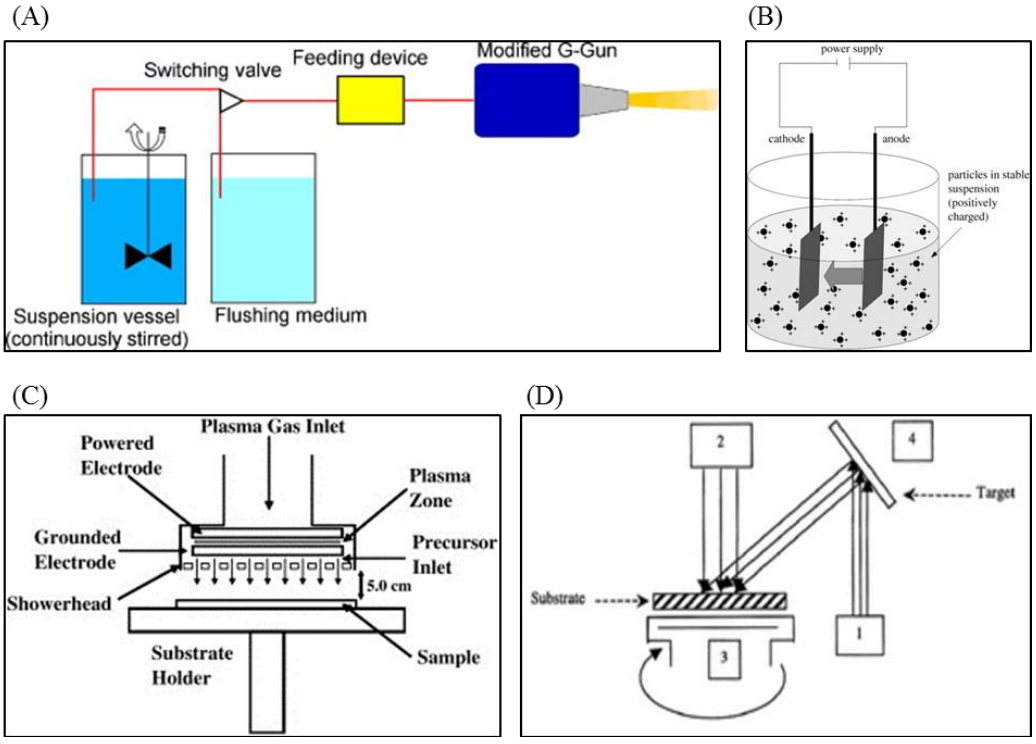

Figure 2.7: Alternative coating deposition methods for deposition of bioactive glasses. (A) Suspension flame spraying [126] (B) Electrophoretic Deposition [127](C) Atmospheric plasma [131](D) Ion beam [132].

Sol-gel coatings may be formed at room temperature by placing or coating a 3D material with a sol metal oxide suspension which is polymerised by a hydrolysis reaction to form a gel. Subsequent drying of the gel leads to densification. Bioactive

amorphous glasses were produced by this method [133]. Sol-gel glasses showed bioactive potential in SBF precipitating CHA layers [134]. Furthermore *in vivo* test in rabbits demonstrated their ability to promote bone apposition and integration of alumina implants [133]. The unique advantage of the sol-gel method is its ability to produce homogenous coatings on substrates from polymers to ceramics [45]. Sol-gel can however be a lengthy process, for example Hamadouche *et al.* produced a 5 μm thick coating, which required 5 d of cumulative aging, drying and stabilisation to produce densified glasses, holding at temperatures of 60 °C followed by a 48 h heat treatment to 900 °C [133]. Liu *et al.* quoted pull out adhesion strengths averaging 44 MPa of HA sol-gel coatings on stainless steel [135] whilst Kim *et al.* showed strengths on Ti of 40 MPa [136].

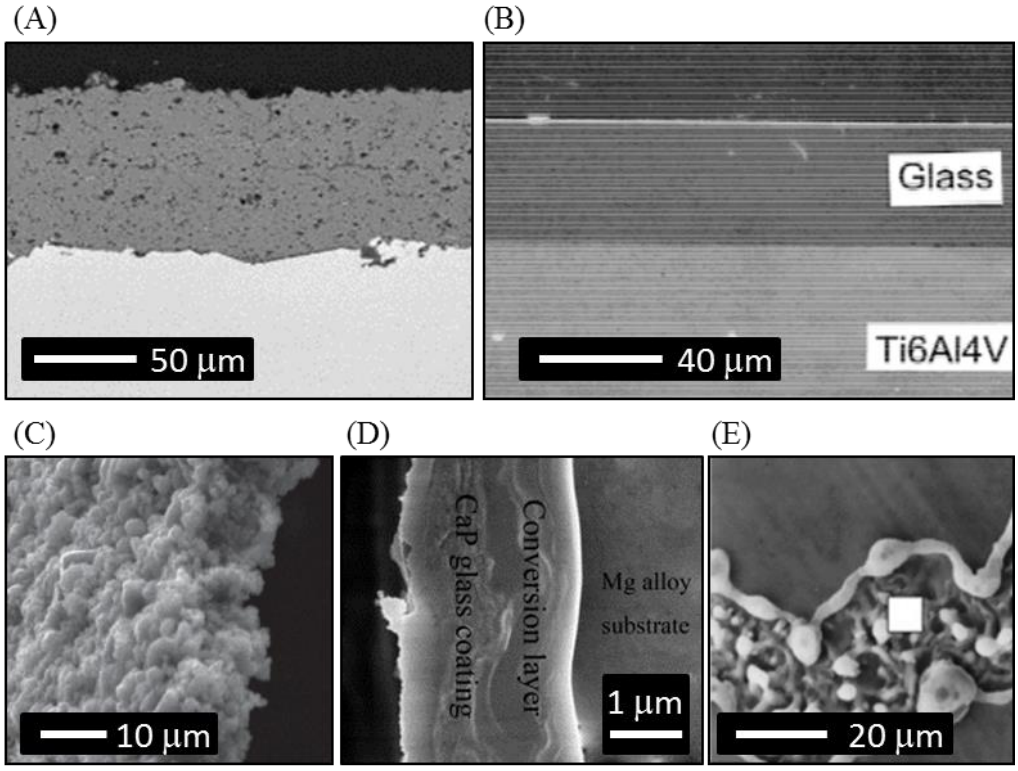

Figure 2.8: SBG glass via (A) Flame spraying [126](B) Enamelling [123] (C) Electrophoretic Deposition [127] (D) Ca:P glass Sol Gel [137] (E) Ion Beam SBG [132].

Polymer substrates were coated via an atmospheric plasma deposition method in which a precursor suspension was injected into a helium/oxygen plasma and

deposited at temperatures of 70-120 °C. Nowling *et al.* deposited these coatings at rates of up to 91 nm min^{-1} however the structures were compromised outside of vacuum conditions via the inclusion of carbon and hydrogen into the structures [138]. A similar methodology was used by Ladwig *et al.* on Fe substrates (*Figure 2.7C)*[131]. The PVD methods of ion beam sputter deposition [132] have been used for both SBG production and for the deposition of Ca:P coatings (*Figure 2.7D and Figure 2.8E*). Scratch adhesion testing up to 1 N showed no delamination whilst Ong *et al.* deposited Ca:P coatings quoting adhesion strengths of up to 40 MPa [139].

Table 2.2: Review of coating methods for the production of HA coatings. Table taken from Yang et al. [140].

Technique	Thickness	Advantages	Disadvantages
Thermal spraying	30–200 μm	High deposition rates; low cost	Line of sight technique; high temperatures induces decomposition; rapid cooling produces amorphous coatings
Sputter coating	0.5–3 μm	Uniform coating thickness on flat substrates; dense coating	Line of sight technique; expensive time consuming; produces amorphous coatings
Pulsed laser deposition	0.05–5 μm	Coating with crystalline and amorphous; coating with dense and porous	Line of sight technique
Dynamic mixing method	0.05–1.3 μm	High adhesive strength	Line of sight technique; expensive; produces amorphous coatings
Dip coating	0.05–0.5 mm	Inexpensive; coatings applied quickly; can coat complex substrates	Requires high sintering temperatures; thermal expansion mismatch
Sol–gel	< 1 μm	Can coat complex shapes; Low processing temperatures; relatively cheap as coatings are very thin	Some processes require controlled atmosphere processing; expensive raw materials
Electrophoretic deposition	0.1–2.0 mm	Uniform coating thickness; rapid deposition rates; can coat complex substrates	Difficult to produce crack-free coatings; requires high sintering temperatures
Biomimetic coating	< 30 μm	Low processing temperatures; can form bonelike apatite; can coat complex shapes; can incorporate bone growth stimulating factors	Time consuming; Requires replenishment and a constant of pH of simulated body fluid
Hot Isostatic pressing	0.2–2.0 mm	Produces dense coatings	Cannot coat complex substrates; high temperature required; thermal expansion mismatch; elastic property differences; expensive; removal/interaction of encapsulation material

HA and glass ceramic structures are prominent within the literature by all previously mentioned methods, however the deposition of PBGs and more specifically Bio-related applications remains scarce. Ren *et al.* produced Ca:P glass/MgF_2 multi-layer for corrosion resistance of Mg in SBF via sol gel (*Figure 2.8D)*. Glass was produced using a alkyl phosphate sol, reporting the overall adhesion strength of the glass/MgF_2 layer as 12.3 MPa [137]. RF sputtering and Ion beam sputtering were used for metal-free PBGs as early as 1992 and 1993 respectively for semiconductor applications [121, 141]. Yang *et al.* reviewed 45 publications to assess the pros and cons of production by each method for HA as presented in *Table 2.2* [140].

2.8 RF Sputtering of Ca:P, HA and Bioactive Glass

The available literature demonstrates extensive work on the sputtering of amorphous Ca:P, subsequently crystallised to form HA coatings. In addition, little work has been carried out on the sputtering of SBG whilst no references have been found to explore the potential of PBG. Therefore this section firstly reviews the literature relating to sputtering of Ca:P and HA coatings followed by sputtering of SBG and a final section reviewing the mechanical properties of sputtered coatings.

As early as 1992 Ong *et al.* utilised Ion beam sputtering to deposit amorphous Ca:P coatings of between 0.6 and 1 μm thick. Samples were heat treated in air at 600 °C for 1 h prior to slow cooling or quenching in water [139]. As sputtered coatings dissolved within 4 h by observation of the Ca/Ti ratio in EDX beginning at 0.27 and declining by 73%, 97% and 100% within 1, 2 and 3 h. Heat treated samples in saline solution, degraded over a 9 week period.

RF sputtering of Ca:P glasses including pyrophosphates and HA were explored by a number of groups from as early as 1993 and has been found to be an appropriate

coating method, producing uniform, thin coatings, with excellent adhesion strength [142-147]. In what was the first known deposition from literature, of amorphous Ca:P by magnetron sputtering Jansen *et al.* formed crystalline coatings of Ca:P ratio 1.9-2.5, showing *in vitro* and *in vivo* biocompatibility [148] and then subsequently explored varying processing methods for production as shown in *Table 2.3*, which reviews the processing parameters used by those in literature to produce RFMS HA and Ca:P coatings. Others such as, Yamashita *et al.*, Ong *et al.,* Ding *et al.* and Lo and Grant, explored amorphous and crystalline HA over the following decade [149-155]. Since then Boyd *et al.*, Coe *et al., and* Marriot *et al.* explored doped-HA and co-deposition methods [71, 156-160], As-sputtered coatings have typically been deposited amorphous as evidenced from their X-ray diffraction patterns [143].

In 1994, Yamashita *et al.* produced a range of binary Ca:P glasses with target ratios between 0.6 and 0.75, producing as deposited amorphous thin film-coatings with Ca:P ratios of HA (1.67), pyrophosphate (1.0) and tri-calcium phosphate (1.5) [151]. The variation between target and coating stoichiometry indicated the occurrence of preferential sputtering in PBG leading to increases in Ca:P ratio. Similar this was observed from crystalline HA targets. A variation in stoichiometry was observed from target to coating by all authors mentioned with only Boyd *et al.* showing a decrease in Ca:P ratio to 1.42 when co-sputtering Ti and HA [157] (see section 2.9) for preferential sputtering. Lo *et al.* deposited a multi-layer of TiAlVN using reactive sputtering of 6% N_2/Ar of Ti6Al4V followed by a Ca:P sputtered layer, subsequently heated to form HA, showing that interfacial adhesion was improved by the use of inter-layer [147].

Table 2.3: RFMS of HA coatings found within the literature from 1993 onwards.

Rig	Target and Substrate	Power and Pressure	Deposition Rate and Thickness	Coating	Reference and Year
Edwards ESM 100	Ti6Al4V substrates HA plasma sprayed Target	RF 13.56 MHz 800 W Argon 0.5 Pa	9 nm min^{-1}	Ca:P ratio of 1.93 As deposited with HA phases	[148] 1993
Not Stated	50 mm Target of $CaCO_3$/Orthophosphoric Acid to form Ca:P and annealed. Al_2O_3, Y_2O_3-ZrO_2 , Pt, Ti and fused quartz substrates	RF Not Stated 7.6 w cm^{-2} 0.67 Pa	Thickness not stated 50 mm distance	As deposited amorphous and annealed in air and H_2O vapour up to 1200 °C 1.4 to 1.9 Ca:P ratio (XPS), deposited from targets with ratios 0.60-0.75	[151] 1994
Edwards ESM 100	HA plasma sprayed Target 110 mm diameter substrates were additionally rotated	RF 13.56 MHz 700 W Argon 5 x 10^{-3} mbar	0.5 to 10 µm 200-250 nm min^{-1} 80 mm distance	Amorphous in the case of rotations and static showed crystallite formation. Ca:P ratio ranged from 1.5 and 2.0 (EDX)	[142] 1994
Edwards ESM 100	HA plasma sprayed Target 110 mm diameter P/Rh substrates	RF 13.56 MHz 800 W Argon 5.2 x 10^{-3} mbar	2 mm thickness 8.33 nm min^{-1} 80 mm distance	Amorphous Ca:P of 2.05 decreasing to 1.80 with heat treatment up to 1200 °C	[145] 1996
NCR 3117	Vicor glass substrates HA plasma sprayed Target of unstated diameter	RF (n/s) MhZ 200 W Argon 10^{-4} Torr	3.3 nm min^{-1} 400 nm thickness 80 mm distance	Amorphous Ca:P ratio of 1.9 and 1.8 (XPS) Heat treatment at 700 and 850 °C Time not specified	[149] 1997
Not Stated	Ti6Al4V and Sintered HA Ti6Al4V substrates	RF 13.56 MHz 3.0 w cm^{-2} Argon/ 6% Nitrogen Ar only for HA 2.0 Pa	1 mm thickness 2.1 nm min^{-1} 50 mm distance	TiALVN interlayer beneath as deposited Ca:P of 1.69 Post annealed up to 600 °C to form crystalline phases	[152] 1999
Custom System	HA target bonded to Cu backing via silver loaded epoxy	RF 13.56 MHz 150 W Argon 5 x 10^{-2} mbar	158 nm thickness 0.9 nm min^{-1} 100 mm distance	As deposited Ca:P of 2.09-2.29 (XPS) 4 independent batches	2003 [158]
Edwards ESM 100	2 target co-deposition ($Ca_2P_2O_7$ and CaO) Si (100) substrates	RF 13.56 MHz 200-600 W Argon 5 x 10^{-3} mbar	30 RPM 2 nm min^{-1} 100 nm thickness	Amorphous Ca:P at ratio of 0.6-4.7 (EDX) HT at 650 for 30 min in argon to form HA	[161] 2005
Edwards ESM 100	$Ca_2P_2O_7$ and HA CPTi Substrates	RF (n/s) MHz 400 W Argon 5 x 10^{-3} mbar	2 mm thickness 80 mm distance	Amorphous Calcium Pyrophosphate and HA (EDX) Infrared heat treated 30 s at 650 and 550 °C respectively crystallised the coating	[143] 2006
Custom System	HA Pressed Powder and Ti Target 76 mm diameter Co deposited 45 ° to the substrates Ti6Al4V substrates	RF 13.56 MHz 150 W Argon 2.0 Pa	533 nm and 320 nm for Ti and Ca:P layers 5 h deposition. 100 mm distance	Amorphous Ca:P of 1.42 (XPS) in-situ annealed at 500 and post annealed at 500, 600 and 700 °C	[157] 2008
Custom System	HA and SrHA pressed powder target 76 mm diameter Co deposited from 3 targets 65 ° to the CPTi substrates	RF 13.56 MHz 150 W Argon 15-20 SCCM	204-445 nm thickness 0.7-1.5 nm min^{-1} 100 mm distance	As deposited Ca:P of 1.34-1.79 (XPS) Post annealed at 500 °C to form crystalline phases	[71] 2015

Yongyang *et al.* showed the ratio of Ca:P during dissolution studies of HA were unstable in amorphous structures whilst crystalline coatings displayed steady degradation of the surface, maintaining Ca:P ratio [143].

Van der Wal *et al.* manufactured amorphous Ca:P thin film of 100 nm thick ranging in Ca:P ratio from 0.6 - 4.7. The sample of 1.6 Ca:P ratio was submerged in SBF [161]. Dissolution was quantified as 4.3 and 0.7 x 10^{15} atoms cm^2 min^{-1} following submersion in SBF1 and SBF2. SBF1 referred to stoichiometric SBF solution whilst the Ca and PO_4 concentrations were increase by 1.4x or 2x in solution to produce SBF1.4 or SBF2 [161]. Crystalline coatings annealed for 30 min at 650 °C did not dissolve in SBF1 over a 3 d period however did precipitate a Ca:P layer of 25 nm in thickness in SBF2 after 90 min on the surface with a decreased ratio of 1.2 in comparison to the 1.6 ratio of the coating. This showed that SBF1 was not sufficient for precipitation and a pre-submersion in SBF2 was required to initiate crystal formation. The mechanism of bioactivity was described by an initial induction period in which sediments from solution attached to the coating surface. It was observed that below SBF1.4 all coatings were inert suggesting that manipulation of the *in vitro* assessment was necessary to adhere to the bioactive criteria [161].

Ong *et al.* sputtered coatings from HA targets and heat treated to crystallise coatings at 700 °C and 850 °C. Coatings were compared pre and 1-week post submersion in a simulated fluid described as x-MEM. Fully amorphous coatings dissolved within 3 h of submersion. Pre submersion, crystallite size was significantly greater at 850 °C than 700 °C (58.9 ± 1.1 nm) and (54.7 ± 0.6 nm) respectively attributed to the higher processing temperature. Following submersion, crystal size increased to (59.5 ± 0.8) and (63.8 ± 1.5) nm respectively. The increase in overall crystallinity was attributed to dissolution of the remaining amorphous phases. Ong *et al.* suggested Ca:P ratio was

maintained post treatment and submersion; however the ratio again increased from the target ratio of 1.6 to 1.9 and 1.8 for both samples after deposition and heat treatments. This ratio was reduced 1 week post submersion in SBF to 1.6. A number of reasons could explain these changes in SBF and it is likely coincidence that the Ca:P ratio is the same pre deposition and post processing. Observation of the intermediate Ca:P change suggested preferential sputtering of Ca as the as deposited Ca:P ratio was reported to be different to the target [149].

Wolke *et al.* sputter deposited onto coatings of Ca:P onto Ti substrates 0.1, 1.0 and 4.0 μm were and heat treated via infrared at 425-475 °C. The coatings were tested *in vivo* in rabbits at 1, 4, 8 and 12 weeks. 0.1 and 1 μm amorphous coatings were fully dissolved 1 week post implementation. All heat treated coatings were present 4 weeks post implementation. XRD showed evidence of carbonated apatite. Additionally carbonated apatite was present on the 4 μm thick coated amorphous samples after 4 weeks. The heat-treated coatings detached 12 weeks post implementation, which has been attributed to residual stresses induced through heat treatment as well as the thermal expansion mismatch. Heat treated 1 μm thick coatings on roughened Ti ($Ra \sim 1.40 \pm 0.03$ μm) showed bioactivity within the 12 weeks implementation period, with degradation of only the coating surface. It was concluded that the amorphous phases are unstable whilst overly crystalline phases suffered from cracking, more pronounced in thicker coatings. Bioactivity was not improved by the use of thick coatings so long as the coating was sufficiently thick, stable and adherent to the substrate [162].

Yamashita *et al.* post annealed Ca:P in water vapour via a steam stream between 600-1200 °C to form apatite by hydration of the Ca:P layer, specifically HA [151].

For comparison, the same annealing process was conducted in air. This introduced multiple crystalline phases of different Ca:P ratio. Higher annealing temperature increased the Ca:P ratio of the glasses by reducing P, which evaporated with increasing temperature. Annealing in water vapour was deemed more effective for producing uniform layers [151]. Van Dijk *et al.* crystallised HA in dry argon and argon with water vapour showing crystalline phase formation at ~600 °C [145].

Similarly Yang *et al.* examined the effect of post deposition heat treatment via the inclusion of water vapour during crystallisation. Whilst deposited amorphous, an HA phase was developed at 450 °C in water vapour with crystallisation quantified at 68 ± 2%. Heat treatment in water below this temperature had little effect, crystallising to 2.8 ± 0.6 at 400 °C. Heat treatment in the absence of water vapour at 500 and 600 °C increased crystallinity to (62 ± 2 %) and (67 ± 2 %) respectively, water vapour having no effect. Observation of the coating cross section showed dense homogenous as-deposited coatings, whilst crystallisation at 450 °C in water vapour caused crack formation, attributed to crystal growth within the lattice and material expansion (*Figure 2.9B vs. C*). FTIR PO_4 peaks were observed in as deposited coatings, whilst crystalline coatings exhibited more intense PO_4 peaks with additional the OH^- peak, indicating HA phases [163].

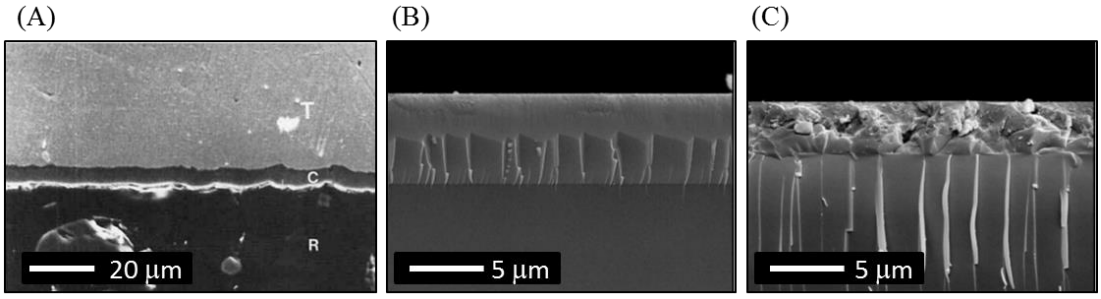

Figure 2.9: As deposited Ca:P coating on Ti6Al4V embedded in resin [164]. Amorphous Ca:P coating and crystalline coating following water vapour heat treatment [163].

Heat treatment during sputtering or post-sputtering has been used to tailor the crystallinity of the deposited coatings for biological stability. Amorphous coatings of both HA and Ca-pyrophosphate applied by RF have been observed to degrade in SBF within 4 weeks [142, 143]. The pyrophosphate coatings have shown a greater tendency to resist crystallisation under post deposition infrared (IR) radiation at 650 °C in comparison to HA coating which crystallised below 650 °C [143]. Gross *et al.* found that crystallisation of Amorphous Calcium Phosphate (ACP) began as low as 500 °C, increasing up to 700 °C, dependent upon the hydroxyl content in the amorphous phase such that greater hydroxyl content required lower activation energy for crystallisation [165].

More recently specifically Boyd *et al.* deposited HA coatings with co-deposition of titanium and Ca:P films to form HA phases with the structural inclusion of TiO_2 [157]. Boyd used various target ramp-in procedures to prevent HA cracking by thermal shock. They explored the compositional changes on the target surface following deposition showing that after 12 h of deposition by ion bombardment, the Ca:P ratio changed from 1.74 to 2.31 as analysed by X-ray photoelectron spectroscopy (XPS) [158]. The ability to control Ca:P ratios by co-deposition of HA, TCP and DCP targets was confirmed [156]. Boyd *et al.* also observed that for films annealed at 600 °C and 700 °C, the Ca:P ratio decreased, whilst at 500 °C, Ca:P ratio were reported to increase, explained by volatile phosphorous evaporating from the surface at lower annealing temperatures. This phenomenon was also observed for *in-situ* annealing at 700 °C [157]. Results showed that complete diffusion of a rutile Ti layer to the surface of the coating occurred at temperatures of 700 °C. XPS surface analysis may not be characteristic of the entire coating [157].

The difference in behaviour between *in-situ* and post annealing has been attributed to the oxygen content in the annealing environment facilitating the formation of TiO_2 and its subsequent diffusion through the coating layers, to prevent phosphorous evaporation and yield a higher phosphorous content at higher temperatures in air. Oxidation of the TiO_2 layer may occur at a lower rate in argon [157]. Takakuwa *et al.* completed an XPS study of TiO_2 formation as temperature increased to 400 °C, showing oxygen deficiency in the surface, which had diffused into the bulk structure. Most recently in 2015 co-deposition was used to formulate Sr substituted HA coatings [71].

Alternatively, coatings have been deposited crystalline by increasing the deposition power. Narushima *et al.* deposited Ca:P films as amorphous at 75 W deposition power however formed HA crystals at 100 and 150 W. This was attributed to an increase in thermal energy upon condensing at the substrate causing crystallisation of the coating [166]. Similarly in deposition of Co2FeSi thin films crystalline grain sizes were found to increase with power and pressure. Pressure of 0.67, 1.34, 2.00 and 2.67 Pa and powers of 25, 75, 100 and 125 W were tested independently. Although not stated this was likely a temperature effect [167]. Yoshinari *et al.* heat treated deposited coatings with infrared radiation at 300, 400, 500, 600 and 700 °C. Degradation was observed in SBF such that amorphous coatings heat treated at 300 °C degraded within 1 day whilst 600 °C were deemed optimal as steady degradation was observed. At 700 °C coatings did not degrade. Observation of the diffraction data showed absence of any amorphous phase from 500 °C suggesting that complete crystallisation by 700 °C stabilised the coating layer. Infrared heating prevented crack formation whilst furnace heating was shown to produce coating cracks [168].

In 2003, Mardare *et al.* was the first to sputter bioactive SBG by RFMS. The applied coatings appeared bioactive in SBF as precipitation of an apatite layer was suggested [169]. Stan *et al.* has published extensive research on the sputtering of bioactive glass, determining the influence of parameters such as gas pressure and sputtering environment on coating deposition and coating stoichiometry [170-177]. The sputtering processing parameters found in literature are presented in *Table 2.5*.

Sputtering tests of bioactive glass of composition 17.25MgO-52.75 $3CaOP_2O_5$-30Si (wt %) showed a successfully deposited thin film layer displaying the formation of an "apatite" layer in SBF solution. Two days immersion showed Ca:P/Mg precipitants at the surface of a coating heat-treated at 950 °C in air for 30 min, as shown in *Figure 2.10* [169]. In critique to this finding by Mardare *et al.,* no XRD, EDX, FTIR or other were presented to support apatite formation whilst the image in *Figure 2.10* is not characteristic features of apatite as shown in *Figure 2.11*.

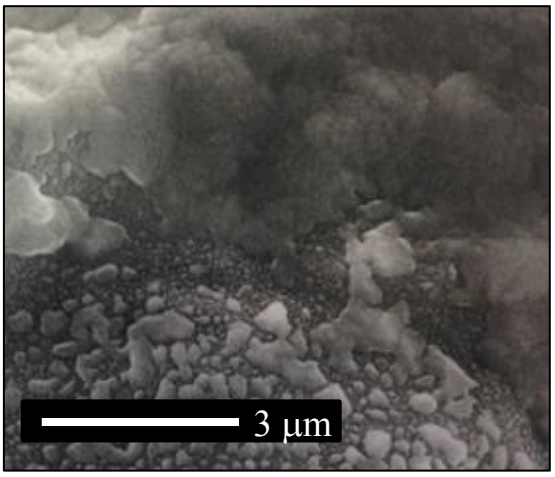

Figure 2.10: Ca:P/Mg precipitation to the surface in bioactive silica glass after two days in SBF [169].

Stan *et al.* deposited from bioactive glass targets, onto Si substrates which were immersed for 30 days in SBF, and appeared to follow the stages of "Hench's bioactivity theory", beginning with the solubility and degradation of the Si network,

followed by the formation of a Ca:P apatite layer at the surface. Si leaching ceased after 7 d in SBF indicating that a continuous formation of a protective Ca:P layer had been formed. 15 d post-submersion signs of crystalline ordering were evident. A partially crystallised CHA layer appeared within the 30th d of testing [173, 178]. The HA layer grew from 500 nm after 15 d with Ca:P ratio of 1.3 to 1200 nm by 30 d with a ratio of 1.77, indicating continuous Ca precipitation [173]. Similarly, the formation of a crystalline CHA layer above a partially dissolved bioactive glass has been reported by Stan *et al.* [172]. Biomineralisation was most efficient in the thickest grown CHA layer [172]. Heat treatment to form silicate crystalline phases Wollastonite and Combeite improved the tendency of Ca:P to form apatite, increasing osteoblast cell proliferation and protein attachment, enhancing bioactivity [175]. The thicknesses of the CHA layers, following 30 d in SBF as shown in *Table 2.4* was formed from a coating deposited in 93% argon and 7% oxygen.

Atmosphere	BG Film Thickness (μm)	CHA Growth 30 d (μm)
100% Argon	0.510	0.7-1.7
93% Argon 7% oxygen	0.380	2.3-3.9
80% Argon 20% Oxygen	0.330	0.3-1.3

Table 2.4: Bioactivity of sputtered bioactive glass with varying argon: oxygen ratio [172].

Resulting from preferential sputtering, as observed with Ca:P coatings, the compositions varied with deposition parameters, specifically due to alteration of gas atmosphere. This ultimately affected the coatings ability to dissolve in SBF solution and to form a silica rich layer, favouring mineralisation of CHA by precipitation of Ca and phosphate ions to the surface. The coatings created in 7% oxygen had the highest Na concentration, favouring dissolution, silica hydration and therefore enhanced bioactivity [172]. An increase in the Na:Ca ratio was thought to increase the growth rate of HA by causing rapid silica hydration as the dissolution process is improved [172].

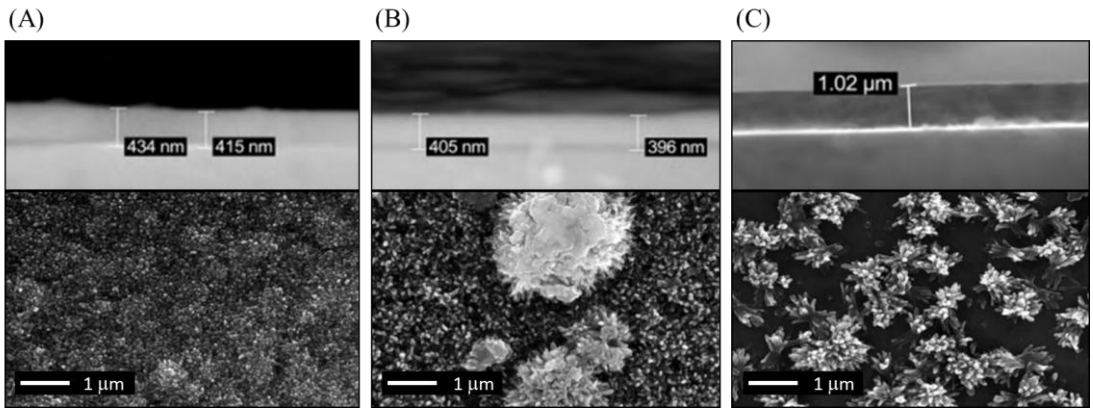

Figure 2.11: (A) BG1 (B) BG2 (C) BG3. Precipitated CHA layer following 30 d of submersion in SBF solution of three compositions produced by Stan et al. [171].

Bioactive glass coatings with film thickness of 646, 510 and 480 nm submerged in SBF for 30 d showed formation of non-stoichiometric CHA layers of 400, 435 and 1000 nm respectively (*Figure 2.11A*, *B*, *C*). The Ca:P ratio of the grown apatite increased with ratios of 1.4, 1.5 and 1.8 respectively [171].

Bioactive glass samples showed preferential leaching of Si, Mg, and Na from the coating [178]. The pH stabilised within 7 d indicating stabilised dissolution, as the soluble silica leached into solution and the Ca:P formed a CHA layer. Ca:P ratio of the grown apatite increased from 1.0 to 1.3 and 1.77 at 7, 15 and 30 d [178].

Table 2.5: RFMS of bioactive glass compositions found in literature. Pull off adhesion has been stated when tested.

Rig	Target and Substrate	Power and Pressure	Deposition Rate and Thickness	Coating	Pull off adhesion	Reference and Year
Not Stated	17.25MgO-52.75 3CaOP_2O_5-30Si (wt %) glass/ceramic sintered powder to 51 mm CPTi substrate and Si wafers	RF 1.78 MHz 100 and 150 W Argon/O_2 1.0 Pa	3.0 and 6.6 nm min^{-1} 120 min Distance not stated	A Ti sub layer was deposited and sample subsequently heat treated at 750 850 in situ or 900 950 and 100 °C for 30 min in air.	Amorphous films ~41.1 MPa HT950 ~16.3 MPa	2003 [169]
UVN-75R1	45S5 Bioglass powder cold pressed to 110 mm CPTi substrate	RF 1.78 MHz 100 W Argon 0.16 and 0.45 Pa	17.0 and 7.0 nm min^{-1} 1020 and 420 nm respectively 60 min 30 mm distance	Ti was co-sputtered as a grading layer for 70 nm Post heat treatment at 700 for 2 h	N/a	2010 [175]
UVN-75R1	Bioactive glass powder comp. SiO_2- 40.1, CaO-29.1, MgO-9.0, P_2O_5-6.3-CaF_2-5.8 B_2O_3-5.2 Na_2O-4.6 wt% cold pressed to 110 mm Si (100) and Corning glass substrates	RF 1.78 MHz 100 W Argon 0.2, 0.3 and 0.4 Pa	9.2,7.3 and 6.9 nm min^{-1} 646.0, 510.0, 480.0 nm respectively 70 min	Deposited amorphous 150 °C substrate temp	N/a	2010 [171] 480 nm samples repeated 2012 [174]
UVN-75R1	Bioactive glass powder comp. SiO_2- 40.1, CaO-29.1, MgO-9.0, P_2O_5-6.3-CaF_2-5.8 B_2O_3-5.2 Na_2O-4.6 wt% cold pressed to 110 mm CPTi and Corning glass substrates	RF 1.78 MHz 100 W Argon and Ar/O_2 7% and 20% 0.3 Pa	7.3, 5.4 and 4.7 nm min^{-1} 510, 380 and 330 nm 70 min 30 mm distance	Deposited amorphous 150 °C substrate temp	~75 MPa Interfacial failure	2009 [172]
UVN-75R1	Bioactive glass powder comp. SiO_2- 55.0, CaO-15.0, MgO-5.0, P_2O_5-10 K_2O-10 Na_2O-5 wt% cold pressed to 100 mm Ti6Al7Nb and Corning glass substrates	RF 1.78 MHz 100 W Argon 0.16, 0.22 and 0.30 Pa	16.3, 13.5, 12.5 nm min^{-1} 980, 810 and 750 nm 60 min 30 mm distance	Deposited amorphous 150 °C substrate temp Post heat treated at 550 °C and 750 °C for the 0.3 sample and subsequently pull off tested	As deposited and HT550 exceed glue strength ~85 MPa HT750 failed at 72.0 MPa	2009 [173]
UVN-75R1	Bioactive glass powder comp. SiO_2- 30.0, CaO-28.6 MgO-17.3, P_2O_5-24.2 Na_2O-5 wt% cold pressed to 110 mm CPTi and Si (100) substrates	RF 1.78 MHz 100 W Argon 0.4 Pa	7.4, 6.1 nm min^{-1} 445.0 and 364.0 nm 60 min 35 and 55 mm distance	Deposited amorphous 150 °C substrate temp Post heat treated at 750 °C	As deposited ~38.2 and ~31.5 MPa and HT750 ~60.3 MPa	2013 [179]
UVN-75R1	Bioactive glass powder comp. SiO_2- 46.1, CaO-28.7, MgO-8.8, P_2O_5-6.2 CaF_2-5.7 Na_2O-4.53 wt% cold pressed to 110 mm CPTi and Corning glass substrates	RF 1.78 MHz 75 W Argon 0.3 and 0.4 Pa and Ar/O_2 10%	20 nm min^{-1} 1000 nm 50 min 25 min distance	Deposited amorphous	51.2 – 62.7 MPa	2014 [180] Adapted in 2015 [177] for dental implants

Silica glasses showed similar behaviour to Ca:P of reduced degradation with increased crystallisation [173]. Massera *et al.* found a peak crystallisation temperature for Bioglass 45S5 of 715 °C, with nucleation occurring from 566 °C [181]. Stan *et al*. showed that post annealing at 700 °C for 2 h resulted in partially crystallised bioactive silica glass coatings deposited onto commercially pure Ti [170]. In addition, Ti oxide micro pores grown up to the oxygenated surface during deposition were reduced by annealing [170]. In a separate study, annealing in air at 950 °C for 30 min showed oxidation of the Ti substrate which had diffused to the coating's surface and introduced crystalline Ti phases as displayed in (*Figure 2.12)*[169]. The oxidation of Ti from 300-1000 °C was studied by Kofstad *et al.* They suggest four rate mechanisms of cubic, parabolic and linear oxidation rates at ranges up to 300 °C, 300-600 °C, 600-850 °C and above 850 °C respectively [182].

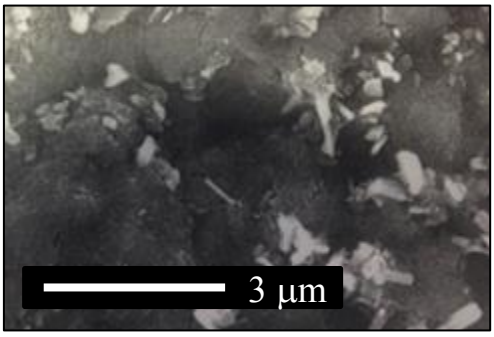

Figure 2.12: Diffused surface Ti during the annealing process of a sputtered bioactive silica glass [169].

Recent publications by Popa *et al.* in 2015, within the same group demonstrated the ability to coat 3D objects by sample rotation of dental implants. In a separate 2016 publication Popa *et al.* investigated cone-like sub-micrometre growths which were formed due to manipulation of adatom behaviour through parameter variation on the sputtered Bioglass surface by TEM [176].

2.8.1 Mechanical Properties and Coating Adhesion

Scratch, pull off tensile and shear adhesion tests are commonly used for failure of coatings. For a description of scratch and pull off testing see methodology *Sections 3.18 and 3.19*. The failure mechanisms of coatings are dependent upon the coating/substrate combination such that the coatings will either plastically deform and/or fracture. Hard coatings are prone to brittle fracture mechanism such as buckling and spallation and are likely to exhibit these failure mechanisms when applied to soft substrates [183, 184]. As postulated by Bull *et al. Figure 2.13* displays the likely failure regimes for substrate and coating hardness combination [185].

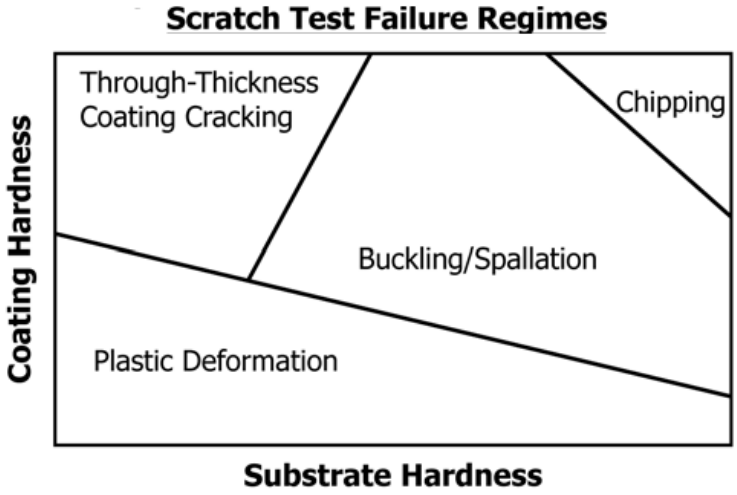

Figure 2.13: Scratch test failure regimes for varying hardness coating/substrate combinations [185].

Buckling is the most common failure mode for hard coatings of <10 μm in thickness. Compressive stresses ahead of the indenter cause the coating to fold in on itself at regions of localised stress. The cracks may then propagate in the direction perpendicular to the path. Extending the buckling to the width of the scratch [183-185]. Buckle spallation shown in *Figure 2.14B* results as compressed coating builds up ahead of the scratch indenter [185]. Torque *et al.* described buckling spallation as "trackside spallation" (*Figure 2.16*).

Through thickness tensile cracking may occur as tension builds behind the moving indenter. In hard coatings the tension will cause failure by brittle fracture similar to *Figure 2.14D* [185, 186]. As the compressive stresses are relieved, trailing the indenter, tensile residual stresses cause propagation along the perpendicular crack and eventual spallation occurs at the sides of the scratch track as shown in *Figure 2.14C* [185].

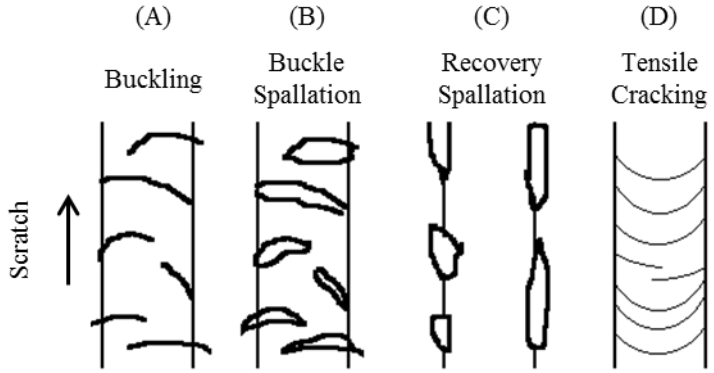

Figure 2.14: Scratch failure modes hard coatings (A) Buckling (B) Buckle spallation (C) Recovery spallation (D) Tensile cracking.

A comprehensive review by Mohseni *et al.* of HA on Ti6Al4V concluded that magnetron sputtering produced the greatest interfacial adhesion from 9 deposition methods of plasma spraying, hot isostatic pressing, thermal spray coating, dip coating, pulsed laser deposition, electrophoretic deposition, sol gel, ion beam assisted deposition and sputtering. See *Figure 2.15* as produced by Mohseni *et al.* [187].

Filiaggi *et al.* reported on Plasma sprayed HA on grit-blasted substrates, 135 μm thick coating on Ti6Al4V with tensile interfacial bond strength of up to 6.7 ± 1.5 MPa. Observation of the interface displayed mechanical and chemical bonding, notably diffusion of phosphorus 20-30 nm into the Ti layer [188]. Kim *et al.* showed coatings of glass/HA produced sol-gel slurry method to have adhesive strengths of 30-33 MPa [189].

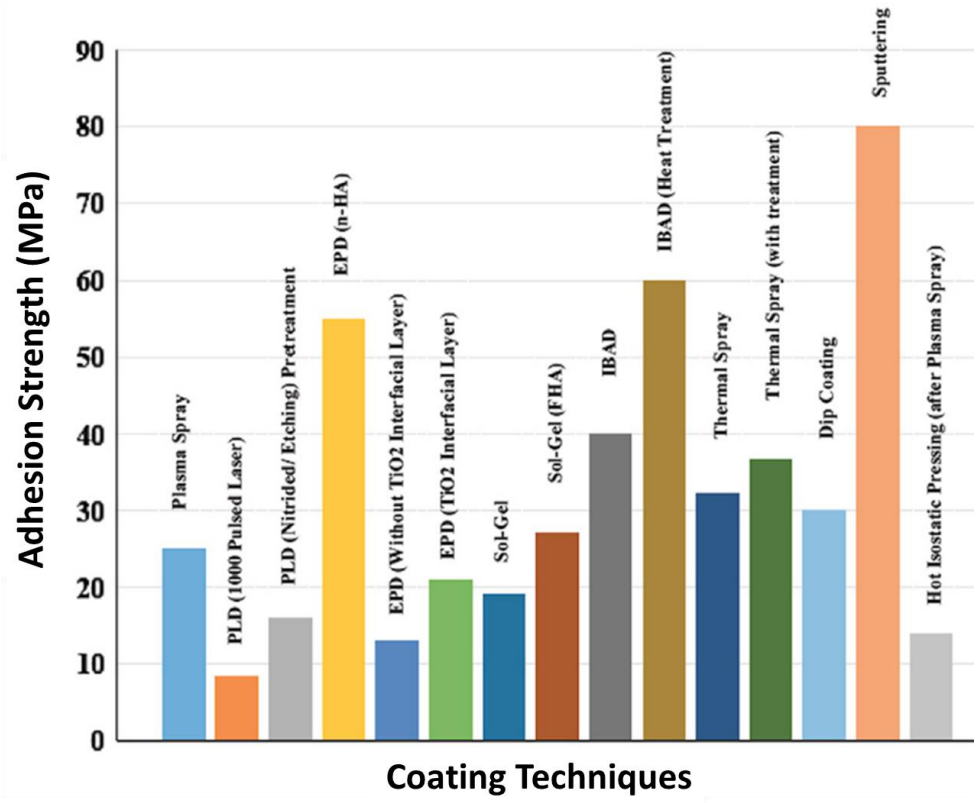

Figure 2.15: Comparative review of coating adhesion strengths based on process. Figure taken from Mohseni et al. [187].

Bioglass 45S5 has been plasma sprayed with little success as failure occurred from thermally induced residual stresses at the Ti coating interface with adhesion strength of approximately 8.6 ± 0.6 MPa [190]. The use of a bonding coat (60 wt% Al_2O_3 40 wt% TiO_2) to accommodate the TEC mismatch, induced cohesion, improving bonding strength to 27.2 ± 2.2 MPa with failure otherwise occurring by coating delamination [190]. The development of bioactive glasses applied by enamelling with similar TEC to Ti has been developed at the expense of composition by substituting CaO with MgO and Na_2O with K_2O [191].

HA coatings applied to 316L stainless steel of surface roughness 0.075 μm were processed by RFMS. The Ca:P ratio of the as deposited film was 1.15 with crystalline phases of TCP and HA. The behaviour was highly dependent upon deposition parameters, coating thickness and test parameters. Scratches were conducted from

0.4 N to 1 N at progressively increasing load. The failure modes were recorded to indicate cohesive and adhesive failures with increasing load. As deposited coatings initially failed by trackside cracking then trackside delamination as the tensile stresses built up behind the indenter with eventual steady delamination as the crack width was constant. The annealed coating failed by progressive delamination whilst the signs of fracture associated with brittle failure diminished (*Figure 2.16*) [186].

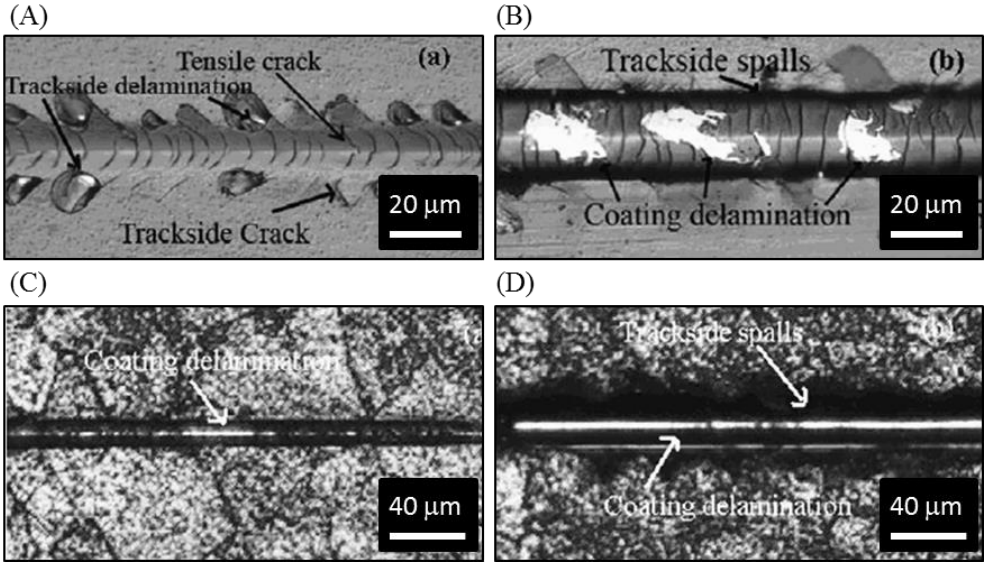

Figure 2.16: Failure of annealed HA coating under scratch loading [186]. (A and C) Represent low load whilst (B and D) represents higher loads. (A and B) As deposited. (C and D) annealed. Figure taken from Toque et al. [186].

A comparison of Ion beam sputtered Ca:P coatings was conducted by Ong *et al.* via pull off strength for amorphous, and heat treated coatings. As deposited amorphous, quenched and furnace cooled coatings had pull of strengths of 38.0 ± 8.2 MPa, 17.0 ± 6.5 MPa and 9.0 ± 9.0 MPa respectively, with failure either occurring at the coating interface or cohesively [139].

A further study by Ong *et al.* examined pull off strengths for RFMS coatings implanted *in vivo*. The pull out strengths of sputtered coated Ca:P coatings were tested 3 and 12 weeks post implementation. As sputtered amorphous and heat treated Ti cylinders were surgically inserted into the mandibles of 10 dogs. Five dogs were used

at 3 and 12 weeks each [150]. Pull of strength of as deposited coatings were 2.29 ± 0.14 MPa whilst heat treated were 1.28 ± 0.04 MPa for the 3 weeks samples. The Ti implant on its own was 0.67 ± 0.13 MPa. The Ti implant displayed no bioactive behaviour and no interfacial bonding. Both as deposited and heat treated coatings bonded to the cortical bone through interfacial bone attachment. 12 week samples resulted in 2.7 ± 0.3, 2.2 ± 0.3 and 2.6 ± 0.3 MPa showing no statistical difference. It was suggested that degradation of the amorphous phases facilitated bone formation leading to the result observed, in which 3 weeks post implementation bonding was strongest [150]. In a comparable study plasma sprayed coatings showed ultimate interfacial strength of 2.7 ± 0.3 MPa. Additionally the percentage of bone contact length (*Figure 2.17*) was determined with amorphous coating exhibiting the highest values at 3 and 12 weeks of 50.3 ± 4.2 and 70.4 ± 1.6 % respectively whilst heat treated coating were 30.3 ± 6.7 and 58.2 ± 4.5 % respectively. The Ti only implants were 33.7 ± 0.8 and 53.1 ± 7.5 % respectively at 3 and 12 weeks showing no difference to the heat treated coatings whilst as deposited coatings had greater interfacial strength. A comparative study elsewhere for plasma sprayed coatings showed 50 % and 75 %, 12 and 24 weeks post implementation indicating improved contact in sputtered coatings, obtaining similar interfacial properties in less time [150].

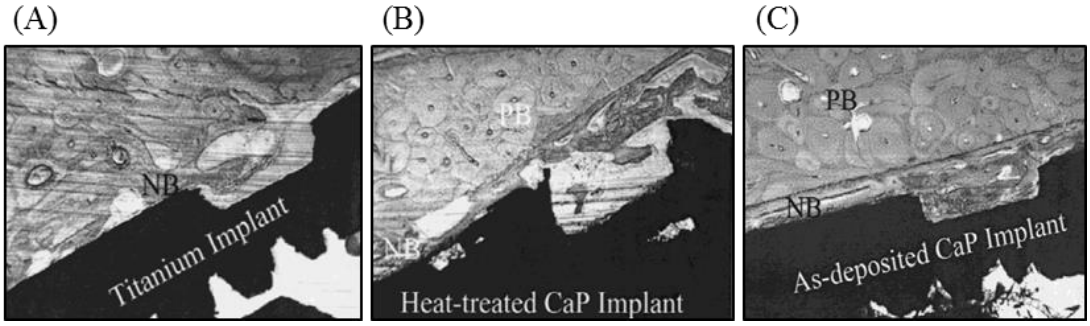

Figure 2.17: Bone formation from non-coated Ti compared to HT and As deposited Ca:P coating implants 12 weeks post implantation new bone formation was most apparent for AD – Ca:P coatings. [150]

A study by Ding *et al.* examined the adhesion of HA coatings following submersion in SBF and showed improvements to above 60 MPa for coating compositions containing above 10% Ti with no coating delamination present 14 weeks post submersion and no notable decrease in adhesion strength with time [154]. Pure HA sputtered coatings had declining adhesion strength with time and began spalling within 1 week followed by delamination characteristic of random dissolution within 3 weeks in SBF. Increased delamination occurred with 5% Ti in the coating composition [154] . The adhesion strength of the as-sputtered HA was measured as ~45.1 MPa [154].

The behaviours of a 3.5 – 4 μm thick, Ca:P sputtered coatings which were heat treated at 650 °C, and amorphous as deposited coatings were examined in SBF under cyclically loaded conditions in three points bending. The as deposited coatings were unstable, specifically at the locations of increased residual stress, determined by XRD, whilst crystalline coatings appeared stable under loading. The amorphous phases, which did not delaminate, precipitated a Ca:P layer. The maximum interfacial stress of 280-300 MPa was applied on the coated rods. Delamination was observed at the location of maximum stress, where the load was applied in three points bending for the amorphous coatings in SBF. Heat treated crystalline coatings in air showed signs of delamination however amorphous coatings did not. However crystalline coatings in SBF delaminated; whilst amorphous coatings delaminated in the highly stressed zones and precipitated a Ca:P layer [192].

Adhesion of Bioactive glass 17.25 MgO-52.75 $3CaOP_2O_5$-30Si (wt%) were tested by Mardare *et al.* via pull off tests, reporting adhesion strength of 41.0 ± 4.5 MPa for 300 nm bioactive glass on Ti substrates. Post-deposition heat treatment of the coating layer at 900-1000 °C caused crystallisation and subsequent reduction in adhesion to

16.3 ± 1.9 MPa [169]. Stan *et al.* suggested that Mardare's work was carried out above the phase transition temperature of Ti in which the Ti changes in crystal structure and reduces in volume, inducing stress in the materials [169, 193].

Increasing adhesion via heat treatment above the glass transition temperature to facilitate diffusion between coating and Ti substrate proved successful. Stan *et al.* utilised post deposition annealing for interfacial diffusion between Ti/Bioglass at 750 °C showing enhanced pull off strengths of 60.3 ± 4.6 MPa. Crystal formation of Mg/Si compounds were identified in the coating layer. Inter-diffusion was confirmed by the formation of Ti/Si compounds suggesting alloying at the interface [193]. Post deposition annealing may be conducted in air or may utilise an inert gas. *In situ* annealing during sputtering occurs in an inert argon atmosphere.

A bioactive glass with composition 55-SiO_2 CaO-15 P_2O_5-10 K_2O-10 Mg-5 Na_2O-5 (wt%) was applied to Ti6Al7Nb substrates [173]. The adhesion strength of crystalline and amorphous coatings annealed at 750 °C and 550 °C were 72.9 ± 7.1 and ~85.0 MPa. Crystallisation can cause micro cracking as grain size increases; however, thermal expansion mismatch is the more pronounced cause of poor adhesion at higher temperatures [173]. At 750 °C conversion of an anatase to rutile structure may further explain the reduced adhesion by creating concentrated stress points. Heat treatment, caused a noticeable diffusion of Ti into the glass at the interface, forming chemical bonding [173].

Stan *et al.* demonstrated that the use of Bioglass-Ti buffer layers could improve bioactive glass adhesion onto Ti substrates. The more adherent bonding was due to closer TEC between the substrate and coating, preventing cracking of the coating upon cooling. Whilst pure Bioglass coatings had adhesion strength of 29.2 ± 7.0 MPa,

the poor adhesion was due to the high TEC of 17 x 10^{-6} K^{-1}. Co-sputtered $Bioglass_{1-x}Ti$ (x=0-1) improved coating's adhesion to 50.3 ± 5.8 MPa. The graded layer was created by sputtering a moving substrate from Ti to Bioglass, therefore phasing out the Ti and increasing Bioglass as displayed in *Figure 2.18* [175] .

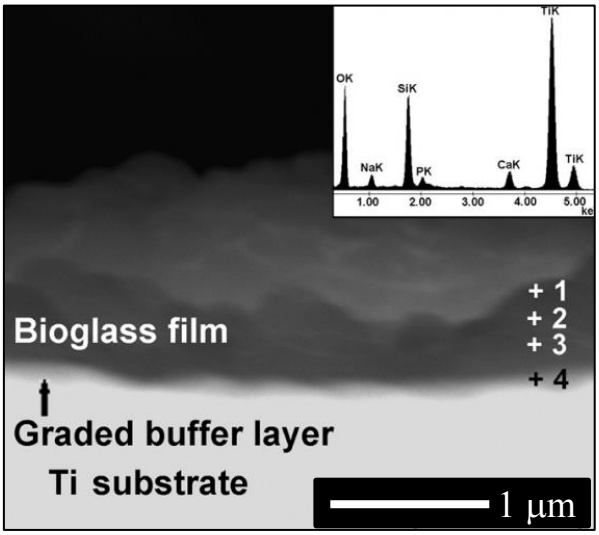

Figure 2.18: Graded Ti buffer layer for improved adhesion [175].

Improvements in adhesion without graded layers have been successful by matching the TEC. A glass coating composition produced with TEC of 10 x 10^{-6} K^{-1} was applied to Ti substrates with TEC of 9.2 - 9.6 x 10^{-6} K^{-1} [174]. The adhesion strength for this glass was measured as ~75 MPa, with improvement partially attributed to the sputter cleaning of the substrate prior to deposition to remove the TiO_2 layer inhibiting bonding. Whilst bonding is dramatically improved this method restricts the flexibility of coating compositions which can be applied [172] .

Popa *et al.* conducted nano indentation tests drawing comparison between Ti samples and four compositions of SBGs of 1 μm in thickness. Results at a depth of 750 nm suggested relative elastic modulus of ~150, and ~90-120 GPa for Ti and the four glass coating compositions respectively. The four compositions were deposited under varying oxygen/argon mixtures producing variable compositions. The author suggests

the increase in Ca and reduction in Na as the dependent variable for increased hardness between the tested samples [180].

2.8.2 Culturing of MG63 Osteoblast Cells on MQ glasses and Sputtered Coatings

Popa *et al.* reported clear improvements in cell proliferation of MG63 osteoblasts cells for four formulations of Bioactive glasses on Ti substrates after 30 h of seeding and clear improvements over the Ti control reporting relative cell numbers of 15,000 seeded on all samples and 15,000 cells on Ti after 30 h. The improvement of bioactive silicate glass compositions was between 24,000 and 27,000 varying between the four compositions tested. Popa *et al.* suggested variations in dissolution behaviour between glass compositions was responsible for variation and that the more durable glasses, containing less Na were less viable for cells [180]. Additionally Popa *et al.* extracted human dental pulp stem cells from donors in a separate study, showing significantly lower absorbance intensity with respect to the Ti control sample. They did however attach, proliferate and successfully differentiate, indicating promising biocompatible behaviour [177]. Most recently, Popa *et al.* cultured Human umbilical vein cells on Bioglass coatings using borosilicate glass and Ti as controls. They showed no significant difference in proliferation or cytotoxicity of the samples over the controls [176].

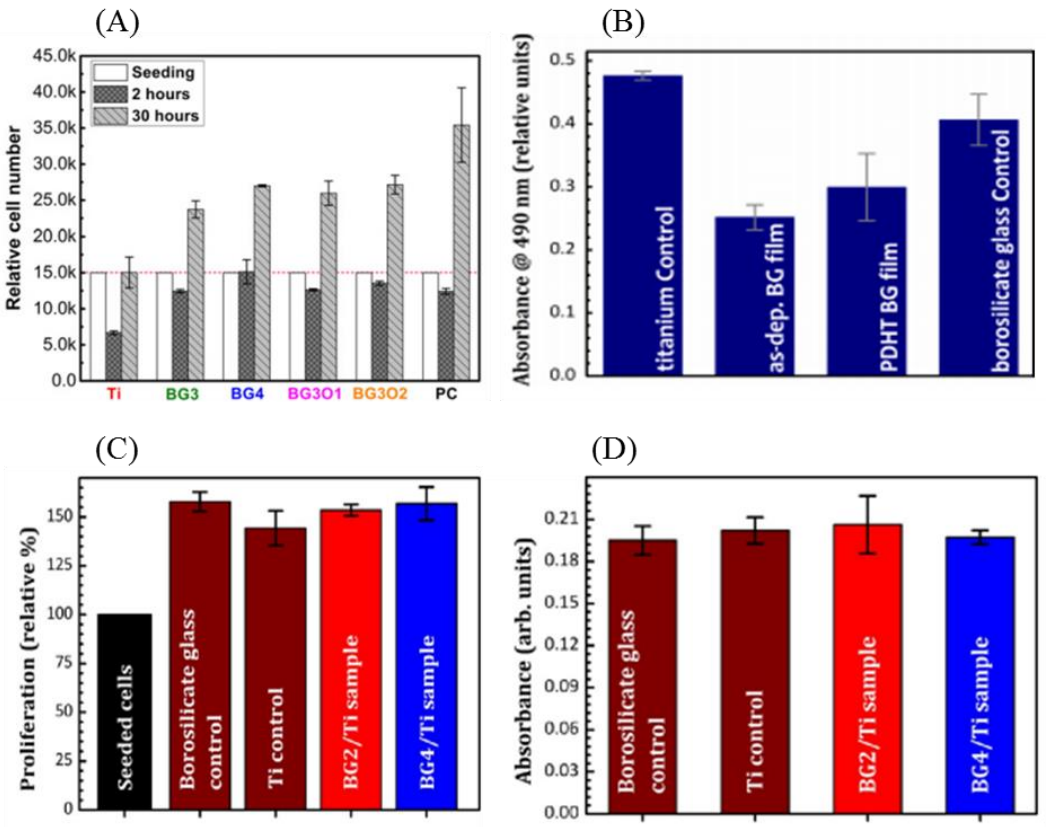

Figure 2.19: Cell culture studies performed on Bioactive glass coatings by Popa and Stan et al. for the assessment of (A) MG63 Osteoblast proliferation [180]*(B) Human dental pulp stem cell proliferation* [177] *(C) and (D) Human umbilical vein cells, proliferation and differentiation respectively* [176].

Magnetron sputtered Ca:P coatings of HA, Pyro-calcium phosphates have been associated with enhanced cellular responses as expected from bulk HA [194]. 600 nm HA films containing 0.8 wt% Si was deposited amorphous and subsequently heat treated for 3 h at 700 °C. Human osteoblast cells cultured for 4 d developed an extracellular matrix. Interestingly the direction of the matrix was observed to grow along the crystalline grooves whilst for amorphous coatings the alignment of the matrix was random [195].

Kim *et al.* applied HA and heat treated HA onto ZrO_2 substrates by slurry and demonstrated improved cell proliferation and differentiation after 5 d, suggesting that such coatings are appropriate for enhancing biocompatibility of implant surfaces [196]. Kim *et al.* produced PBG/HA composite coatings of 30-40 μm via the sol gel

method, with a phosphate glass/HA porous slurry on commercially pure Ti, subsequently densified by an HA sol gel precursor. The coatings demonstrated a favourable cellular response towards human osteoblast cells *in vitro* over the Ti control [189]. They indicated further improvements in Alkaline Phosphatase and Cell viability after 3 d of seeding [189].

4-5 mol% Fe_2O_3 additions into the PBG structure has shown to improve durability and enhance proliferation of MG63 cells [59]. A comparison of six PBG composition from P_2O_5-40 Fe_2O_3-0 to P_2O_5-50 Fe_2O_3-4 including the composition P_2O_5-40 MgO-24 CaO-16 Na_2O-16 Fe_2O_3-4 mol% were analysed in a separate study to observe the variation in degradation rates, relating to seeding of MG63 osteosarcoma cells. The results suggested an as expected increase in durability as Fe_2O_3 content increased to 4 mol%. Hasan *et al.* found the composition P_2O_5-40 MgO-24 CaO-16 Na_2O-16 Fe_2O_3-4 mol% to be the most durable of the glasses and found it to be the second most viable environment of the tested compositions for cells by neutral red uptake [197].

Cytotoxicity due to degradation of PBG has been attributed to variation in pH due to ions in the surrounding media. Rapid degradation leading to ion release can saturate the media and lead to local pH changes, unfavourable for cell viability [105].

The topography of HA coatings has an effect of osteoblast differentiation and implant attachment [198]. Greater cell differentiation was evident for micro rough surfaces with Ra ~2 μm. Smooth surfaces of Ra ~1 μm exhibited greater osteoclast activity [198].

In a study by Webster *et al.*, osteoblast proliferation and cell colonisation was improved on nanophase (grains less than 100 nm) ceramics of alumina, HA and

titania for the 21 and 28 d testing periods. Higher cell counts were noticeable 3 and 5 d post immersion for nanophase HA by approximately 30-50%. However, the cells cultured on nanophase HA showed decreased colonisation at 4 and 6 d, by approximately half. Alkaline phosphatase increased by 37% on nanophase HA in comparison to conventional HA (grain size >100 nm) after 28 d while calcification of the extracellular matrix was doubled for HA nano-ceramics [199]. This study suggests that nanophase ceramics enhance osteoblast activity; therefore grain size manipulation is desired for osseointegration.

2.9 Magnetron Sputtering and Preferential Sputtering

A description of the magnetron sputtering process can be found in the methodology *Section 3.4*. Direct current (DC) sputtering may be ineffective for insulating materials as resistance may cause the build-up of charged particles on the materials surface. Pulse DC can sometimes be an effective means to prevent this. The comparably low frequency of the pulse can provide limitation to highly insulating materials such as glasses [200]. In contrast, Radio Frequency (RF) sputtering is effective in deposition of low conductivity materials [201] by preventing the build-up of positive particles on non-conducting target surfaces by alternating between positive and negative electron flow, enabling the ionic momentum at negative current to outweigh the electron flow at positive current as a consequence of the greater mass of approaching ions in comparison to electron build up [200].

The ability to break down a target material into atoms and clusters of atoms leads to great flexibility when choosing target materials and the desired substrate conditions. Targets may be a mixture of multiple materials such as the individual oxides that make up glasses, metallic alloys or single elements. Sputtering will ionise the individual constituents of the target material and condense an alloy, oxide, nitride or

other, based on the reactive presence, onto the substrate. *Figure 3.2A* shows a condensed glass coating on Ti6Al4V. The condensed material that manifests to the substrate may differ in composition, governed by sputtering conditions [201].

The particle physics involved in the sputtering process is largely unstable and unpredictable on an ionic scale. As argon ions blast the target, ions are not simply ejected. In contrast, an uncontrolled process of atomic interactions and energy exchanges occur within the target, until an atom has sufficient energy to be released by overcoming the elemental binding energies [201]. Ion bombardment can affect the structure of the lattice planes on the substrate and target, causing chaotic changes in the microstructure characteristic of "radiation damage" [201]. These include amorphisation of a crystalline structure. Radiation damage effects can thus aid roughening the surface of the substrate for more effective coating substrate adhesion [201]. Introduction of a substrate bias can similarly facilitate this effect.

The sputtering atmosphere can be manipulated by adding proportions of reactive gasses into the chamber during deposition to produce oxides, nitrides, sulphides [200]. Whilst argon is often chosen as the inert gas, other inert gasses may be used such at krypton or xenon for sputtering, and result in different momentum transfer as each varies in atomic weight [201].

Sputtering yield is defined as "the number of sputtered atoms/incident energetic ion", however in relative terms, refers to differential sputtering rates for individual elements, or elements within a compound. Berg *et al.* explained this behaviour through ballistic interactions and chemical bonding [202]. The term "preferential sputtering" has been defined here as the disproportionate sputtering of target materials affected by multiple processing parameters, including the inert gas used, vacuum pressure, binding energies of the target elements, sputtering distance, and atomic

weights which make predictive modelling of the sputtering yields difficult. The problem is exacerbated with the use of multicomponent targets, for which the combination of bonded components increases complexity [201].

2.9.1 Ballistic Cascade Effects

Ion bombardment results in various cascade scenarios in which the incoming ion can behave in a variety of ways. Ideally, the incoming ionised argon atoms or neutrals are propelled towards the target and collide to either facilitate further gas ionisation or to elastically transfer momentum to the surface atoms of the target, thus ejecting the atom. Ionisation is relative to RF potential, leaving the majority of particles as neutrals [203]. In reality, a number of bombarding ions are backscattered, with insufficient energy. Those, which have sufficient energy, may penetrate into the depth of the target layer and can be trapped or redirected from the original incident angle. Nonetheless, a momentum transfer occurs, which in the case of trapped molecules causes a release of thermal energy in light of momentum losses from inelastic collisions. This thermal release will heat the target [201]. *Figure 2.20A* from Sree Harsha *et al.* shows the complex nature of the ion-solid interactions, including the natural changes of the material through ion bombardment [201].

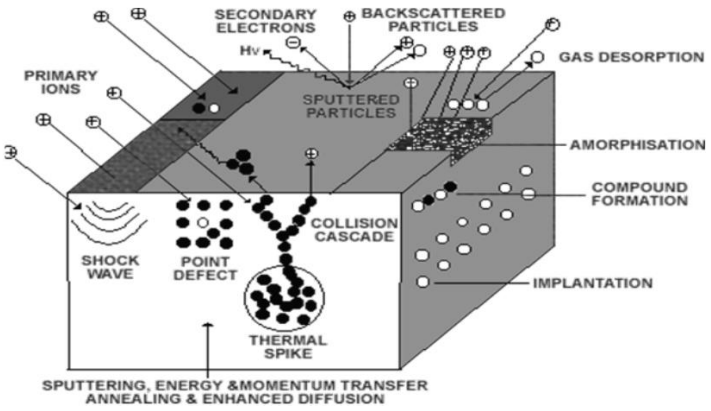

Figure 2.20: Ion-material interactions during ion bombardment and surface penetration. Inelastic energy transfer and momentum exchange leads to electron scattering, amorphisation, thermal spikes and reactions within the materials lattice. Figure taken from Alfonso et al. [201, 204].

For single element targets, the lighter ions may experience preferential sputtering, such that they may have increased ejection velocity in a fully elastic collision during kinetic energy exchanges. In the practical case where atoms penetrate the surface and bombard surrounded atoms, the path of particles ejected can be disrupted (*Figure 2.20B)* [202]. The interactions show ion penetration, resulting in various collisions within the material lattice [201]. Whilst not all ejected atoms have the same path to the substrate, intermediate collisions can disperse the kinetic energy of particles to surrounding atoms. In this situation where all atoms are of a single element the cascade is simple as all atoms have the same atomic mass. [201]. The presence of multiple elements within compound targets of varying atomic masses and atomic densities causes variation in argon penetration and changes in ejection velocity from rebounds between elements of different masses [202].

Sputtering Yield Amplification

In unique circumstances yields can be increased by what is known as "sputtering yield amplification" [202]. This mechanism is applicable for layered compositions and compound targets with variable atomic masses. Depending on the thickness of the target's surface and the atomic density of the materials, bombarding atoms will penetrate to a depth to eject either the top layers or layers beneath. For high atomic density target layers, the bombarding ions will have difficulty penetrating the target. Therefore, the sputtering yield of the top layers will increase if the bottom layer has a high atomic density [202]. If the bottom layer has a lower atomic density, the argon atoms will penetrate to that layer and increase the sputtering yield of the lower material. Additionally, atoms may be reflected kinetically by the element with which they collide. As the mass of the bombarded atom increases the kinetic energy with

which the atom is reflected will be greater and will increase the yield of the surrounding elements as illustrated in *Figure 2.21A and B* [202].

Multi-layered Targets

Berg *et al.* tested the sputtering yield amplification effect using Al on top of both, Si and W substrates [202]. Al and Si have similar atomic weights of 26.98 g mol^{-1} and 28.08 g mol^{-1} respectively. As argon penetration depth increased with power, layer 2's yield increased whilst layer 1's was reduced *Figure 2.21B.* This indicated that the lower materials mass is not great enough to reflect the ions. In contrast, a bottom layer of tungsten, which has an atomic weight of 183.84 g mol^{-1} resulted in an increased sputtering yield, from ionic reflections as can be observed in *Figure 2.22* [202].

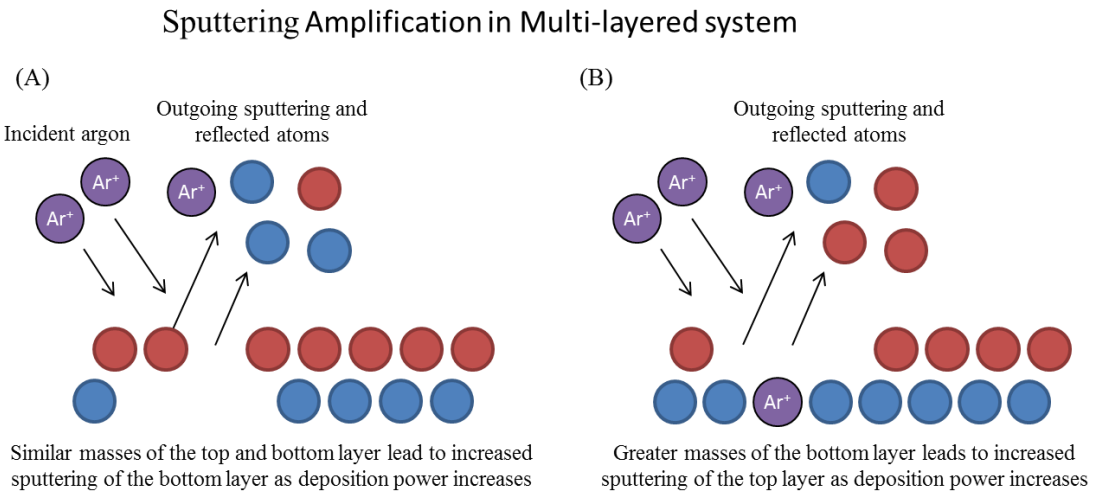

Figure 2.21: Sputtering yield amplification in multi layered targets. (A) Similar masses and high power. (B) Greater mass in bottom layer with high power.

By these mechanisms the sputtering yield would increase with greater atomic density and thickness whilst high atomic mass, correlating with increasing atomic number would cause preferential sputtering and increased yield of the surrounding, lighter elements. Berg *et al.* suggested that reflections due to differential atomic mass are the dominant cause of sputtering yield amplification, confirmed by testing multiple substrate materials with less dense, low atomic mass substrates resulting in a reduced

amplification effect. Amplification effect is a function of coating thickness, such that beyond a thickness the ions do not penetrate the upper layer and therefore reflections do not occur to cause amplification as illustrated in *Figure 2.22* [202]. As the momentum of the incoming ion increases, penetration of the ion deepens to the tungsten sub layer. The ions are initially reflected and the sputtering yield increases for the top layer [202]. As the top layer of Al increases in thickness, the argon atoms bombard the lower layer of tungsten until the Al layer increased to a thickness at which reflections from the bottom tungsten layer are at their greatest. Beyond this point the thickness of the Al layer increases to reduce penetration to the bottom layer, preventing the sputtering yield amplification effect. On Si the amplification effect does not occur because the atomic masses are similar [202].

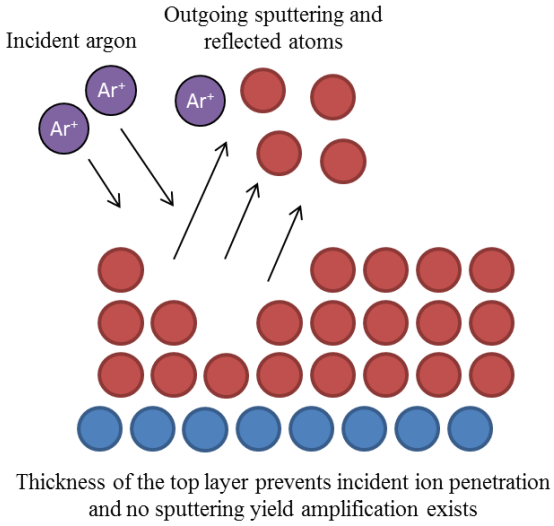

Figure 2.22: Sputter yield amplification is prevented when the top layer is thick.

The implications of the ballistic interactions imply a sputtering yield dependence on the surrounding atom as the yield of element A on its own is altered by the introduction of element B and further altered by the subsequent introduction of new elements, C and D. Sputtering yields must therefore be experimentally determined at given parameters for any composite materials. By changing compositional ratios the effects of ion reflections are variable meaning that yields are not constant for an

element within a composite, therefore in predicting yields the element itself, its bonding and the properties of the surrounding elements must be examined [202]. These properties will have a considerable impact when applied to multi component glasses.

Compound Targets

The ballistic approach for compound targets in comparison to multi-layered target is similar; however, the elements are instead mixed and often bound together. The cascade theory explains preferential sputtering according the ionic interactions as atoms collide and penetrate the surface of the target leading to momentum transfer, energy conservation and subsequent deposition [202]. The ballistic interaction in compound targets is not purely explained as collision and ejection, rather the elements interact to cause multiple collisions with varying momentum exchanges within the lattice of the bulk target as a result of the relative atomic masses and atomic densities [202]. In addition, chemical bonding will cause variation in sputtering behaviour. Therefore the target's composition and structure is critical [202].

Assuming a compound target, composed of 2 elements A and B, if A has a greater sputtering yield then B, then the bombarded target will be initially depleted in element A [202]. Thus the sputtering yield will reduce with time for A, and B will have a relative increase due to the change in surface composition. With time this leads to steady state compositional values on the surface, different from the initial bulk target composition. Steady state sputtering implies that the sputtering yield is always changing and composition varies with coating depth, however, the change that exists for a homogenous material is cyclical and fixed for given film thickness. The cyclical

variation in sputtering is illustrated in *Figure 2.23* for a tungsten/aluminium composition [202].

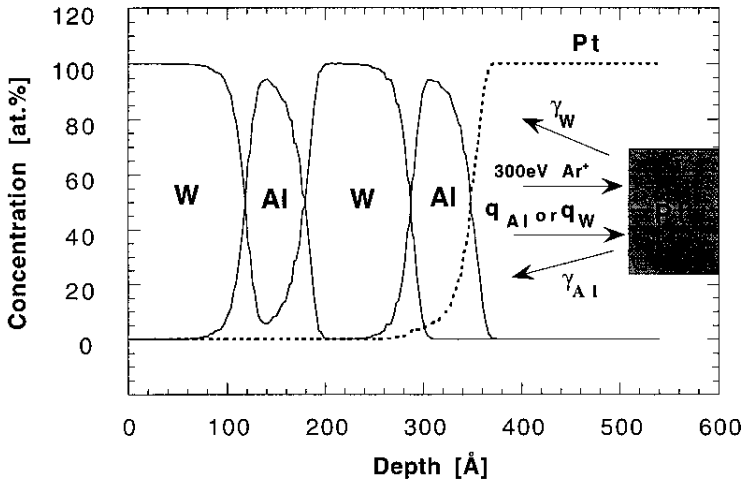

Figure 2.23: Preferential sputtering leading to elemental surface depletion and cyclical variation in coating composition [202].

2.9.2 Sputtering Diffusion effects

Material diffusion may occur under high energies as an element with low surface free energy diffuses to the surface to reduce the bulk surface free energy, a theory termed "Gibbsian segregation" [205]. Argon bombardment induces particle energies of 2-3 orders greater than those induced by thermal energy [205]. Bombarding ions which become trapped in the bulk material facilitate thermally activated diffusion of the excited atoms [201, 205].

For example, ion beam bombardment can cause segregation and desorption of alkali and alkali earth metals in silicate glasses [206]. The inherent bonding of the glass structure, consisting of strongly bound covalent bonds and weak ionic, alkali and alkali earth elements allows segregation to occur at low energy. Miotello *et al.* suggests that the negative charge of the network former tetrahedron is "shielded" by the segregation of positively charged alkali metal ions. High energy atoms segregate to the surface to enhance surface free energy [206]. Segregation has been reported to occur at room temperature in the first 0.3 nm without bombardment [206].

Battaglin *et al.* examined the alkali depletion region in ion doped silicate glass under varying ion irradiation intensities [207]. Their findings suggest that independent of the incoming ion kinetics the mechanism of alkali depletion remained the same. However, increasing power extended the depth of the depleted region. The depletion of alkalis reached a maximum steady state value beyond which the alkali concentration remained the same with increasing depth [207]. The effect was confirmed to be independent of the specific alkali as tests of rubidium, potassium and sodium reached the same steady state value.

Sublimation Energy

Malherbe *et al.* tested the effects of incident angle and varying energy on preferential sputtering of GaAs, used in semiconductors. Incident angles between 18° and 70° showed no difference in sputtering yield outside experimental uncertainty [208]. This is contrary to the generally accepted theory that sputtering yield varies with incident angle [201]. Ga and As have similar atomic weights of 69.72 g mol^{-1} and 74.92 g mol^{-1} respectively and preferential sputtering has been attributed to their binding energies rather than preferential sputtering of the lighter ions since in this example the heavier As has been preferentially sputtered. The binding energies are deemed indicative of the sublimation energy therefore sublimation energy rather than ballistic theory has been used to explain variations in sputtering yields for elements. In this example As has a sublimation energy of 29 kcal mol^{-1}, whilst Ga is 64.9 kcal mol^{-1} [208]. *Figure 2.24* shows a matching correlation between sublimation energy and measured sputtering yield [201].

$$Sublimation\ Energy = \frac{\Delta H_{fusion} + \Delta H_{vaporization}}{Avogadro's\ Number} = \frac{\Delta H_{sub}}{Avogadro's\ Number}$$

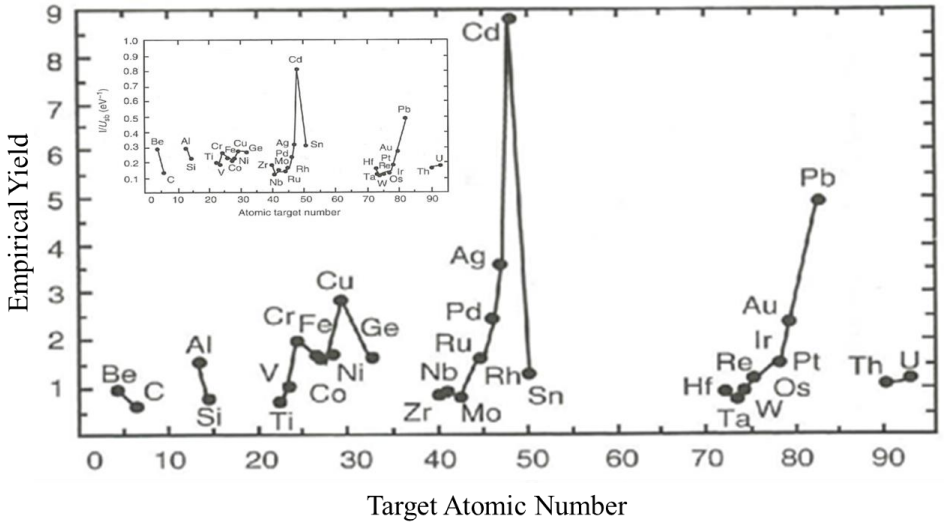

Figure 2.24: Empirical sputtering yields relative to (Insert) sublimation energy of elements [201].

At room temperature, the sublimation energy for an particles within a single element is governed by the equation in *Figure 2.24* [201].

There is also an influence of the incoming argon ion energy on preferential sputtering. This is illustrated with the variation in preferential sputtering of Ga in the GaAs alloy with changes in ion energy. There is a range in which preferential sputtering changes with varying power; however, as energy increases preferential sputtering becomes constant. This is a useful result as it implies that beyond a certain argon bombardment energy, preferential sputtering may be treated as constant; allowing for effective processing development [208].

It has also been observed that at low energy levels, ions do not provide enough energy to break chemical bonds and therefore sputtering may not occur. Typically ion energy must exceed the binding energy by 2-10 eV for sputtering [201]. As the ion penetrated intensifies with energy, and the energy transfer mechanism changes within the material lattice, sputtering yield may not be constant with changing power over the entire profile. At lower power the yields are quadratic until a steady state condition in

which the profile becomes linear. Above a material dependent energy level, the ions have enough energy to become trapped within the lattice and can no longer efficiently sputter causing a decline in sputtering yield. The linear regime for sputtering yield begins at energies between 0.1-1.0 KeV [201].

2.9.3 Preferential Sputtering in Ca:P structures and Silicate Based Glass

Preferential sputtering in PBG, SBG and Ca:P ceramics were identified in literature; however the phenomenon has not been explored in great depth [142-146, 151, 154, 157, 162, 169, 171-175, 178, 209].

A prevalent theory is that lighter ions are pumped away in the vacuum, favouring sputtering of heavier species. HA coatings applied by RF support the theory as Ca:P ratio of the sample increases from the target composition. Many authors have observed an increase in Ca:P ratio resulting from the preferential sputtering of Ca over P and have explained this by the differential atomic weights of 40.08 g mol^{-1} and 30.97 g mol^{-1} respectively [143, 149, 151]. A phosphorous deficiency has additionally been explained by the inability to form stable bonds without enough oxygen, as oxygen is readily pumped away with an atomic weight of 16.00 g mol^{-1} [145]. Although this theory has been presented, no author has provided supporting evidence to suggest that ions are extensively pumped away in the vacuum to cause preferential sputtering.

In contrast, Boyd *et al.* found a reduction in Ca:P ratio in as-deposited films. The variation in Ca:P stoichiometry is a product of the wide range of parameters [156]. A high variation in the sputtering yield was observed for targets of different Ca:P ratio at the same parameters. Ca:P ratios between 0.83 and 1.35 were deposited from target compositions of between 1.00 and 1.60 [156]. Utilisation of multi-component targets,

with different atomic ratios showed that crystallinity and stoichiometry may be controlled by altering processing parameters such as power and atmosphere [156].

Pyrophosphate coatings (Ca:P ratio=1) (β-$Ca_2P_2O_7$) by RFMS in 100% argon showed a decrease in Ca:P ratio deposited on the coating due to preferential sputtering of P [143]. This is contradictory to the theory that lighter elements are pumped away in the vacuum and implied that whilst this occurrence is likely, the sputtering yield is affected by stronger bonding of Ca in the pyrophosphate structure [143].

The more reactive elements will acquire their oxidation states, increasing sputtering yield whilst the less reactive elements will less efficiently form oxides, decreasing sputtering yield. Additionally, the oxidation state of elements may differ from target to coating, depending on the bonding preference under the atmospheric chamber conditions [171]. Furthermore, with increasing argon pressures a reduction in the number of non-bridging oxygens has been observed for the coating, favouring the bonding of alkali and alkali earth metals [170, 171].

Materials composed of oxygen bonds such as glasses; metallic oxides and HA have a tendency to be highly affected by the sputtering environment [146, 172]. As sputtering breaks down the target's components ion by ion, the oxide bonds are broken allowing ejection of individual ions to the substrate. The oxide nature of the glass provides an abundance of free oxygen to reactive with ions condensing onto the substrate. Thus, due to its high reactivity, stoichiometry may be effected [146]. Research has been conducted to attempt to explain the variation in sputtering deposition and yield with partial oxygen pressure into the sputtering chamber [146, 172] .

Increases in partial oxygen pressure of up to 5% for sputtering of HA targets showed reductions in Ca:P ratios at the substrate, explained by increased ability to form phosphate bonds with sufficient oxygen [146]. At 1% oxygen the deposition rate was reduced by 60%, suggesting that increased oxygen bonds to Ca and P, and prevents sputtering. Below 1% the deposition rate was not affected [146].

In a study using Bioactive SBG, increases in oxygen up to 20% showed a reduction in overall deposition rate attributed to "target poisoning". This occurs when oxygen ions bombard the surface of the target and form an oxide layer, preventing sputtering of the target material beneath [172]. In a separate paper, the same author suggested that increased partial pressure of oxygen would enable more reactive elements to form oxides, therefore increasing composition of the elements such as Si and P [171].

A materials path to the substrate is blocked by an overabundance of free argon therefore a proportion of ejected ions are backscattered in the intermediate space, thus do not reach the substrate. This effect should be taken into account when increasing ionisation density, such to optimised deposition rates [170, 171, 173]. The mean free path of a particle is the average distance a particle will travel before colliding with a particle in its path described by *Eq 1* as a function of pressure temperature and diameter of a gas particle.

$$\lambda = \frac{k_B * T}{\sqrt{2} * \pi * p * d^2} \quad Eq\ 1$$

The diameter of an argon atom is 3.69 x 10^{-10} m. *Table 2.6* shows the mean free path of argon at various vacuum pressures and temperatures. The mean free path reduces with increased pressure, increasing collisions [201].

Table 2.6: The mean free path of argon at various temperatures and pressures. The pressures and temperatures chosen may be encountered during the sputtering process of glass at the RF powers described within the results.

Temperature (°C)	0.25 Pa	0.54 Pa	1.05 Pa	1.50 Pa
0	2.5×10^{-2}	1.2×10^{-2}	0.6×10^{-2}	0.4×10^{-2}
100	3.4×10^{-2}	1.6×10^{-2}	0.8×10^{-2}	0.6×10^{-2}
200	4.3×10^{-2}	2.0×10^{-2}	1.0×10^{-2}	0.7×10^{-2}
300	5.2×10^{-2}	2.4×10^{-2}	1.2×10^{-2}	0.9×10^{-2}
400	6.1×10^{-2}	2.8×10^{-2}	1.5×10^{-2}	1.0×10^{-2}
500	7.1×10^{-2}	3.3×10^{-2}	1.7×10^{-2}	1.2×10^{-2}
600	8.0×10^{-2}	3.7×10^{-2}	1.9×10^{-2}	1.3×10^{-2}
700	8.9×10^{-2}	4.1×10^{-2}	2.1×10^{-2}	1.5×10^{-2}

* Mean free path in metres.

Research into multicomponent bioactive glasses has yielded similar increases in Ca:P ratio in as deposited coatings [144, 169-175, 178]. The highest sputtering yields were found with Na and Mg, which have atomic weights of 22.98 g mol^{-1} and 24.31 g mol^{-1} respectively, contradicting and discounting the theory that preferential sputtering is caused by pumping away of lighter species. Stan *et al.* varied the argon gas pressure to 0.2-0.3-0.4 Pa, stating that the most likely cause of decreased sputtering yield is a reduction in the kinetic energy associated with the charge transfer due to argon bombardment [171]. This group reported that increases in argon working pressure improved Ca yield and reduced P yield shown in *Figure 2.25A* [171] and C [170]. This was explained by a reduction in kinetic energy of lighter ions as more collisions take place to cause backscattering. The greater argon pressure will increase the number and intensity of collisions to cause backscattering for which the greatest momentum transfer will be upon the lightest ions, resulting in backscattering in the order Na, Mg, Si, P, Ca with atomic weights of 22.99, 28.09, 30.97 and 40.08 g mol^{-1} respectively [201]. *Figure 2.25D* supports this theory as deposition rate was shown to decrease with increasing argon pressure, suggesting particles are increasingly backscattered [171] and shows the variation in compositional analysis with an

increase in injected argon pressure reported by Stan *et al.* for a BG 45S5 target [171]. The explanation that they postulated suggests a change in tendency towards oxidation states with variations in partial oxygen pressure, which is reduced at higher argon pressure. Oxygen partial pressure can increase by injecting oxygen gas into the chamber or by reducing argon injection pressure. This implies that as argon pressure increases, the elements cannot reach stability at their higher oxidation states and the composition is reduced as the material forms at lower oxidation states. Although they observed some trends in the results, Ca does not appear to follow this theory whilst the results presented for Na and Si are questionable.

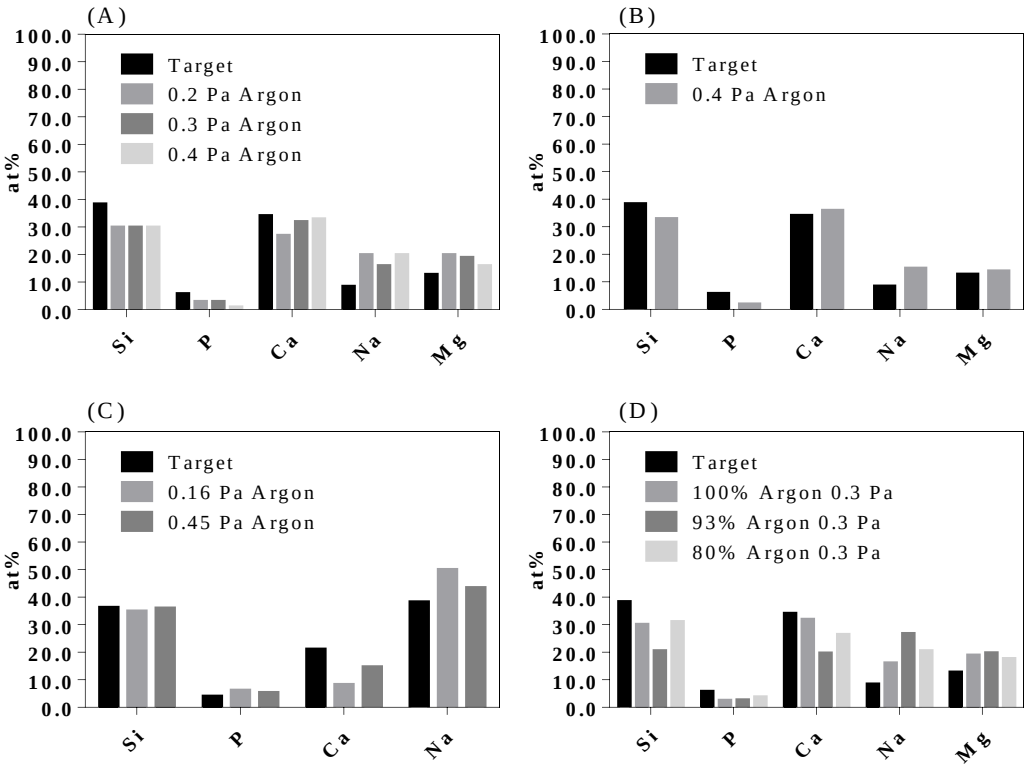

Figure 2.25: Sputtering yield of bioactive silicate glass variation with argon pressure [171].(B) Constant Pressure 0.4 Pa [170] (C) Bioglass target and variation in pressure [174] (D) Variation in argon partial pressure [172].

Visible coating surface alterations have led to the suggestion that coating density, morphology and microstructural bonding can be controlled by increasing the kinetic energy of the coating atoms [171]. In a second study, Stan *et al.* varied the working

pressure using BG 45S5 targets [170]. This study yielded different results with respect to variation in argon pressure suggesting that the most efficient coating stoichiometry occurred at higher argon pressure shown in *Figure 2.25C*. Whilst *Figure 2.25C* suggests an improvement in stoichiometry from increasing argon pressure, *Figure 2.25A* does not, therefore it cannot be concluded that stoichiometry is improved [170, 171].

Stan *et al.* reported spherical voids on the substrate, increasing in diameter with increased argon pressure as illustrated in *Figure 2.26*. This was explained by an increase in transverse diffusion from lower energy particles at higher working pressure, supporting backscattering theory [171].

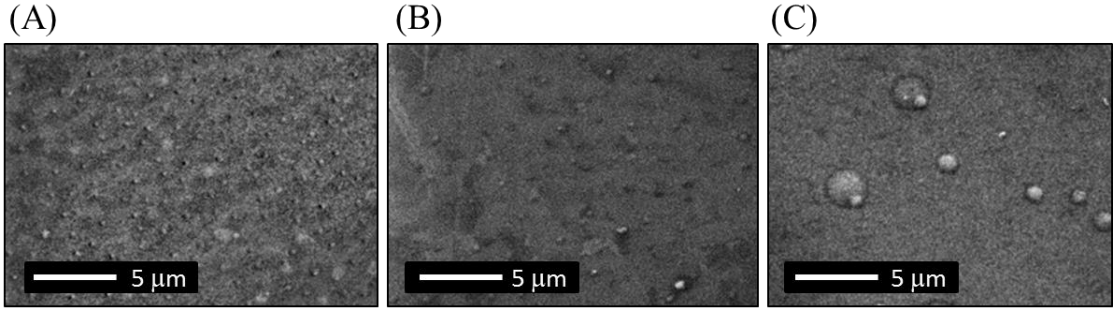

Figure 2.26: Spherical voids at (A) 0.2 Pa (B) 0.3 Pa (C) 0.4 Pa [171].

A trade-off must be made between coating stoichiometry and coating thickness, however, it can be seen that stoichiometry in sputtering is highly dependent upon sputtering parameters, such as working atmosphere and electrical potential. These effects are not well understood in the literature.

The chemical bonding configuration of the glass structure has been outlined whilst the atomic interactions between bombarding ions with target surface and subsurface layers have been analysed to understand the ballistic momentum exchanges between particles. Understanding of these topics is required and will be applied to sputtering of PBG targets.

2.10 Summary of Literature

This review has highlighted structural characteristics of melt derived PBGs and their functionality for orthopaedic applications. A number of competing technologies such as sol-gel or electrophoretic deposition for the production of glass coatings on to load bearing implants materials have been assessed.

HA was deposited by RFMS from 1993 onwards and showed superior capability for producing adhered, biocompatible films. RFMS was used for the deposition of SBG layers demonstrating their bio mineralisation potential. On this basis RFMS was considered to be the preferred method for the production of PBG thin films for their ion leaching capabilities to facilitate osseointegration or to deliver antimicrobial ions.

The structure of PBGs in their melt quenched form is well documented however the properties of thin films will depend upon composition, structural polymerisation and the inclusion of network modifying ions whilst their functionality will depend upon their dissolution and ion release properties to facilitate cellular activity or precipitate bioactive layers. Optimisation of mechanical and dissolution properties in Ca:P and SBG coatings by heat treatment has been shown.

As outlined in the aim and objectives in *Section 1.4*, PBG targets will be used as the preform for deposition of PBG coatings. The application of the sputtering process as it influences coating, morphologies, structures and stoichiometries must be understood prior to assessing degradation and bio functionality.

The following section details the experimental methodology used to create glass targets and subsequently deposit material onto substrates. Furthermore the processes for compositional, structural, morphological characterisation and coating optimisation will be presented prior to assessment of *in vitro* dissolution and Bioactivity.

3. Materials and Methodology

3.1 Preparation of Sputtered Substrates

The substrates for coating were 1 mm thick, 10 mm diameter discs Commercially pure Ti (CPTi) (grade 1) wire eroded from sheet. Ti6Al4V (grade 5) discs were 1 mm and 1.5 mm thick.

All Ti and Ti alloy discs were wet polished to a 6 μm finish using Si carbide paper from grades P200-P4000 and further polished on a 0.25 μm polishing pad (Struers® chemomet) with the application of colloidal silica. The substrate roughness of polished CPTI was measured as Ra 160 ± 30 nm whilst Ti6Al4V was measured as 110 ± 11 nm (n=10) using a 3D Interferometer (Fogale Photomap 3D).

Roughened samples were sandblasted with 220P alumina sand particles at a distance of 50 ± 5 mm and an air pressure of 7 x 10^5 Pa. The roughness was measured as 790 ± 60 nm (n=10). All Photomap 3D measurements were collected over a scan area of 800 μm^2. Additionally Ti6Al4V substrates were analysed via AFM over a 20 μm^2 area as 7.4 ± 0.6 nm for polished and 696 ± 57 nm for sandblasted (n=9). Prior to coating, samples were ultrasonically cleaned for 10 min in acetone, followed by distilled water (dH_2O) and ethanol.

Borosilicate cover slips (VWR No. 631-0155, 130 μm thick and 15 mm in diameter) were coated to measure the coating thicknesses achieved by SEM observation of the cross sections. Prior to coating, the slides were platinum coated for 90 s at 1.2 keV in an SC7640 Polaron sputter coater to enhance the interfacial contrast between coating and glass for microscopy analysis.

3.2 Manufacture of the Sputtering Targets

Nomenclature: Target glass is labelled (TxU or TxT to denote either UoN or TEER UDP 650 rigs respectively, where x, from 1-9 represents the target number. Similarly melt quenched glasses are labelled as (MQx) and coatings as (CxU or CxT). The codes in text are followed by the samples P_2O_5 and the dopant oxide mol%, of Fe_2O_3, TiO_2 or CuO, forming an overall example code of T6U: P51.5 Fe5, See *Table 3.2*.

Pre-calculated (mol%) proportions of the glass precursors were thoroughly mixed in their powdered forms, then preheated at 400 °C in a platinum: rhodium crucible 90:10% for 30 min to dehydrate. The mixture was then melted at 1200 °C for 2 h in air. The crucible was gently swirled within the furnace at 40 min intervals to facilitate mixing. The furnace temperature was increased to 1350 or 1370 °C based on the melting temperature of the precursor and viscosity of the melts. Targets were formed by quenching the molten mixture at 450 °C followed by natural furnace cooling to room temperature.

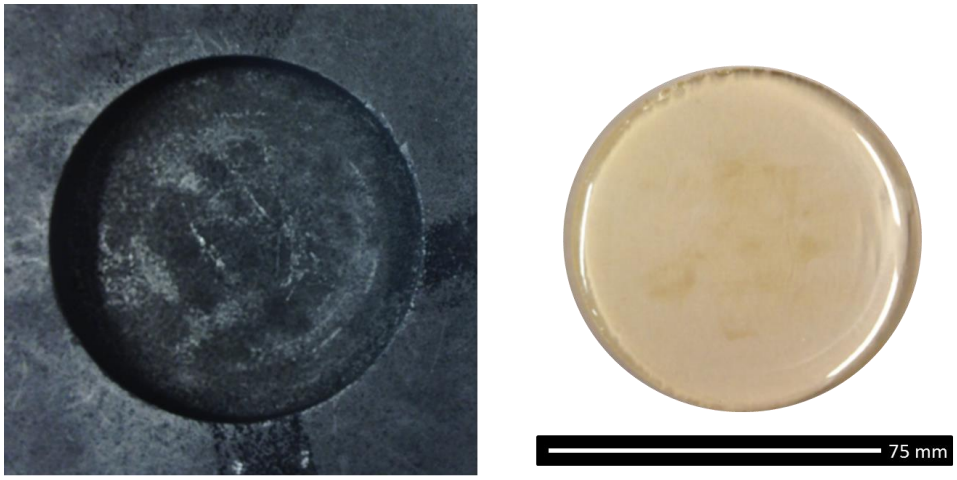

Figure 3.1: The molten glass melt was poured into a graphite mould to form 75 mm diameter glass targets.

The target mould and the subsequent target measured 75 ± 2 mm in diameter (*Figure 3.1*) and 6 ± 1 mm in thickness (UoN PVD) or 57 ± 2 mm in diameter (TEER UDP 650). The target was then polished to a 6 μm diamond finish for the

magnetron/water cooled side. P80 SiC paper was used to remove bulk material prior to polishing. Papers of P280, P400, P800, P1200 were then used for ~1 min each for polishing, using industrially methylated spirits as lubricant. As prepared (AP) target compositions were assessed via EDX compositional analysis in *Table 3.2*.

Table 3.1: Precursors for glass melting and target manufacture. Precursors were thoroughly mixed, dehydrated, melted and quenched to form sputtering targets.

Elements	Precursors	Chemical Formula	Purity	Molecular weight (g mol^{-1})
Na/P	Sodium dihydrogen phosphate	NaH_2PO_4	>99%	119.98
Ca:P	Calcium hydrogen phosphate	$CaHPO_4$	98-105%	136.06
Mg/P	Magnesium phosphate dibasic trihydrate	$MgHPO_4.3H_2O$	>97%	174.34
Fe/P	Iron (III) phosphate dihydrate	$Fe\ PO_4.2H_2O$	Not Stated	186.85
P	Phosphorous pentoxide	P_2O_5	>98%	141.98
Ti	Titanium Oxide	TiO_2	≥99%	79.87
Si	Silicon Dioxide	SiO_2	Not Stated	60.08
Ca/C	Calcium Carbonate	$CaCO_3$	≥99%	100.09
Na/C	Sodium Carbonate	Na_2CO_3	≥99.5%	105.99
Mg/C	Magnesium Carbonate (anhydrous)	$MgCO_3.H_2O$	Not Stated	84.31

3.3 Target Compositions and Melting Regimes

The nominal sputtering target compositions and the actual target compositions confirmed by EDX are listed in *Table 3.2* and in the results *Table 4.1*.

Table 3.2: Nominal Target Compositions. UoN PVD Target (TxU), TEER UDP 650 (TxT) Targets. x=1-9 based on target number.

	mol%									
	Target	**SiO_2**	**P_2O_5**	**MgO**	**CaO**	**Na_2O**	**Fe_2O_3**	**TiO_2**	**CuO**	**Melt Temp (°C)**
UoN PVD	**T1U: P40**	-	40.0	24.0	16.0	20.0	-	-	-	1200
	T2U: P45	-	45.0	24.0	16.0	15.0	-	-	-	1200
	T3U: P50	-	50.0	24.0	16.0	10.0	-	-	-	1200
	T4U: P50 Fe2	-	50.0	22.0	14.0	12.0	2.0	-	-	1200
	T5U: P50 Fe4	-	50.0	20.0	14.0	12.0	4.0	-	-	1200
	T6U: P51.5 Fe5	-	51.5	18.5	14.0	11.0	5.0	-	-	1200
	T7U: P50 Ti5	-	50.0	-	40.0	5.0	-	5.0	-	1350
	T8U: P50 Ti7 Cu5	-	50.0	-	23.0	15.0	-	7.0	5.0	1350
	T9U: P51.5 Fe10	-	51.5	13.5	14.0	11.0	10.0	-	-	1200
TEER UDP 650	**T1T: P57 Fe3**	-	57.0	14.0	12.0	14.0	3.0	-	-	1200
	T2T: Si46 (BG 45S5)	46.1	2.6	-	26.9	24.4	-	-	-	1370

Target T2T: P57 Fe3 contained carbonate precursors and was further decarbonated at 600 °C and 800 °C for periods of 30 min. All targets were cast at 450 °C into a graphite mould, and were left to furnace cool.

3.4 Magnetron Sputtering Process

Transfer of materials from a sputtering target to the substrate occurs by a momentum transfer process following ion bombardment [201]. A gas which is either inert of reactive is ionised by an oscillatory or static electric field between the anode and the cathode, propelling atoms in the direction of the target. The process relies on momentum transfer, involving particle collisions to remove neutral target material and eject it in the direction of the substrate with sufficient kinetic energy to overcome the distance between the target and substrate and ultimately condense to form a coating [201]. The glow discharge created by the ionisation gas is referred to as the plasma [200]. The electric potential may either be formed by DC, Pulse DC, or RF current.

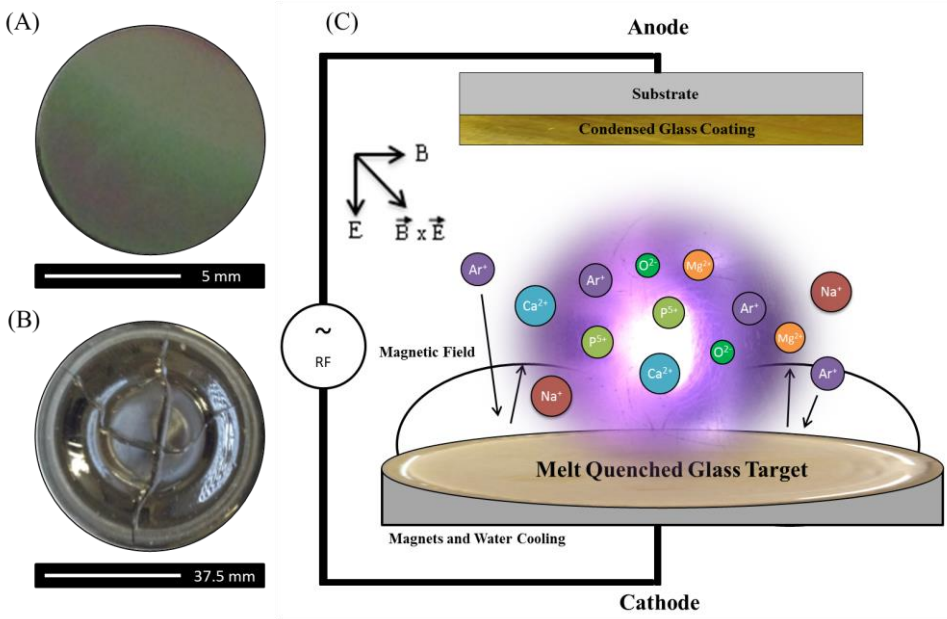

Figure 3.2: (A) Glass coating (C7U: P40 Fe4) on Ti6Al4V substrate. (B) PBG glass target after >3000 h of use. (C) RFMS system schematic. The resultant force vector to confine electrons in the magnetic field has been shown in accordance with the Lorentz law.

Magnetron sputtering utilises magnets placed below the target to induce a magnetic field. The resultant E x B vector field as suggested by Lorentz Law, confines free electrons in the vicinity of the target. This increases ionisation efficiency of the inert gas and may increase deposition rate by up to ten times [200]. *Figure 3.2C* displays the most basic RF sputtering system, utilising an alternating current RF power source and a magnetron. Target material is removed unevenly during deposition due to the confinement of the plasma above it, forming a "racetrack" on the used target, signifying the area over which atom ejection is greatest (*Figure 3.2B)* [200]. Sputtering yields can be improved by introducing a bias to the substrate, thus increasing the attraction of the ejected ions to the substrate [201].

The magnetron sputtering process was conducted in either the custom UoN PVD pilot scale rig or the industrial scale, TEER Coatings UDP 650.

3.5 UoN PVD Rig Operating Procedure

The manufactured glass targets were ion bombarded for deposition of coatings via RF (13.56 MHz) magnetron sputtering system with water cooled targets; see *Table 3.2* for compositions manufactured. The coatings were deposited via a custom in-house designed PVD rig built at the University of Nottingham (UoN PVD). The chamber was pumped down to a vacuum utilising a combination of a rotary (Edwards E2M-18) and turbo molecular pump (Edwards EXT250) to a base pressure $<7 \times 10^{-3}$ Pa.

The manufactured target was placed on top of a backing plate and clamped in place horizontally in the UoN PVD or vertically in the UDP 650 Rig. The substrates were fixed to the substrate holder via carbon sticky tape or polyimide (Kapton Tape) and were placed in the rig, parallel to the target.

The chamber was pumped to vacuum by consecutive rotary and turbo molecular pumping stages. The reactive gas was input through a mass flow controller (MKS 2982). The Argon pressure was controlled using an (MKS 250) pressure controller, monitored by a temperature controlled capacitive manometer (MKS Baratron 627B). The mass flow controller, varied argon flow rate based on the pressure settings and was connected to a four channel ratio controller (MKS 247C) for the use of multiple gas flows [210].

The magnetron cooling water was fixed at 13 ± 2 °C to extract heat from the target. The power source was turned on to ionise the working gas. The target was cleaned for a minimum of 30 min at 30 W then increased to the operating power for a further 30 min, allowing sufficient time for the target's temperature to stabilise.

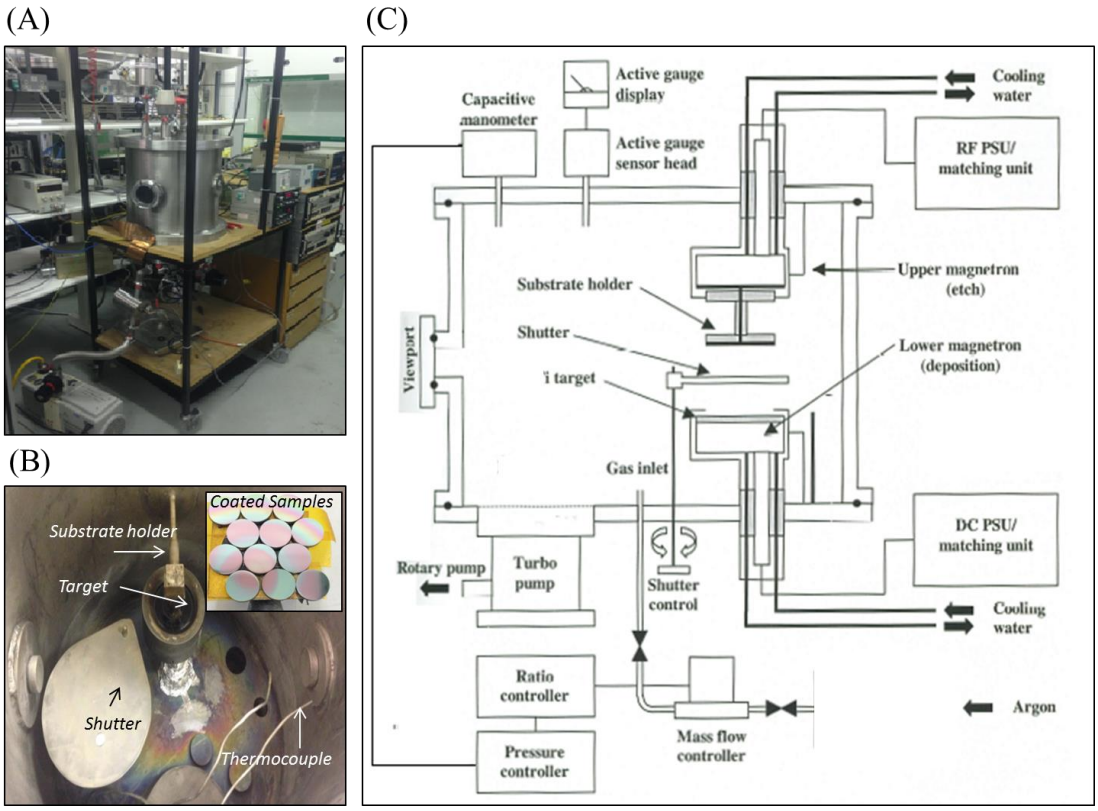

Figure 3.3: (A) UoN PVD and (C) its schematic diagram modified from Botterill et al. [210]. (B) Inside of the UoN PVD. (Insert) Sample holder loaded with Ti6Al4V discs post coating.

3.6 TEER UDP 650 Rig Operating Procedure

The UDP 650 is a fully automated vacuum system; containing four planar cathode targets, allowing for 360° sample rotation. The rig is similarly pumped down by consecutive rotary and diffusion pumping stages to a base vacuum of <11 x 10^{-3} Pa. Functions include substrate DC and pulse DC biases with the capability to blend multiple target materials during rotation of the substrate within the chamber make the industrial rig unique in its potential applications. Rig functionality and design parameters are stated in (*Table 3.3*).

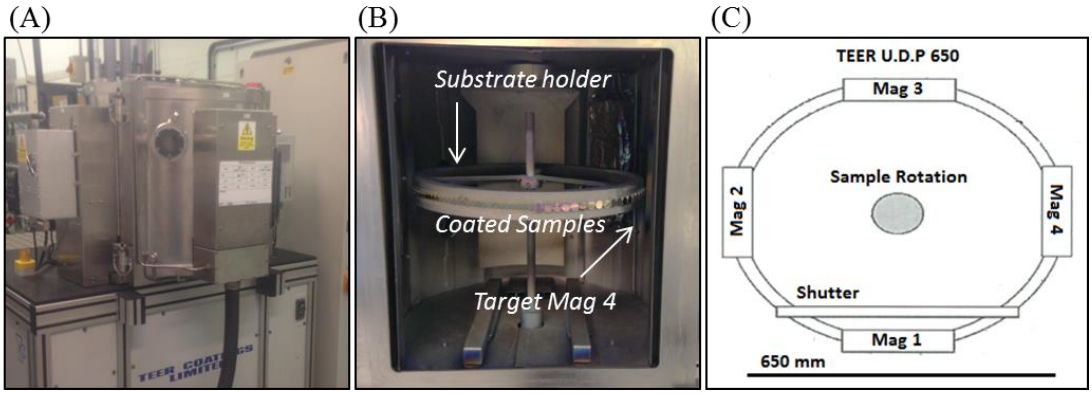

Figure 3.4: (A) TEER UDP 650 for industrial scale operation (B) Inside of the sputtering chamber (C) Inner chamber schematic showing the configuration of the 4 magnetrons.

The power applied to the target is stated in terms of power density for the purpose of cross rig work for which the target size may vary. For clarity of presentation results have been stated in terms of applied power, however a conversion chart has been given for the UoN PVD and UDP 650 for comparison (*Table 3.3*).

Table 3.3: Rig functionality and working parameters. The UoN PVD and UDP 650 utilise cathode diameters of 75 and 57 mm respectively therefore a power density conversion chart has been provided.

	UoN PVD	**UDP 650**
Power Source	DC/RF 13.56 MHz	DC/RF 13.56 MHz
Rotation/Static	Static	Static/Rotation (0-10 RPM)
Target Diameter (mm)	75 ± 2	57 ± 2
Throw Distance (cm)	4.0 – 6.0	4.0 – 20.0
Target Capacity	2	4
Target Position	Horizontal	Vertical
Substrate Bias	N/a	(y)
Power (W)	**Power Density (kW m^{-2})**	
20	4.5	8.4
40	9.1	16.8
60	13.6	25.3
80	18.1	33.7
100	22.6	42.1
120	27.2	50.5
140	31.7	59.0

3.7 Scanning Electron Microscopy and Energy-Dispersive X-ray Spectroscopy

A scanning electron microscope (SEM) focuses a beam of electrons over the sample area, which interact with atoms to emit electrons in the subshells (secondary electrons) and radiation in the form of X-rays. A third interaction involves the backscattering of electrons. On the basis of these interactions, images may be formed and materials elemental properties may be determined [211]. SEM was also used for Energy Dispersive X-ray Spectroscopy (EDX) quantification, coating surface and cross sectional imaging.

The development of the SEM vastly improved imaging resolution based on *Eq 2 and 3* for which the resolution power; d is a factor of λ=wavelength of the electron, n=index of refraction and α=the angle of the electrons entering the objective. The potential qV accelerates the electrons, via conversion of potential to kinetic energy. The subsequent velocity of the electron, input into the de Broglie (*Eq 3*) dictates the wavelength λ associated with the movement of electrons such that λ is

inversely proportional to the velocity of the electron. On this premise, as the electron accelerating voltage and thus velocity is increased, a decrease in the wavelength of the source leads to higher imaging resolution [211].

$$d = \frac{0.612\lambda}{nsin(\alpha)} \quad Eq\ 2$$

$$\lambda = \frac{h}{mv} \quad Eq\ 3$$

Sample Preparation and Working Parameters

Samples for EDX and low resolution imaging of less than 4000 x magnification were fixed onto carbon sticky tabs on stainless steel mounts and carbon coated for ~30 s using an (Edwards Coating System E306A). Samples for high resolution >4000-200,000x imaging were platinum coated for 90 s at 1.2 keV using a Polaron sputter coater.

Coated borosilicate cover slides were fractured to expose a cross sectional view. The cross sections were mounted vertically for cross sectional microscopy and to measure deposition rates.

Elemental analysis was conducted via a Phillips XL30 SEM-EDX. EDX was conducted at a working distance of 10 mm at a minimum of 200,000 counts and a beam voltage of 10-20 kV. The beam voltage was varied depending on coating depth to avoid excessive substrate signal as sampling depth increased with accelerating voltage. The electron beam current was optimised by increasing the spot size to obtain a minimum acquisition rate of 4,000 counts s^{-1} whilst maintaining an acquisition dead time <30%. Elemental mapping was performed under the same conditions for a minimum collection time of 300 s.

Imaging at >4000x magnification which includes cross sectional micrographs of coatings on borosilicate cover slips were collected via a Phillips XL30 FEG-ESEM.

3.8 Focussed Ion Beam Scanning Electron Microscope

A Focussed Ion Beam (FIB) uses an aligned ion-milling source to micro-machine the sample. Coating cross sections can therefore be milled and polished during microscopy to observed coating/substrate interfacial features. Coatings on Ti6Al4V substrates were sectioned and polished using a Zeiss NVision 40 FIB with a gallium milling source. The working distance was kept constant at 5 mm utilising a beam voltage of 5.0 kV. All sections were cut at a tilt angle of 54°.

3.9 X-ray Diffraction

X-rays are generated by a source Cu Kα X-ray gun which functions by electron bombardment of the copper source to emit electrons from the inner electron shell and subsequently form X-rays which are directed towards the sample. The X-ray interaction with the sample causes the X-rays to diffract based on the long-range structure of the material. An X-ray detector determines the angle and scattering of diffraction for constructive interference which satisfies Braggs law (*Eq 4*). The set of diffraction angles and intensities are unique for a crystalline phase and crystal size. The crystal lattice is defined by a three dimensional matrix (h, k, l) from which multiple diffraction angles may be generated. The spacing between lattice planes is termed (d) spacing. (θ) refers to the incident X-ray angle whilst (λ) is its wavelength. This information is the basis for Braggs law (*Eq 4*) from which the information regarding crystal structure and size may be determined [211].

$$2dsin\theta = n\lambda \qquad Eq\ 4$$

Sample Preparation and Working Parameters

Samples of melt quenched glass were ground to a fine powder by mortar and pestle and flatly pressed into the sample holder. Coated Ti and Ti6Al4V discs were centred and horizontally placed into the sample holder.

All XRD analysis was conducted using a Bruker D8 Advance, (Cu Kα source, λ=1.5418 Å, 40 kV, 35 mA). Powder XRD was over a 2θ range from 15° to 65° with a step size of 0.04° in 2θ, and a dwell time of 5 s.

Glancing angle thin-film XRD was performed on the deposited coatings utilising a step size of 0.02° in 2θ. The angle of the incident X-rays was held constant at 2° in 2θ. For samples following SBF submersion the 2θ range was from 3° to 50°.

Phase ID and peak matches were modelled via Rietveld Refinement in Topas Software.

3.10 Fourier Transform Infrared Spectroscopy

An elemental bond may be excited during the absorption of infrared radiation. In particular covalent bonding is characterised by vibrational, stretching, rocking modes. By determining the frequency converted to wavenumber of excitation during infrared absorption, the presence of covalent compounds may be determined. The molecular vibrations absorbed in the IR wavenumber range ~10-14,300 cm^{-1} makes the source useful for analysis of bonding configurations [211, 212].

Sample Preparation and Working Parameters

Melt quenched glass was ground to a fine powder by mortar and pestle and pressed onto an Attenuated Total Reflectance (ATR) crystal for analysis. An ATR diamond crystal refracts an infrared beam ~0.5-1.0 μm within the sample. The localised reflections are detected as infrared radiation passes back through the crystal [212].

Thin film surfaces on their substrates were pressed onto the crystal. A baseline background was collected for all samples with no sample present and was subsequently subtracted from the spectra. If the film was less than 500 nm (the approximate depth of the IR beam) the Ti6Al4V substrates were scanned separately for background subtraction.

A Bruker Tensor Fourier Transform Infrared Spectrometer (FTIR) with an ATR attachment was used for all Infrared absorption measurements. A spectral resolution of 4 cm^{-1} over the wavenumber range 500-4000 cm^{-1} was set. All spectra obtained represent the average of 64 scans over the sample area. All spectra were analysed using OPUS spectroscopy software.

3.11 ^{31}P MAS-NMR Nuclear Magnetic Resonance

The basis for Magic Angle Spinning Nuclear Magnetic Resonance (MAS-NMR) is the variable magnetic properties unique to the chemical states of Q^0, Q^1, Q^2, or Q^3 species in the glass structure which refers to the number of bridging oxygen's per PO_4 tetrahedral where n is between 0-3 due to the presence of a 4^{th} terminal double bond (see *Figure 2.3* and *Section 2.1* for a detailed explanation of Q^n structures). NMR is a process by which a magnet manipulates the magnetic dipole moment of the nucleus under investigation. The application of an RF power source manipulates the nucleus to resonate in alignment with the induced external magnetic field. Removal of the RF source allows the resonating nucleus to relax to its ground state, producing electrical signal. The NMR signal is converted by Fourier transformation into the conventional spectrum of chemical shift measured in Parts Per Million (PPM) and resonance intensity.

Sample Preparation and Working Parameters

Substrates used for coating were pure borosilicate cover slips (VWR No. 631-0155, 130 μm thick and 15 mm in diameter). Samples were coated for a period of 160 h and subsequently ground into a powder for analysis.

Quantitative ^{31}P NMR spectra were recorded at room temperature on a Varian Chemagnetics Infinityplus spectrometer at a Larmor frequency of 121.468 MHz using a 4 mm Magic angle spinning (MAS) probe spinning at 10 kHz. The ^{31}P $\pi/2$ pulse duration was 3.5 μs, the spectral width was 100 kHz and the acquisition time was 10.24 ms. Chemical shifts are quoted relative to 85% H_3PO_4 using $Na_4P_2O_7.10H_2O$ as an external secondary reference. Prior to acquiring ^{31}P spectra the spin-lattice relaxation time T_1 was determined for each sample by saturation recovery. Saturation was achieved by 100 ^{31}P $\pi/2$ pulses spaced by delays of 5 ms with recovery delays of between 10 s and 1000 s. Quantitative ^{31}P NMR spectra required relaxation delays (5 T_1) of the order of 250 s for the films and 600 s for the bulk samples. The resulting spectra were deconvoluted into a set of Gaussian lineshapes, which were integrated in order to quantify the proportions of the different Q environments in the sample. MAS sidebands above 1% of the maximum spectral intensity were included in the analysis.

3.12 Atomic Force Microscopy

Atomic force microscopy (AFM) enabled the detailed topographical mapping of atomic scale surface features. In tapping mode a cantilever AFM tip resonates over the surface of a specimen. As the tip moves in 2D space over the sampling region the cantilever taps the surface. The material interaction causes the tip to deflect due to short range attraction or Coulomb repulsion. The deflection of the cantilever is quantified, enabling analyses of the surface topography. AFM is capable of

differentiating forces such as cantilever/surface adhesion and electrostatic forces [211].

3.12.1 Sample Preparation and Working Parameters

AFM micrographs and roughness measurements were acquired in tapping mode via a Bruker Dimension Icon. AFM tips; model TAP525A 0.01-0.025 Ohm-cm Antinomy (n) doped Si were used. All measurements were acquired over a scan area of 20.0 μm^2. AFM analysis software "Gwyddion" was used to analyse the average maximum pit depth and diameters for the largest pit in the scan field over n=5 scans.

3.13 X-ray Photoelectron Spectroscopy

X-ray Photoelectron Spectroscopy (XPS) enables the elemental quantification of the first 1-10 nm of a material, as beyond this depth photoelectrons cannot escape the solid. As X-rays bombard the surface of the material photo-electrons are emitted from the electron shells. The photodetector measures the maximum kinetic energy upon which a photoelectron imparts the surface. On the basis of an electrons attraction to its nucleus the kinetic energies are well defined. Conventionally the kinetic energies are converted to electron binding energies for standardised comparison as kinetic energy depends upon the energy applied to eject the electron from its subshell. *Eq 5* relates the kinetic energy (E_k) to the electron binding energy (E_b), and the work function (Φ_f), dependent upon X-ray energy where Planks constant (h) and radiation frequency (v). In order to have E_k, the X-ray energy (hv) must be greater than the electron binding energy (E_b), and the minimum energy required to for the electron to escape the atom (Φ_f) as dictated by *Eq 5*.

$$E_k = hv - E_b - \Phi_f \qquad Eq\ 5$$

XPS has also been shown to be useful in determining chemical states of elements as shifts in the binding energy due to variation in electrostatic attraction resulting from various bonding interactions. Shifts due to variable chemical states could vary by between 0.1 and 10 eV [211, 213].

Sample Preparation and Working Parameters

Melt quenched glass was ground to a fine power by mortar and pestle and spread over a carbon sticky tab. Thin films deposited on Ti6Al4V discs or CPTi were analysed.

XPS was conducted using a VG Scientific EscaLab Mark II with an Al kα non-monocromatic X-ray source. Scans were collected at 20 mA and 12 kV emissions. Analysis and peak fitting was conducted using Casa XPS, with the application of a Shirley background subtraction. Constraints including, the Full Width at Half Maximum (FWHM) were fixed for similar elemental states. Relative peak positioning and peak areas due to spin orbit splitting were constrained based on the electron subshell.

3.14 Thermo Mechanical Analysis

A TMA Q400 was used to determine glass thermal expansion coefficients. The increase in normalised sample length $\frac{\Delta L}{L}$ ie. strain, as a function of temperature ΔT (*Eq 6*) is indicative of the expansion coefficient α [214]. The instrument uses a distance probe over the sample to determine unidirectional expansion in the vertical direction during heating.

$$\frac{\Delta L}{L} = \alpha \Delta T \qquad Eq\ 6$$

Sample Preparation and Working Parameters

50 mm long, 10 mm diameter glass rods were prepared by casting molten glass into a graphite mould following the glass melting procedure outlined in *Section 3.2*. The glass rods were cut into 7 mm long rods using a diamond saw. The samples were ramped up to 400 °C at 10 °C min^{-1}. The TEC measurements were obtained from a best fit between 50-300 °C. All expansion measurements represent the Standard Error Mean of n=3 samples.

3.15 Differential Thermal Analysis

An SDT Q600 was used for differential thermal analysis (DTA) to determine the glass transition temperature (T_g), crystallisation temperatures (T_c) and melting temperatures (T_m). DTA relies on the exothermic and endothermic changes within the glass during the heating cycles indicated by changes in enthalpy [214]. An empty reference pan is heated in parallel to calculate the enthalpy reactions due to the sample presence on its own. An endothermic peak will be detected during the T_g or T_m to maintain equilibrium between reference and sample. Similarly as energy is released during crystallisation an exothermic reaction occurs. Enthalpy during the reaction may be calculated by integration of the peaks [211].

Sample Preparation and Working Parameters

For thermal analyses of melt quenched glasses, ~30 ± 0.5 mg of glass was ground to powder and placed in platinum crucibles within the DTA. Prior the sample analysis, an empty crucible was assessed for baseline subtraction. The DTA was ramped up to 1000 °C from room temperature at a heating rate of either 10 or 20 °C min^{-1} in a 100 cm^3 s^{-1} flow of nitrogen or argon. As sputtered coatings were deposited onto copper foil and flexed off the substrate for coating separation utilising ~5.0 ± 0.5 mg.

The T_g was determined as the onset of the first endothermic peak. The T_c was determined at the temperature of the peak heat flows of the exotherms. The T_m was determined at the peak temperatures of endotherms beyond crystallisation.

3.16 Helium Pycnometry

By flowing a gas through a known mass of material the infiltration volume may be assessed by variation in pressure between the sample and reference cell, to provide a measure of skeletal density of a material [215].

Sample Preparation and Working Parameters

Helium pycnometry was carried out using an AccuPyc II 1340 from Micromeritics in 99.9995% helium at a maximum pressure of 19.5 psi, utilising an equilibrium rate of 0.005 psi/sec. Samples were degassed for 24 h at 50 °C. 100 mg of sample was analysed in a 1 cm^3 sample cell. Samples were purged 10 times followed by 10 cycles to assess skeletal density.

3.17 Contact Angle

The contact angle of a liquid/solid interface is an indication of a materials ability to adhesively deform a liquid. If the adhesive forces of the surface towards a test liquid are greater than the cohesive forces holding the liquid together, the liquid will wet the materials surface. *Eq 7* shows Young's equation of the contact angle (θ_Y) relationship between the liquid-vapor (γ_{lv}), solid-vapor (γ_{sv}) and solid-liquid (γ_{sl}) tensions [216].

$$\gamma_{lv} cos\theta_Y = \gamma_{sv} - \gamma_{sl} \qquad Eq\ 7$$

By this method the adhesion of a glass surface toward the degradation media may be assessed. A materials surface energy is the ability of a surface to deform a liquid to

increase its surface area. Therefore a material with high surface energy is defined as hydrophilic. Conversely hydrophobic materials produce contact angles of >90°.

Sample Preparation and Working Parameters

Melt quenched glass was fixed in a solution of 7.5:1 ratio epoxy resin:hardener for a period of 24 h. The glass surface was polished using P200 - P1200 Si carbide paper using industrially methylated spirit as lubricant followed by polishing with 6 μm and 1 μm diamond polishing pads.

Contact angle was assessed on polished Ti6Al4V coated specimens unless otherwise stated within the results.

The contact angle was assessed utilising distilled water (dH_2O) (pH~7.0). A polar liquid was chosen due to the hydration interacting with phosphate glasses. dH_2O was pumped out at a rate of 1.0 μl s^{-1} and dropped at a height of 4.0 ± 0.5 mm. The drop was allowed to settle for 10 s prior to collecting results for analysis of the static contact angle. The contact angle was analysed using First Ten Angstrom software. For each sample type (n=5)

3.18 Scratch Adhesion Testing

The scratch test is a qualitative method for determining the failure modes of a coating/substrate combination under a normal load dragged across the coating surface. At specified loads failure modes of the coatings will emerge providing quantitative comparisons [217].

Sample Preparation and Working Parameters

All scratch tests used a CETR (now Bruker) scratch tester and a Rockwell C Indenter. Constant loads were trialled for coatings on CPTi for detailed SEM analysis of failure

mechanisms. Loads were applied of 2, 3, 5, 6, 8, 10, 12, 14, 18 N over a distance of 5 mm 10 s^{-1} with a 1 mm loading length for a period of 10 sec.

All quantitative data was analysed by progressive loading in accordance with the BS EN 1071-3:2005 standard. Loads were applied over a distance of 3 mm with a pre load of 0.5 N followed by progressive loading to 30 N over a period of 180 sec. For all scratches, sampling number was n=10. The critical loads (L_{cn} where n = critical load number), were defined as the initial appearance of the failure mechanism along the scratch path.

3.19 Tensile Pull off Adhesion Testing

Sputtered thin films have been measured using the pull off method, in which an adhesive bonds a parallel stub to the coating surface which is pulled in tension until detachment [170]. Adhesion of Fe films as thin as of 25 nm has been reported by this method. The method is limited by the strength of the adhesive and may be particularly problematic when adhesive failure occurs at the glue interfaces [217]. Regulatory bodies such as the FDA have set tensile standards for coating failure, emerging from the quantitative comparison such tests provide.

Sample Preparation and Working Parameters

The pull off test was conducted in accordance with ASTM-D4541-09 using a precision adhesion testing apparatus (PAT Handy) manufactured by DFD instruments. Pull off stubs of 2.81 mm in diameter were used with a sampling number of n=8. A thermally curing epoxy resin (DFD E1100S) was applied over the area of the stub and pressed onto the coating surface to remove air bubbles. The stub/substrates were placed on a heated plate at 140 °C for 60 min to cure. Excess adhesive surrounding the stub was removed using a HSS steel cutting tool.

3.20 Post Deposition Heat Treatment

PBG coatings were deposited amorphous and subsequently heat treated (HT) to various temperatures (specified in results) using a Lenton furnaces® tube furnace. Annealing was either conducted in air, nitrogen or 99.99% pureshield argon. Gas inflow was controlled via a flow regulator. All samples were heated at 10 °C min^{-1} and held constant for a specified dwell time. Sample specific parameters can be found in *Table 3.4*. All samples were left to cool naturally to room temperature.

Nomenclature: Heat treated sample are denoted by the original coating code, limited to CxU, following by the heat treatment temperature in °C and the dwell time in minutes (eg. C7U-500°-30) to denote heat treatment of C7U: P40 Fe4 as shown in *Table 3.4*.

Table 3.4: Heat treatment parameters for C7U: P40 Fe4 and C8U: P31 Ti6.

Coating	Gas and Flow rate ($l\ m^{-1}$)	Temperature (°C)	Dwell Time (min)
C7U-500°-30	Argon 0.6	500	30
C7U-500°-120	Argon 0.6	500	120
C7U-550°-30	Argon 0.6	550	30
C7U-610°-30	Argon 0.6	610	30
C7U-610°-30-Air	Air	610	30
C8U-500°-30	Nitrogen 0.6	550	30

3.21 Degradation of Melt Quenched Glass

Glass rods were produced following the procedure in *Section 3.3* and subsequently quenched into 9 mm diameter graphite moulds. The rods were cut into 5 mm cylinders using a testbourne diamond saw. Three cylinders were placed into separate containers of 30 ml of dH_2O or PBS pH ~7.40 and incubated at 37 ± 2 °C. The cylinders were left in solution for 2, 4, 6, 8, 10, 12 and 24 h followed by 2, 3, 5, 8, 12, 16, and 20 d, then every 7 d until 83 d. At each time point the cylinders were removed, dried with tissue and placed in an oven at 50 °C for 1 h to remove excess surface water. The surface area and mass were measured using a Vernier calliper and a Mettler Toledo precision scale accurate to 0.01 mg. The samples were then

re-submerged until the next measurement time point. The PBS and dH_2O were changed at each time point until 7 d then subsequently twice per week. The pH was measured before and after degradation at room temperature when using PBS. The pH was measured after degradation when using dH_2O. Pre prepared tablets of PBS from Sigma Aldrich were dissolved in 200 mL of dH_2O.

3.22 Degradation of Thin Film Coatings

Thin film coatings were applied to both polished and sandblasted Ti6Al4V (Grade 5) substrate by RFMS. The coated discs were submerged in 15 mL of solution PBS or dH_2O and incubated at 37 ± 2 °C. 3 isolated coated samples were observed by SEM at each time point. The solution was not changed over the test period. Removed samples were not re-submerged to prevent from disturbing the coating layer. The pH was measured pre and post degradation to ensure the solution did not become saturated. Samples could not be re-submerged following conductive coating for imaging due to contamination inhibiting degradation.

Mass loss data was recorded for coatings on sandblasted substrates, as bulk coating lift off or delamination had been observed on polished substrates. All samples were weighed prior to deposition and post deposition to determine the mass of the coatings. Samples were subsequently submerged in 15 mL of solution and incubated at 37 ± 2 °C (utilising three repeat test samples). For coatings C7U: P40 Fe4 and C12U: P28 Fe6 up to 24 h in solution the samples were not re-submerged, however for all data points beyond 24 h, the 24 h samples were re-submerged. For all other coatings 3 samples were resubmerged at every time point. At each time point the discs were removed, and placed in an oven at 50 °C for 1 h to remove surface moisture. The surface area was assumed constant as the coated Ti6Al4V surface parallel to the

plasma. Coatings for degradation were masked at the side to prevent edge effects. The mass was weighed after drying and loss was calculated via the following equation (*Eq 8*).

$$\frac{Mass\ Loss}{Surface\ Area} = \frac{(M_{initial} - M_{time})}{Surface\ Area_{time}} \qquad Eq\ 8$$

3.23 Inductively Coupled Plasma

Inductively coupled plasma injects an ion containing liquid into a plasma source. Following ionisation the use of a Mass Spectrometer assesses the number of ions within the plasma [218]. To assess ion release, isolated samples (n=3) for time points of 2, 16, 24 and 48 h were submerged in 15 ml of ultrapure Milli-Q water. Multi-element analysis of solutions was undertaken by ICP-MS (Thermo-Fisher Scientific iCAP-Q) utilising internal and external calibration standards, whilst samples were processed using the Qtegra™ software (Thermo-Fisher Scientific).

3.24 Simulated Body Fluid

A revised methodology and formulation proposed by Kokubo *et al.* was prepared as outlined in ISO 23317:2014 "Implants for Surgery- In Vitro evaluation for apatite-forming ability of implant materials" [86]. The reagents as shown in *Table 3.5* were weighed and dissolved one by one and magnetically stirred in a scratch free polymer container. The temperature was maintained at 37 ± 1 °C during preparation using a heated water bath. The pH was adjusted to 7.40 ± 0.01 by drip-feeding 1 mol HCL. Room temperature SBF was filtered through 20 μm particle filters. Samples were then placed in 0.1 ml mm^{-2} of SBF (~20 ml) of solution and incubated at 37 °C in 5% CO_2 for the duration of the test. All SBF tests were conducted over a period of 28 d at time points 1, 3, 7, 14, 21, and 28 d. Submerged samples were not re-submerged. Following removal, samples were washed with dH_2O and were left to

dry in a desiccator. XRD, XPS, SEM and FTIR were used to assess potential bioactivity. At all-time points non-coated Ti6Al4V samples and melt quenched BG 45S5 (2 mm thick 9 mm diameter rods) were used controls. For quenching parameters see *Table 3.2*.

Table 3.5: Preparation of Kokubo's 1000 ml of SBF as outlined in ISO 23317:2014 "Implants for Surgery - *In Vitro* evaluation for apatite-forming ability of implant materials" [86].

	Reagent	**Amount**	**Purity (%)**	**Molecular Weight (g mol^{-1})**
1	NaCl	8.035 g	99.5	58.44
2	$NaHCO_3$	0.355 g	99.5	84.01
3	KCl	0.225 g	99.5	74.55
4	$K_2HPO_43H_2O$	0.231 g	99	228.22
5	$MgC_{l2}6H_2O$	0.311 g	98	203.3
6	1.0m-HCl	39 ml	-	-
7	CaC_{l2}	0.292 g	75	110.98
8	Na_2SO_4	0.072 g	99	142.04
9	Tris	6.118 g	99	121.14
10	1.0m-HCl	0-5 ml	-	-

Ion Concentration (mM)								
	Na^+	**K^+**	**Mg^{2+}**	**Ca^{2+}**	**Cl^-**	**HCO_3^-**	**HPO_4^{2-}**	**SO_4^{2-}**
Human Blood Plasma	142.0	5.0	1.5	2.5	103.0	27.0	1.0	0.5
SBF ISO2014 [219]	142.0	5.0	1.5	2.5	103.0	4.2	1.0	0.5
SBF ISO2007 [220]	142.0	5.0	1.5	2.5	147.8	4.2	1.0	0.5

4. Results

The results here present the novel application and investigation of PBG coatings by RFMS. Until now the deposition of PBG thin films remained limited to the production of doped amorphous Ca:P which was subsequently crystallised to form HA coatings and the direct formation of HA through high power depositions [71, 157]. The formation of sputtered SBG has been under investigation since 2003 and remains the closest indicator of comparative sputtering behaviour [169].

Section 4.1 will assess the manufacturing challenges associated with vapour deposition followed by a brief application of coatings onto 3D meshes and organic materials in S*ection 4.2.* The structural and thermal characterisation of PBG coatings will be compared to compositionally equivalent melt quenched glasses in *Section 4.3* prior to assessing the degradation properties of PBG coatings in *Section 4.4.* The effects of post deposition heat treatment on the structural, mechanical, degradation and ion release properties have been assessed in *Section 4.5*. *In vitro* bioactive potential of a variety of PBGs and a SBG are present in *Section 4.6* by submersion in SBF solution.

4.1 Manufacturing and Processing of Glass Targets and Deposited Coatings

4.1.1 Production of Glass Sputtering Targets

As stated in the introduction the primary objective of this work is to apply and investigate the behaviour of various melt quenched glass systems under ion bombardment to subsequently determine the optimal processing parameters to obtain dense customised compositions of nano and micro thick coatings of PBG.

Therefore in (*Section 4.1.1*) the production of the PBG melt quenched "target" and the *in situ* effects of ion bombardment on target integrity have been addressed in (*Section 4.1.2*). Process reproducibility will be observed in (*Section 4.1.3*) and the effects of variation in processing parameters on both the integrity of, and the compositions of applied coatings, towards the ability to tailor compositions will be addressed (*Section 4.1.4*).

The targets (T1U-T9U) and (T1T-T2T) were manufactured for the UoN PVD and the TEER UDP 650 respectively and were utilised with the following objectives.

- (T1U-T6U) – To investigate the translational process ability of melt quenched glasses to be used as target materials for the production of vapour deposited thin films. The target integrity under ion bombardment was evaluated with varying target compositions, whilst the plasma induced heating effects on the target and glass thermal properties were accounted for. The consequences of parameter variations of power, pressure and atmosphere within the manufacturing process on sputtering yields and deposition rates were investigated.
- T1U: P40, T2U: P45 and T3U: P50 - Investigate any trends in preferential sputtering behaviour with an increase in the P_2O_5 network former substituting for 5 and 10 mol% of the Na_2O network modifier.

- T4U: P50 Fe2, T5U: P50 Fe4, T6U: P51.5 Fe5 and T9U: P51.5 Fe10 - Explored the addition of Fe oxide [47] since 1-10 mol% Fe_2O_3 is believed to stabilise the glass dissolution process by orders of magnitude [59]. The desired coating composition targeted due to its cytocompatibility based on prior research conducted within the group and as published by Hasan *et al.* [59, 197], was P_2O_5-40 MgO-24 CaO-16 Na_2O-16 Fe_2O_3-4 mol% which has been denoted as C7U: P40 Fe4 and was intended to be applied and tested as an initial benchmark to assess durability, mechanical properties, and potential bioactivity.
- T7U: P50 Ti5, T8U: P50 Ti7 Cu5 – Explored the modification with Ti for its potential in inducing apatite formation by development of Ti-OH nucleation points in PBG [52] and Cu for antibacterial properties [60].
- T1T: P57 Fe3 and T2T: Si46 BG 45S5 – Examined the scale up from pilot to industrial rigs. Whilst the main scope of this work was the novel exploration of resorbable PBG coatings the application of SBG was briefly explored via T2T: Si46. Work related to sputtering of bioactive SBG has been covered by Stan *et al.* from 2008 onwards [170-174, 177, 179, 221]. Finally the novel application of multi-layered phosphate/silicate glasses was explored through deposition of C7T: Multilayer from T1T: P57 Fe3 and T2T: Si46 BG 45S5.

All nominal target compositions from *Table 3.2* within the methodology were analysed via EDX analysis and have been presented in *Table 4.1* (below). Compositions were observed to vary by maximums of 2.1-SiO_2 2.7-P_2O_5 1.6-MgO 3.1-CaO 2.2-Na_2O 1.3-Fe_2O_3 1.4-TiO_2 0.4-CuO mol% from their intended compositions.

Table 4.1: As prepared sputtering targets. Composition represents average of 3, >10 μm² locations on the melt quenched glass as analysed by EDX. Nominal compositions can be found in Table 3.2.

	Target	mol%							
		SiO_2 ± 0.1	P_2O_5 ± 0.2	MgO ± 0.1	CaO ± 0.3	Na_2O ± 0.3	Fe_2O_3 ± 0.1	TiO_2 ± 0.1	CuO ± 0.1
UoN PVD	T1U: P40	-	38.9	24.8	14.8	21.5	-	-	-
	T2U: P45	-	43.9	25.2	14.8	16.1	-	-	-
	T3U: P50	-	48.6	25.3	14.9	11.2	-	-	-
	T4U: P50 Fe2	-	47.3	23.0	13.4	14.2	2.0	-	-
	T5U: P50 Fe4	-	47.7	21.5	13.1	14.0	3.7	-	-
	T6U: P51.5 Fe5	-	50.0	19.0	13.9	12.5	4.6	-	-
	T7U: P50 Ti5	-	50.4	-	38.8	7.1	-	4.6	-
	T8U: P50 Ti7 Cu5	-	50.6	-	22.7	16.5	-	5.6	4.6
	T9U: P51.5 Fe10	-	50.4	15.1	12.9	14.2	7.4	-	-
TEER UDP 650	T1T: P57 Fe3	-	56.2	15.1	12.1	13.4	2.8	-	-
	T2T: Si46	48.2	2.7	-	23.8	25.3	-	-	-

XRD (*Figure 4.1*) showed all sputtering targets to be amorphous in structure. The amorphous humps present between 15-35 2Θ (°) showed broad diffraction and the absence of any sharp peaks; characteristic of short-range order.

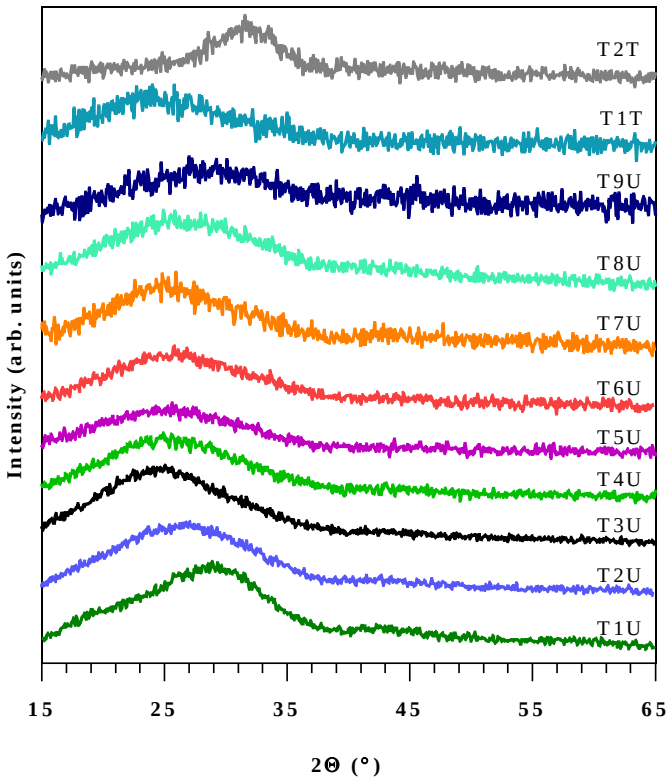

Figure 4.1: XRD of as prepared sputtering targets showing amorphous microstructures of all sputtering targets. All targets quenched at 450 °C and left to slow cool within graphite moulds.

4.1.2 Processing Window for Glasses under High Energy Ion Bombardment

The temperature of a target during processing was estimated during deposition of T1U: P40 using 99.99% pureshield argon at a pressure of 1.05 Pa. All targets were water-cooled at 13 °C. *Figure 4.2* shows the heating regime and the maximum temperature induced by the plasma at each power level, from 20-140 W. The data was recorded by placing a thermocouple $\sim 5.0 \pm 0.5$ mm above the centre of the target measuring the temperature as a function of time and power. The thermocouple was not in contact with the surface to avoid grounding the target.

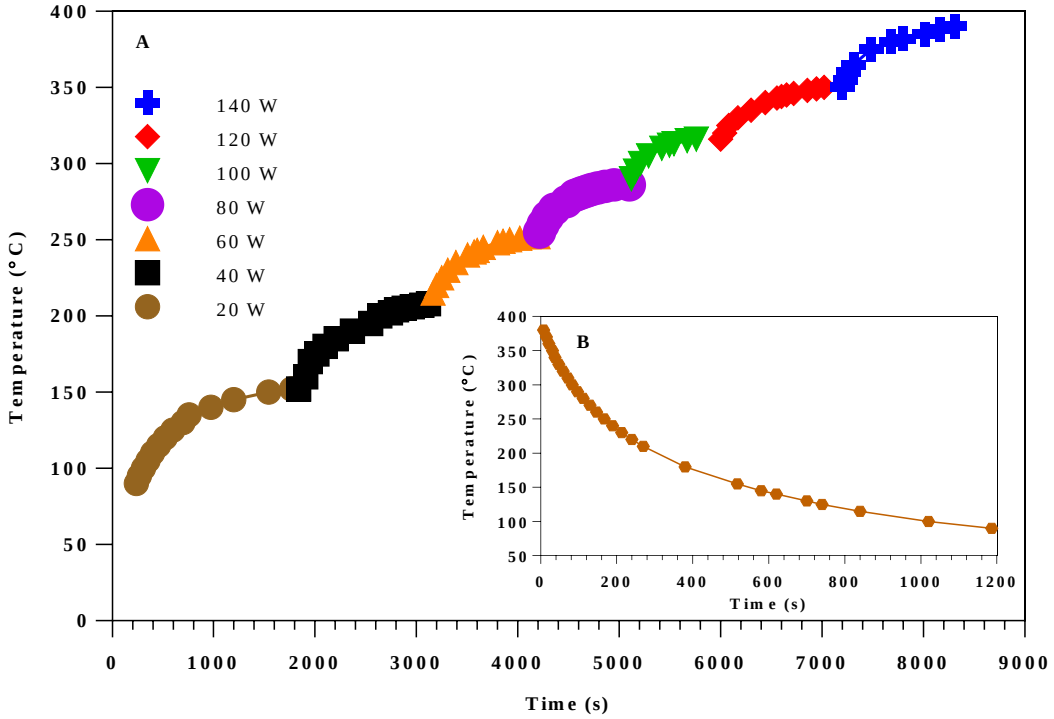

Figure 4.2: (A) Heat of the plasma at 5.0 ± 0.5 mm above the target measured during deposition from T1U: P40. (B) Cooling time upon turning off the plasma. Error bars are within the plot (± 2.0 °C).

The target temperature rose from room temperature to 90 °C within 240 s. The greatest temperature increase with time was upon activating the plasma followed by a plateau and an eventual maximum temperature of 150 °C after 1545 s. The trend continued as the power increased at each 20 W interval, levelling off at a maximum for each input power. The RF power supply was turned off at 140 W, recording a

maximum measured temperature of 390 °C. This was followed by a rapid decline in temperature as shown by *Figure 4.2B.*

T1U: P40 had the lowest T_g, T_c and T_m temperatures of (T1U-T7U) of 435, 585, and 764 °C respectively. Deposition powers of 60, 80, 100, 120 W were tested for T1U: P40, and were shown to inflict various degrees of target damage relative to processing parameters. Target cracking intensified with power (see *Figure 4.3)*.

The TEC and thermal properties for the glass targets (T1U–T7U) are presented in *Table 4.2*. All experimental samples for TMA and DTA analysis were cast as rods at 450 °C to mimic the quenching process for production of the sputtering targets.

Table 4.2: DTA and TMA thermal analysis of (T1U- T7U). (B) Table of thermal expansion coefficients, T_g and T_{c1} T_{m1} based on DTA and TMA analysis.

Target mol%	Thermal Expansion Coefficient (K^{-1})	Tg (°C) ± 2	Tc (°C) ± 2	Tm (°C) ± 2
T1U: P40	16.0 [47]	435	585	764
T2U: P45	14.5 [47]	450	631	825
T3U: P50	12.9 [47]	465	625	828
T4U: P50 Fe2	12.2 ± 0.1	446	649	836
T5U: P50 Fe4	-	458	718	788
T6U: P51.5 Fe5	11.6 ± 0.1	460	725	811
T7U: P50 Ti5	12.3 ± 0.3	491	707	910

T1U: P40 targets processed at 120 W crystallised during processing. (*Figure 4.3*) shows a target, which crystallised *in situ* during a trial deposition at 120 W over a period of 240 min. The damage was observed to radiate from the centre. XRD revealed a highly crystalline material following deposition for 600 min at 120 W (*Appendix 9, 3.0*).

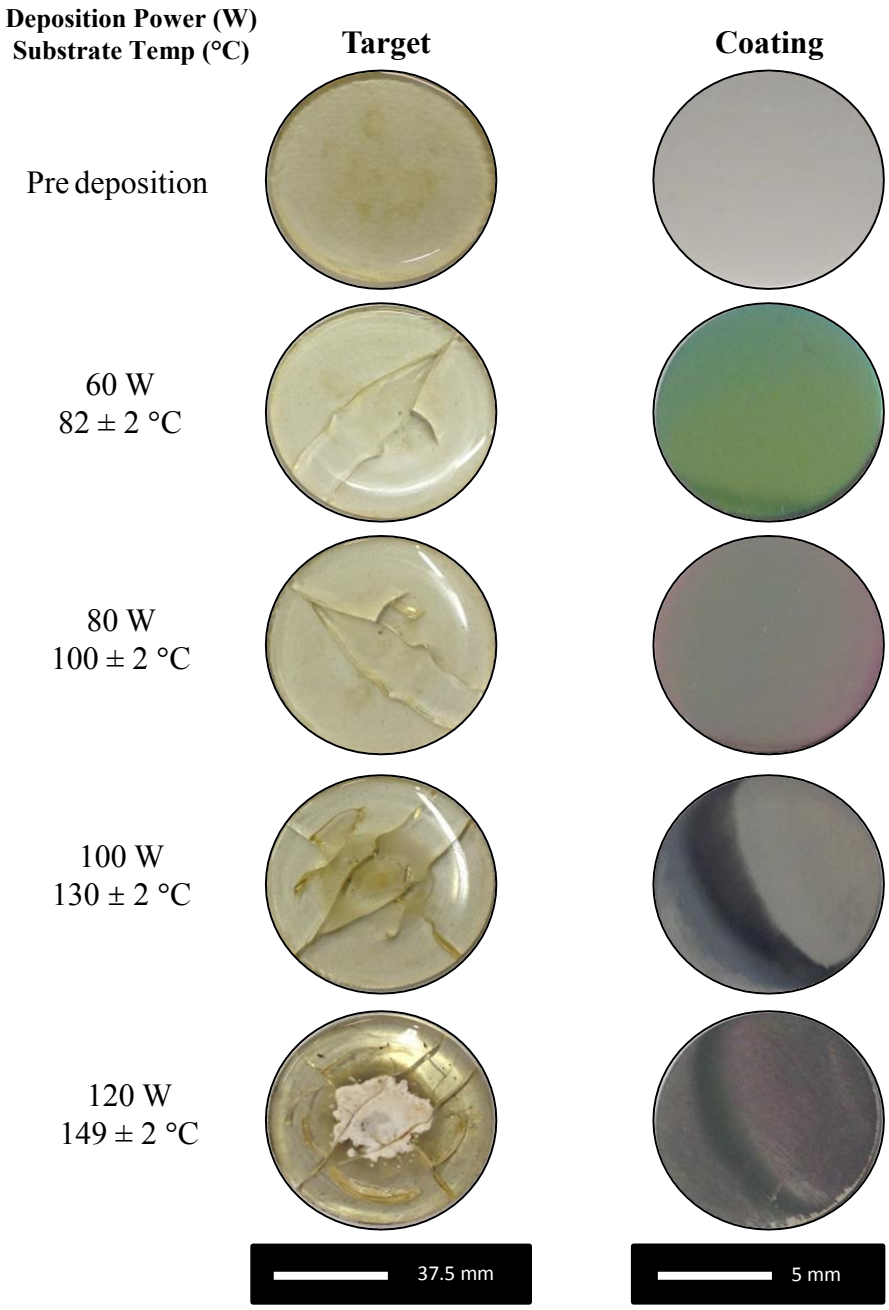

Figure 4.3: Images of post-use target composition T1U: P40 following variation in deposition powers from 60 W to 120 W. (B) Observation of the deposited coating on CPTi. Deposition rate with power calculated as 0.11 ± 0.01 × Power nm min^{-1} with an r^2 of 0.97.

Target T6U: P51.5 Fe5 was found to be the most thermally stable composition (TEC=11.61 ± 0.07 K^{-1} T_c=727.4 °C) see *Table 4.2*. T6U: P51.5 Fe5 suffered from thermal shock and cracked similarly to target (T1U-T5U). T6U: P51.5 Fe5 however was the first target to withstand thermal shock during a 20 hour deposition at 60 W, cracking during runs thereafter.

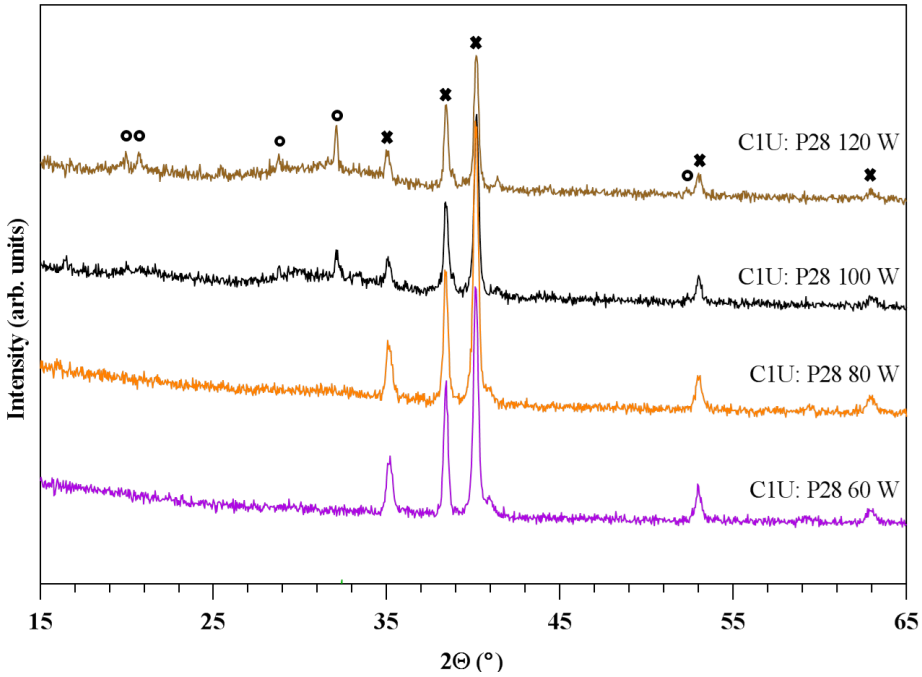

Figure 4.4: XRD patterns for In situ plasma induced crystallisation of the target by ion bombardment; crystalline and pre-sputtered glass target: T1U: P40 and XRD for C1U: P28 deposited from 60-120 W. (✖) Titanium ICDD PDF-00-001-1197(o) Sodium Titanium Phosphate $NaTi_2(PO_4)_3$ ICDD PDF-00-033-1296.

The identified phase for C1U: P28 60 W and 80 W corresponded to ICDD-PDF-00-001-1197 Ti, and was from the substrate as X-rays penetrated the thin film (*Figure 4.4*). Extrapolated deposition rates from (*Figure 4.5*) showed a linear increase in rates of $0.11 \pm 0.01 \times$ Power nm min^{-1} with an r^2 of 0.97.

Coatings deposited at 100 and 120 W showed evidence of particle nucleation as observed from the coating SEM micrographs (*Figure 4.5E and G*); this was confirmed as crystal formations of Sodium Titanium Phosphate via XRD analysis (*Figure 4.4*). Elemental mapping exhibited inhomogeneous distribution of elements following deposition at 100 and 120 W whilst 60-80 W showed uniform distributions. Elemental mapping has been shown for 120 W, following deposition (*Figure 4.6*). Notably the crystals observed on the coating EDX micrograph appeared to be sodium rich.

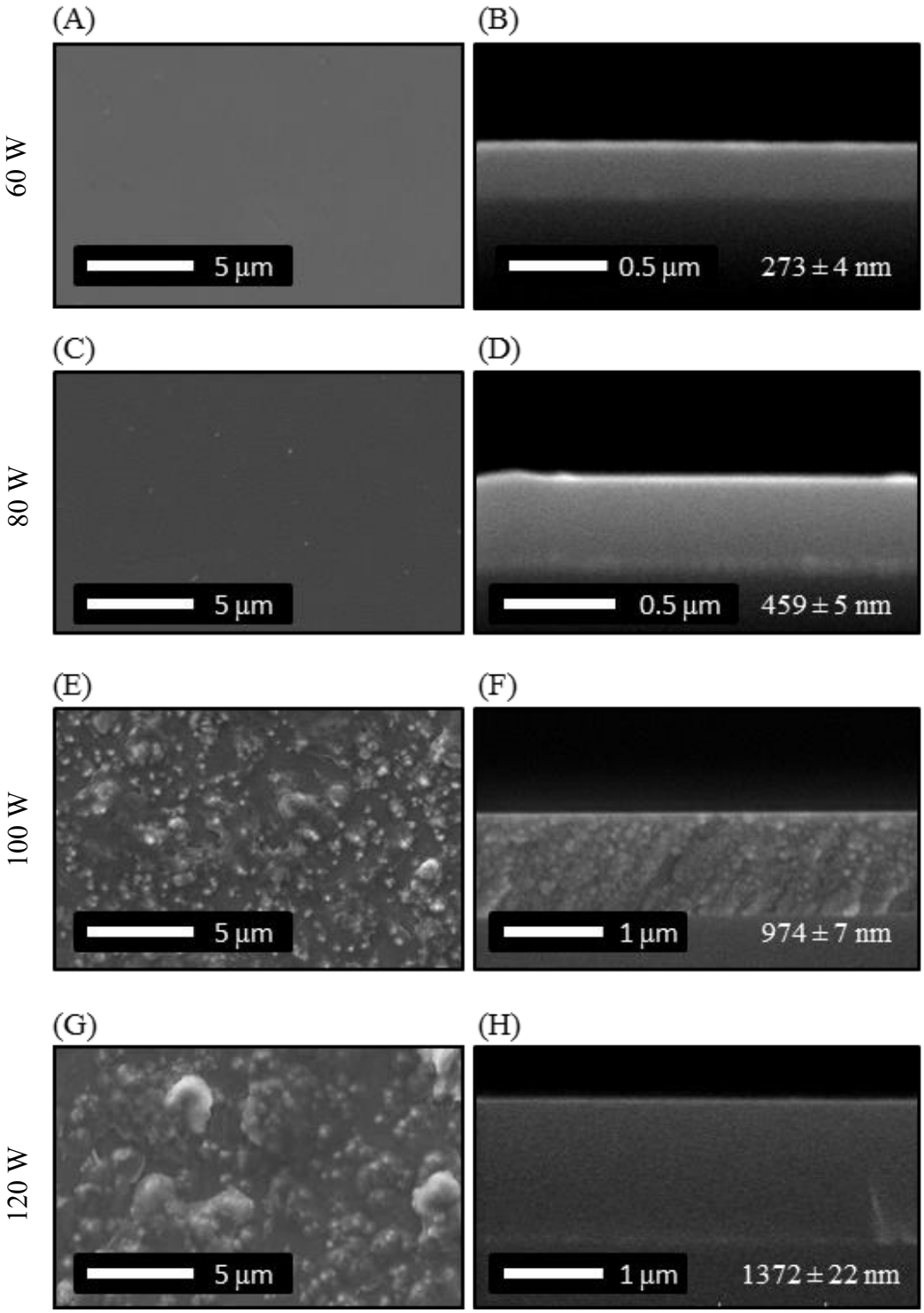

Figure 4.5: (A, C, E and G) Deposition from T1U: P40 to produce C1U: P28 following variation in deposition powers from 60 W to 120 W. Observation of the deposited coating on CPTi. (B, D, F, H) Observation of the deposited coating cross section on borosilicate cover slips. Linear increase in rates 0.11 ± 0.01 × Power nm min^{-1} with an r^2 of 0.97. Coating thickness presented within SEM micrographs.

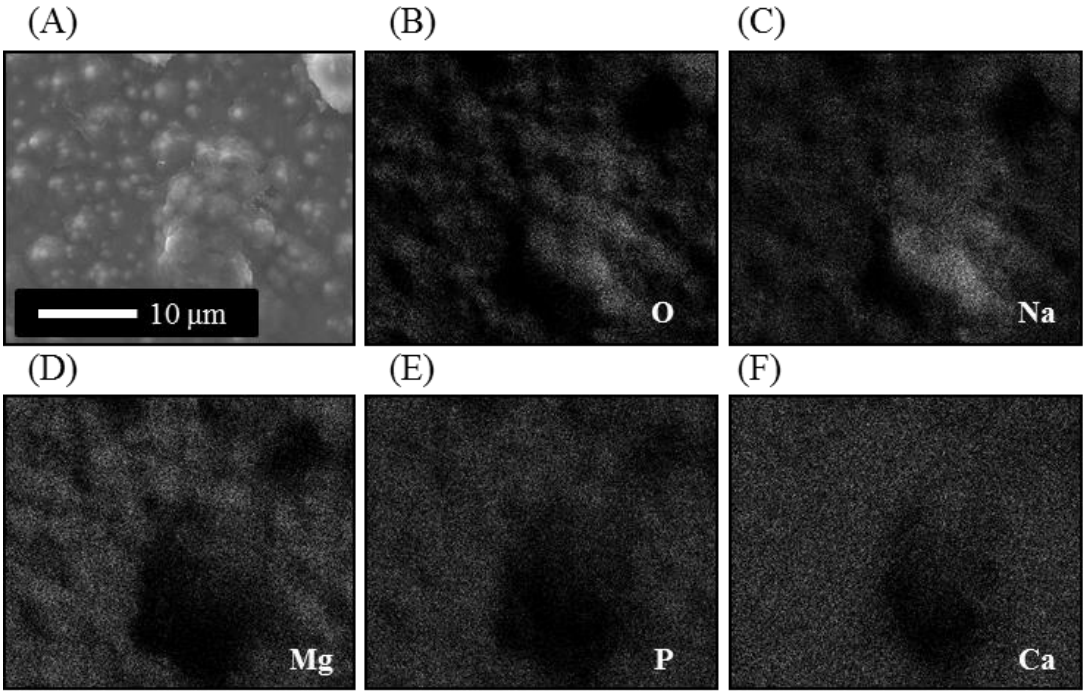

Figure 4.6: Elemental Mapping of the coating C1U: P28 following deposition from T1U: P40 at 120 W. Noticeable inhomogeneity within elemental distribution. Crystals appear to be rich in Na. Mg, Ca and P are distributed throughout the sample.

Characteristic EDX spectra have been presented in *Figure 4.7* for 60 W compared with 120 W, following deposition from T1U: P40. Of crucial importance, the Ti K peak intensity is larger for 60 W leading to 24.3 at% in comparison to 0.3 at% at 120 W. Coating compositions were assessed by EDX at 3 random locations over the 10 mm diameter sample area as show in *Table 4.6.*

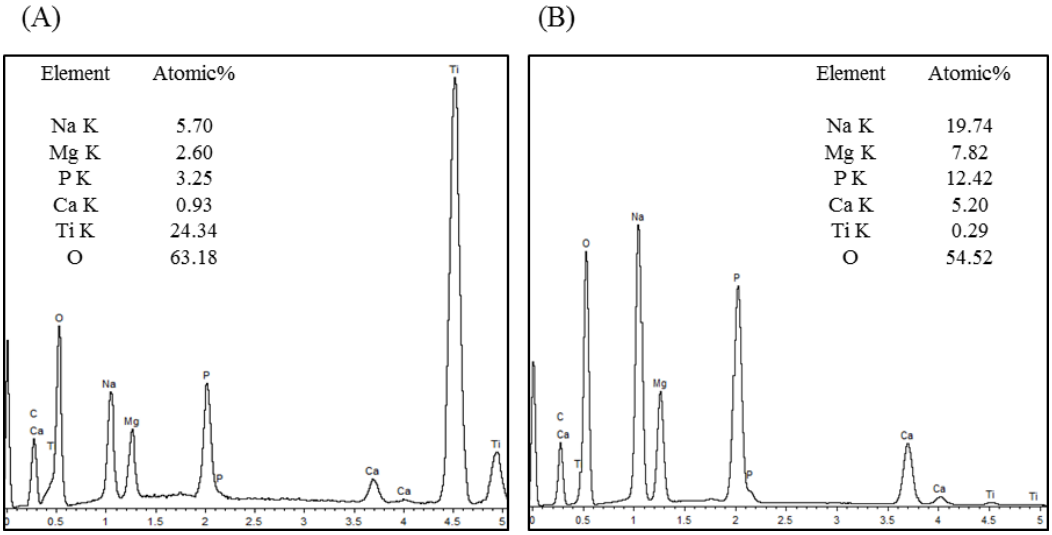

Figure 4.7: EDX Spectra for coatings C1U: P28 deposited at (A) 60 W compared with (B) 120 W deposited from T1U: P40. A notable increase in the intensity of the Ti peak is present for (A).

XPS Surface Composition

The surface compositions and structural oxidation states were assessed for power levels from 60-120 W for T1U: P40. The XPS survey spectra confirmed the surface composition of coatings and melt quenched glass containing P, Mg, Ca, and Na in *Table 4.3*. Notably the surface phosphorus reduced from 21.8 at 60 W to a minimum of 3.9 and 6.6 at% following 100 W and 120 W depositions.

Table 4.3: Composition of the coating surface via XPS and the bulk via EDX. Compositions were assessed with increasing deposition power from 60-120 W, following deposition of C1U: P28 from T1U: P40. Relative ratios of bridging (BO) to non-bridging oxygens (NBO) assessed via XPS. The Na KLL was found to overlap the O 1s peak and therefore has been subtracted to normalise ratios. EDX measurements conducted at n=3 random >10 μm^2 areas over the sample. Orthophosphate $(PO_4)^{3-}$, Pyrophosphate $(P_2O_7)^{4-}$, Metaphosphate $(PO_3)^-$, (Q^0, Q^1 and Q^2 respectively) [48, 222-224].

Element	**60 W**		**80 W**		**100 W**		**120 W**	
	at% XPS	**at% EDX**	**at% XPS**	**at% EDX**	**at% XPS**	**at% EDX**	**at% XPS**	**at% EDX**
Na	2.4	16.2 ± 0.1	5.8	15.7 ± 0.2	32.3	19.1 ± 0.8	29.2	20.1 ± 0.1
P	21.8	13.8 ± 0.1	20.7	14.4 ± 0.1	3.9	12.9 ± 0.1	6.6	12.6 ± 0.1
Ca	6.4	4.1 ± 0.1	6.9	4.0 ± 0.1	2.2	5.0 ± 0.1	2.8	5.2 ± 0.1
Mg	6.1	9.6 ± 0.2	4.8	9.0 ± 0.1	2.9	8.1 ± 0.3	2.1	7.7 ± 0.1
O	63.3	56.3 ± 0.2	61.8	56.9 ± 0.1	58.6	54.9 ± 0.3	59.3	54.4 ± 0.1
Surface Structure								
PO^- and P=O %*	65.2		68.7		92.7		91.4	
P-O-P %*	34.8		31.3		7.3		8.5	
P $2p_{3/2}$ (eV)	134.4		134.3		133.7		133.2	
Majority Q^n Distribution	Q^2		Q^2		Q^0, Q^1, Q^2		Q^0 and Q^1	

* Normalised O 1s following subtraction of the overlapping Na KLL

High resolution scans showed the presence of adventitious carbon in the form of C-C, C-O-C and O-C=O bonds at their respective locations ranging (284.78-284.88), (286.39-287.25), and (288.28-289.31) eV (*Figure 4.8C and D)* matching positions shown by Dementjev *et al.* [225]. An increase in O-C=O was observed with deposition power, increasing from 4.1 to 15.1%. Suggestions of metal phosphate bonds, PO^-, P-O-P bridges and oxides associated with ionic linkages for the alkali metals Na, Mg and Ca connected to the PO^- sites supported the presence of glass.

High resolution spectra associated with P 2p, Na 1s, Ca 2p, Mg 2s, showed oxidation states characteristic of metal oxides for all XPS spectra (not shown here however similar to *Figure 4.26*). At 60 W compared with 120 W the ratios of non-bridging oxygens to bridging oxygens as determined by the ratio of peaks within the O 1s spectra increased from 65.2/34.8% to 91.4/8.5% (*Table 4.3* and *Figure 4.8*). As shown by Wagner *et al.,* to definitively attribute the states to Q^1 and Q^0, the P 2p peak location should be positioned at ~133.2 eV and for Q^2 at ~134.6 eV [224]. A number of coatings showed the location of the P $2p_{3/2}$ to be at intermediate locations, suggesting the presence of all three states as shown in (*Table 4.3*, *P 2p spectra not shown in figure*).

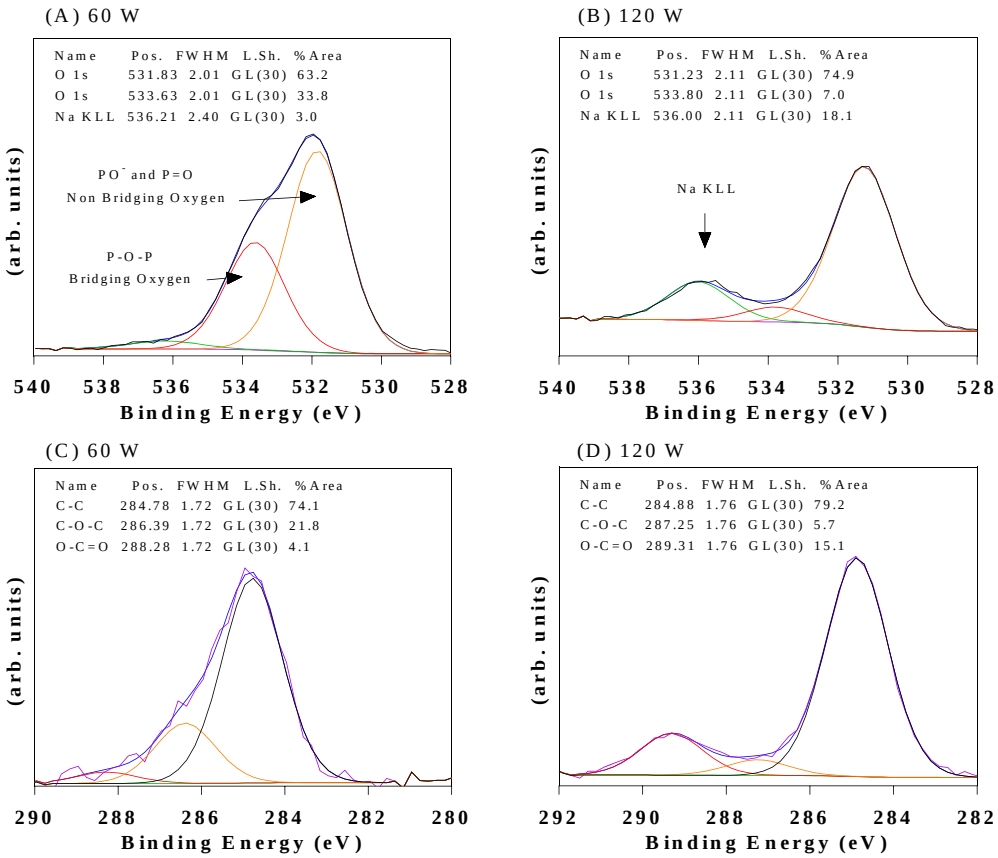

Figure 4.8: O 1s following deposition of C1U: P28 from T1U: P40 at (A) 60 and (B) 120 W showing the variation in ratio of Bridging to Non Bridging Oxygens within the surface layer. (C) (D) Analysis of the C 1s showing states of surface carbon.

4.1.3 Coating Uniformity, Process Precision and Reproducibility

The reproducibility of the coating processes were analysed and quantified in both the UoN PVD and the TEER UDP 650.

UoN PVD

Coating composition

The compositional variation of a coating was analysed following deposition from T5U: P50 Fe4. Deposition was conducted at 80 W, 1.05 Pa, for 1200 min. The elemental composition at 12 random locations on the sample was determined by EDX. The average composition and calculated standard error of the mean for each oxide have been presented. P_2O_5, CaO, Na_2O, Fe_2O_3 and MgO ranged 0.45, 0.59, 0.56, 0.72 and 0.79 mol% respectively over the sample (*Figure 4.9)*.

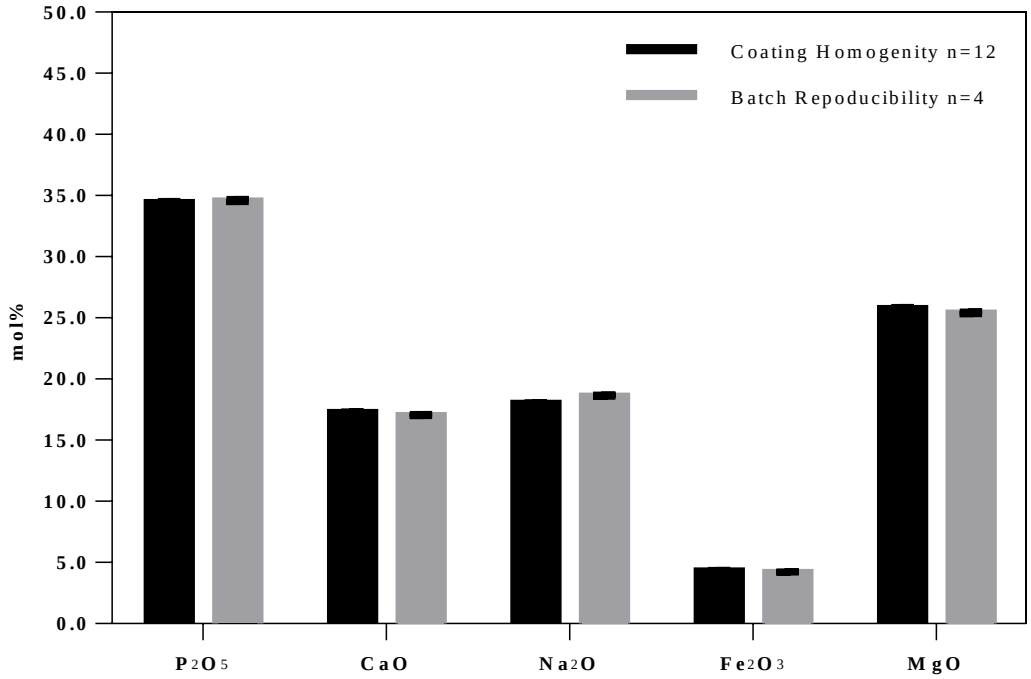

Figure 4.9: Batch repoducibility within the UoN PVD following deposition from T5U: P50 Fe4 at 80 W. The sputtering yield by compositional EDX analysis on a single sample at 12 locations and 4 independent batches over 3 locations/sample was assessed, The ranges and batch variation were analysed by calculation of the Standard Error of the Mean.

The sputtering process was independently repeated in (n=4) batches to observe batch reproducibility. The EDX results are presented in *Figure 4.9.* P_2O_5, CaO, Na_2O, Fe_2O_3 and MgO ranged from 0.67, 0.48, 0.43, 0.22 and 0.47 mol% respectively.

All batch-to-batch coating compositions were analysed as the average of three random area analyses of >10 μm^2 on each coated sample. The instrumental precision for the EDX process via the Phillips XL30 was analysed by collecting 5 repeated spectra over a single area, showing calculated standard errors for P_2O_5, CaO, Na_2O, Fe_2O_3 and MgO of 0.11, 0.10, 0.11, 0.53 and 0.08 mol% respectively.

Deposition Rates

Coating thickness measurements were obtained by imaging of coating cross sections following deposition onto borosilicate cover slips of C7U: P40 Fe4. *Figure 4.10A* shows polished Ti6Al4V samples prior to coating. Following the deposition of C7U: P40 Fe4, light interference effects were optically observed as shown in *Figure 4.10B* and *C*.

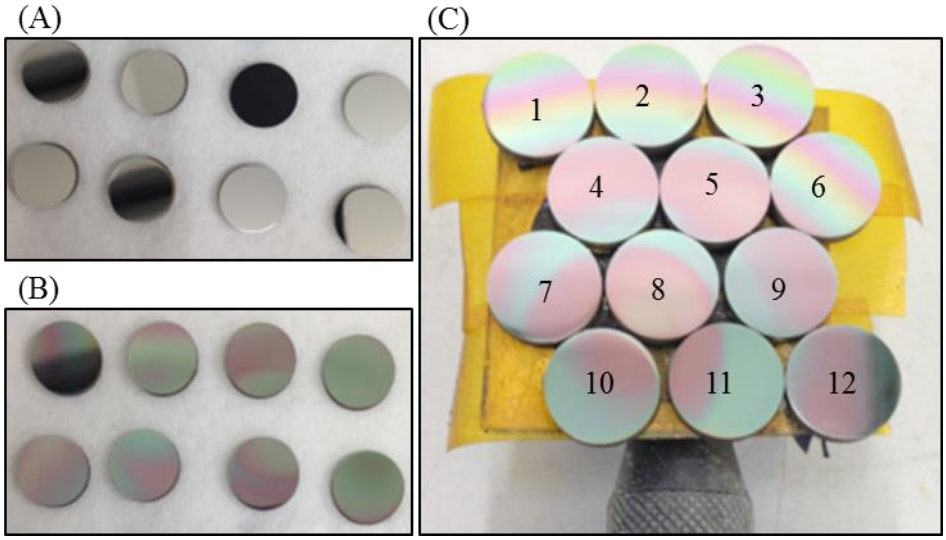

Figure 4.10: (A) Pre deposition polished Ti6Al4V and (B and C) as deposited coatings C7U: P40 Fe4 from T6U: P51.5 Fe5. Light interference showing thickness variation. Locations in (C) referring to measured masses at locations corresponding to Figure 4.11.

Deposition rates measured at n=16 locations ~4 mm apart on 4 coated borosilicate glass substrates was between 2.2 and 2.5 nm min^{-1}; a maximum variation of 12.0%. Similarly, batch to batch (n=3 batches) analysis by measuring coating mass for the 12 disc locations in *Figure 4.11* showed random mass variation from 5.2 – 5.9 x 10^{-4} g, a variation of up to 13.4%. The sides were masked for dissolution to restrict deposition to the substrate surface area perpendicular to the plasma. Approximate density measurments have been calculated ranging from 2.45-2.78 kg m^{-3}. Futher density analysis by Helium Pycnometry for compositions of PBG can be found in *Section 4.3.6*.

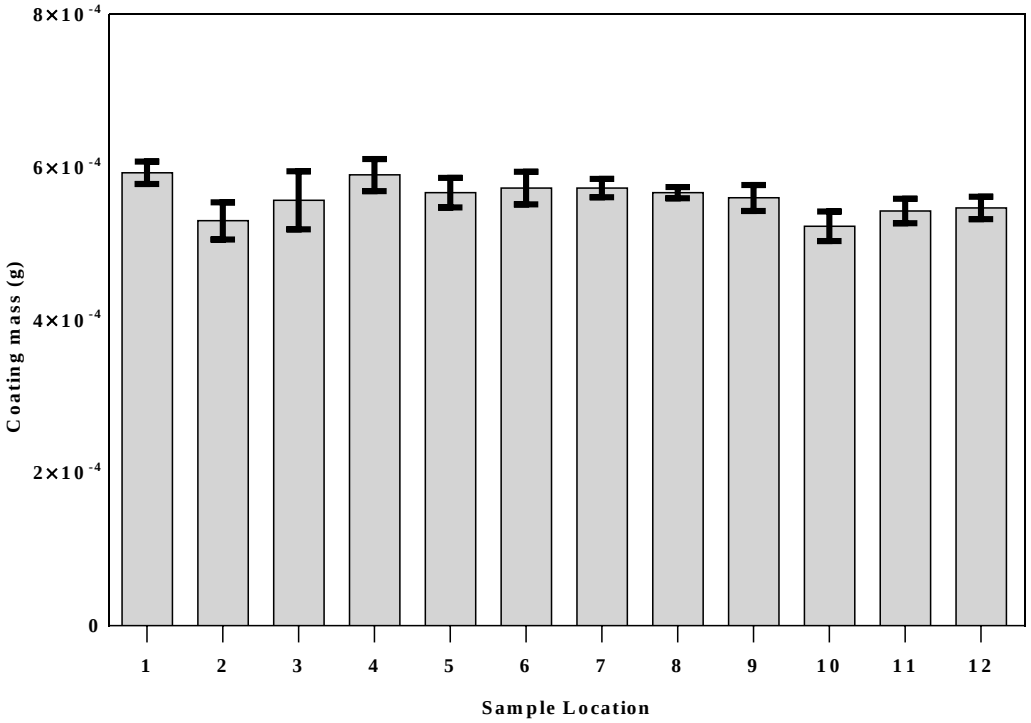

Figure 4.11: (A) C7U: P40 Fe4 deposited from T6U: P51.5 Fe5. Analysis of coating masses for 12 locations along the sample holder, assessed for 3 independent batches on masked substrates. Mass variation across the sample holder was measured as 13.4%. Sample locations refer to Figure 4.10C.

TEER UDP 650 PVD

Coating composition

The TEER UDP 650 can accomadate up to 4 DC targets or 2 RF targets on Mag 2 and Mag 4. See *Figure 3.4* for locational schematic. Sputtering behaviour for both static and 5 RPM rotation were analysed in Mag 2. A single batch from Mag 4 was studied to observe potential compositional variability with respect to cathode location. Analysis of 12 random locations of >10 μm^2 over the sample showed that composition variations for Mag 2 static of P_2O_5, CaO, Na_2O, Fe_2O_3 and MgO ranged from 2.16, 1.35, 1.58, 0.38 and 2.06 mol% respectively whilst batch to batch variation ranged from 5.10, 2.46, 2.12, 0.74 and 3.62 mol% respectively for the different oxides. Sample rotation improved the batch reproducibility ranging from 1.48, 0.17, 0.87, 0.30 and 0.71 mol% respectively as shown in *Figure 4.12*. Static depositon in mag 2 produced coating thicknesses of 2040 ± 41, 2114 ± 34 and 2064 ± 32 nm for 5 sample locations over 3 batches. Similarly sample rotation in front of Mag 2 at 5 RPM led to indentical thickness of 262 ± 4 nm over 2 batches and a coating thickness of 264 ± 3 nm for samples rotated in mag 4 during a single batch demonstrating reproducibility.

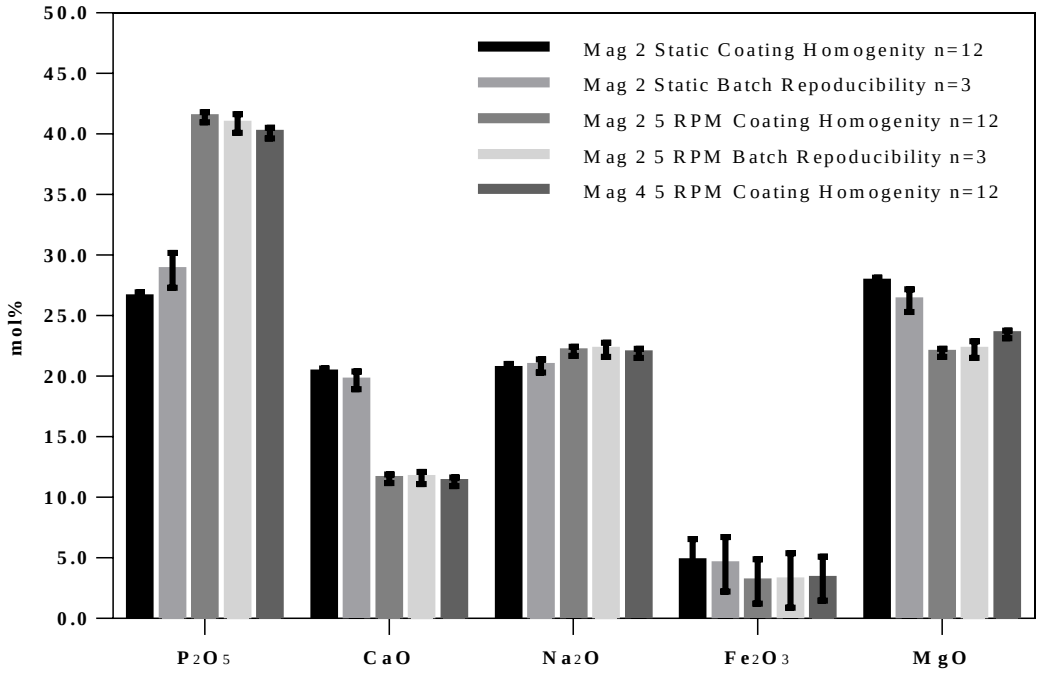

Figure 4.12: Single sample and batch to batch reproducibility within the TEER UDP 650 during static sputtering and 5 RPM from T1T: P57 Fe3. Variable sputtering yield observed due to static compared with rotational deposition.

Coating SEM micrographs showed significant pitting present during static coating deposition. This was eliminated when rotated through the plasma as shown in *Figure 4.13A* compared with *B* and *C.*

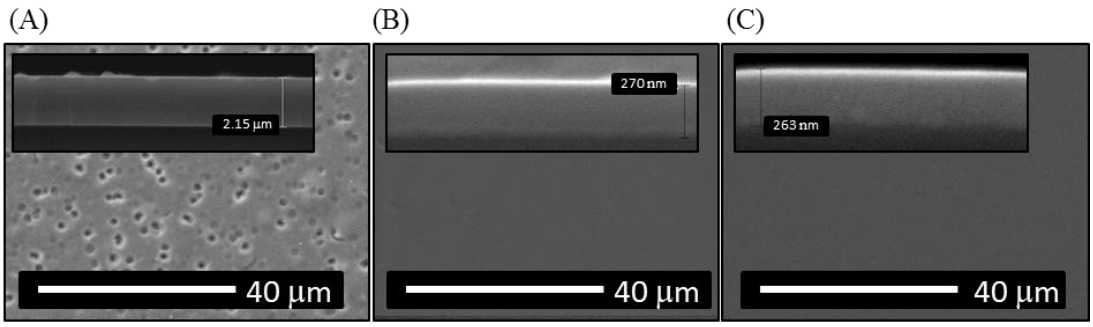

Figure 4.13: Deposition from T1T: P57 Fe3 (A) static Mag 2. Deposition pits were dispersed over the sample surface compared with (B) 5 RPM rotation Mag 2. (C) 5 RPM rotation Mag 4. (Inserts) representative of coating cross section on borosilicate cover slips.

4.1.4 Sputtering Effects and Preferential Sputtering

Resulting from the momentum interactions between the ionised working gas (argon) during the bombardment of the sputtering target, non stoichiometric transfer from target to coating compositions was observed. Compositional variation is a factor of the physical interactions dictated by deposition parameters.

Preferential Sputtering with Variation in Power

Results presented in *Figure 4.14* comparing the sputtering yield and deposition rates at powers of 60, 70 and 80 W showed a linear variation in deposition rate with increasing power, whilst displaying a decline in P_2O_5 of 2.0 mol% and an increase in CaO, Na_2O and MgO of 0.8, 1.2 and 0.4 mol% respectively.

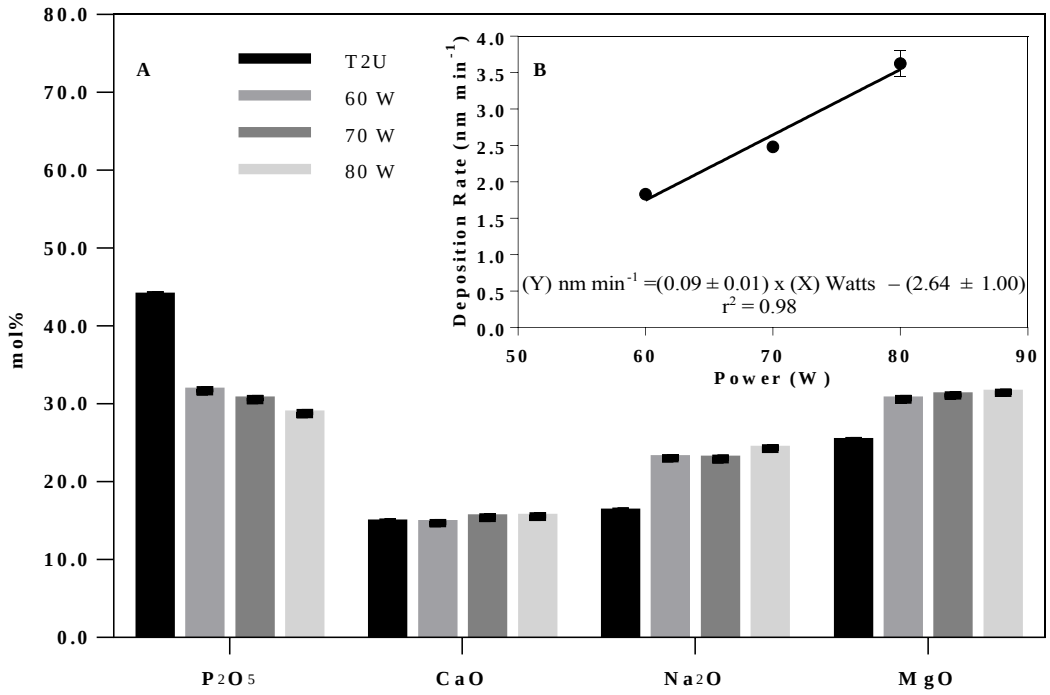

Figure 4.14: (A) Variation in relative sputtering yield with varying powers using T2U: P45 at 60, 70 and 80 W. A marginal reduction in P_2O_5 content was observed with increasing power. (B) Variation in deposition rate with increasing power from 60-80 W.

Preferential Sputtering at Constant Pressure

Depositions of targets (T1U-T9U) revealed significant variations between target and coating compositional stoichiometries. Coating compositions labelled (C1U-C11U) are presented in *Table 4.4.* In all cases a reduction in P_2O_5 mol% content was observed whilst the proportion of network modifying alkali metal oxides increased following transfer to the coating composition. The changes observed from the 6 target compositions to their respective coating compositions (C1U-C6U) sputtered under constant parameters specifically at pressure of 1.05 Pa and 60 W, showed a reduction in P_2O_5 and Fe_2O_3 of between (10.3 to 15.2), (0.2 to 0.6) mol% respectively and an increase in MgO, CaO and Na_2O of (4.8 to 6.0), (0.1 to 3.8), (3.0 to 6.9) mol% respectively. These changes in mol% of the elements deposited are shown in *Table 8* and indicate sputtering yields in the order Na > Mg > Ca > Fe > P in at%. (C8U-C9U), sputtered at 1.33 Pa explored the additions of Ti and Cu and were not particularly compositionally altered to explore sputtering trends in particular, they however showed changes of (-9.6 to -19.2)-P_2O_5, (2.1 to 16.7)-CaO, (0.6 to 7.0)-Na_2O, (-0.6 to 1.1)-Fe_2O_3, (3.3 to 7.1)-MgO, (1.1)-TiO_2, (-0.3)-CuO mol%. Therefore showing a resultant relative sputtering yield of Na > Ca > Mg > Ti > Fe > Cu > P. The results show a consistent reduction in phosphorous and an increase in the alkali and alkali earth metals whilst transition metals showed similar sputtering yields (*Table 4.4)*. C11U: P32 Fe5 was not compared as it was produced at 90 W.

Table 4.4: Coating compositions (C1U-C6U) deposited from (T1U-T6U) at 60 W and 1.05 Pa for 1260 min. (C7U-C11U) were deposited at 1.33 Pa over a period of 1165 min. Absolute change in mol% from target to coating composition for targets to coatings (T1U-T9U) to (C1U-C11U) presented in brackets. Deposition rate calculations based n=5 locations. C11U: P32 Fe5 was deposited under the same parameters as C7U: P40 Fe4 however at 90 W vs. 60 W.

Deposited Coating (mol% change)	Deposition Rate (nm min^{-1}) ±0.05	P_2O_5 ±0.2 (0.2)	CaO ±0.1 (0.2)	Na_2O ±0.2 (0.2)	Fe_2O_3 ±0.5 (0.5)	MgO ±0.2 (0.6)	TiO_2 ±0.1 (0.1)	CuO ±0.2 (0.1)
		mol%						
C1U: P28 (T1U-C1U)	1.73	28.4 (-10.5)	14.7 (+0.1)	27.4 (+5.9)	-	29.6 (+4.8)	-	-
C2U: P32 (T2U-C2U)	1.83	31.7 (-12.2)	14.7 (+0.1)	23.0 (+6.9)	-	30.6 (+5.4)	-	-
C3U: P35 (T3U-C3U)	1.59	34.6 (-14.0)	17.1 (+2.2)	17.2 (+6.0)	-	31.2 (+5.9)	-	-
C4U: P37 Fe1 (T4U-C4U)	1.90	37.0 (-10.3)	15.8 (+2.4)	17.2 (+3.0)	1.4 (-0.6)	28.5 (+5.5)	-	-
C5U: P35 Fe3 (T5U-C5U)	1.86	34.8 (-12.9)	16.3 (+3.2)	18.6 (+4.6)	3.3 (-0.4)	27.0 (+5.5)	-	-
C6U: P34.5 Fe4 (T6U-C6U)	1.93	34.6 (-15.2)	17.1 (+3.8)	18.8 (+5.7)	4.2 (+0.2)	25.3 (+6.0)	-	-
C7U: P40 Fe4 (T6U-C7U)	2.29	40.2 (-9.6)	15.4 (+2.1)	16.8 (+3.6)	3.8 (-0.6)	23.8 (+4.5)	-	-
C8U: P31 Ti6 (T7U-C8U)	0.89	31.3 (-19.2)	55.4 (+16.7)	7.7 (+0.6)	-	-	5.5 (+1.1)	-
C9U: P35 Ti7 Cu5 (T8U-C9U)	1.65	34.5 (-16.0)	30.3 (+7.8)	23.8 (+7.0)	-	-	6.7 (+1.1)	4.7 (-0.3)
C10U: P40 Fe8 (T9U-C10U)	2.29	39.3 (-11.1)	16.6 (+3.7)	17.2 (+3.0)	8.4 (+1.1)	18.4 (+3.3)	-	-
C11U: P32 Fe5 (T6U-C11U)	4.89	31.5 (-18.3)	18.9 (+5.6)	18.3 (+5.1)	4.9 (+0.5)	26.4 (+7.1)	-	-

Cross sectional images of the coatings deposited (C1U-C11U), *Figure 4.15A,* onto borosilicate cover slips indicated deposition rates of 1.59-1.93 nm min^{-1} at 1.05 Pa, 0.95-2.29 nm min^{-1} at 1.33 Pa and 4.89 nm min^{-1} at 90 W (see *Table 4.4).*

SEM images of (C1U-C11U) are not presented here as they displayed similar features to the cross-sectional images shown in *Figure 4.15A and B (*for C7U: P40 Fe4). The coating surfaces were seen to be free from cracks, pores and voids and appeared homogenous. Notably C11U: P32 Fe5 at 90 W was also observed to be void free.

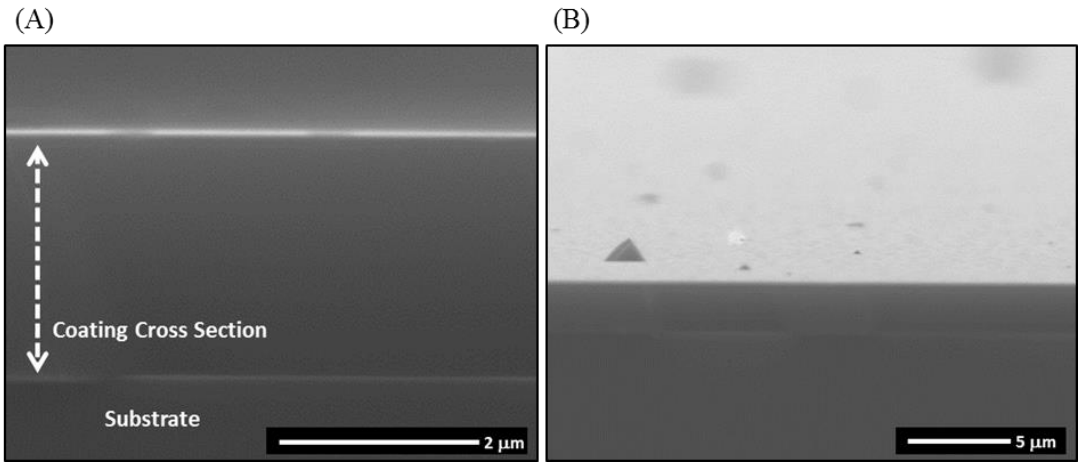

Figure 4.15: Coating C7U: P40 Fe4 deposited from T6U: 51.5 Fe5 at 1.33 Pa and 60 W. (A) Coating cross section. (B) Coating surface at a 7° from the cross section. Coatings C1-C11U displayed similar featureless cross sections.

The control composition for benchmark analysis for this project; P_2O_5-40 MgO-24 CaO-16 Na_2O-16 Fe_2O_3-4 mol% was obtained by sputtering T6U: P51.5 Fe5 at 60 W, 1.33 Pa and was subsequently applied to Ti6Al4V substrates.

X-ray Diffraction of Coatings (C1U-C11U)

Coatings (C1U-C11U) were deposited onto CPTi (C1U-C6U) and Ti6Al4V (C7U-C11U) substrates from targets (T1U-T9U) and were analysed via glancing angle XRD (see *Figure 4.16*). All films deposited were amorphous characterised by broad diffraction between 15 and 35 2Θ (°). The identified phases corresponded to either crystalline Ti or Al_2O_3, embedded into the substrate from the sandblasting stage. Notably an unidentified peak was present at 29.5 2Θ (°), which appears to be within the CPTi substrate.

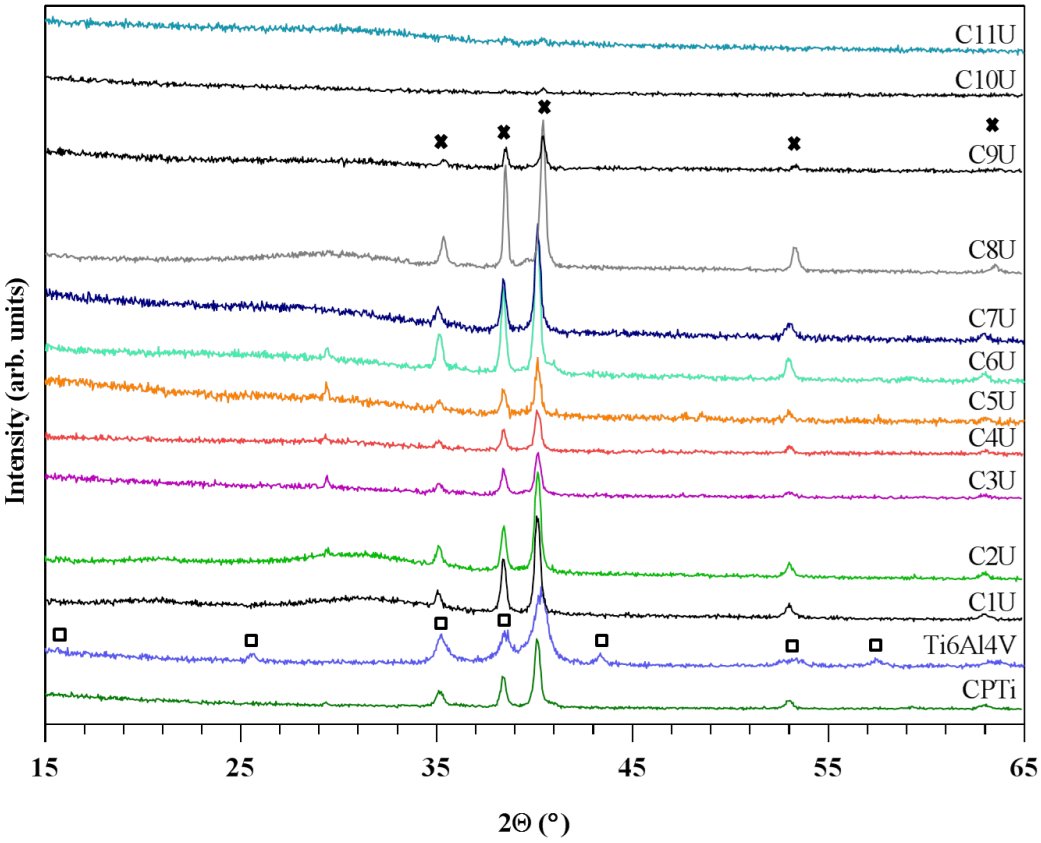

Figure 4.16: X-ray Diffraction of a blank CPTi and sandblasted Ti6Al4V substrates and the as deposited coatings (C1U-C11U). The Ti phase has been identified as ICDD-PDF-00-001-1197 (✖). An additional peak in the substrate at 29.5 2Θ (°) has not been identified and appeared to be associated with impurities within the substrate or the introduction of contamination from the polishing process. Al_2O_3 ICDD-PDF-00-081-1667 (□).

Preferential Sputtering with Varying Chamber Pressure

The effect of variation in argon pressure on deposition rates and relative sputtering yields was examined. As the pressure increased from 0.28 Pa to 1.60 Pa the stoichiometry of the coatings approached the original stoichiometry of the target. The sputtering yield of the network modifying alkali metal ions increased whilst the sputtering yield of the phosphate network former reduced. The relative sputtering yield of Fe oxide remained constant. At 1.87 Pa the coating stoichiometry began to diverge from the target (see *Figure 4.17*).

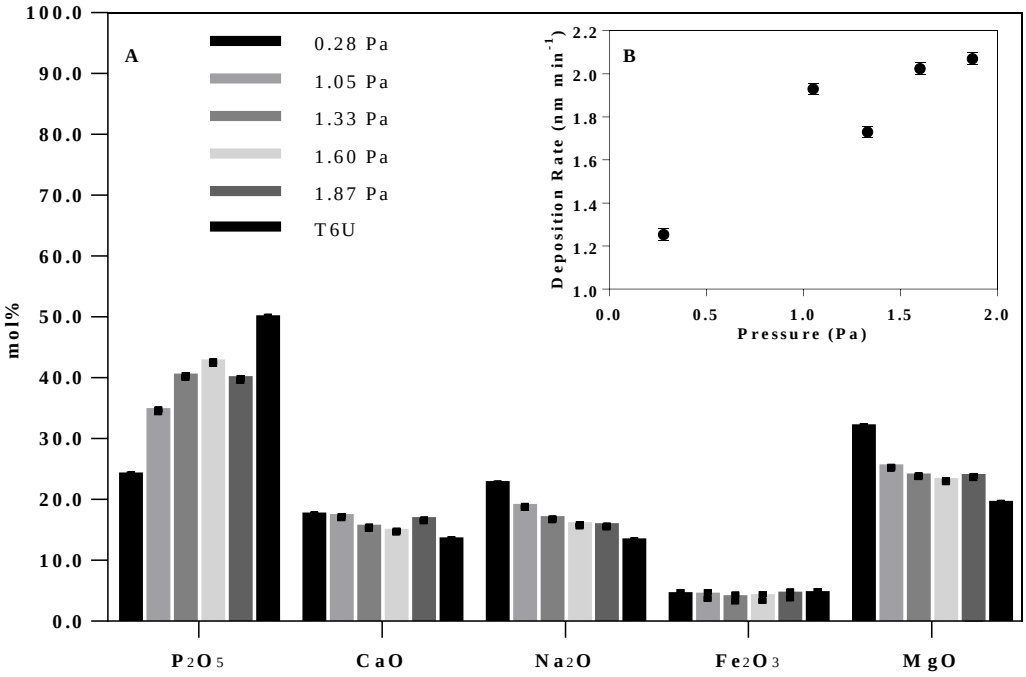

Figure 4.17: (A) Sputtering yield variation with varying argon pressures from 0.28 Pa to 1.60 Pa. Deposition from T6U: P51.5 Fe5. (B) Deposition Rates.

The deposition rates increased from 1.25 to 2.07 nm min^{-1} as the pressure was increased from 0.28 Pa to 1.87 Pa. The variation in deposition rate appeared to approach an asymptotic value of 2.07 nm min^{-1} within the pressure range investigated (see *Figure 4.17B*).

Surface voids of varying sizes (ranging ~6 μm to 33 μm in diameter) were observed for the coating deposited at 0.28 Pa as shown in *Figure 4.18A and C*. The coating cross section appeared dense and homogenous as shown in *Figure 4.18B*. Other portions of the same coating were dense in the absence of voids as shown in *Figure 4.18D*. Coatings deposited at all pressures above 0.28 Pa were also dense and similar in appearance to *Figure 4.18D.*

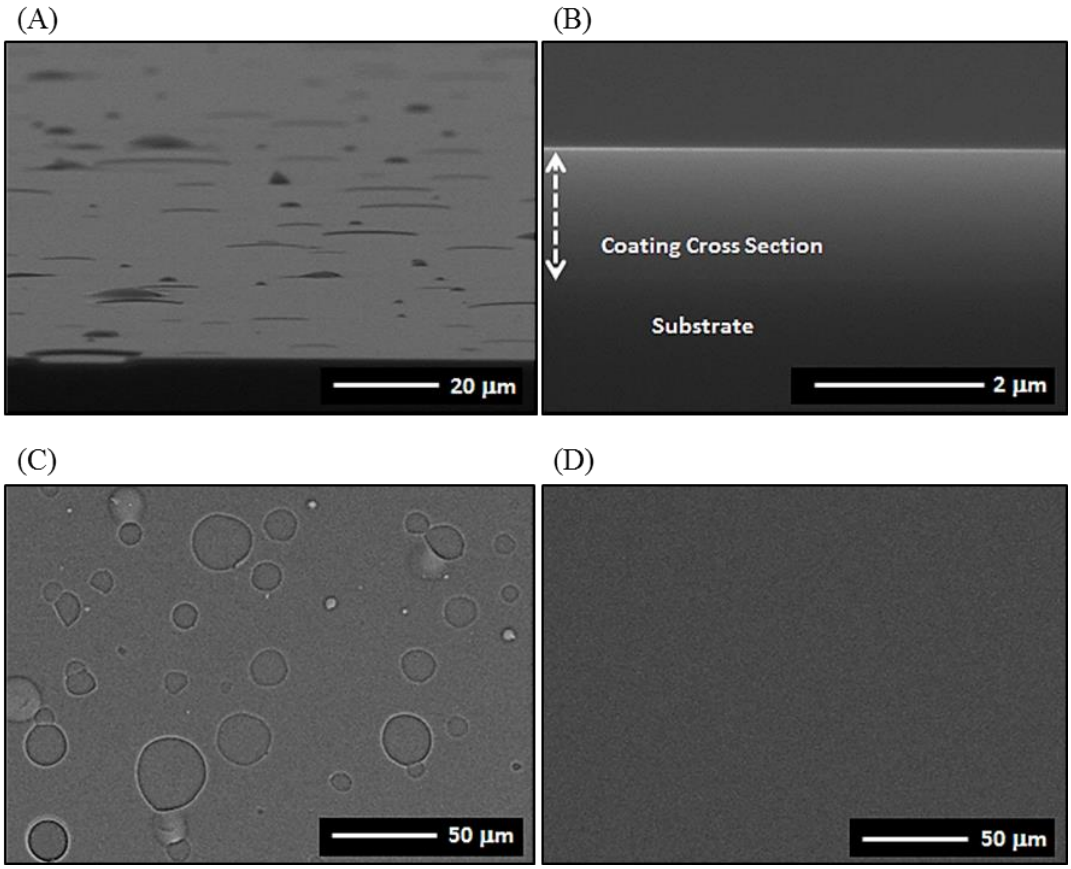

Figure 4.18: Deposition from T6U: P51.5 Fe5 at 0.28 Pa (A) Coating surface at a 7° from the cross section. *(B) Micrograph of the coating surface at location 1. (C) Coating cross section 1.58 µm thick. (D) Micrograph of the coating surface at location 2.*

Preferential Sputtering in Oxygen/Argon Chamber Environment

The effect of oxygen injection into the sputtering atmosphere on sputtering yield was examined using 99.99% argon, 90/10% and 80/20% argon/oxygen mixtures at a chamber pressure of 1.05 ± 0.05 Pa and 80 ± 1 W (see *Figure 4.19A, B*).

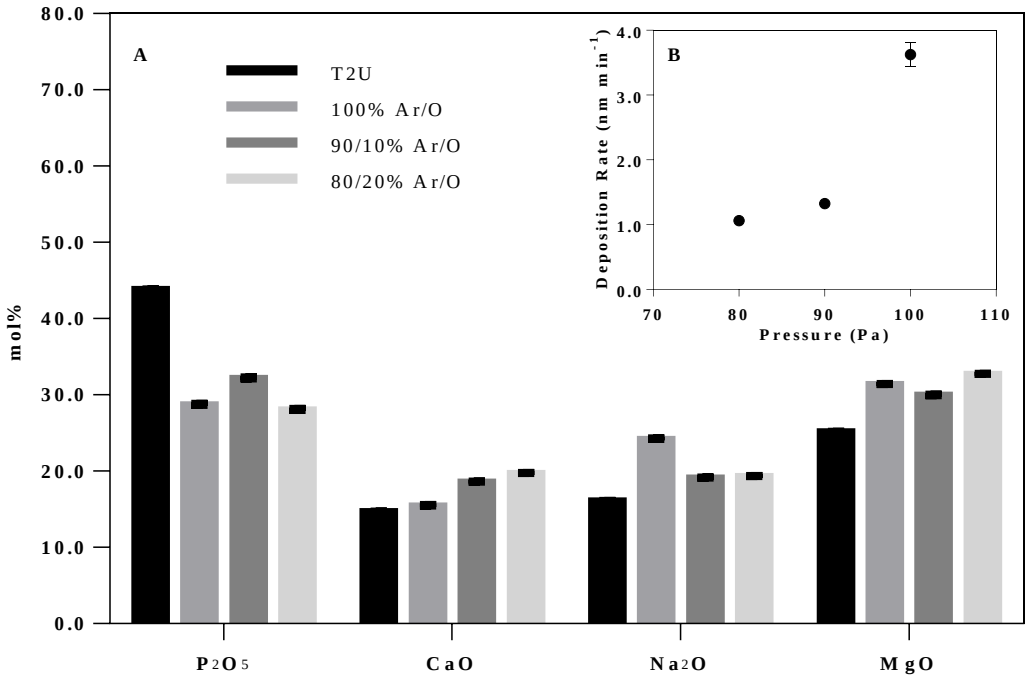

Figure 4.19: (A) Effect on sputtering yield with varying oxygen content using T2U: P45 at 80 W and 1.05 Pa. (B) Deposition rates were observed to increase exponentially with argon content.

Preferential Sputtering TEER UDP 650 Compositions

The TEER UDP 650 was designed with the ability to rotate samples past the cathode giving the ability to coat >200 sample discs at any one time. The rig offers potential for industrial scale operation. This however leads to reduction in deposition rates as each sample is rotated, past the cathode in this case, every 12 seconds at 5 RPM. Argon pressures of 1.33 and 0.36 Pa, corresponding to relative flow rates of 140 and 125 standard cubic cm (SCCM) were examined. As previously shown in *Figure 4.13*; the proximity of the sample to the cathode during static deposition led to significant pitting and sample compositional variation. Rotation appeared to reduce such behaviour producing void free coatings. The compositions C1T-C4T were used to assess process ability whilst C5T: P40 Fe4 and C6T: Si50 BG 45S5 were utilised going forward for dissolution and bioactive potential of PBG, SBG. Notably the

composition of C5T: P40 Fe4 again mimics the desired targeted control composition P_2O_5-40 CaO-16 Na_2O-16 MgO-24 Fe_2O_4-4 mol%.

Table 4.5: TEER UDP 650 coating compositions. C2T-C4T were investigated to assess reproducibility under identical parameters, altering either static or sample rotation in either Mag 2 or Mag 4. Variation is representative of n=3 >10 μm^2 locations on the sample. C2T, C3T represent n=3 batches.

Deposited Coating	Deposition Rate (nm min^{-1})	mol%						Argon Pressure (Pa)	Rotation and Distance (RPM cm^{-1})	Mag/ Target	Power (W)
		SiO_2	P_2O_5	CaO	Na_2O	Fe_2O_3	MgO				
C1T:	N/M	-	36.5	14.9	18.3	3.6	26.7	1.33	Static	2/T1	80
C2T:	1.30 ± 0.01	-	28.8 ± 1.3	19.7 ± 0.6	20.9 ± 0.3	4.5 ± 0.1	26.2 ± 0.9	1.33	Static	2/T1	100
C3T:	0.16 ± 0.01	-	40.9 ± 0.6	11.6 ± 0.3	22.2 ± 0.4	3.1 ± 0.3	22.2 ± 0.6	1.33	(5.0/6)	2/T1	100
C4T:	0.17 ± 0.01	-	39.9 ± 0.3	11.0 ± 0.3	22.1 ± 0.1	3.6 ± 0.1	23.4 ± 0.2	1.33	(5.0/6)	4/T1	100
C5T: P40 Fe4	0.21 ± 0.01	-	40.4 ± 0.1	16.7 ± 0.1	15.1 ± 0.1	4.4 ± 0.1	23.4 ± 0.1	0.36	(5.0/6)	2/T1	100
C6T: Si50	0.09 ± 0.01	50.4 ± 0.1	1.7 ± 0.1	30.9 ± 0.1	17.0 ± 0.1	-	-	1.33	(5.0/6)	2/T2	90
C7T: Multi layer	0.10 ± 0.01	C4T was deposited onto Ti6Al4V for a period of 24 h. C4T was deposited for a period of 24 h. A blend time of 2 h was used for interfacial blending.								2/T1 & T2	100/ 90

4.2 Coating of 3D Metallic and Organic Materials

Coatings of C7T: Multilayer and C5T: P40 Fe4 were successfully applied to chitosan and Poly Lactic Acid (PLA) respectively showing the potential to coat materials with low thermal durability. PLA was supplied by a PhD colleague (Michael Ward). The T_g tested by DSC was quoted as ~66.0 °C. Flexing of the PLA sheet post coating led to cracks throughout the glass layer (*Figure 4.20A and B*). Similarly, cracks were observed on the coated chitosan substrates (*Figure 4.20C*).

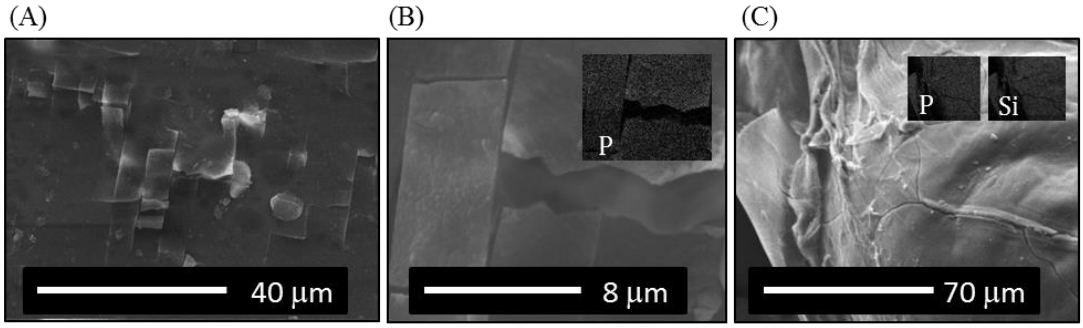

Figure 4.20: C5T: P40 Fe4 applied to (A)(B) medical grade PLA, notable cracking associated with flexing of the polymer. (C) C7T: Multilayer applied to a chitosan porous scaffold. All inserted figures showing elemental mapping of P or Si for the multi-layer composition.

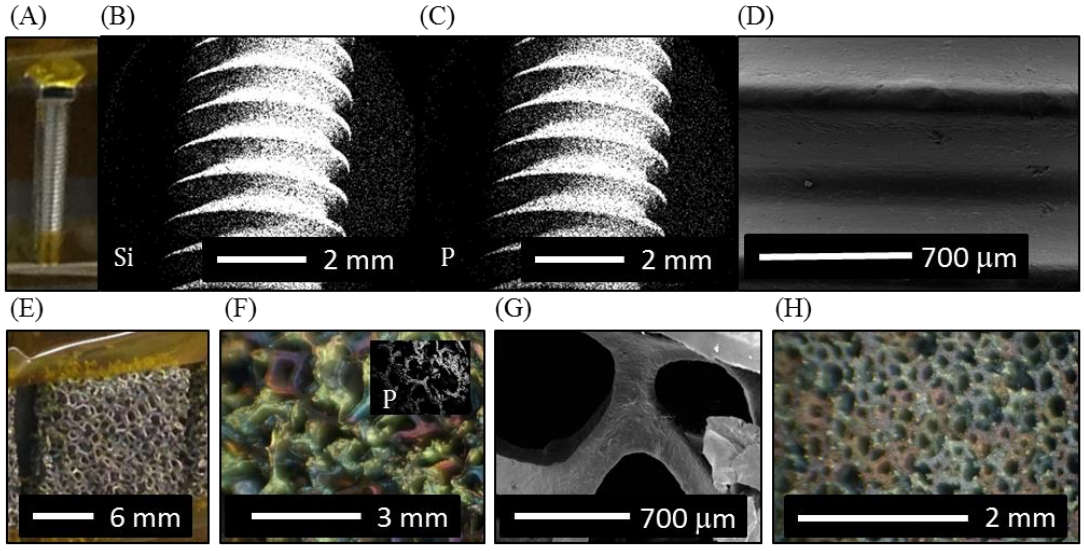

Figure 4.21: M4 stainless steel thread coated with C7T: Multilayer. (A) Uncoated mounting position. (B) and (C) elemental mapping of Si and P respectively. (D) Micrograph of coating on screw thread. Coating of porous meshes to observe potential for coating of various geometries. (E)(F)(G) Nickel based mesh with pore size of ~1.0 mm. (H) Pore ~0.25 mm in diameter.

Elemental mapping for Si and P confirmed coating of an M4 screw within the thread grooves (*Figure 4.21C and D*) whilst SEM microscopy showed a uniform adherent layer *(E)*.

Nickel based meshes with pore sizes of ~1.0 and 0.25 mm (*Figure 4.21E-H*) showed deposition beyond the surface layer, showing that atomic deposition could coat intricate pore shapes and sizes, however analysis was restricted as X-rays were blocked by the inner pores during EDX.

4.3 Structural Variance in Melt Quenched and Magnetron Sputtered PBG Films

Previous publications relating to RFMS of bioactive glasses have lacked detailed structural analysis to disseminate their short-range structures. The short range structures of PVD glasses have been the subject of review since the 1960's and have frequently been scrutinised and confirmed to be dissimilar to their melt quenched counterparts using techniques of wide angle X-ray Diffraction (WA-XRD) [41, 79]. Developments of nuclear magnetic resonance (NMR) and neutron diffraction have also been used to characterise the short-range structure found in melt quenched glasses [48, 77, 226]. However, these methods remain widely limited to powdered or bulk samples and consequently have not been utilised to investigate the structural chemistry of RFMS PBG.

Following topographical and interfacial analysis in *Section 5.1*, the results presented in this Section were investigating the average short-range structural relationship of RFMS quaternary PBG coatings by means of solid-state NMR and via complimentary techniques including FTIR, XRD, and XPS as shown in *Section 5.2*. Conventional MQ glasses of similar composition were manufactured and analysed in comparison to the RFMS coatings. Further structural characterisations by XPS, and FTIR can be found for quinternary phosphate compositions, containing additions of Fe, Ti, and Cu in the *Section 4.4*. *Section 5.2* assessed thermal characterisation and density of compositionally equivalent RFMS coatings.

MQ glass compositions MQ1: P32.5, MQ2: P37, MQ3: P37 were produced using the precursor $CaCO_3$ to replace $CaHPO_4$. Glasses were quenched to room temperature, extracting heat between two steel plates.

4.3.1 EDX

Three compositionally equivalent melt quenched (MQ) glasses; MQ1: P32.5, MQ2: P34, MQ3: P37 were prepared for structural comparison to their RFMS coating counterparts. The as prepared MQ glasses were similarly analysed by EDX and observed to differ by a maximum of P_2O_5-1.0 ± 0.1, MgO-1.3 ± 0.1 CaO-0.7 ± 0.1 Na_2O-0.7 ± 0.1 mol% from their nominal compositions (see *Table 4.6*).

Table 4.6: Deposition parameters of power and argon pressure were varied for target T3U: P50 to produce coatings. Nominal and as prepared target (T), and as prepared melt quenched (MQ) compositions and deposited coatings (C) were analysed by EDX. All compositions were analysed via EDX elemental analysis as the average of 3 areas (> 1 mm^2) over the sample. Standard error of means were calculated from the average composition and the variation in precision of the EDX process by repeated (n=5) analysis of a single area.

Glass Code	Power (W)	Target	Deposition Time (h)	Ar Pressure (Pa)	Coating Thickness (μm)	Deposition Rate (nm min^{-1})
C13U: P32.5	80 ± 1	T3: P50	160	12.0 ± 0.1	25.03 ± 0.15	2.61 ± 0.02
C14U: P34	60 ± 1	T3: P50	160	10.0 ± 0.1	20.36 ± 0.08	2.12 ± 0.01
C15U: P37	60 ± 1	T3: P50	160	12.0 ± 0.1	13.92 ± 0.03	1.45 ± 0.00

Glass Code (AP)	P_2O_5 ± 0.1	MgO ± 0.2	CaO ± 0.1	Na_2O ± 0.1
	mol%			
C13U: P32.5	33.0	32.7	19.3	15.0
C14U: P34	34.2	31.9	17.3	16.5
C15U: P37	37.3	31.8	16.4	14.6
MQ1: P32.5	32.5	34.1	18.3	15.2
MQ2: P34	33.5	33.3	16.0	17.2
MQ3: P37	36.0	33.7	15.8	14.6

The RFMS coatings were deposited from T3U: P_2O_5-50 MgO-24 CaO-16 Na_2O-10 mol%. The three coating compositions; C13U: P32.5, C14U: P34 and C15U: P37 were prepared in a 99.99% pureshield argon atmosphere via variation of gas pressure and deposition powers, parameters presented in (see *Table 4.6*). The as prepared coatings were analysed by EDX and observed to differ by a maximum of P_2O_5-0.5 ± 0.1, MgO-0.8 ± 0.2 CaO-0.8 ± 0.2 Na_2O-0.5 ± 0.1 from their nominal compositions (see *Table 4.6*).

4.3.2 AFM and Cross Sectional Microscopy

Coatings C13U: P32.5, C14U: P34 and C15U: P37 were deposited onto both Ti6Al4V polished discs, borosilicate cover slips, and copper sheet. The cover slips were sectioned, imaged and compositionally analysed via EDX and ground to a powder for ^{31}P-NMR of the coating. Coatings were deposited onto copper sheet to flex the coating layer away from the substrate for thermal analysis. The distributions of compositional elements within the coatings were determined by X-ray elemental mapping and were found to be homogenous throughout the depth of coatings. Coatings C13U: P32.5, and C14U: P34 were similar to C15U: P37. *Figure 4.22A* of C15U: P37 typifies the cross sectional SEM micrographs of the coatings whilst *B-F* show elemental distributions of P, Mg O, Na and Ca respectively. *Figure 4.22D and E* show distributions of O, and Na for the substrate also, as they were present in the composition of the glass cover slip.

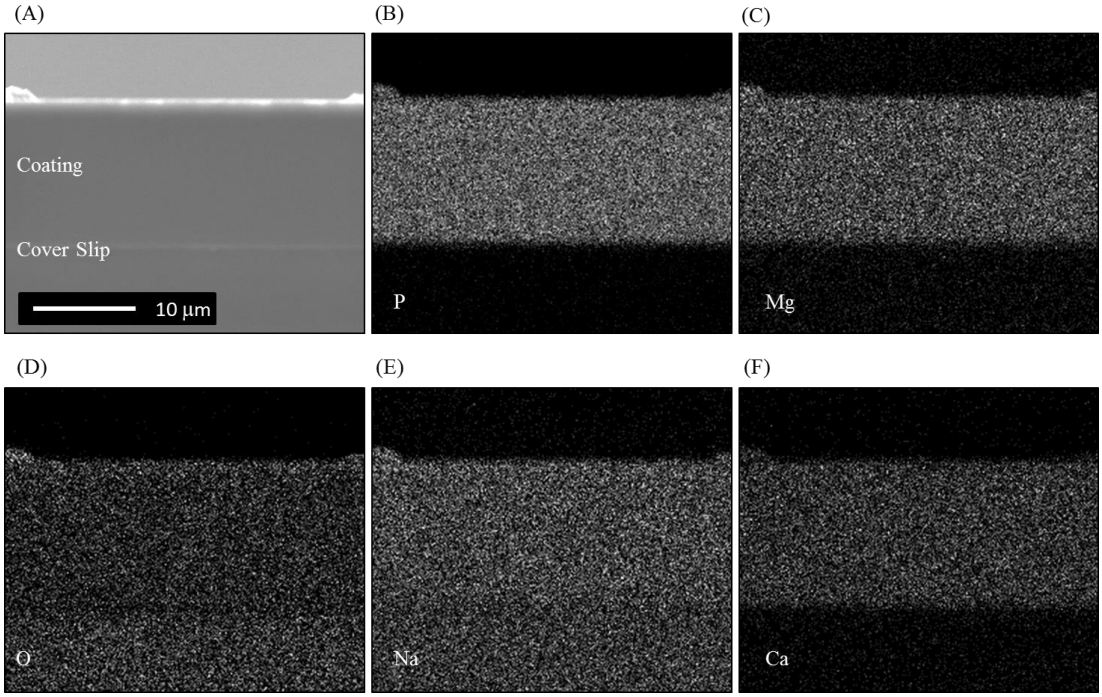

Figure 4.22: RFMS coating C15U: P37 on a borosilicate cover slip (A) cross sectional micrograph (B)(C)(D)(E)(F) Elemental mapping of P, Mg, O, Na, and Ca respectively indicating homogenous elemental distribution within the coating layer.

The interfaces between the borosilicate cover slips and the coatings as shown for C15U: P37 and C13U: P32.5 (*Figure 4.22A and Figure 4.23A Insert*) appeared continuous and adherent, following the topography of the substrate. Notable surface pits were observed on the surface of C14U: P34 (*Figure 4.23B*). Following higher power deposition from 60 to 80 W these craters became enlarged for C13U: P32.5 (see *Figure 4.23A).* Observation of the C15U: P37 and C13U: 32.5 cross sections suggested that the craters were restricted to the surface. All cross sections were similar in appearance to (*Figure 4.23D)*

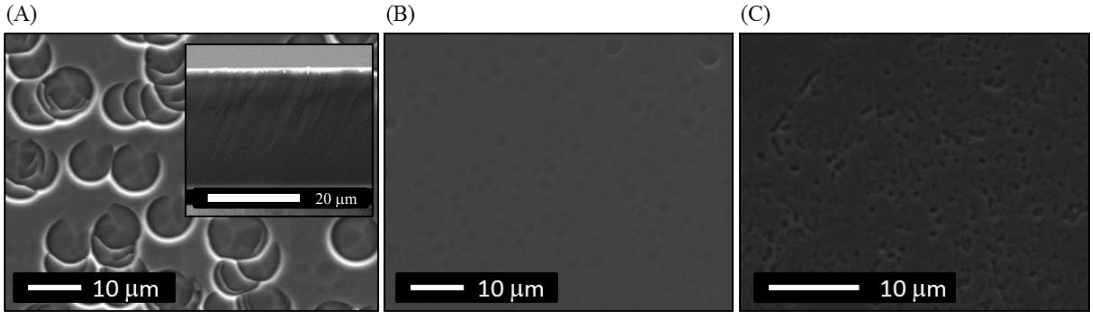

Figure 4.23: (A) (B) and (C), C13U: P32.5, C14U: P34, C15U: P37 and surface images on Ti6Al4V substrates respectively. Noticeable surface craters were observed on all surfaces. (A inset) Cross sectional SEM micrograph of C13U: P32.5 on a borosilicate cover slip, showing continuity throughout the coating.

Topographical features of the Ti6Al4V substrate were analysed and compared to as deposited coatings C13U: P32.5, C14U: P34, C15U: P37 via AFM. A series of 9 measurements on 3 Ti6Al4V substrates indicated an average substrate roughness Ra 7 ± 1 nm (*Figure 4.24A*). All roughness values for as deposited coatings represented an average of 5 measurements on the sample. The roughness of the coatings C14U: P34 (*Figure 4.24C*) and C15U: P37 (*Figure 4.24D*), which were both deposited at a power of 60 W, increased to 32 ± 3 and 19 ± 4 nm respectively. The coating C13U: P32.5 (*Figure 4.24B*); deposited at 80 W contained remarkably larger pits leading to a significant increase in Ra 167 ± 21 nm. (*Figure 4.24E*). The average

maximum pit depths and diameters recorded were consistent with the roughness variation (*Figure 4.24E*).

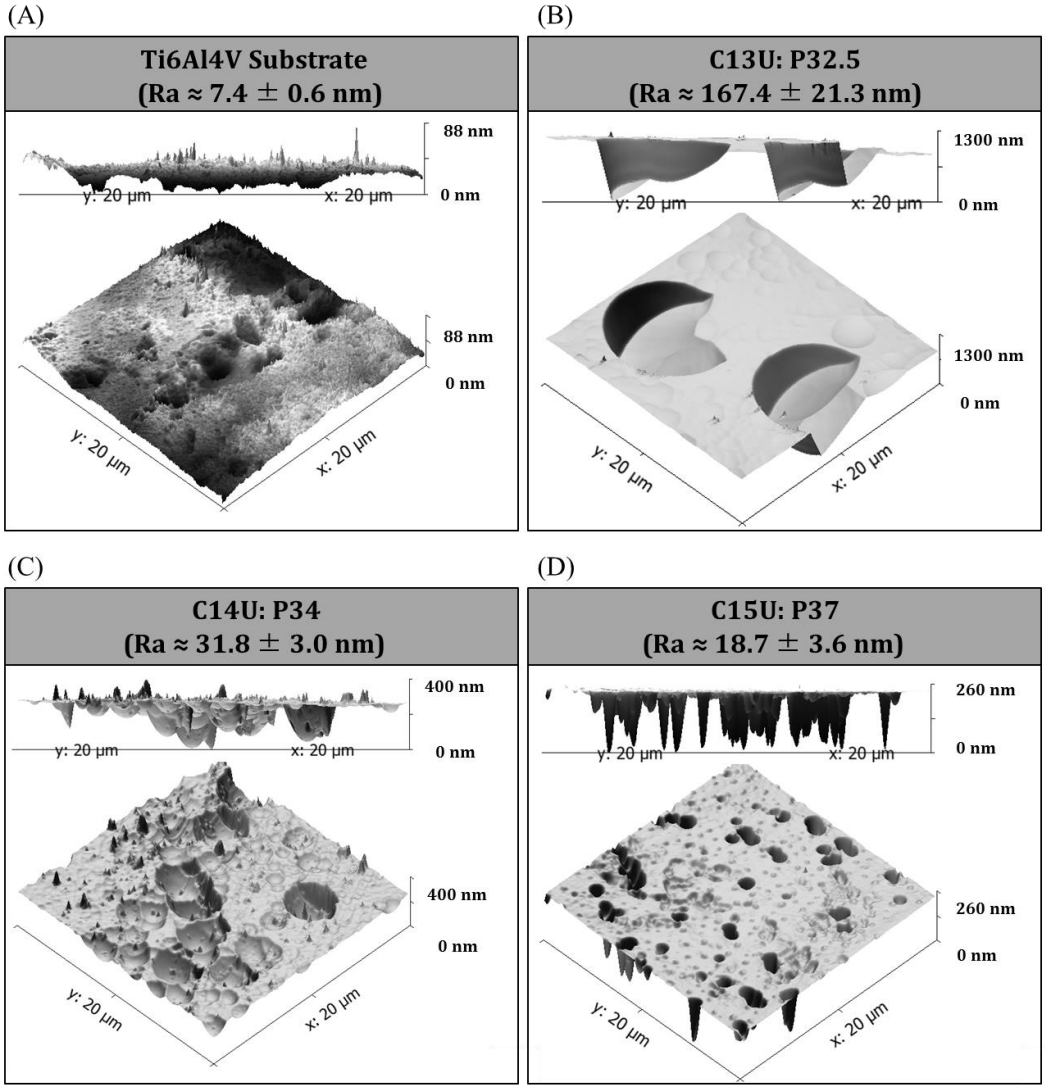

	C13U: P32.5	C14U: P34	C15U: P37
Roughness Ra (nm)	167	32	19
Standard Error n=5	21	3	4
Pit Diameter (nm)	10189	3624	1240
Standard Error n=5	294	71	74
Pit Depth (nm)	790	260	192
Standard Error n=5	101	20	13

Figure 4.24: AFM micrographs (A) Ti6Al4V substrate (B) C13U: P32.5 (C) C14U: P34 (D) C15U: P37. (Table) Average maximum surface pit sizes (diameter and depth) in coatings. Analysis represents 5, 20 µm^2 scan areas.

The pits grew in size as deposition power increased from 60 to 80 W and notably with the increase in deposition rates from 1.45 to 2.61 nm min^{-1}, for C15U: P37 to C13U: P32.5 respectively, leading to a relative increases in roughness, maximum pit

diameter and pit depths of (18.7 to 167.4 nm), (1240.0 to 10189.0 nm) and (228.4 to 865.5) respectively (*Figure 4.24 table Insert*).

4.3.3 FTIR and XRD

The IR absorption spectra and attributed vibrational modes observed for the PVD coatings and MQGs are presented in *Figure 4.25*.

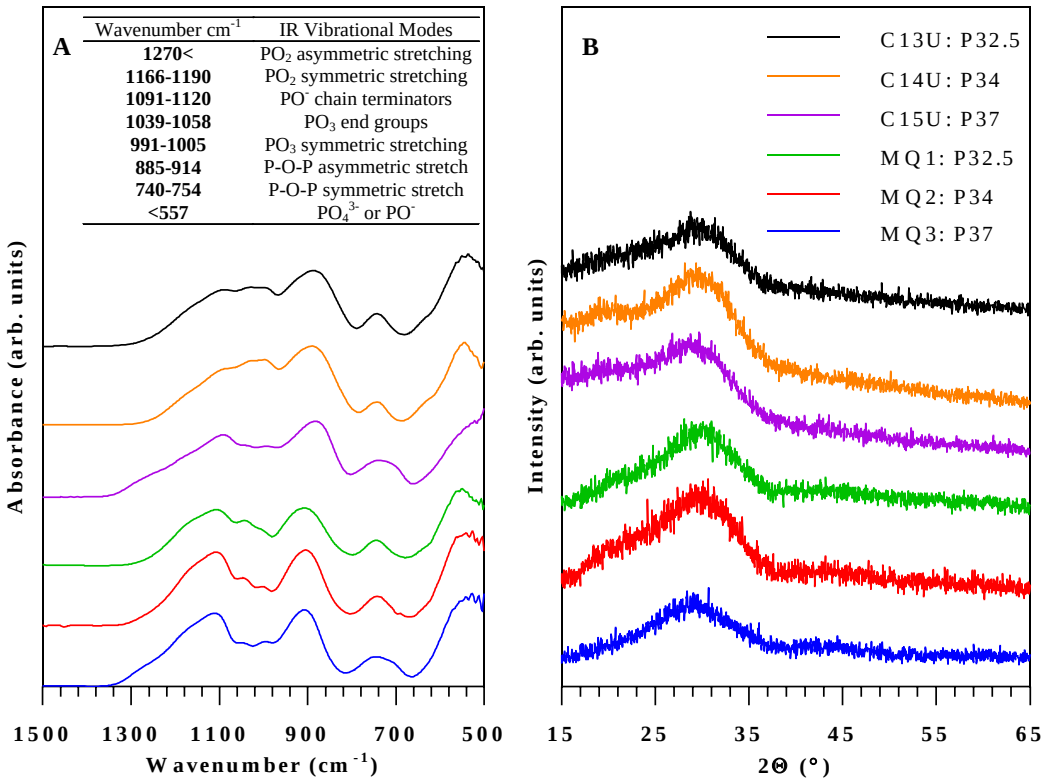

Figure 4.25: (A) IR absorption peaks found in RFMS coatings and MQG. Peak positions varied based on structural variations as demonstrated in the range of wavenumbers per vibrational mode [49, 76, 77, 227]. (B) XRD patterns of RFMS coatings and MQ glasses.

A notable feature of the coatings C13U: P32.5, C14U: P34, C15U: P37 at ~1091, 1101 and 1091 cm^{-1} respectively was a weak absorption intensity attributed to the PO^- chain terminators (i.e. Q^1 structures) [49, 76, 77, 227]. Additionally weak intensities of the Q^1 structures situated at 997 and 995 cm^{-1} for C13U: P32.5, C14U: P34, C15U: P37 and could have been due to fewer Q^1 species [49, 76, 77, 227]. All samples absorbed IR around 557 cm^{-1}, which corresponded to the

orthophosphate PO_4^{3-} attributed to Q^0 [49, 76, 77, 227]. All coatings revealed shifts of the (P-O-P) asymmetric stretching bands and PO^- chain terminators to lower wavenumbers in comparison to MQG compositions. Shoulders present for C15U: P37 and MQ3: P37 at approximately 1270 cm^{-1} corresponded to PO_2 bonds and were indicative of Q^2 tetrahedral sites [49, 76, 77, 227].

Figure 4.25B shows the characteristic amorphous XRD pattern indicative of the broad diffraction humps associated with the short-range order for the MQ glasses and the RFMS coatings. Two broad diffraction peaks are centred at approx. 19° and 28°.

4.3.4 XPS

Compositional analysis by XPS of the surface of PVD coatings indicated a greater proportion of phosphorous compared to the MQG surfaces. For example C13U: P32.5, C14U: P34, C15U: P37, were composed of 23.9, 23.2, 24.0, at% phosphorous compared with 19.9, 19.8, 18.9 at% in MQG compositions. The coating surfaces were also oxygen rich. The compositional variation is listed in *Table 4.7*. All compositions were calculated in at% and mol% to reflect the quantitative variation due to the structural arrangements and to maintain consistency with conventional PBG formulations, described in mol% [36, 66, 98].

Deconvolution of the high resolution spectrum for MQG (*Figure 4.26A*) specifically MQ2: P34 indicated two peaks within the O 1s associated with P-O-P bridges (BO) and (PO^- and P=O) non bridging oxygen bonds (NBO) at 533.3 and 531.6 eV respectively [48, 76]. Relative areas indicated 11.7% : 88.3% ratio of (BO : NBO) for MQ1: P32.5, increasing to 16.2% : 83.8% for MQ2: P34 and 17.7% : 82.3% for MQ3: P37 showing increased network polymerisation with greater P_2O_5 content (see *Figure 4.26A* O 1s). Peaks fitted to the P 2p spectral peak, specifically the P $2p_{3/2}$ and P $2p_{1/2}$ spin orbitals located at 133.5 and 134.5 eV (see *Figure 4.26A P 2p*) could

be attributed to metal phosphates in particular $(PO_4)^{3-}$ and $(P_2O_7)^{4-}$, also found in MQ1: P32.5 and MQ3: P37 [222, 223]. Deconvolution of the Ca 2p spectral peak suggested the presence of CaO located at 347.6 eV. The Ca $2p_{1/2}$ was present at 351.2 eV [228]. However, the overlapping of the Mg KLL was found to distort the spectral peak due to its location at 352.0 eV [224]. Analysis of the Mg 2p located a peak at 50.5 eV was associated with MgO [229].

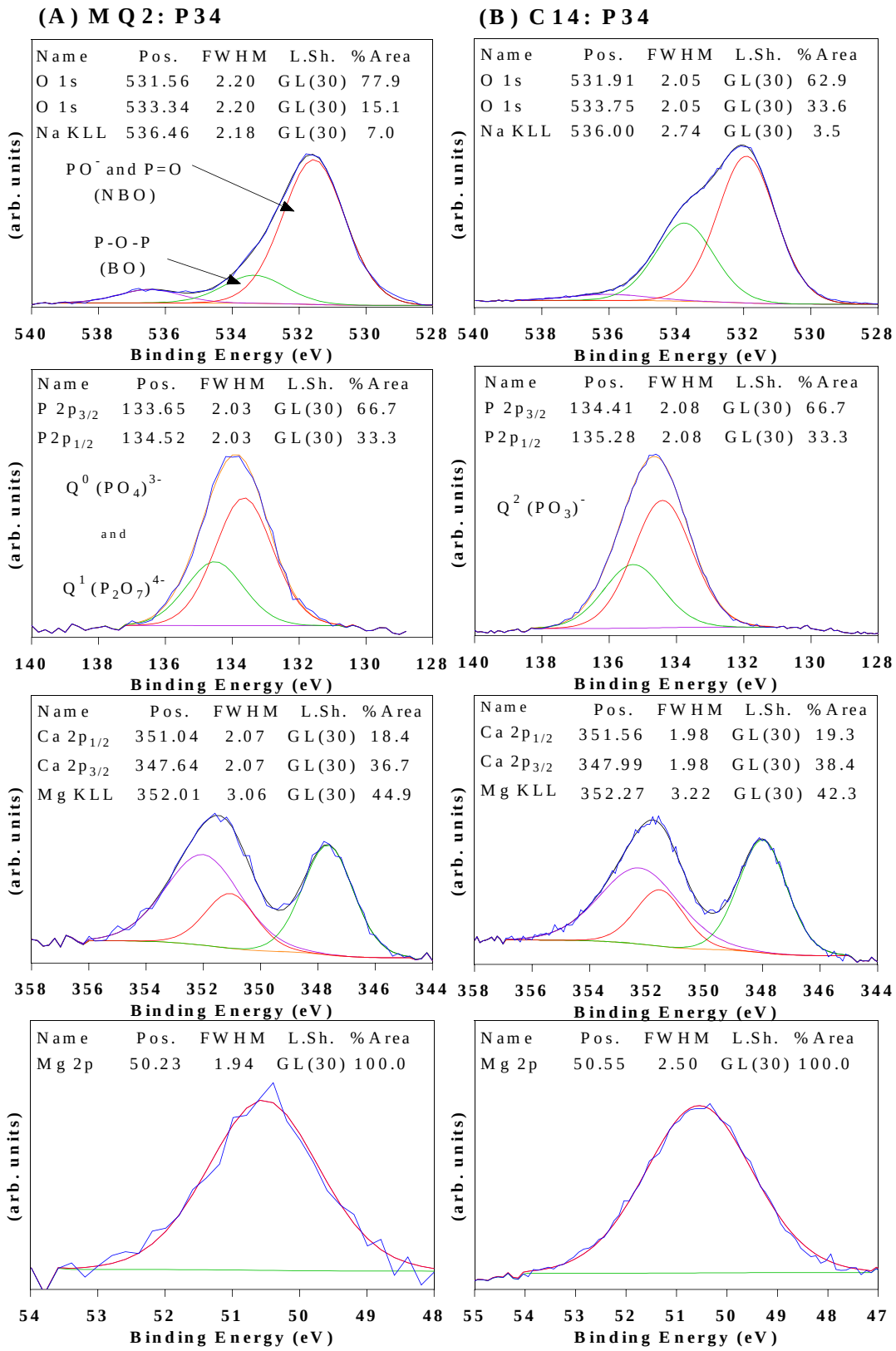

Figure 4.26: Deconvoluted high-resolution XPS spectra of (A) MQ2: P34 and (B) C14U: P34 for O 1s, P 2p Ca 2p and Mg 2p. Distinct variation in the O 1s and P 2p spectra were observed in MQG such as (A) compared to PVD coatings (B) showing a greater proportion of BO vs. NBO in coating compositions.

Deconvolution of the high resolution spectrum of the coating C14U: P34 (*Figure 4.26B*), showed varied peak positions and notably a larger peak associated with BO's leading to a ratio of (BO : NBO) of 34.8 : 65.2%. C13U: P32.5 and C15U: P37 had similar ratios of 35.1 : 64.9% and 36.1 : 63.9 % respectively.

A significant shift of the P $2p_{3/2}$ to between 134.4-134.5 eV, suggested $(PO_3)^-$ metaphosphate bonds. Tabulated XPS ratios of all the bulk and coating samples are shown in *Table 4.7*.

Table 4.7: Surface compositions of the coatings compared with MQG determined by XPS. Determination of the peak positions of O 1s and P 2p for the attibuted oxidation states via analysis of the high resolution spectra. The ratio of bridging to non-bridging oxygens in PVD coatings compared to MQG by deconvolution of the O 1s and P 2p spectra. Orthophosphate $(PO_4)^{3-}$, Pyrophosphate $(P_2O_7)^{4-}$, Metaphosphate $(PO_3)^-$, (Q^0, Q^1 and Q^2 respectively) [48, 222-224].

	C13U: P32.5		C14U: P34		C15U: P37		MQ1: P32.5		MQ2: P34		MQ3: P37	
	at%	mol%	at%	mol%	at%	mol%	at%	mol%	at%	mol%	at%	mol%
P/P_2O_5	23.9	45.3	23.2	46.5	24.0	49.1	17.9	28.4	18.9	31.8	19.8	35.5
Mg/MgO	6.8	25.8	6.3	25.3	5.8	23.7	9.9	31.4	6.6	22.2	7.5	26.9
Ca/CaO	7.0	26.5	5.6	22.4	5.8	23.7	8.7	27.6	8.0	26.9	6.9	24.7
Na/Na_2O	1.3	2.5	2.9	5.8	1.7	3.5	7.9	12.5	11.4	19.3	7.2	12.9
O	60.9		62.0		62.6		55.5		55.1		58.7	
Surface Structure												
PO^- and P=O %*	64.9		65.2		63.8		88.3		83.8		82.3	
P-O-P %*	35.1		34.8		36.1		11.7		16.2		17.7	
P $2p_{3/2}$ (eV)	134.4		134.4		134.5		133.8		133.6		133.9	
Majority Q^n Distribution	Q^2		Q^2		Q^2		Q^0, Q^1, Q^2		Q^0, Q^1, Q^2		Q^0, Q^1, Q^2	

* Normalised O 1s following subtraction of the overlapping Na KLL

4.3.5 ^{31}P NMR

Figure 4.27 shows the ^{31}P NMR spectra for MQGs and PVD coatings. In all cases peaks corresponding to Q^0 (orthophosphates), Q^1 (pyrophosphates), and Q^2 (metaphosphate) species were observed, with isotropic shifts ranging from -0.9 to +2.5 ppm for Q^0, -9.7 to -7.9 ppm for Q^1 and -24.5 to -17.8 ppm for Q^2. Their comparable compositions contained 32.7, 34.5 and 37.9 P_2O_5 mol%, which showed isotropic shifts ranging +4.0 ppm for Q^0, -6.4 to -6.5 ppm for Q^1

and -16.3 to -21.0 ppm for Q^2 [230]. In addition, all the spectra in *Figure 4.27* show first-order spinning sidebands resulting from the chemical shift anisotropy that were included in the quantification. The chemical shifts and integrated intensities for all species in the samples tested can be found in *Figure 4.27* inserts.

MQ1: P32.5 was composed of 8.2% Q^0 species, 83.2% Q^1 species and 8.6% Q^2 species. The increase in phosphate content in MQ2: P34 (*Figure 4.27 and Figure 4.28*) led to a composition of 83.4% Q^1 species and an increase in polymerisation indicated by 14.3% Q^2. The Q^2 species were formed at the expense of Q^0 species. Further polymerisation of the network was evident in MQ3: P37, for which the proportion of Q^2 increased to 31.9% at the expense of Q^1 which reduced to 67.3% (*Figure 4.27B and Figure 4.28)* and Q^0 reduced from 8.2% to, 2.4% and 0.8% with increasing P_2O_5 content from MQ1: P32.5 MQ2: P34 to MQ3: P37 (*Figure 4.27A, C & E and Figure 4.28)*.

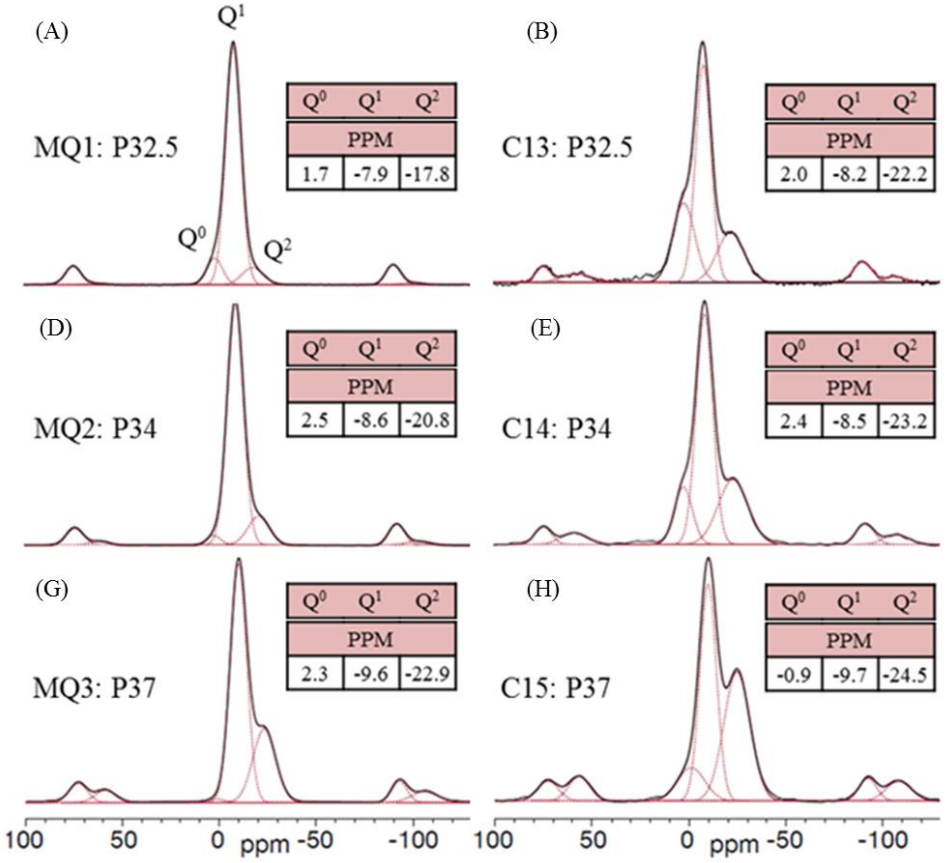

Figure 4.27: ^{31}P NMR spectra of (A) MQ1: P32.5 (B) C13U: P32.5 (C) MQ2: P34 (D) C14U: P34 (E) MQ3: P37 (F) C15U: P37. Isotropic chemical shifts were location at (-0.9 to +2.5 for Q^0), (-9.7 to -7.9 for Q^1), and (-24.5 to -17.8 for Q^2). In addition, first-order spinning sidebands due to the chemical shift anisotropy were observed for each site. Coatings (B) (D) (F) were observed to have significantly larger Q^2 and Q^0 than MQG (A) (C) (E) counterparts whilst the Q^2 was observed to increase with P_2O_5 content for all MQGs and PVD coatings.

Coatings C13U: P32.5, C14U: P34 and C15U: P37 demonstrated a similar trend of increasing polymerisation with increasing network former content as Q^2 varied with phosphorous content from 23.0% to 30.9% and 45.4%. The noticeably larger Q^0 presence in C15U: P37 of 23.0%, C14U: P34 of 12.8% and C13U: P32.5 of 9.4% was unique to PVD coatings. This together with substantially higher proportion of Q^2 of 30.9, 45.2, 23.0% in coatings C13U: P32.5, C14U: P34, C15: P37 compared with 14.3, 31.9, 8.6% in MQ1: P32.5, MQ2: P34, and MQ3: P37 respectively showed

structural disparities between the two forms (*Figure 4.28)*. The considerable presence of Q^0 tetrahedral was unique to the RFMS structures.

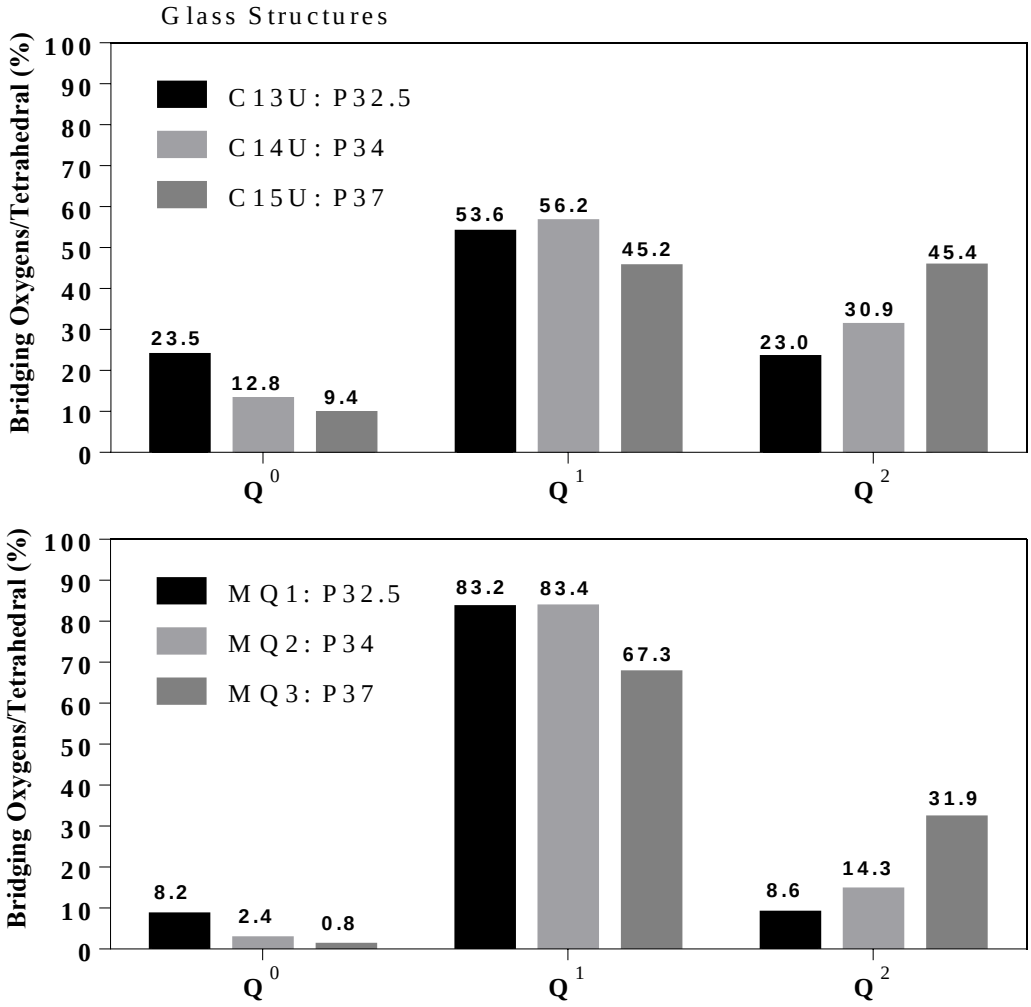

Figure 4.28: Proportions of Q species within the tetrahedral of coatings C13U: P32.5 C14U: P34 and C15U: P37 and their compositionally equivalent melt quenched glasses MQ1: P32.5, MQ2: P34 and MQ3: P37.

4.3.6 Thermal Analysis and Density

The T_g for C13U: P32.5, C14U: P34 and C15: P37 ranged from 464 to 488 °C whilst MQ compositions ranged from 477 to 508 °C with both processes showing a notable increase in T_g with decreasing P_2O_5 content from P37 to P32.5 mol%. The T_g for coatings ranged 14 to 20 °C less than their respective MQ equivalent glasses. Notably T_c decreased from 608 to 595 °C for (C13U-C15U) and conversely increased from 578 to 624 °C for (MQ1-MQ3). Two or three distinct melting peaks were observed

from 826 to 883 °C showing no notable trend with composition or processing method. Both MQ3: P37 and C15U: P37 showed an addition melting peak at 754 and 766 °C respectively. The processing window increased from 101, 106, 112 °C for (C13U-C15U), whilst the window increased from 61, 81, and 131 °C for (MQ1-MQ3), ranging 11 and 70 °C for coatings and MQ compositions respectively.

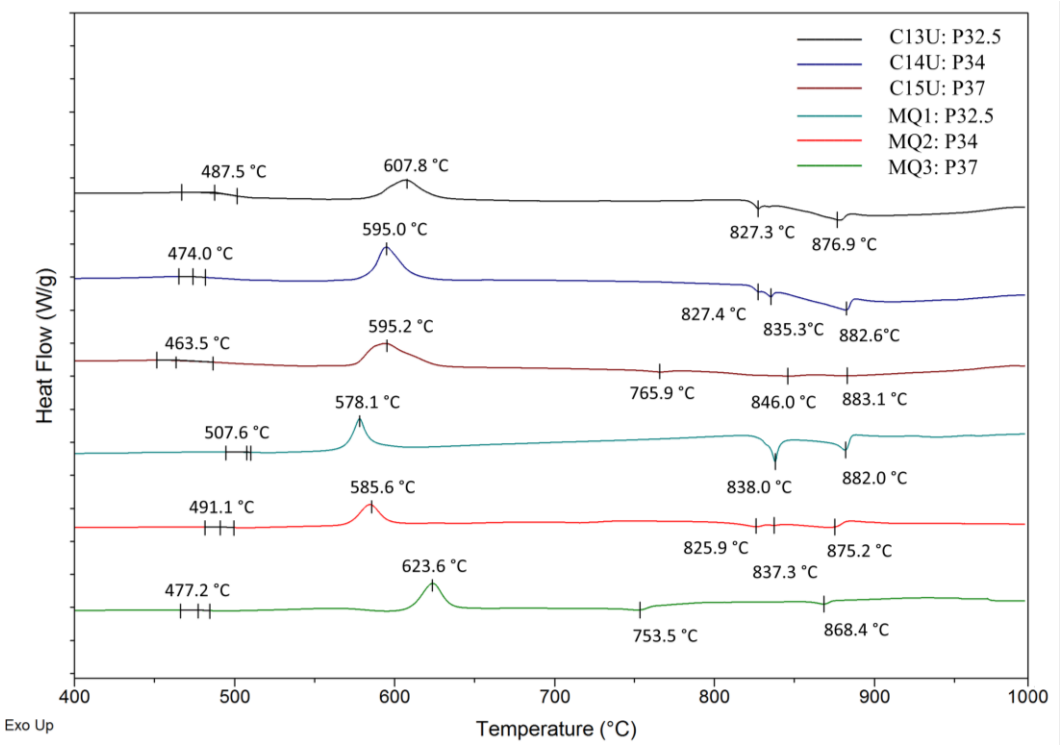

Figure 4.29: DTA thermal traces for (C13U-C15U) and (MQ1-MQ3). The T_g was determined at the onset of the primary endothermic peak. The peak locations of the T_c exothermic and T_m endothermic peaks have been assessed. See Appendix 4.0 for magnified thermal event of the glass transitions.

Coatings and MQ skeletal densities were assessed by helium pycnometry for coatings flexed off copper substrates, revealing densities of 2.06-2.48 g cm^{-3} for coatings, whilst MQ formulations varied considerably from there equivalent counterparts as 2.69-2.72 g cm^{-3}.

Table 4.8: Density assessment of MQ glass and RFMS coatings by Helium Pycnometry.

Glass Compositions	Coating Helium Pyc. g cm^{-3}	Melt Quenched Helium Pyc. g cm^{-3}
P32.5	2.48 ± 0.02	2.72 ± 0.01
P34	2.06 ± 0.04	2.71 ± 0.01
P37	-	2.69 ± 0.01

4.4 Degradation of Phosphate Glass Coatings

Five PBG compositions were deposited in the UoN PVD and one PBG composition was deposited in the TEER UDP 650 and degraded in distilled water (dH_2O) and PBS. The PBG compositions were deposited to an approximate thickness of 2.67 μm, 5.66 μm and 1.69 μm and the C5T: P40 Fe4 PBG to a thickness of 1.16 μm. Degradation of the composition C7U: P40 Fe4 was compared to its equivalent melt quenched composition (MQ5: P40 Fe4).

Table 4.9: As prepared coatings for degradation. As previously shown coatings were deposited for 1165 min to determine deposition rate by observation of the cross section (Table 4.4). Coatings were re-deposited for various time periods based on the deposition rates at 60 W. In addition C11U: P32 Fe5 was deposited at 90 W for 1165 min to observe variability due to deposition power as compared to C7U: P40 Fe4 therefore was measured as 5.66 μm.

Glass Code Nominal (N) vs. As Prepared (AP)	Coating Thickness (μm)	Deposition Time (min)
MQ4: P28 Fe6	N/A	Composition melt quenched at 450 °C as rods.
MQ5: P40 Fe4	N/A	
C7U: P40 Fe4	2.67 ± 0.09	1165 min
C8U: P31 Ti6	2.67 ± 0.06	3000 min
C9U: P35 Ti7 Cu5	2.67 ± 0.08	1535 min
C10U: P40 Fe8	2.67 ± 0.02	1165 min
C11U: P32 Fe5	5.66 ± 0.01	1165 min
C12U: P28 Fe6	1.69 ± 0.01	1165 min
C5T: P40 Fe4	1.16 ± 0.02	4200 min

4.4.1 XRD and FTIR Pre and Post Degradation

C12U: P28 Fe6 and C7U: P40 Fe4 coatings were degraded via 3 independent samples at each time point, without resubmission. All other coatings were assessed, weighed and re-submerged until the subsequent time point.

The melt quenched compositions of MQ4: P28 Fe6 and MQ5: P40 Fe4 were produced for comparative analysis to their compositional equivalent coatings. Quenching MQ4: P28 Fe6 was attempted however it could not be produced in an amorphous state as it was shown to contain multiple crystalline phases *(see Figure 4.30).* MQ5: P40 Fe4 was confirmed to be amorphous via XRD (*Figure 4.30*). The equivalent coating composition of C7U: P40 Fe4 was confirmed amorphous, whilst C12U: P28 Fe6 contained minor phases associated with Wuestite (FeO) and Iron Phosphate ($FePO_4$) (*Figure 4.30*). A remaining broad diffraction humps confirmed the production of a glass/ceramic coating (*Figure 4.30)*. All other degraded coatings (C8U-C11U) and C5T: P40 Fe4 were confirmed amorphous previously (*Figure 4.16*).

28 d post submersion XRD analysis of C7U: P40 Fe4 and C12U: P28 Fe6 showed the absence of any associated crystalline structure, as shown in (*Figure 4.30)*. The phases attributed to the substrate Ti6Al4V and Al_2O_3 from sample preparation were also found to be present.

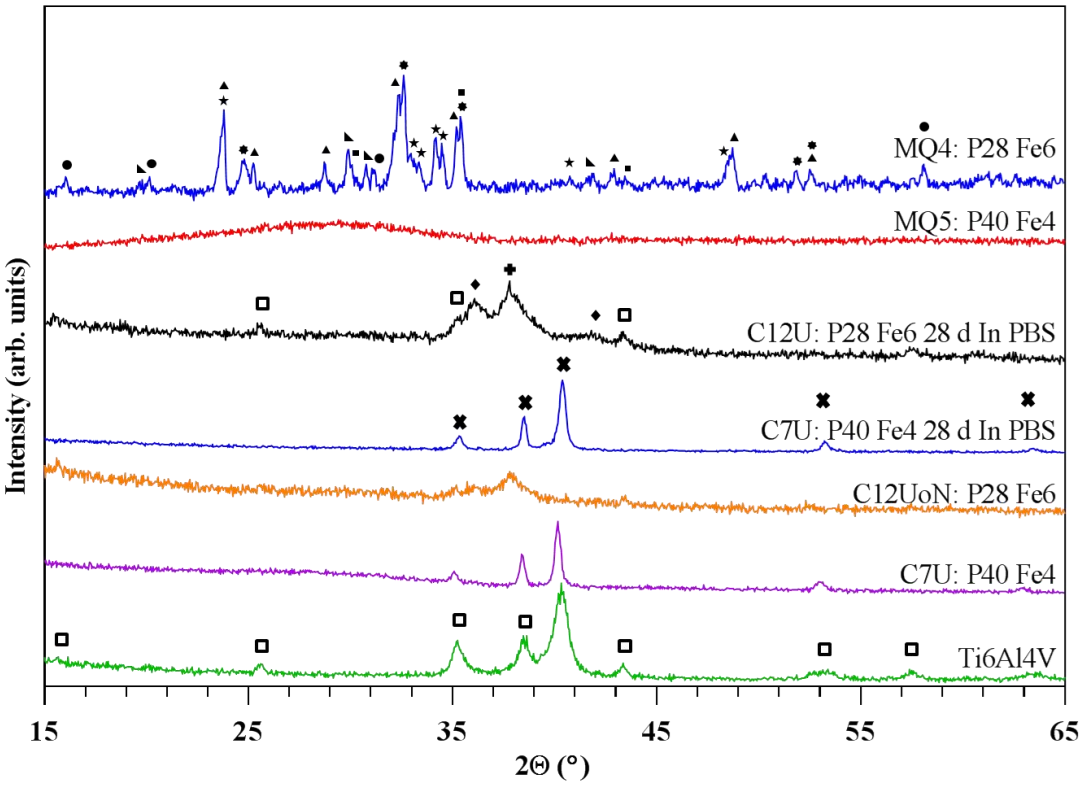

Figure 4.30: XRD of MQ4 and MQ5. Crystalline rod MQ4 phases corresponding to (★) Brianite $Na_2CaMg(PO_4)_2$ ICDD-PDF-01-088-1549 (▲)Sodium Iron Phosphate $Na_3Fe_2(PO_4)_3$ ICDD-PDF-00-045-0319. (■) Magnetite Fe_3O_4 ICDD-PDF-01-075-1610 (◣) Magnesium Phosphate Oxide $Mg_2P_2O_7$ ICDD-PDF-00-032-0626 (✸) Iron Phosphide FeP_4 ICDD-PDF-01-071-0473 (●) Main peaks attributed to unidentified phases. XRD of coatings C12U: P28 Fe6, and C7U: P40 Fe4 as deposited and 28 d post degradation in PBS. Crystalline phases corresponding to (□)Al_2O_3 ICDD-PDF-01-081-1667 (◆)Wuestite FeO ICDD-PDF-01-089-0686 (✚) Iron Phosphate $FePO_4$ ICDD-PDF-01-075-2990 (✖) Titanium Ti ICDD-PDF-00-001-1197.

The IR absorption results showed structural similarities suggested by the positioning of the absorption bands reflected for all degraded coatings as shown in (*Figure 4.31A*). In addition the MQ4: P28 Fe6, and MQ5: P40 Fe4 were similar to their compositionally equivalent C12U: P28 Fe6 and C7U: P40 Fe4.

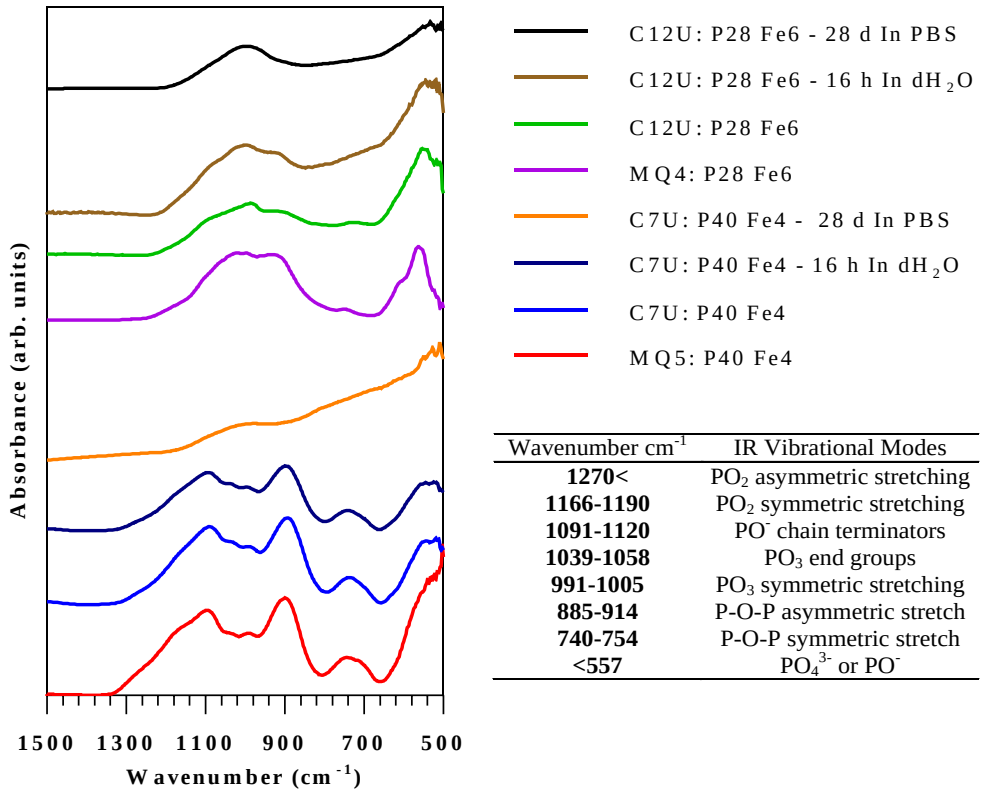

Wavenumber cm^{-1}	IR Vibrational Modes
1270<	PO_2 asymmetric stretching
1166-1190	PO_2 symmetric stretching
1091-1120	PO^- chain terminators
1039-1058	PO_3 end groups
991-1005	PO_3 symmetric stretching
885-914	P-O-P asymmetric stretch
740-754	P-O-P symmetric stretch
<557	PO_4^{3-} or PO^-

Figure 4.31: IR absorption spectra for compositions of coatings, MQG/ceramic P28 Fe6 and MQ5: P40 Fe4. IR absorbance spectra of C12U: P28 Fe6 and C7U: P40 Fe4 16 h post degradation in dH_2O and 28 d post degradation in PBS of C12U: P28 Fe6 and C7U: P40 Fe4.

Post degradation IR and diffraction data were collected for the coating composition C7U: P40 Fe4 and C12U: P28 Fe6 to examine potential structural variability due to degradation.

For degradation in dH_2O (*Figure 4.31)* in comparison to as prepared coatings, no significant variation was observed in IR absorption following the 16 h degradation time points for coating C12U: P28 Fe6, or C7U: P40 Fe4.

Following 28 d of degradation in PBS, the absorbance at 993 cm^{-1} for C12U: P28 Fe6 and C7U: P40 Fe4 confirmed remaining bonds associated with $(PO_3)^-$ symmetric stretching. Peaks around 532 cm^{-1} indicated remaining PO^- deformation modes [49, 76, 77, 227].

4.4.2 Degradation of MQ and RFMS Coatings

The MQ5: P40 Fe4 exhibited a linear degradation profile over the 83 d test period in both PBS and dH_2O (see *Figure 4.32A*). Based on the slope of the degradation, dissolution occurred at a rate of 1.38 times faster in dH_2O than PBS for MQ5: P40 Fe4 over the 83 d test period. Degradation from 2-24 h (*Figure 4.32B*) was 9.7 x 10^{-5} and 6.8 x 10^{-5} mg mm^{-2} h^{-1} for dH_2O and PBS, respectively; an increase in dH_2O by a factor of 1.43. The pH measurements indicated that the pH of the PBS solution for all coatings and MQ5: P40 Fe4 was stable in the range 7.27-7.40 throughout testing. The pH of dH_2O was found to be between 6.77-7.02.

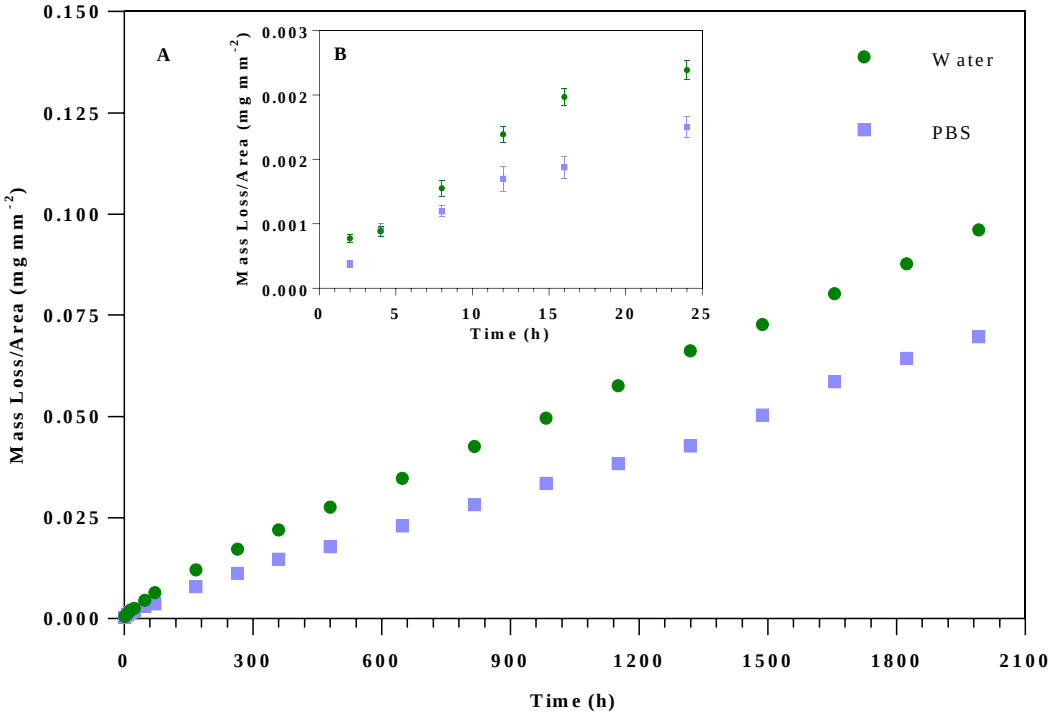

Figure 4.32: Degradation of MQ5: P40 Fe4 in PBS and dH_2O. (A) Full degradation period of 0-83 d (B) Data up to 24 h. Error bars within.

Precipitation on the surface of MQ5: P40 Fe4 glass was observed following degradation in PBS, as shown after 4 d (*Figure 4.33)*. This precipitation was found to be floating freely within the media. No further analysis was conducted.

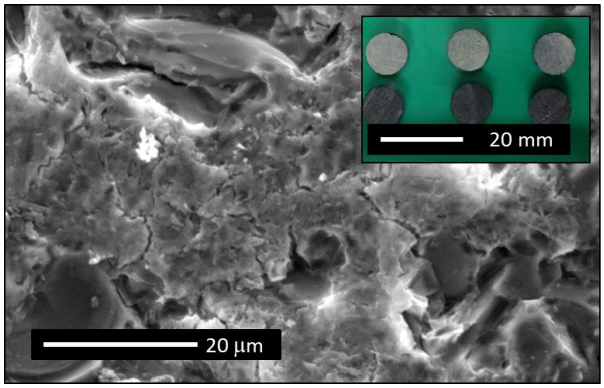

Figure 4.33: MQ glass degraded for 4 d in PBS. Surface SEM micrographs (Inset) Top in PBS and bottom in dH_2O

Degradation rates in dH_2O revealed a linear profile between 2 and 24 h as 7.8×10^{-5} and 21.2×10^{-5} mg mm^{-2} h^{-1} for C12U: P28 Fe6 and C7U: P40 Fe4 respectively (*Figure 4.34A).* After 24 h no further mass loss was observed. Comparative mass losses at 2 h for C12U: P28 Fe6 and C7U: P40 Fe4 were 1.4 and 3.8 x 10^{-3} mg mm^{-2}. This indicated an increased solubility for both coating compositions during the first 2 h and also that C7U: P40 Fe4 degraded 2.7 times faster than C12U: P28 Fe6.

Coating compositional variation due to degradation for C7U: P40 Fe4 was tracked in dH_2O and PBS (*Figure 4.35A and B)*. The compositional changes were followed up to 24 h in dH_2O and 21 d in PBS, as determined by EDX (see *Figure 4.35*).

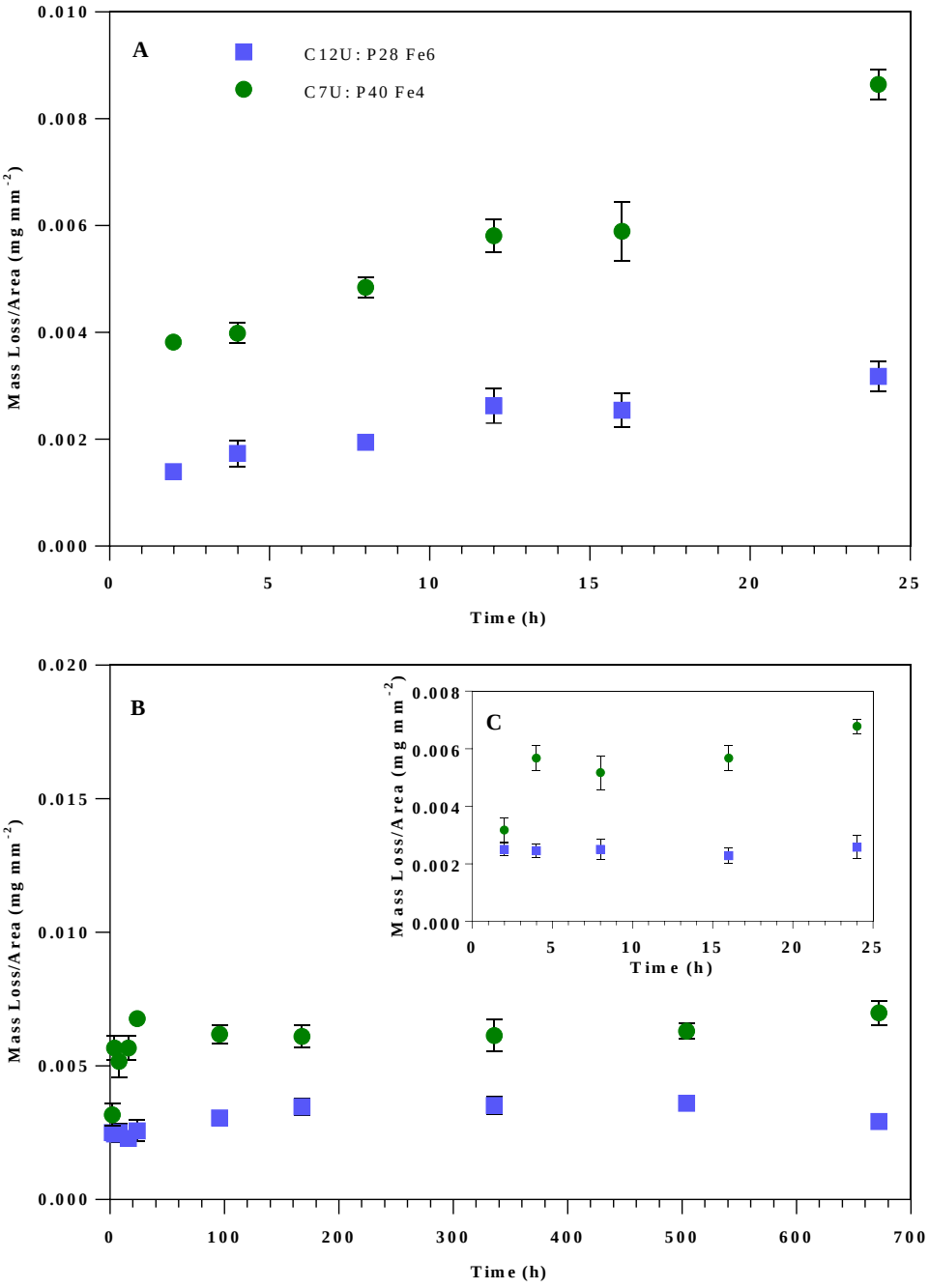

Figure 4.34: (A) Degradation of C12U: P28 Fe6 and C7U: P40 Fe4 on Ti6Al4V in dH_2O up to 24 h. (B and C) Degradation in PBS up to 21 d and 24 h respectively.

Dissolution in PBS caused compositional changes in the first 24 h. Tracking of the dissolution rate similarly showed coating degradation followed by stabilisation within 24 h, after which no further mass loss was observed over the 28 d period (*Figure 4.34B*). This profile could have possibly been associated with formation of a precipitate. The composition appeared to be stable by 24 h. In contrast, dissolution in

dH_2O led to no such compositional changes (*Figure 4.35A*). However, thinning of the coating layer led to significant EDX error by 24 h making interpretation at this time point difficult as suggested in *(Section 4.1.2*).

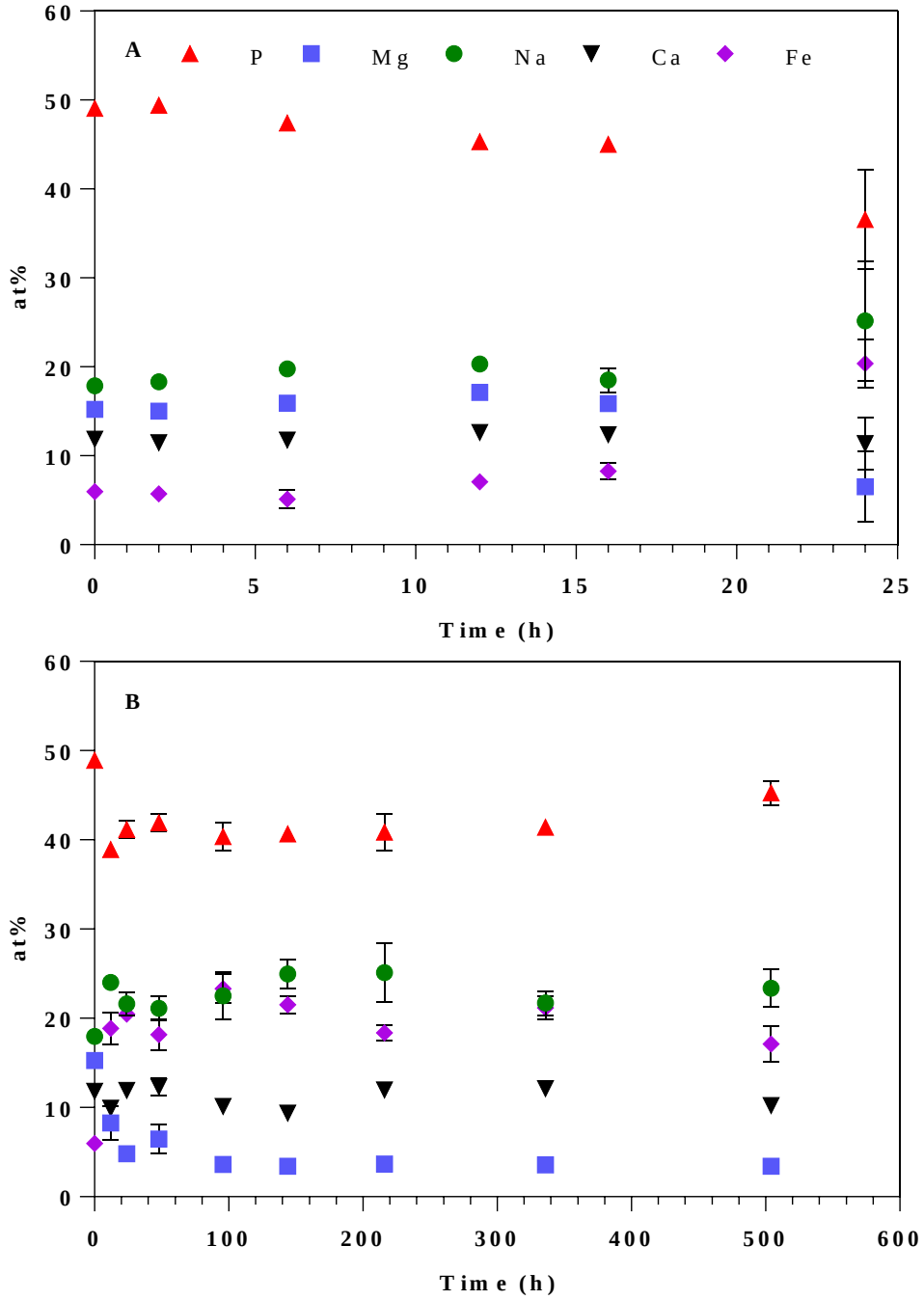

Figure 4.35: (A) EDX analysis of C7U: P40 Fe4 up to 24h during degradation in dH_2O indicating consistent composition within the coating, suggestive of surface degradation. Thinning of the coating layer led to inaccurate analysis at the 24 h time point (B) Composition on the surface of C7U: P40 Fe4 at time points 0-21 d in PBS Solution indicating a variable composition in the first 24 h.

4.4.3 SEM and AFM of C7U: P40 Fe4 in dH_2O Pre and Post Degradation

FIB-SEM cross sections were ion milled for C7U: P40 Fe4 as presented in Figure 4.36*A* and *D* on both polished and sandblasted substrates respectively. Coatings followed the topographies of their substrates. Surface micrographs were collected by SEM in *Figure 4.36B* and *E* showing distinct pitting at 16000 times magnification on polished substrates. Pitting can more clearly be observed in *Figure 4.36C*, via AFM microscopy.

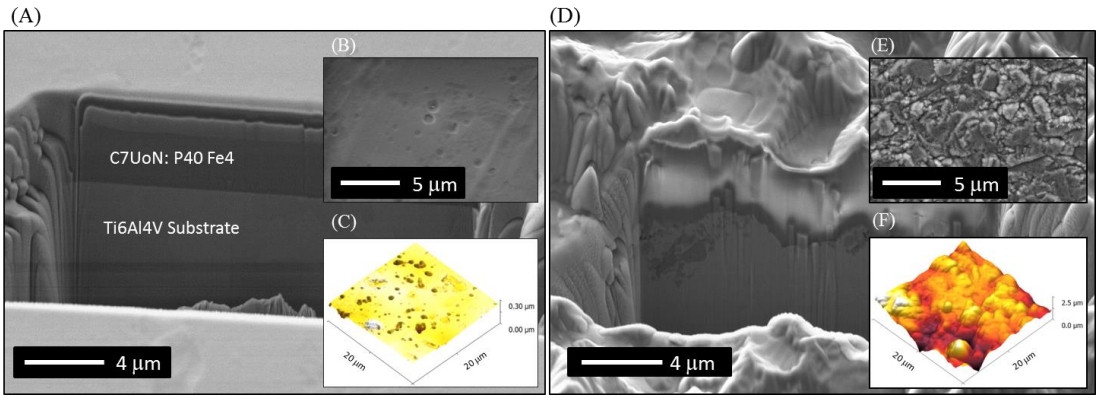

Figure 4.36: C7U: P40 Fe4 as deposited. (A and D) Cross sectional FIB-SEM on Ti6AL4V polished and sandblasted substrates. (B and E) Surface micrograph, (C and F) AFM micrographs of coating surface.

Post degradation SEM micrographs of C7U: P40 Fe4 at time points 0, 4, 16 and 24 h showed the development of pores from the surface through to the depth of the coating whilst degraded in dH_2O as shown in *Figure 4.37A, B, C and D* respectively. Void formation was observed to spread outwards from the centre of the pore until the coating was entirely degraded by the 48 h time points. Similar behaviour was observed on coatings deposited on sandblasted substrates as shown in the inserts for *Figure 4.38C* compared with *D* showing a coating surface view, similar to *Figure 4.37*.

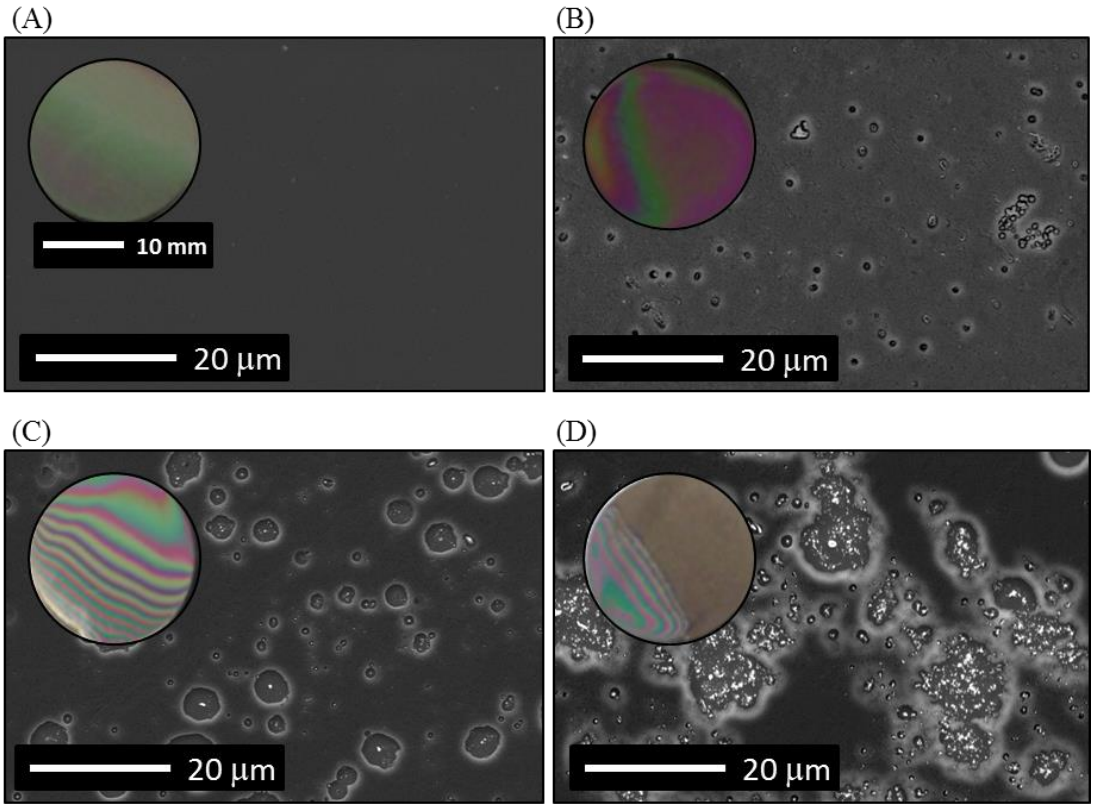

Figure 4.37: Complete coating degradation of PBG on polished substrates. C7U: P40 Fe4 in dH_2O representing (A) coated and subsequent degradation for (B) 4 h, (C) 16h (D) 24 h.

To investigate this further, a cross section was milled through the post-degraded coatings via a FIB-SEM for both polished (*Figure 4.38A and B*) and sandblasted substrates (*C and D*). Observation of the corrosion pits appeared to suggest preferential sites for degradation.

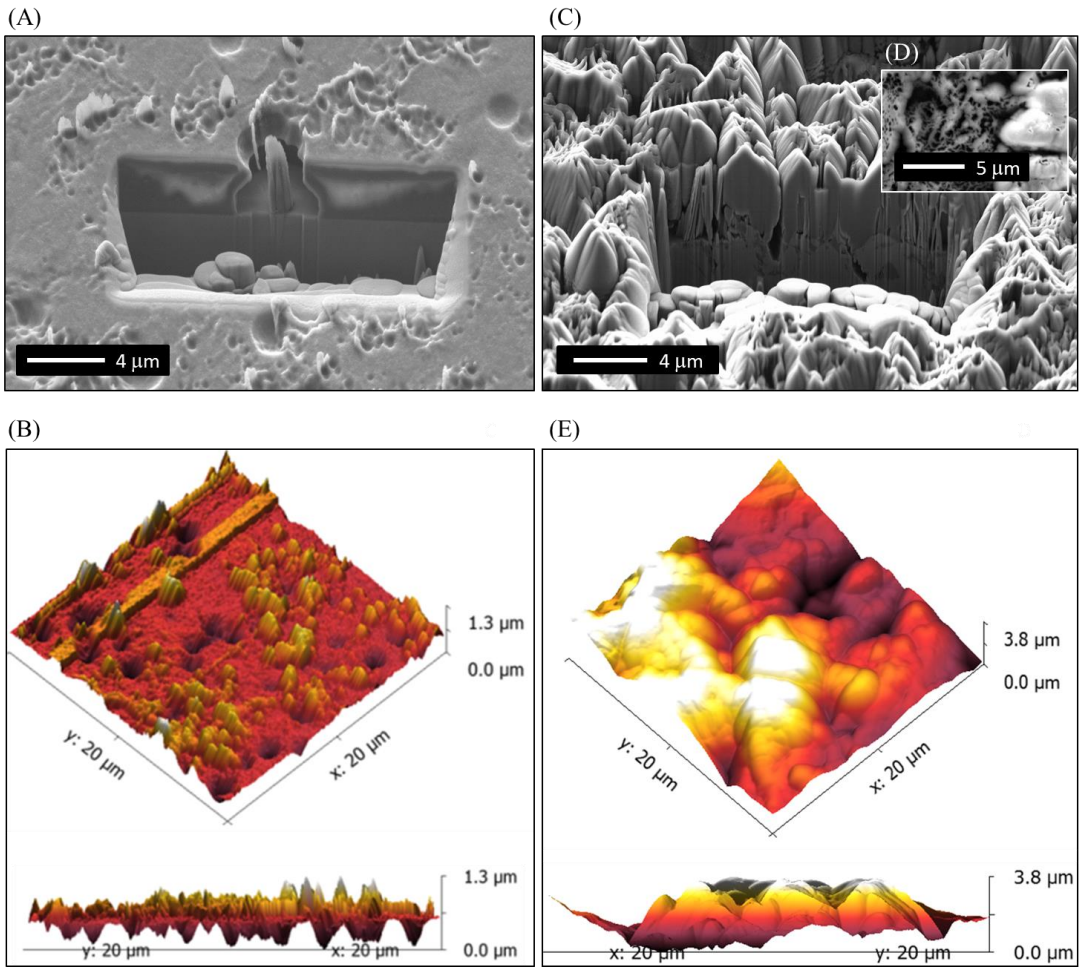

Figure 4.38: C7U: P40 Fe4 in dH_2O 16 h. (A and C) FIB-SEM micrographs of a 16 h degraded coating on polished and sandblasted substrates respectively, milled into a corrosion pit. (D) SEM micrograph of the sandblasted surface following 16 h of degradation (B and E) AFM micrographs of degraded coatings on polished and sandblasted substrates respectively. Pits may have been sites for pitting corrosion.

4.4.4 SEM of C7U: P40 Fe4 in PBS Pre and Post Degradation

Micrographs of the samples degraded in PBS up to 21 d suggested uneven coverage of particulates and remaining coating over the surface area of the sample as shown in *Figure 4.39A*, *B* and *C* for 4 h, 6 d and 21 d respectively. *Figure 4.39F* shows precipitates forming over a half coated specimen after 24 h whilst *G and H* show precipitation of coatings on sandblasted substrates after 48 h in solution at 2000x and 4000x.

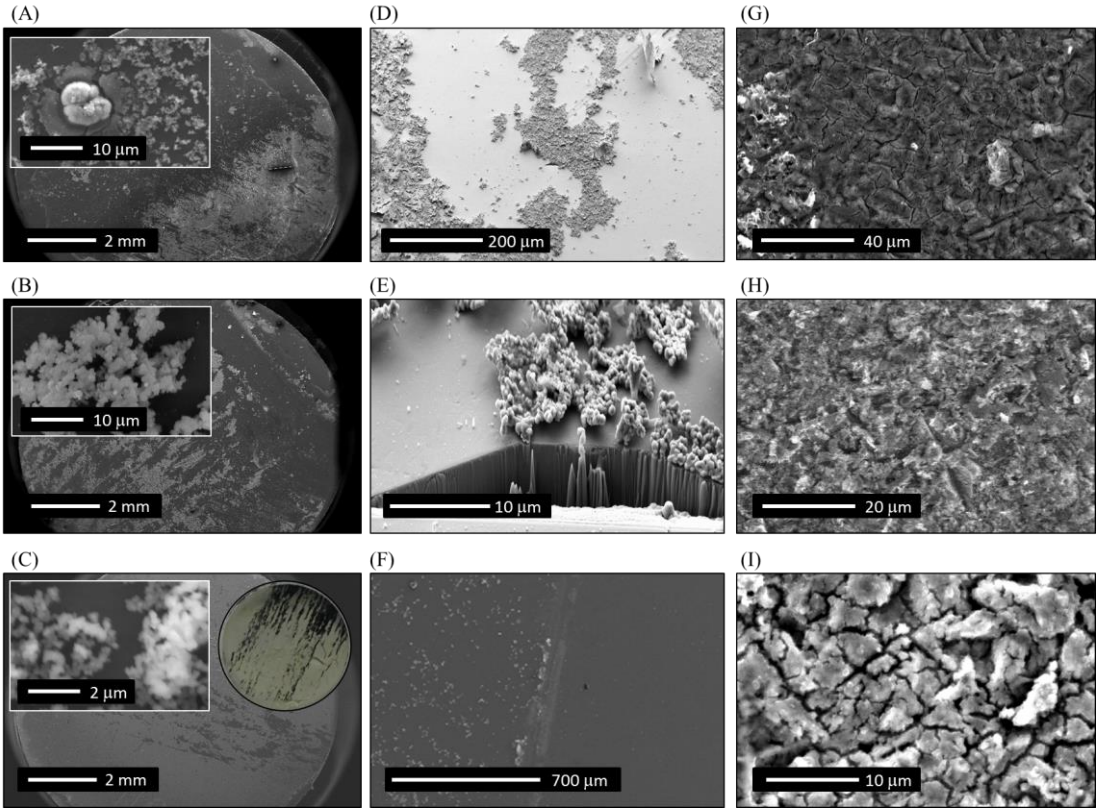

Figure 4.39: Degradation of C7U: P40 Fe4 PBG on polished substrates in PBS representing (A) 4h, (B) 6 d, (C) 21 d degraded (D and E) FIB-SEM 21 d degraded. (F) Half coated samples (coated on left, uncoated on right) degraded for 24 h. (G) Precipitation following degradation of a coating deposited onto a sandblasted surface after 48 h at 2000x and (H) 4000x. (I) 4 d in PBS on C8U: P31 Ti6.

FIB-SEM micrographs provided improved resolution of the precipitate formation and showed precipitation of the coating in its entirety, resting on the surface of the Ti6Al4V substrate *Figure 4.39E*. Additionally a micrograph *Figure 4.39I* of composition C8U: P31 Ti6 following dissolution on a sandblasted Ti6Al4V substrate after 4 d in PBS confirmed that the precipitation reaction was not isolated to a single coating composition. Compositions C8U: P31 Ti6 and C9U: P35 Ti7 Cu5 on polished substrates were also examined and assessed via EDX after 4 d in PBS as shown in *Figure 4.40.*

4.4.5 Degradation of Coatings (C8U-C11U)

Degradation rates revealed linear profiles between 2 h and 24 h, as presented in *Table 4.10.* Most notably, the expected trend of increased durability due to cationic cross linking was not observed. This was most apparent between compositionally similar C10U: P40 Fe8 and C7U: P40 Fe4 for which relative dissolution rates were 2.57 and 2.12 x 10^{-4} mg mm^{-2} h^{-1} respectively with C10U: P40 Fe8 exhibiting increased solubility. For all compositions comparative mass losses at 2 h ranged from 1.40 to 3.81 x 10^{-3} mg mm^{-2}. This indicated an increased solubility during the first 2 h for all coating compositions *(see Figure 4.41*). Samples dissolved in dH_2O were assessed by XPS following the 7 d time point from which it was determined that all coatings apart from C11U: P32 Fe5 had entirely degraded. In contrast coatings immersed in PBS were continued until 7 d. XPS, SEM and EDX after 4 d confirmed remaining elements associated with the original coatings (*Figure 4.41).*

Table 4.10: Cumulative dissolution by 2 h, 24 h and degradation rates for compositions of PBG coatings produced in UoN PVD.

Glass Code Nominal (N) vs. As Prepared (AP)	dH_2O 2-24 h	dH_2O 2 h	dH_2O 24 h	PBS 2 h	PBS 24 h
	mg mm^{-2} h^{-1} x 10^{-3} (r^2)	mg mm^{-2} x 10^{-3}	mg mm^{-2} x 10^{-3}	mg mm^{-2} x 10^{-3}	mg mm^{-2} x 10^{-3}
MQ5: P40 Fe4	0.97 ± 0.01 (0.95)	0.58 ± 0.05	2.54 ± 0.12	0.29 ± 0.04	3.73 ± 0.16
C7U: P40 Fe4	0.21 ± 0.02 (0.96)	3.81 ± 0.10	8.64 ± 0.28	3.18 ± 0.42	6.78 ± 0.25
C8U: P31 Ti6	0.08 ± 0.01 (0.93)	1.40 ± 0.12	2.92 ± 0.20	1.57 ± 0.24	3.60 ± 0.18
C9U: P35 Ti7 Cu5	0.12 ± 0.01 (0.96)	1.44 ± 0.19	3.94 ± 0.32	1.78 ± 0.16	5.4 ± 0.33
C10U: P40 Fe8	0.26 ± 0.04 (0.90	2.33 ± 0.25	7.88 ± 0.36	2.75 ± 0.25	6.5 ± 0.23
C11U: P32 Fe5	0.29 ± 0.04 (0.95)	3.18 ± 0.16	9.45 ± 0.94	2.63 ± 0.13	5.76 ± 0.28
C12U: P28 Fe6	0.08 ± 0.01 (0.94)	1.40 ± 0.12	3.18 ± 0.28	2.50 ± 0.21	2.58 ± 0.40

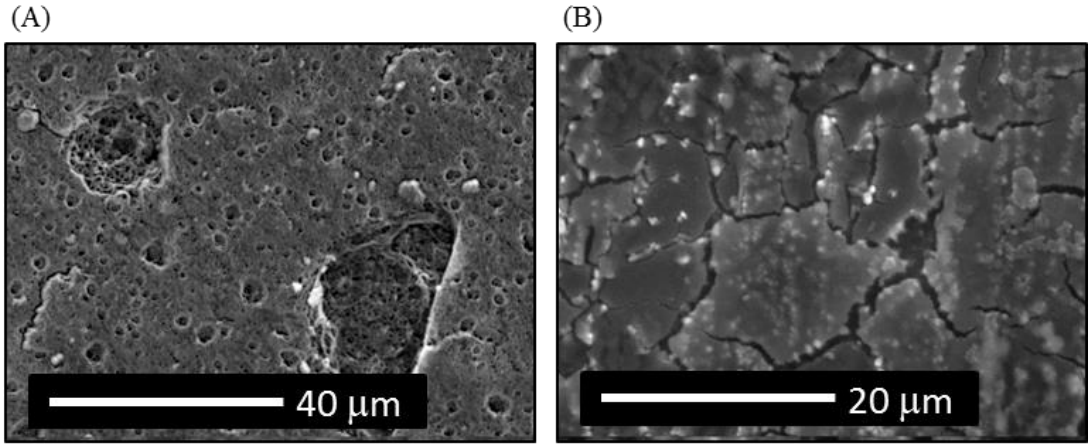

Figure 4.40: Precipitation following 4 d in PBS on polished C8U: P31 Ti6 and C9U: P35 Ti7 Cu5.

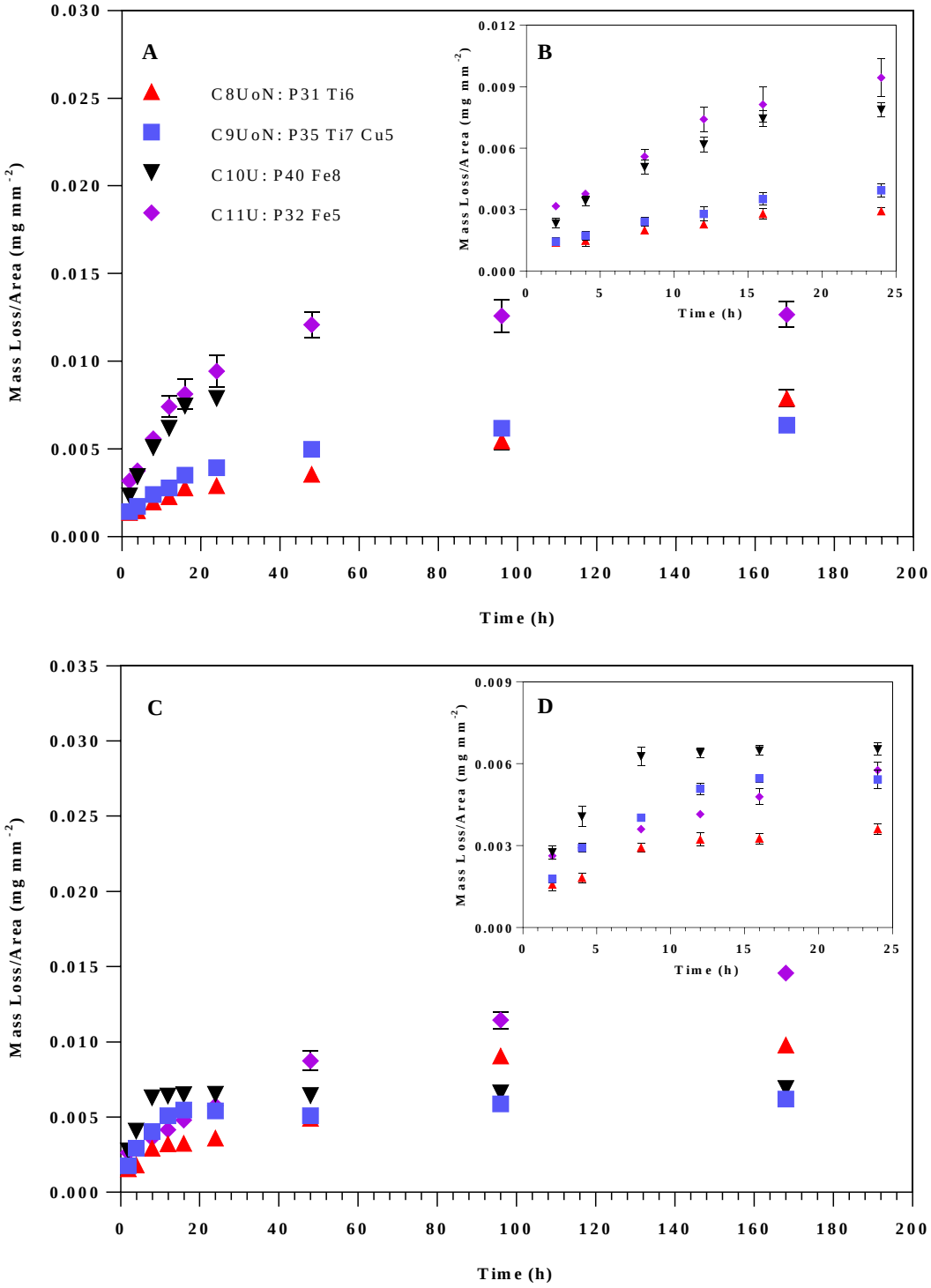

Figure 4.41: Degradation of coating compositions on Ti6Al4V in (A and B) dH_2O (C and D) PBS up to 24 and 168 h. All coatings were assessed by XPS at the 7 d time point and were found to be fully degraded with the exception of C11U: P32 Fe5.

4.4.6 Contact Angle

In addition to the stated PBG compositions, as previously mentioned in (*Section 4.1*), a SBG C6T: Si50 was deposited in the TEER UDP 650 to a thickness of 490 nm. Deposition was conducted from T2T: Si46 BG 45S5. The hydrophilic and surface properties of C6T: Si50 were tested and were compared with regards to *in vitro* apatite forming ability compared to PBG coating compositions in *Section 4.6*.

Contact angle was measured to observe the hydrophilicity with dH_2O and *Table 4.11* indicated a variation between MQG and coatings of equivalent elemental compositions (*Table 4.11*). For all PBG coatings the contact angle was unquantifiable (<3.0°), indicating super hydrophilicity. In contrast sandblasted Ti6Al4V on its own had a contact angle of 44.6 ± 3.7°. (n=5) for all contact angle experiments. The hydrophilic nature as shown by contact angle correlates with the variable surface chemistries between MQ5: P40 Fe4 and C7U: P40 Fe4 by means of increased P-O-P polymerisation as shown by XPS. The deposited silicate glass C6T: Si50 in contrast was comparable to MQ PBG with a contact angle of 31.9 ± 1.4°.

Table 4.11: Contact angle of MQG and PVD glasses with dH_2O. All coatings were deposited onto sandblasted Ti6Al4V. Prepared samples for dissolution.

Composition	Contact Angle (°)	Standard Error (°) n=5	Coating Thickness (μm)
Ti6Al4V	44.6	3.7	-
MQ5: P40 Fe4	24.8	0.6	-
C7U: P40 Fe4	Completely Wetted	Not Measureable	2.67
C8U P31 Ti6	Completely Wetted	Not Measureable	2.67
C9U: P35 Ti7Cu5	Completely Wetted	Not Measureable	2.67
C10U: P40 Fe8	Completely Wetted	Not Measureable	2.67
C12U: P28 Fe6	Completely Wetted	Not Measureable	1.69
C5T: P40 Fe4	Completely Wetted	Not Measureable	1.16
C6T: Si50	31.9	1.4	0.49

4.4.8 XPS Pre and Post Degradation

The surface structure of C7U: P40 Fe4 was compared to its MQ5: P40 Fe4 counterpart. The respective ratio of bridging oxygen to non-bridging oxygen bonds on the surface of C7U: P40 Fe4 was 34.8% : 65.2% compared with 20.5% : 79.5 % in MQ5: P40 Fe4. Majority metaphosphate $(PO_3)^-$ (Q^2) species were formed in C7U: P40 Fe4 compared to less soluble $(P_2O_7)^{4-}$ (Q^1) and $(PO_4)^{3-}$ (Q^0) in MQ5: P40 Fe4. This relationship was similarly shown previously during a comparison of MQ and RFMS coatings in *Section 5.2*.

See *Table 4.12* for deconvolution of the high resolution P 2p and O 1s spectra for all coating compositions tested. Peaks were associated with phosphate glass, notably, for MQ5: P40 Fe4, two peaks within the O 1s corresponding to P-O-P bridges and (PO^- and P=O) non-bridging oxygen bonds at 533.44 eV and 531.72 respectively as suggested by Brow *et al.* and Shih *et al.* [48, 76]. MQ5: P40 Fe4 showed deconvolution of the P $2p_{3/2}$ and P $2p_{1/2}$ high-resolution spectral peaks, specifically the P $2p_{3/2}$ and P $2p_{1/2}$ spin orbitals at 134.4 and 133.5 eV, attributed to $(P_2O_7)^{4-}$ and $(PO_4)^{3-}$ [222, 223]. In contrast the surface of the coating C7U: P40 Fe4, was deconvoluted, containing peaks located at the P $2p_{3/2}$ and P $2p_{1/2}$ locations of 134.3 and 135.1 eV which were suggested to be attributed to metaphosphates $(PO_3)^-$ (*Table 4.12*) [224, 231].

The additives of Fe, Ti and Cu in their respective composition were shown to form surface oxides from analysis of the Fe 2p, Ti 2p and Cu 2p high resolution spectra. The oxidation state of Cu was shown to be Cu_2O/Cu^{1+} whilst the positioning of Ti $2p_{3/2}$, located at 459.3 eV is most closely associated with Ti^{4+} [224].

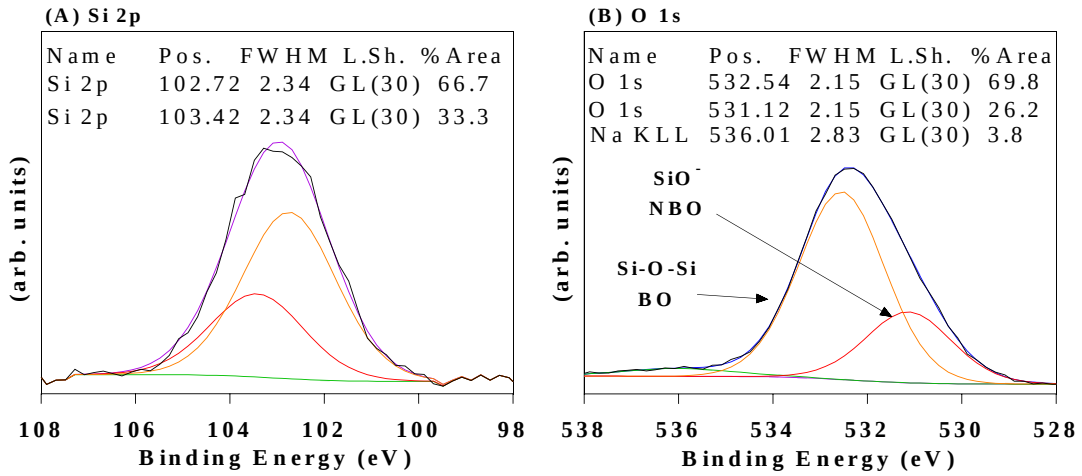

Figure 4.42: XPS Profile of C6T: Si50 (A) Si 2p and (B) O 1s to determine the ratio of NBO to BO within the surface layer.

Analysis of C6T: Si50 showed Si-O-Si BO to SiO^- NBO ratio of 72.6 to 27.4% from deconvolution of the O 1s (*Figure 4.42B*). (*A*) Suggested a shift toward the higher energy range for SiO_2 suggesting relatively higher proportion of silica within the structure [232].

Table 4.12: Deconvolution of the O 1s and P 2p to determine the ratio of Bridging to Non Bridging Oxygen's and states of phosphorus in the structures. Ratios have been normalised to remove Na KLL from the peak deconvolution. Orthophosphate $(PO_4)^3$, Pyrophosphate $(P_2O_7)^{4-}$, Metaphosphate $(PO_3)^-$, (Q^0, Q^1 and Q^2 respectively) [48, 222, 223].

Glass Code Composition	O 1s P-O-P or Si-O^- (BO) %*	O 1s PO^- and P=O or SiO^- (NBO) %*	Na KLL % (Overlapping O 1s)	P $2p_{3/2}$ or Si $2p_{3/2}$ (eV)	Majority Q^n Distribution
MQ5: P40 Fe4	20.5	79.5	5.0	133.5	Q^0, Q^1
C7U: P40 Fe4	34.2	65.8	5.5	134.3	Q^2
C7U: P40 Fe4 16 h dH_2O	22.5	77.5	5.4	133.6	Q^0, Q^1
C7U: P40 Fe4 4d PBS	19.3	80.7	23.7	134.8	Q^2
C5T: P40 Fe4	33.1	66.9	3.5	133.9	Q^0, Q^1, Q^2
C6T: Si50	72.6	27.4	3.8	103.4	-
C8U: P31 Ti6	28.5	71.5	6.0	133.7	Q^0, Q^1, Q^2
C9U: P35 Ti7 Cu5	28.6	71.4	10.8	133.8	Q^0, Q^1, Q^2
C10U: P40 Fe8	36.7	63.3	2.6	134.5	Q^2
C11U: P32 Fe5	31.0	69.0	5.5	134.1	Q^0, Q^1, Q^2

* Normalised O 1s following subtraction of the overlapping Na KLL

Table 4.13: Surface compositions of the coatings compared with melt quenched glasses determined by XPS. Determination of the peak positions of O 1s and P 2p for the attibuted oxidation states via analysis of the high resolution spectra.

Element at%	MQ5: P40 Fe4	C7U: P40 Fe4	C7U: P40 Fe4 16 h In dH_2O	C7U: 4 d In PBS	C5T: P40 Fe4	C6T: Si50	C8U: P31 Ti6	C9U: P35 Ti7 Cu5	C10U: P40 Fe8	C11U: P32 Fe5
O (O 1s)	66.0	58.5	60.4	52.5	65.7	61.6	59.5	57.4	67.3	60.0
P (P 2p)	16.7	15.7	18.6	10.9	19.7	1.3	19.8	17.8	20.3	19.7
Mg (Mg 2s)	4.9	1.2	4.9	0.5	4.5	-	-	-	2.6	5.9
Ca (Ca 2p)	8.5	4.1	7.3	2.5	4.8	7.4	8.7	4.4	4.3	5.3
Na (Na 1s)	3.3	14.6	6.1	30.6	4.2	6.7	10.7	18.9	3.2	7.9
Ti (Ti 2p)	-	-	-	-	-	-	1.3	1.3	-	-
Fe (Fe 2p)	0.5	6.0	2.7	2.9	1.1	-	-	-	2.3	1.2
Cu (Cu 2p)	-	-	-	-	-	-	-	-	-	-
Si (Si 2p)	-	-	-	-	-	23.1	-	-	-	-

Following 4 d of degradation in PBS the P 2p deconvolution was attributed to $(PO_3)^-$, in support of the FTIR results shown previously. A notable increase from 5% to 23.7 % Na KLL Following 4 d degradation in PBS of C7U: P40 Fe4 indicated a surface compositional increase in Na or possible precipitation of Na onto the surface (*Table 4.12*).

Section 4.5 will detail the effectiveness of post deposition annealing on the mechanical, structural and degradation properties with a specific interest in stabilising the dissolution properties of the PBG layer.

4.5 Post Deposition Annealing; Mechanical, Structural and Degradation Properties

Post deposition heat treatment has been used to relieve internal stresses in glasses, or to nucleate and grow crystals to initiate the formation of ceramic phases, therefore stabilising their dissolution properties. The work presented here investigates the RFMS coating compositions; C7U: P40 Fe4 and C8U: P31 Ti6 applied to Ti6Al4V, exploring the effects of post deposition annealing and crystallisation on structural, mechanical and dissolution properties. In addition the ion-release properties of the as deposited and 500 °C heat treated (HT) variations of C7U: P40 Fe4 were assessed.

As discussed previously in *Section 4.1*, C7U: P40 Fe4 was the benchmark composition whilst C8U: P31 Ti6 specifically P_2O_5-31 CaO-55 Na_2O-8 TiO_2-6 mol% was manufactured to test bioactive potential in *Section 4.6*, to utilise it's potential to form Ti-OH nucleation points for apatite precipitation. Kasuga *et al.* found that heat treatment of a similar titanium containing melt quenched glass led to enhanced bioactive potential in SBF therefore heat treatment was conducted here. The specific formulation of Kasuga *et al.* was P_2O_5-30 CaO-60 Na_2O-7 TiO_2-3 mol% whilst heat treatment produced phases of β-$Ca_3(PO_4)_2$ and β-$Ca_2P_2O_7$ [57]. See *Section 3.20* for heat treatment methodology.

Nomenclature: The coating code is followed by the heat treatment temperature and dwell time. Coating C7U: P40 Fe4, heat treated at 500 °C for a dwell time of 30 minutes would therefore become C7U-500°-30. Furthermore as deposited has been denoted (AD).

4.5.1 EDX

The coating composition C7U: P40 Fe4 mol% was investigated to observe the effect of heat treatment on the coating topography, crystallinity, degradation and mechanical

properties. C8U: P31 Ti6 was heat-treated for assessment of structural and dissolution properties. Elemental mol% compositions of C7UAD, C7U-500°-30 and C7U-500°-120 were observed to vary by a maximum of (1.24, 1.53, 1.22, 0.82, 0.63) mol% for (P_2O_5, MgO, CaO, Na_2O, Fe_2O_3) respectively. Coatings crystallised for C7U-550°-30 and C7U-610°-30 showed by EDX, a reduction in phosphorous to 38.4 ± 0.2 and 36.9 ± 0.2 mol% respectively.

Table 4.14: Coating deposition parameters. C7UAD, C7U-500°-30, C7U-500°-120, C7U-550°-30, C7U-610°-30, were deposited under the same conditions and subsequently heat treated in argon. C8U: P31 Ti6 was heat treated in nitrogen. As prepared target and coating compositions mol%. Nominal composition and As prepared were analysed by EDX. Nomenclature: coating code followed by HT temperature and dwell time.

Deposition Parameters	**Argon Pressure (Pa)**	**Deposition Time (min)**	**Target/Power (W)**	**Throw Distance (cm)**	**Rotation (RPM)**	**Coating Thickness (μm)**
C7U: P40 Fe4	1.33 ± 0.01	1165 ± 1	T6 / 60 ± 1	4.0 ± 0.5	Static	2.67 ± 0.09
C8U: P31 Ti6	1.33 ± 0.01	1165 ± 1	T7 / 60 ± 1	4.0 ± 0.5	Static	1.04 ± 0.02
As Prepared	**P_2O_5**		**MgO**	**CaO**	**Na_2O**	**Fe_2O_3**
C7UAD	40.2 ± 0.2		23.8 ± 0.2	15.4 ± 0.2	16.8 ± 0.1	3.8 ± 0.5
C7U-500°-30	40.7 ± 0.1		22.3 ± 0.1	16.6 ± 0.1	16.0 ± 0.1	4.45 ± 0.5
C7U-500°-120	41.5 ± 0.4		22.6 ± 0.2	15.9 ± 0.2	15.9 ± 0.3	4.1 ± 0.5
C7U-550°-30	38.4 ± 0.2		23.4 ± 0.2	18.0 ± 0.1	15.7 ± 0.2	4.6 ± 0.5
C7U-610°-30	36.9 ± 0.2		23.7 ± 0.3	20.6 ± 0.2	13.1 ± 0.2	5.7 ± 0.5
C8UAD	31.3 ± 0.1		-	55.4 ± 0.1	7.7 ± 0.1	5.6 ± 0.1
C8U-500°-30	-		-	-	-	-

4.5.2 XRD

Glancing angle XRD suggested an amorphous AD microstructure for C7UAD and C8UAD. Signal from the substrate produced peaks associated with Ti. A single diffraction peak emerged in C7U-500°-30 and C7U-500°-120 located at ~33 2θ (°). See *Appendix Section 9, 1.0* for slow scan and better resolution of the emerging peak from 30-35 2θ (°). This peak was attributed to hematite (see *Figure 4.43*).

An amorphous diffraction hump remained present from 15° to 35° 2Θ (°) following HT up to 550 °C. Following C7U-610°-30 crystalline phases present may have been

associated with Sodium Magnesium Phosphate, Titanium Oxide, Titanium Oxide Phosphate, Magnesium Phosphate Oxide, Sodium Phosphate, Magnesium Phosphate, Sodium Oxide and Phosphorous Oxide. Ti rutile also formed following C7U-610°-30. In addition the amorphous hump was not visible for C7U-610°-30. A phase of Calcium Phosphate formed in C8U-500°-30. See *Figure 4.43* for diffraction patterns and caption for phases identified.

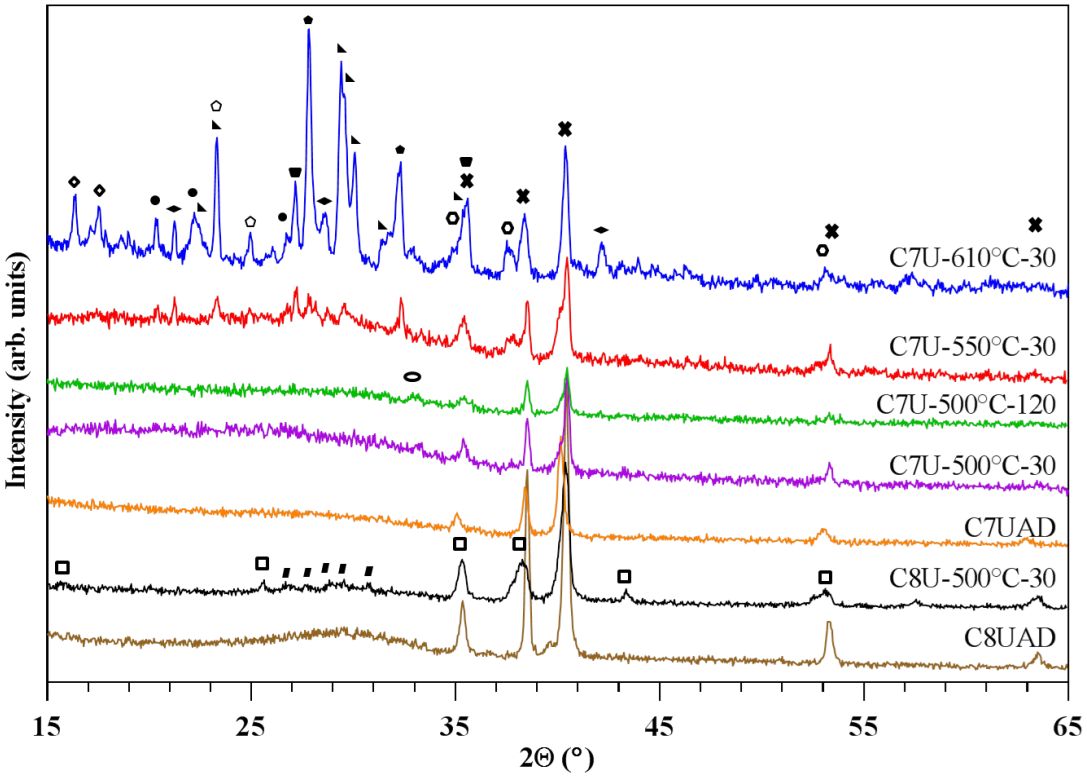

Figure 4.43: XRD of AD and HT coatings. Substrate signal indicated a phase of (✖) Ti alpha ICDD-PDF-00-001-1197. A crystalline phase corresponding to (⬭) Hematite (Fe_2O_3) ICDD-PDF-01-085-0599 emerged following C7U-500°-30 and C7U-500°-120. Amorphous humps were present in all samples from 15° to 35° (2Θ) with the exception of C7U-610°-30. Phases present following C7U-610°-30 corresponded to (◆) Phosphorous Oxide (P_4O_{10}) ICDD-PDF-00-023-1303, (◂▸) Sodium Phosphate ($NaPO_3$) ICDD-PDF 01-076-1112, (◣) Magnesium Phosphate Oxide ($Mg_2P_2O_7$) ICDD-PDF-00-032-0626,(⬠) Sodium Magnesium Phosphate ($NaMg(PO_3)_3$) ICDD-01-072-2341,(■) Calcium Phosphate (β-$Ca_2P_2O_7$) ICDD-PDF-01-071-2123 (⬟) Ti Rutile ICDD-PDF-00-021-1276, (⬟) Sodium Oxide (Na_2O) ICDD-PDF-00-023-0528, (⬣) Titanium Oxide (Ti_3O) ICDD-PDF-01-073-1117, (●) Unattributed peaks.

4.5.3 XPS

Wide angle spectra of C7UAD, C7U-500°-30 to C7U-610°-30 indicated the surface elemental compositions within the first 5-10 nm of the coating layer (*Figure 4.44A, C)* C7U-500°-120 to C7U-610°-30 (not shown) [211].

Following heat treatment at annealing temperature of 500 °C, the peaks previously present in C7UAD for P 2p and P 2s at 132-140 eV and 185-195 eV (*Figure 4.44A*) respectively diminished in the spectra (see *Figure 4.44A* compared with *B*) showing a phosphorus deficiency in the surfaces of all HT coatings. Quantification of the composition in at% showed an increase in Fe content from 1.4 in C7UAD to 22.4, 22.8, 18.1 and 10.6 at% from C7U-500°-30 to C7U-610°-30. (*Table 4.15 for mol% and at%*). Notably surface Ca:P at% ratio following C8U-500°-30 increased to 1.30.

Table 4.15: Surface compositions determined by XPS of AD and HT compositions. Compositions have been calculated in both mol% and at% to maintain consistency with conventional glass formulations and to show absolute elemental compositions. At% is essential as the bonding states due to crystallisation can no longer be considered stoichiometric oxides as reflected in mol%.

	C7UAD		**C7U-500°-30**		**C7U-500°-120**		**C7U-550°-30**		**C7U-610°-30**		**C8UAD**		**C8U-500°-30**	
	mol%	**at%**	**mol%**	**at%**	**mol%**	**at%**	**mol%**	**at%**	**mol%**	**at%**	**mol%**	**at%**	**mol%**	**at%**
(P 2p) P_2O_5/P	44.1	21.6	3.8	1.6	2.9	1.3	4.3	2.1	6.7	3.5	39.2	19.8	25.2	15.1
(Na 1s) Na_2O/Na	8.2	4.0	12.9	5.5	12.5	5.6	17.1	8.4	30.7	16.1	21.2	10.7	4.7	2.8
(Ca 2p) CaO/Ca	22.0	5.4	5.2	1.0	8.0	1.8	23.2	5.7	24.8	6.5	34.5	8.7	65.8	19.7
Mg (2s) MgO/Mg	22.9	5.6	25.4	5.4	25.8	5.6	18.7	4.6	17.6	4.6	-	-	-	-
(Fe 2p) Fe_2O_3/Fe	2.9	1.4	52.7	22.4	50.8	22.8	36.8	18.1	20.2	10.6	-	-	-	-
(Ti 2p) TiO_2/Ti	-	-	-	-	-	-	-	-	-	-	5.2	1.3	4.3	1.3
(O 1s) O		62.0		64.1		62.9		61.1		58.7		59.5		61.2

Due to 1.4 at% concentration of iron within the layer, low intensity of the Fe 2p for the C7UAD coating was observed with no satellite peaks present within the spectra. Fe 2p showed improved resolution following HT, with no apparent difference between C7U-500°-30 and C7U-500°-120. The satellite regions here were observed

between 715.0 - 724.0 and 730.0 - 737.0 eV. Fe 2p has a spin orbit split (Fe $2p_{1/2}$), generating spectral peaks located between 721.0 – 737.0 eV (*Figure 4.44D* and *F*) [233, 234].

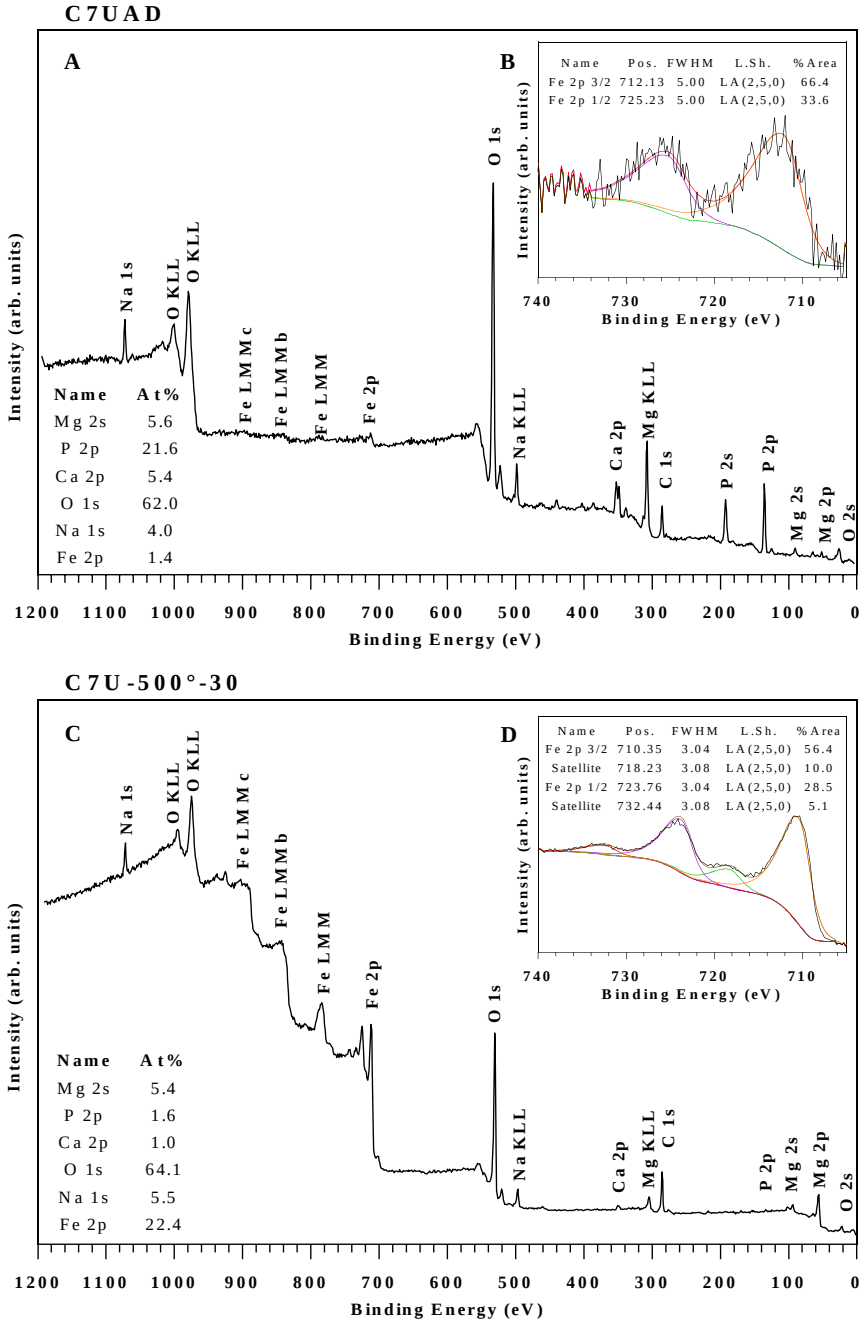

Figure 4.44: XPS survey spectra and high-resolution spectra of Fe 2p. (A) C7UAD survey (B) C7UAD Fe 2p. Broad peak positions suggested multiple oxidation states associated with Fe following deposition (C) C7U-500°-30 survey (D) C7U-500°-30 Fe 2p. Following C7U-500°-30 to C7U-610°-30 the coating surfaces were phosphorous deficient whilst the location of the Fe 2p spectral peaks suggested the prominence of Fe_2O_3. C7U-500°-120 to C7U-610°-30 (not shown).

4.5.4 FTIR

IR absorption of C7UAD, C7U-500°-30 and C7U-500°-120 contained peaks associated with vibrational modes located at 1280, 1200, 1100, 1055, 1012, 912, 769, 530 cm^{-1}. The position ranges (*Figure 4.45*). C7UAD showed weaker relative absorption at 1280 and 530 cm^{-1} attributed to Q^2 (PO_2) groups and Q^0 (PO_4^{3-}) whilst C7U-500°-30 and C7U-500°-120 contained slight Q^2 (PO_2) shoulders at 1280 cm^{-1}. The band attributed to Q^0 (PO_4^{3-}) increased with intensity for C7U-500°-30 and C7U-500°-120. According to Minitti *et al.* Hematite bands are located at 315, 461 and 560 cm^{-1}, overlapping the PO_4^{3-} band at 500-580 cm^{-1} [235, 236]. Furthermore for C7U-550°-30 and C7U-610°-30, following the formation of multiple crystalline phases as shown by *Figure 4.43* peak splitting of the functional groups, position shifts and variation in intensities was observed (*Figure 4.45*).

The IR absorption after 16 h post degradation showed no noticeable peaks associated with dissolution of the bulk coating, specifically the absence of a hydroxyl OH^- group at 3000-3500 cm^{-1} (not shown). A notable decline in the relative intensities of the peaks at 900, 769, and 530 cm^{-1} for all degraded samples was observed whilst P-O-P bonds around 900 and 740 cm^{-1} shifted to higher wavenumbers.

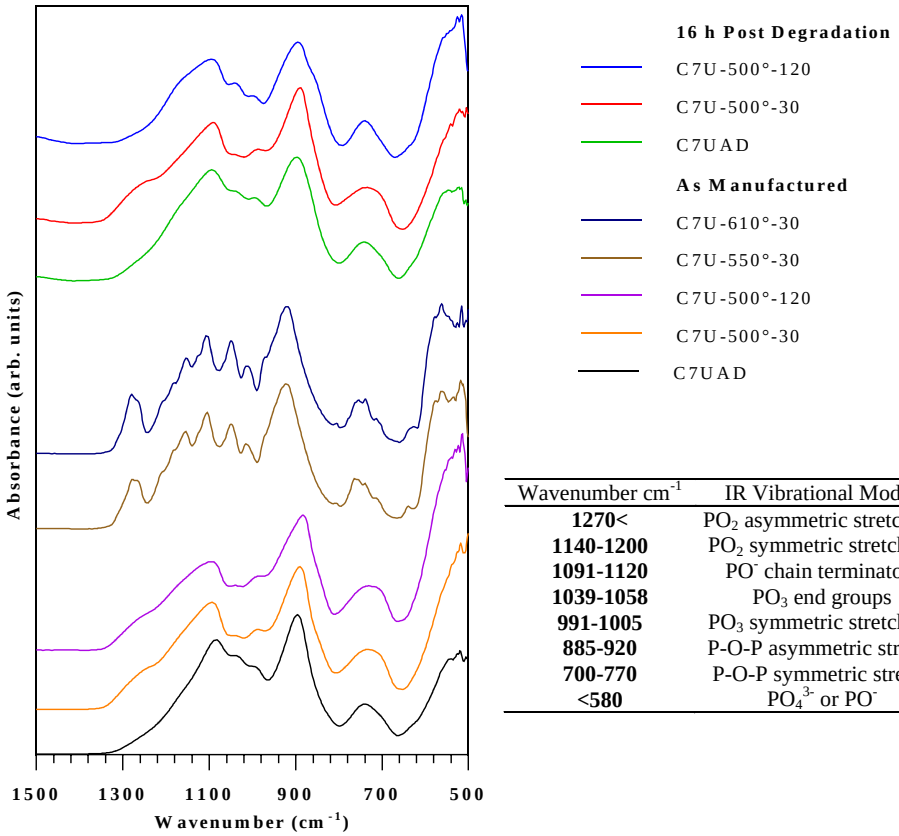

Wavenumber cm^{-1}	IR Vibrational Modes
1270<	PO_2 asymmetric stretching
1140-1200	PO_2 symmetric stretching
1091-1120	PO^- chain terminators
1039-1058	PO_3 end groups
991-1005	PO_3 symmetric stretching
885-920	P-O-P asymmetric stretch
700-770	P-O-P symmetric stretch
<580	PO_4^{3-} or PO^-

Figure 4.45: (A) C7U: P40 Fe4 AD and HT variations. IR absorption spectra for as manufactured coatings and 16 h post dissolution in dH_2O. (Table) Peak labels and ranges.

4.5.5 Adhesion and Interfacial Characteristics

Scratch Testing

The mechanical properties of coatings C7UAD, C7U-500°-30 and C7U-500°-120 were experimentally determined by the methods of progressive scratch testing and tensile pull off testing. A Rockwell C indenter was progressively loaded at 10 N min^{-1} to 30 N, over a scratch length of 3 mm. Post analysis of the scratch showed multiple failure mechanisms associated with brittle fracture detailed in *Figure 4.46*.

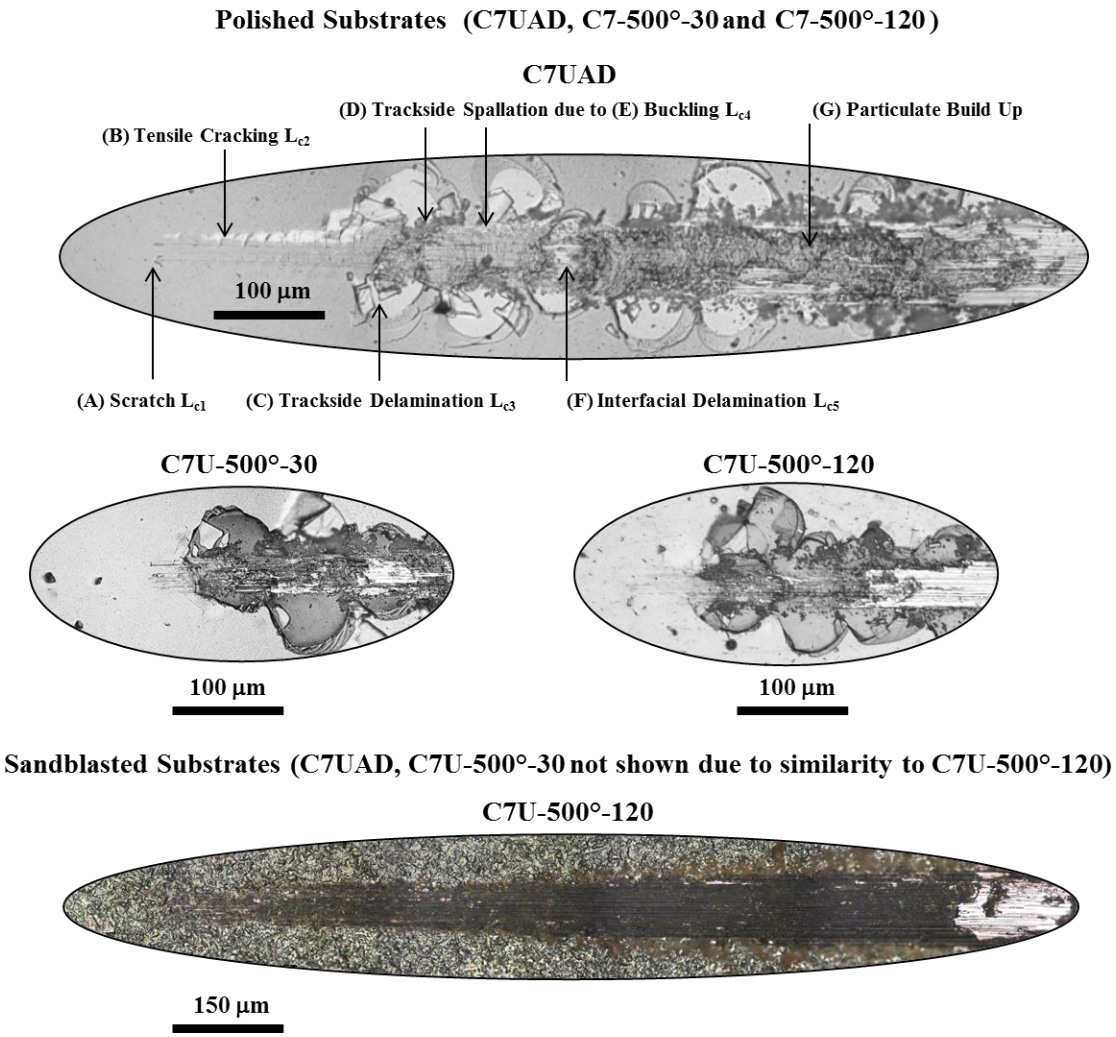

Figure 4.46: Scratch adhesion testing of C7UAD, C7U-500°-30 and C7U-550°-30 on Polished Ti6Al4V substrates. The characteristic wear mechanisms have been labelled in C7UAD (A) Scratch L_{c1}, (B), Tensile cracking L_{c2}, (C) Trackside delamination L_{c3}, (D) Trackside spallation due to buckling L_{c4}, (F) Interfacial delamination L_{c5}, (G) Particulate build up.

The wear mechanisms were established by initial experimentation at constant loading from 2-18 N and examined by SEM and EDX elemental mapping (data not shown). Mechanisms were attributed to the initial indentation (scratch L_{c1}), (tensile cracking L_{c2}), (trackside delamination L_{c3}), (buckling L_{c4}) and (interfacial delamination L_{c5}) (*Figure 4.46* representative sample/image). Buckle spallation and buckling occurred simultaneously and have been described as a single mechanism. On polished Ti6Al4V substrates (*Figure 4.47A)*, the trends showed a

reduction in failure loads of all wear mechanisms following annealing for 30 min in C7U-500°-30 (*Figure 4.47*). The failure strengths appeared to recover following annealing of C7U-500°-120 for 120 min. A closer examination of the scratch results of C7UAD compared with C7U-500°-120 suggested that L_{c1} and L_{c2} occurred at higher loads, increasing from 1.0 to 2.5 N and 2.0 to 3.0 N respectively. The hardness of a material is it's resistance to indentation, suggesting that annealing of C7U-500°-30 may have increased hardness of the coating layer. The primary interfacial failure occurred by the mechanism of trackside delamination at 3.2, 1.5 and 3.0 N respectively for C7UAD, C7U-500°-30, and C7U-500°-120. Notably; the increases in loading from initial scratch L_{c1} until the interfacial delamination L_{c5} were 4.0, 1.3 and 2.0 N for C7UAD, C7U-500°-120, and C7U-550°-30, whilst the failure loads of L_{c2}, L_{c3} and L_{c4} for coatings C7U-500°-30 and C7U-500°-120 were closely spaced ranging from 0.1 and 0.3 N respectively (*Figure 4.47A*). A 2 way anova was conducted, which indicated that the L_{c3}, L_{c4} and L_{c5} were not significantly different for AD compared to C7U-500°-120.

Scratch adhesion testing was additionally analysed for coatings on sandblasted substrates. Observed failure mechanisms were limited to the initial scratch, buckle spallation and interfacial delamination. Notably coating fragmentation due to delamination along the trackside was absent (*Figure 4.46D*). Coatings exhibited improved interfacial properties due to substrate roughening. However, variation of 11.3, 8.6 and 11.0 N for C7UAD, C7U-500°-30 and C7U-500°-120 for interfacial failure loads were observed, suggested to be due to heat treatment whilst application of a 2 way anova showed no significant statistic variation $P<0.05$.

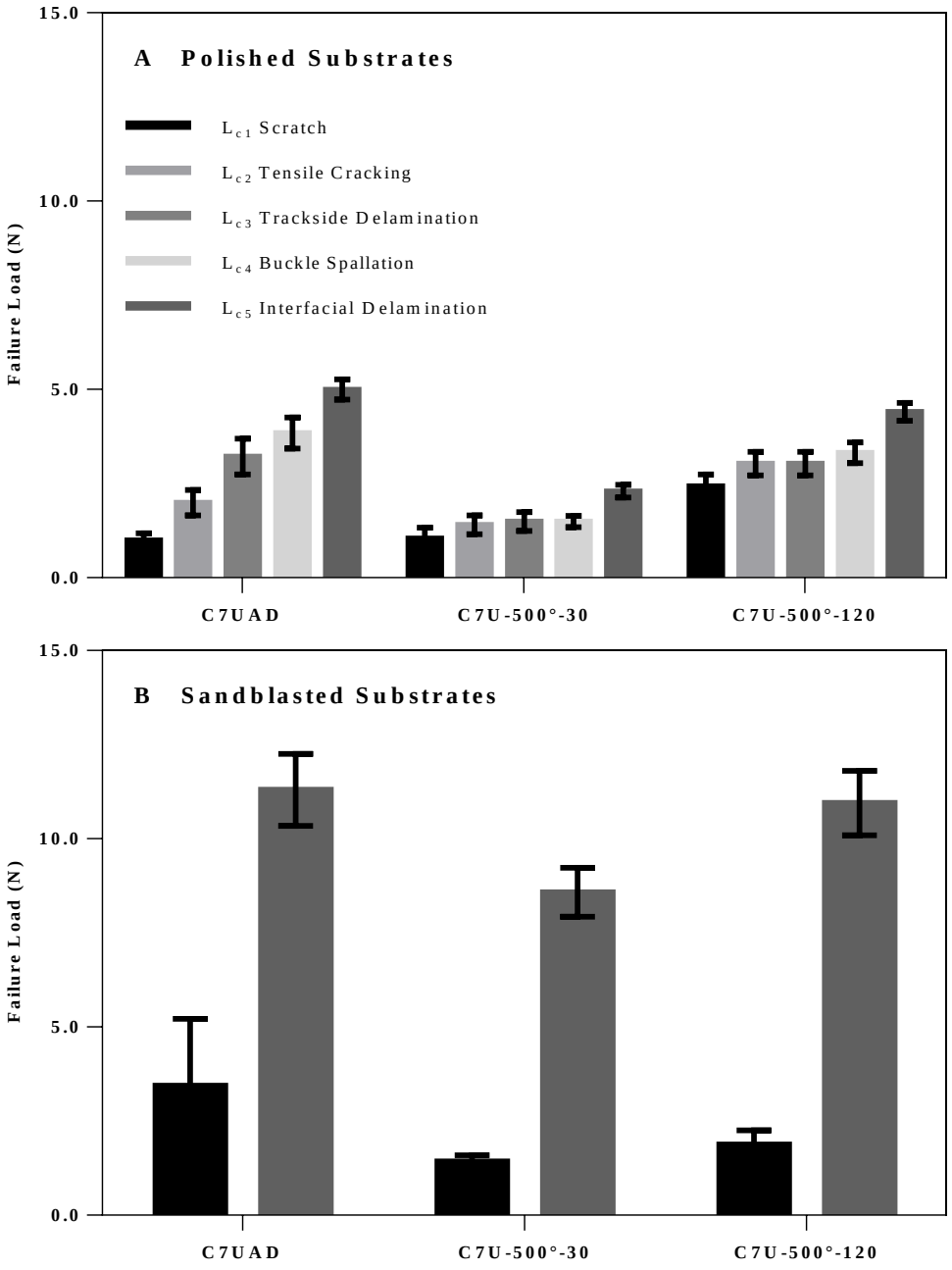

Figure 4.47: Scratch adhesion testing of C7UAD, C7U-500°-30 and C7U-500°-120. Scratch (A) Polished Ti6Al4V, (B) Sandblasted Ti6Al4V. Failure mechanisms were associated with initial scratch, tensile cracking, trackside delamination, buckle spallation and interfacial delamination.

Pull off Testing

The interfacial mechanical strengths of C7UAD, C7U-500°-30 and C7U-500°-120 and the additional coatings produced in the TEER UDP 650, C6T: Si50 and C7T: Multilayer, were assessed by tensile pull off testing for which a pull off stub was

glued to the coating surface and pulled in tension to the point of failure. For a control, the epoxy was used to glue a 'pull off stub to a Ti6Al4V substrate. All coatings were assessed on polished Ti6Al4V as all tested coatings on roughened samples within this project failed by epoxy failure and no comparable analysis could be made.

In all pull off cases (n=8) the epoxy failed cohesively at an average load of 76.8 MPa. The failure loads ranged from a (59.2-87.2 MPa). Coatings C7UAD, C7U-500°-30 and C7U-500°-120 on polished Ti6Al4V failed at 79.3, 78.6 and 73.6 MPa respectively showing ranges (60.8-105.6), (64.0-99.2) and (70.4-80.8) MPa. Microscopic observation of the failure location suggested epoxy cohesive failure in all cases.

Table 4.16: (A) Tensile failure loads and respective failure modes for pull off testing of coatings. All coating strengths exceeded the strength of the epoxy for C7UAD and its HT variations C7U-500°-30 and C7U-500°-120. *Zimmer coatings failed cohesively whilst adhesive failure was apparent.*

Coating	Failure Strength (MPa)	Range (MPa)	Failure Mode
ISO-0-137792-2 "Coatings of HA" [237]	≥15.0	-	Coating failure
FDA Draft Guidance for Ca:P Coatings [19]	≥50.8	-	Coating failure
Epoxy Failure on Ti6Al4V	76.8 ± 3.5	65.6 - 87.2	Epoxy failure
C7UAD	79.3 ± 4.3	60.8 - 105.6	Epoxy failure
C7U-500°-30	78.6 ± 4.1	64.0 - 99.2	Epoxy failure
C7U-500°-120	73.6 ± 1.5	70.4 - 80.8	Epoxy failure
Zimmer Plasma Sprayed HA	76.7 ± 1.1	73.6 – 81.6	Cohesive coating failure
C6T: Si50	14.7 ± 1.0	11.2 – 16.8	Interfacial coating failure
C7T: Multilayer	39.6 ± 1.0	28.0 - 45.6	Blend interface failure Si top layer fully detached

* All errors represent the standard error mean of n=8 samples.

A commercial plasma sprayed HA coating from Zimmer was tested showing cohesive failure towards the upper range of the epoxy at 76.7 MPa (73.6-81.6 MPa) (*Figure 4.48A-D*). The silicate glass coating C6T: Si50, was observed to fail at 14.7 MPa with a range of (11.2-17.6 MPa). C7T: Multilayer demonstrated failure of 39.6 MPa ranging (28.0-45.6 MPa) at the multi-layer blend interface between the P/Si layers. Examples of these failure modes for cohesive, adhesive and blend interface

failure have been presented below in (*Figure 4.48*). Comparative results for all pull off testing can be found in *(Table 4.16)*.

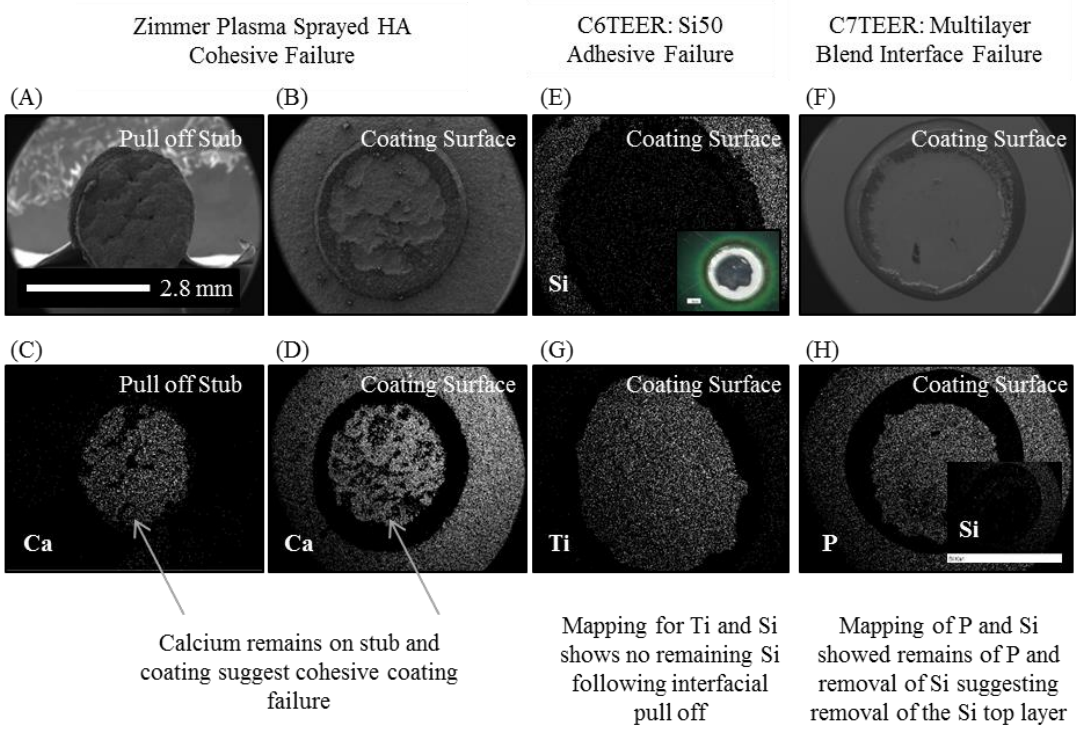

Figure 4.48: (A) Pull off stub (B) Substrate, Cohesive failure of a HA plasma sprayed coatings showing Ca mapping on the pull off stub (C) and (D) Remaining HA coating on the substrates. (E) Interfacial adhesive failure of C6T: Si50 showing no remaining Si at the substrate pull off location. (F) Ti mapping of the substrates indicates complete pull off of the coating. (G)(H) Mapping of the substrate to show remaining phosphorous, however insert shows absence of the top Si layer suggesting blend interface failure.

FIB-SEM cross sections (*Figure 4.49A-C*) were milled for as manufactured coatings of the coating/substrate interface to observe through thickness alterations of the coating features due to heat treatment. C7UAD (*Figure 4.49A, D*) followed the topographical features of the substrate and appeared continuous at the interface. Partial coating discontinuity was observed for C7U-500°-30 (*Figure 4.49B, E*). C7U-500°-120 showed voids spread consistently along the interface on both polished and sandblasted substrates (*Figure 4.49C, F*).

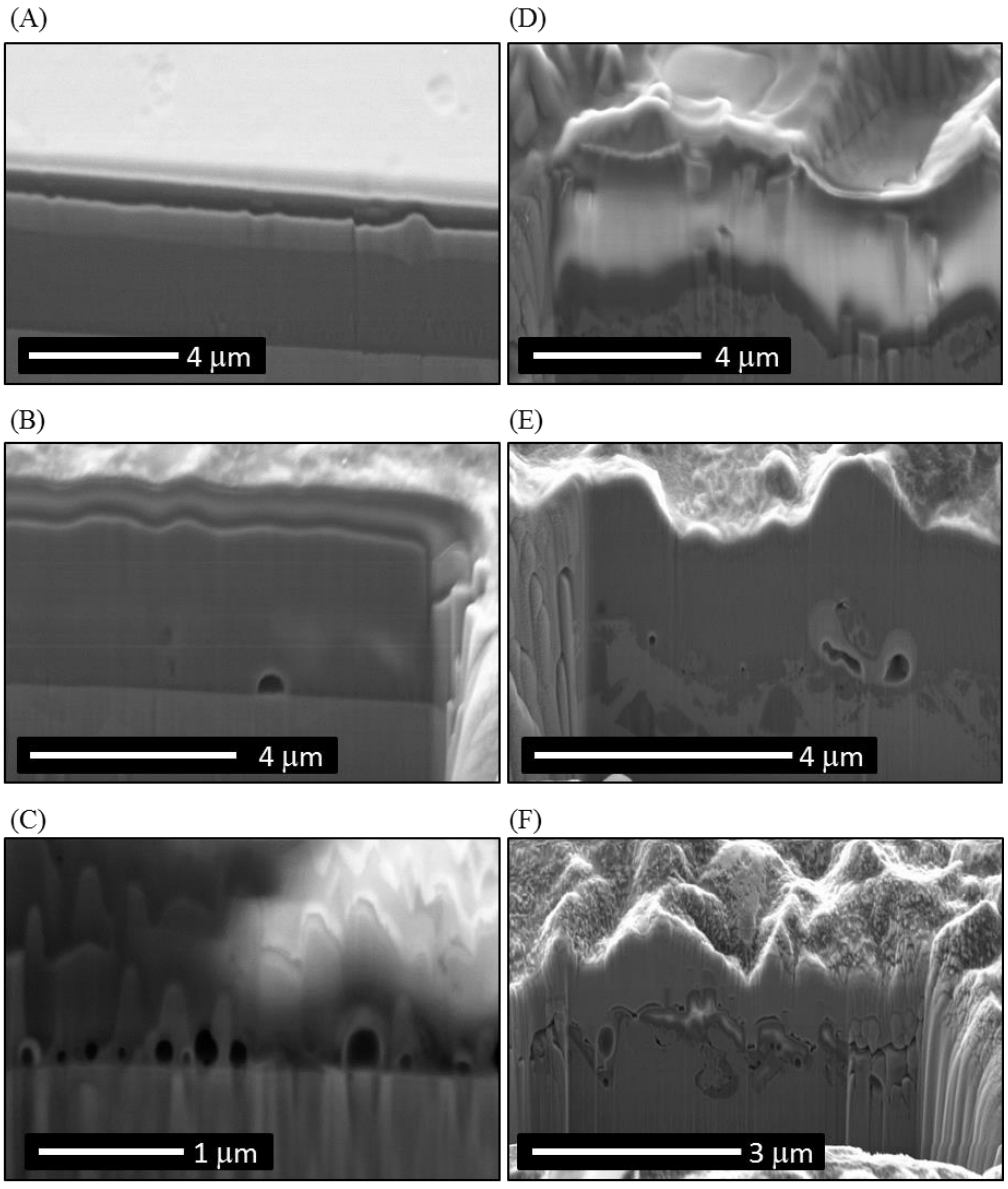

Figure 4.49: FIB-SEM cross sectional micrographs. Polished and sandblasted (A, D) C7UAD, complete interfacial adherence, (B, E) C7U-500°-30, isolated delamination, (C, F) C7U-500°-120, consistent delamination along the substrate/coating interface.

4.5.6 Degradation and Ion Release

All C7U: P40 Fe4 and C8U: P31 Ti6 HT variations were degraded in dH_2O for up to 96 h (*Figure 4.50B)*. Degradation profiles of C7UAD and C8UAD revealed initial exponential profiles in the first 2 h of degradation followed by linear profile from 2-24 h (*Figure 4.50A)*. By the 2 h time point the comparative mass losses were (2.9, 0.7, 0.3, 0.4 and 0.3) x 10^{-3} mg mm^{-2} for C7UAD to C7U-610°-30 respectively, suggesting an increased stability in the first 2 h of degradation due to HT

(*Figure 4.50)*. From 2- 24 h degradation rates were (2.1, 0.6, 0.9, 0.6 and 0.5) x 10^{-4} mg mm^{-2} h^{-1} respectively (*Figure 4.50)*. C7UAD was fully resorbed by the 48 h time point. Continued degradation up to 96 h of C7U-500°-30 and C7U-500°-120, followed similar degradation profiles, degrading at rates of (0.7 and 0.8) x 10^{-4} mg mm^{-2} h^{-1} (*Figure 4.50A*). Linear regression r^2 values ranging from 0.92-0.99 supported a linear correlation for C7UAD to C7U-550°-30, however an r^2 value for C7U-610°-30 of 0.34 showed a poor linear fit due to stabilisation of dissolution by 12 h. Degradation of C7U-550°-30 and C7U-610°-30 were continued up to 28 d. C7U-550°-30 was entirely degraded by 7 d whilst C7U-610°-30 stabilised by 21 d. See *Table 4.17* for comparative dissolution rates.

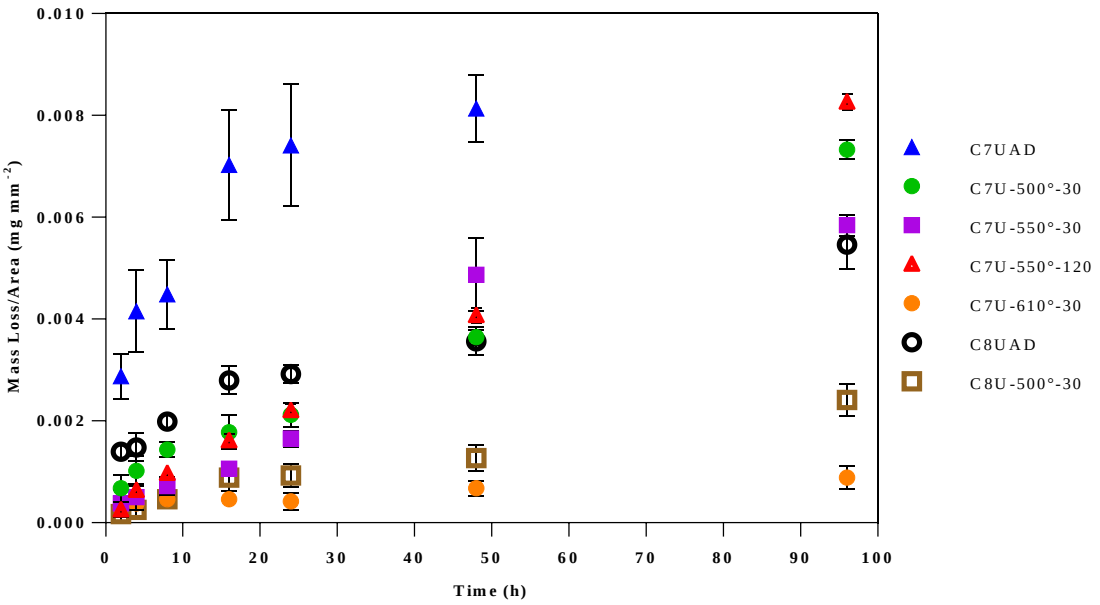

Figure 4.50: C7UAD/HT and C8UAD/HT. (A) Dissolution rates up to 96 h in dH_2O. Degradation rates have been calculated from 2-24 h and 2-96 h in Table 4.17 whilst the ion release profiles are presented in Figure 4.51 for C7UAD, C7U-500°-30 and C7U-500°-120.

Ion release rates were recorded for C7UAD, C7U-500°-30 and C7U-500°-120 (*Figure 4.51*). Linear Ion release profiles were observed for all coatings and ions of Na, P, Mg, Ca and Fe over the 48 h time period in ultra-pure water with the obvious exception of C7UAD which was fully resorbed between 24-48 h. Therefore ion release slopes were calculated from 2-24 h. r^2 values ranged from 0.85-0.89 with the

exception of C7U-500°-120 which had an outlier at 16 h for Na and an r^2 value of 0.72. For the three coatings the release rates ordered P > Na > Mg > Ca > Fe whilst the observed initial exponential solubility in the degradation profile for C7UAD was reflected by the initial surge of ions released by the 2 h time point (*Figure 4.50B*). Ion release rates ranged from 0.39 – 0.05 ppm h^{-1}, 0.10 - 0.02 ppm h^{-1} and 0.10 - 0.02 ppm h^{-1} for C7UAD, C7U-500°-30 and C7U-500°-120. Heat treatment led to a reduction in ion release rates by factors of (4.0, 3.6)-Na (4.1, 4.3)-Mg (3.7, 3.9)-P (3.0, 3.4)-Ca and (7.7, 5.4)-Fe for C7U-500°-30 and C7U-500°-120 respectively. See *Table 4.17* for comparative ion release rates.

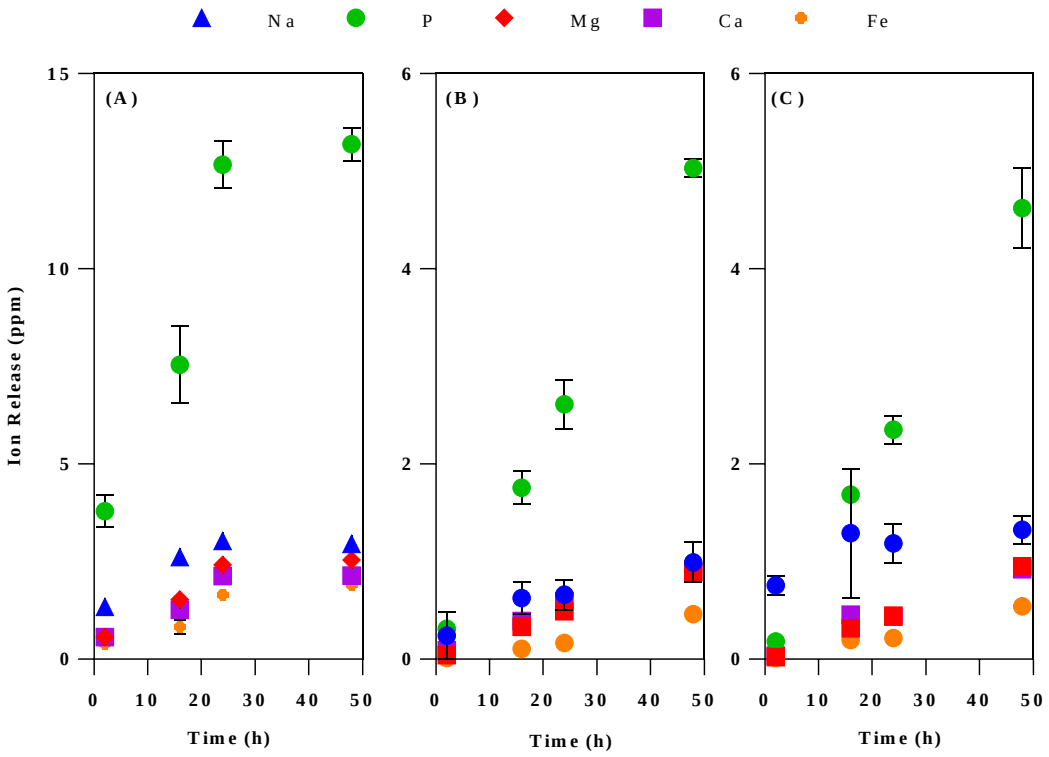

Figure 4.51: Ion release profiles following dissolution in ultra-pure water up to 48 h (A) C7UAD (B) C7U-500°-30 and (C) C7U-550°-120.

Table 4.17: Dissolution and ion release rates in distilled and ultra-pure water respectively. Dissolution rates were calculated between 2-24 h and 2-96 h whilst ion release rates were calculated between 2-24 h for C7UAD, C7U-500°-30 and C7U-500°-120. Ion release however was continued to the 48 h time point in Figure 4.51.

	2 h	2-24 h	2-96 h	Ion release (PPM/h) (r^2) 2-24 h				
	x 10^{-4} mg mm^2	(x 10^{-4} mg mm^2 h^{-1}) (r^2)		Na	Mg	P	Ca	Fe
C7UAD	28.88 ± 4.42	2.05 ± 0.35 (0.92)	Fully degraded by 48 h	0.08 ± 0.01 (0.98)	0.08 ± 0.01 (0.98)	0.39 ± 0.1 (0.94)	0.07 ± 0.02 (0.95)	0.05 ± 0.02 (0.89)
C7U-500°-30	6.78 ± 2.70	0.61 ± 0.10 (0.93)	0.68 ± 0.02 (0.99)	0.02 ± 0.01 (0.92)	0.02 ± 0.00 (0.99)	0.10 ± 0.00 (0.99)	0.02 ± 0.00 (0.99)	0.01 ± 0.00 (0.99)
C7U-500°-120	2.54 ± 0.60	0.85 ± 0.06 (0.99)	0.84 ± 0.01 (0.99)	0.02 ± 0.01 (0.72)	0.02 ± 0.00 (0.99)	0.10 ± 0.01 (0.99)	0.02 ± 0.01 (0.85)	0.01 ± 0.00 (0.92)
C7U-550°-30	3.81 ± 2.61	0.56 ± 0.09 (0.93)	0.63 ± 0.9 (0.99)	-	-	-	-	-
C7U-610°-30	2.97 ± 0.35	0.45 ± 0.04 (0.34)	0.06 ± 0.01 (0.93)	-	-	-	-	-
C8UAD	13.98 ± 1.20	0.76 ± 0.12 (0.93)	0.41 ± 0.04 (0.95)	-	-	-	-	-
C8U-500°-30	1.69 ± 0.69	0.37 ± 0.06 (0.93)	0.22 ± 0.02 (0.97)	-	-	-	-	-

4.5.7 SEM and AFM Microscopy

SEM micrographs of the coating surfaces pre and post heat treatments and pre and 16 h post degradation on both polished and sandblasted substrates have been presented in *Figure 4.52*. *Figure 4.52A,* C7UAD showed no notable surface features. Following heat treatment of C7U-500°-30 the coating colour became blue/violet (*Figure 4.52B* inset). (*Figure 4.52B, C* for C7U-500°-30 and C7U-500°-120 polished showed surface features, consistent with expansion and contraction of the surface layer during heating. Additionally bubbles were observed to be dispersed across the coating surfaces. An initial increase in surface roughness from AD to HT was supported by AFM measurements (*Figure 4.53)* for which 4 x 400 μm^2 regions were chosen for analysis. Roughness Ra values increased from (8 to 27 to 44 nm) for AD, C7U-500°-30 and C7U-500°-120 respectively for coatings on polished substrates.

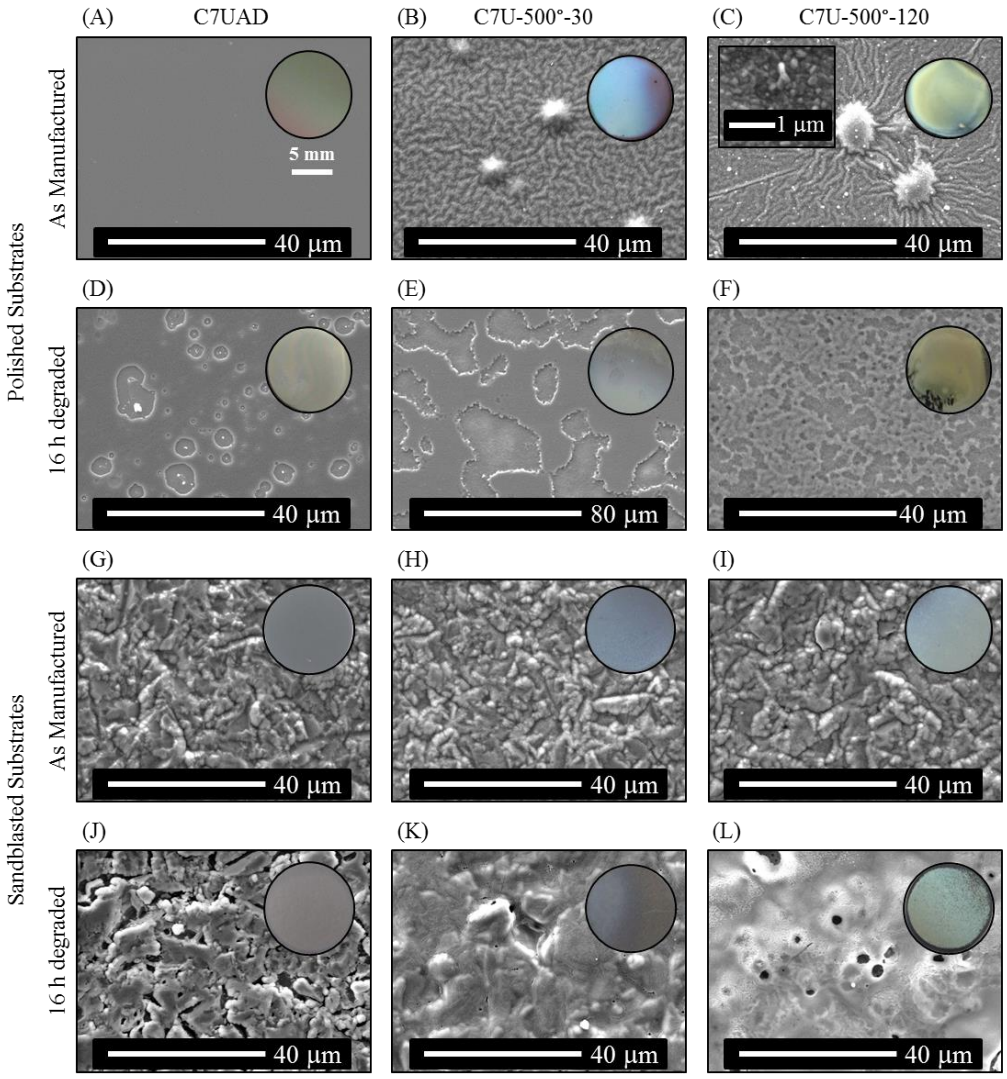

Figure 4.52: Micrographs of coating surface pre and post degradation of as manufactured on polished substrates (A)(B)(C) (C inset) Hematite crystal. On sand blasted substrates (G)(H)(I) and 16 h degradation on polished substrates (D)(E)(F) on sandblasted substrates (J)(K)(L) C7UAD, C7U-500°-30, C7U-500°-120 respectively.

In contrast coatings deposited onto sandblasted substrates showed remarkable surface changes or trends relating to Ra values of 519, 321, 485, 219 and 400 nm following C7UAD to C7U-610°-30 (*Figure 4.52G, H, I, M)*. Coatings on sandblasted substrates showed surface smoothing from the calculated substrate Ra value of 696 nm whilst a steady increase was observed for the polished substrates ranging from 7-44 nm. Notably, surface area analysis by AFM revealed that sandblasted substrates had an area of 18.5% greater than the projected 400 um^2, leading to a 17.7% increase in

surface area for C7UAD. Surface area alterations may have implications for dissolution (*Figure 4.53)*.

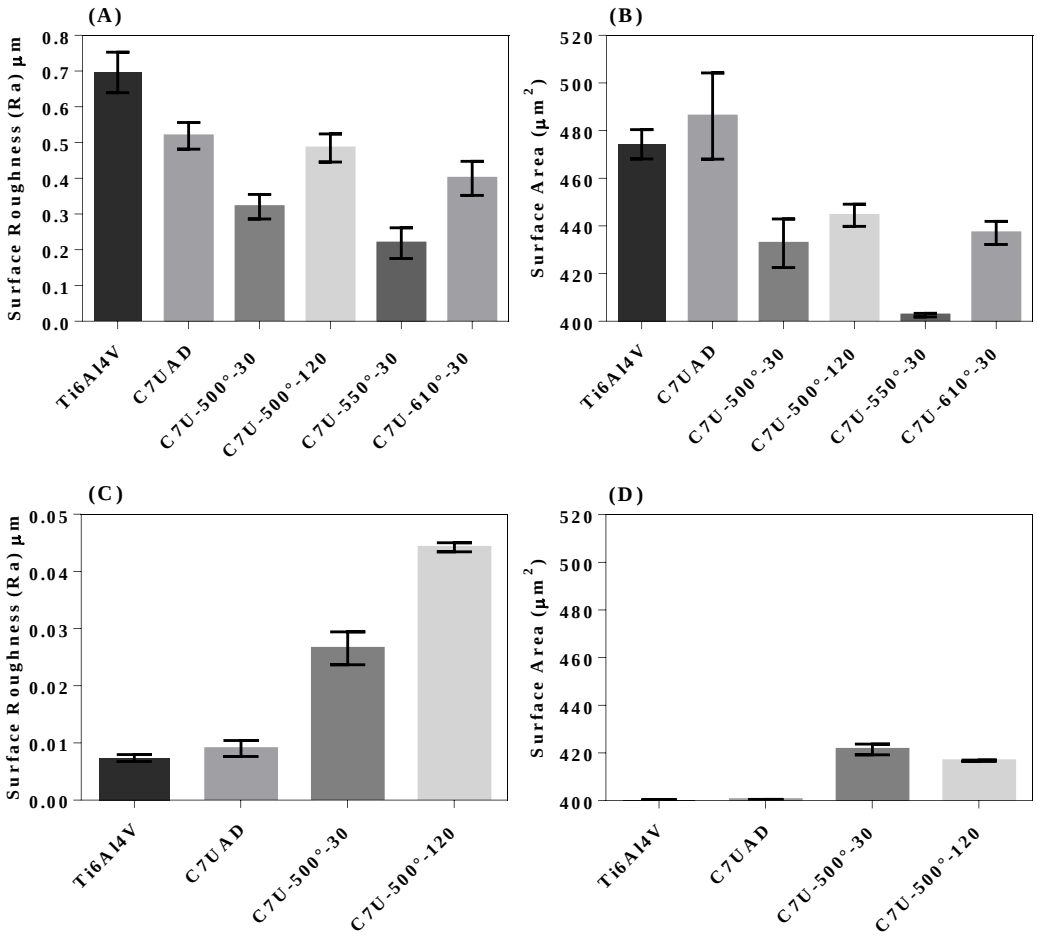

Figure 4.53: Surface roughness variations for AD and HT coatings on (A) Sandblasted and (C) Polished substrates. (B) and (D) Surface area. C7U-550°-30 and C7U-610°-30 on sandblasted substrates were also assessed.

Randomly dispersed degradation pits were formed across all coatings following 16 h in dH_2O on polished substrates and sandblasted C7UAD. The pits were visually observed by SEM (*Figure 4.52D, E, F, J, K, L)*. Pits formed in C7UAD were comparatively small in diameter and penetrated to the depth of the substrate as suggested in (*Figure 4.52D*). In contrast, degradation pits in C7U-500°-30 were interconnected and did not extend through the thickness of the coating by the 16 h time point (*Figure 4.52E).* Coatings on sandblasted substrates showed dissolution pitting following 16h for C7UAD whilst C7U-500°-30 and C7U-500°-120 showed morphological changes associated with uniform dissolution and smoothing of the

surface whilst degradation of C7U-500°-120 revealed holes formed beneath the surface (*Figure 4.52J, K, L*).

C7U-550°-30 contained similar bubble formations and apparent surface roughening. The entirety of the coating surface as shown in *Figure 4.54* formed either intact or fragmented bubbles. For C7U-550°-120 the coating layer appeared to arrange into columnar grains, characteristic of crystal formation. The formation of ordered granular structures with clearly defined grain boundaries was observed as the argon flow rate was increased from 0.6 to 3.0 l m^{-1}. Porosity can be seen specifically following C7U-550°-30, similar to the effect observed on polished samples. The coatings micrograph 28 d post degradation of C7U-610°-30 shows a remaining porous crystalline film.

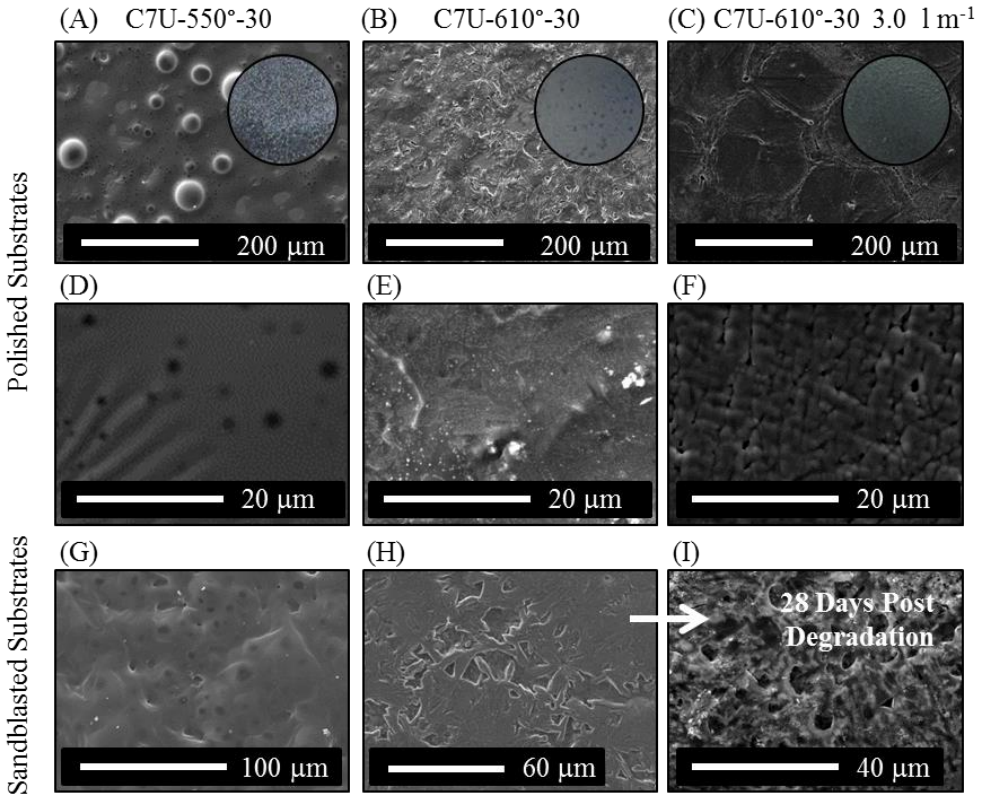

Figure 4.54: (A-F) HT Coatings on polished Ti6Al4V and subsequent SEM micrographs at 600x and 8000x. (G-I) HT coatings were additionally applied to coatings on sandblasted Ti6Al4V substrates for C7U-550°-30 *and* C7U-610°-30 *as shown.*

4.6 The Bioactive Potential of Sputtered Glass Coatings

The bioactive potential of five coating variations, produced within the UoN PVD and TEER UDP 650 PVD systems were assessed by submersion in SBF solution over a 28 d period. All samples for degradation were applied to sandblasted substrates. All tested coatings and deposition parameters have been presented in *Table 4.18*. The composition C7U: P40 Fe4 was assessed in depth using three samples at each time point to observe if a relatively thick PBG coating (2.67 μm) would lead to apatite growth over a 28 d time period. The compositions C8U: P31 Ti6, C8U-500°-30 and a SBG C6T: Si50 utilised a single sample at time points 3, 7, 14, 21 and 28 d. In addition uncoated Ti6Al4V and melt quenched BG 45S5 were cast into rods as controls.

The coating C8U: P31 Ti6 and its heat treated variation were produced and tested based on research by Kasuga *et al.* [57], who suggested that the formation of Ti-OH nucleation points facilitated the precipitation of apatite during the resorption of a melt quenched glass (see *Section 4.1 or 4.5*) for further details. C6T: Si50 was sputtered from the well-known bioactive formulation reflected in T2T: Si46, Bioglass 45S5.

Table 4.18: Prepared coatings for SBF Bioactivity testing and deposition parameters.

Coating Comp	Target Composition	Power (W)	Rig/Argon Pressure (Pa)	Time	Rotation and Distance	Coating Thickness (μm)
C7U: P40 Fe4	T6U: P51.5 Fe5	60	UoN/1.33	1165 min	Static/4 cm	2.67 ± 0.09
C8U: P31 Ti6	T7U: P50 Ti5	60	UoN/1.33	1165 min	Static/4 cm	1.04 ± 0.02
C8U-500°-30						
C5T: P40 Fe4	T1T: P57 Fe3	100	TEER/0.36	5580 h	5 RPM/4 cm	1.16 ± 0.02
C6T: Si50	T2T: Si46 (BG 45S5)	90	TEER/1.33	4200 h	5 RPM/4 cm	0.49 ± 0.01

4.6.1 Degradation in SBF

Only C7U: P40 Fe4 was assessed in triplicates given the sample numbers associated with analysis of all 5 compositions. C7U: P40 Fe4 coating degradation was stable by the first time point of 24 h in solution as shown in *Figure 4.55A*. pH changes over the 28 d showed a stable pH of ~7.40 up to 3 d followed by a steady decline to between 7.10 and 7.16 at 21 and 28 d respectively *Figure 4.55B*.

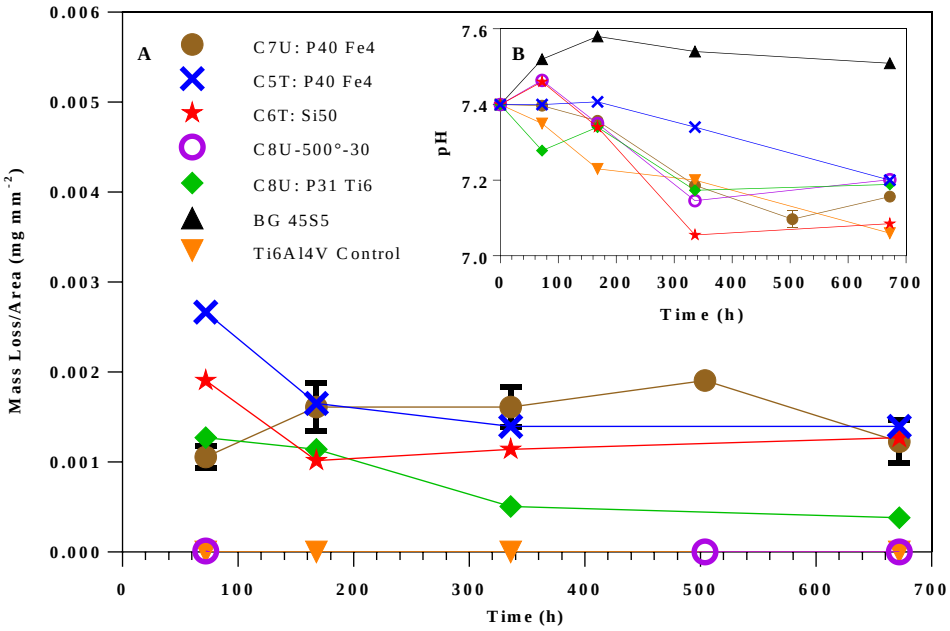

Figure 4.55: (A) Mass Loss and (B) pH measurements of SBF submersed samples over 28 d. All coatings demonstrated initial dissolution with the exception of C8U-500°-30. pH values declined whilst only BG 45S5 increased over the 28 d test period.

For C5T-C6T, C8U: P31 Ti6, C8U-500°-30: P31 Ti6, and the Ti6Al4V control sample, coating stability by assessment of mass loss and pH change (*Figure 4.55)* was observed within the first 3 d showing a maximum increase to 7.45. C8U: P31 Ti6 showed a decline in pH to 7.28. By 7 d all values for coatings had stabilised to 7.35. The PBG coatings solutions remained in accordance with the Ti6Al4V control over the 28 d test period indicating that pH changes were solution dependent over this period. By 14 d the C6T: Si50 solution reached a value of 7.06, remaining stable

within ± 0.02 over the 28 d period. MQ BG 45S5 exhibited contrasting behaviour as the pH of the solution rose to a maximum of 7.58 by 7 d, subsequently declining to 7.54, 7.51 and 7.22 by 14 and 28 d respectively. Mass loss results indicated no mass changes for the Ti6Al4V control or the glass ceramic C8U: P31 Ti6 apart from an apparent mass increase at 7 and 14 d. In combination with the EDX results it is apparent that all PBG coatings remained following 28 d of SBF submersion. Furthermore within ± 0.001 mg mm^{-2} no mass loss changes occurred for any coating composition between 4 and 28 d.

4.6.2 EDX

For C7U: P40 Fe4 the Ca:P ratio varied over the time period at 1, 3, and 28 d from 0.21 ± 0.01, 0.25 ± 0.01 and 0.27 ± 0.02 (*Table 4.19*). MQ BG 45S5 showed a considerable variation in the Ca:P ratio from 4.45:1 and 1.40:1 associated with possible calcium deficient apatite precipitation. Similarly this was observed for C6T: Si50 from 9.03:1 to 1.28:1 Ca:P ratios. Depending on the thickness of the precipitated layer, the signal from a remaining glass layer beneath may have influenced the measured Ca:P ratios as electrons penetrate the layer (*Table 4.19*).

Table 4.19: Assessment of Ca:P ratio as deposited and 28 d post submersion for SBF immersed samples. A significant variation was observed for BG 45S5 and C6T: Si50 to suggest precipitation of apatite.

	As Deposited Ca:P (at%)	28 d SBF Submersion Ca:P (at%)
C7U: P40 Fe4	0.19 ± 0.02	0.27 ± 0.02
C8U: P31 Ti6	0.88 ± 0.03	0.97 ± 0.06
C8U-500°-30	0.88 ± 0.03	0.81 ± 0.07
C5T: P40 Fe4	0.21 ± 0.01	0.27 ± 0.02
C6T: Si50	9.03 ± 0.03	1.28 ± 0.05
BG 45S5	4.45 ± 0.01	1.40 ± 0.37

4.6.3 XRD

All as deposited coatings and MQ BG 45S5 were found to remain amorphous during production. The heat-treated C8U-500°-30: P31 Ti6 was partially crystalline containing a phase attributed to β-$Ca_2P_2O_7$, whilst an amorphous hump remained between 15 and 35 2θ (°) (see *Figure 4.16* and *Figure 4.43* for diffraction patterns). XRD results from 3-28 d submersion in SBF showed no indication of any crystalline growths on any of the 5 PBG or the PBG/Ceramic (not shown). The melt quenched BG 45S5 control exhibited peaks from 7 d onwards at 32.0° and 25.9 2θ (°), which may be attributed to ICDD-00-004-0697 Carbonate Apatite $Ca_{10}(PO_4CO_3OH)_6(OH)_2$ and ICDD-PDF-00-019-0272 Carbonate HA $Ca_{10}(PO_4)_3(CO_3)_3(OH)$. Peaks at 31.5 2θ (°) could also be attributed to ICDD-PDF-01-075-0306 Halite NaCl. No noticeable trends existed relating to variation in peak size. The coating C6T: Si50 may have contained crystals associated with Carbonate Apatite indicated by the peak at 31.5 2θ (°) however this also corresponded to the peak position for NaCl.

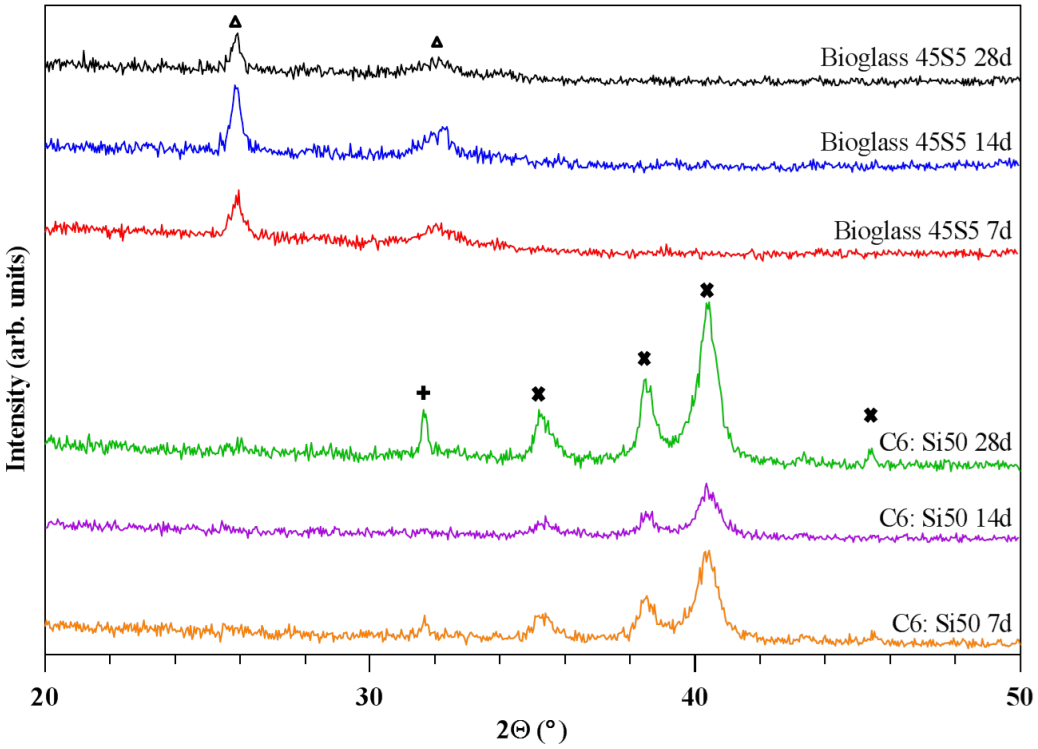

Figure 4.56: Post submersion BG 45S5 control and C6T: Si50 coating up to 28 d. Bragg peaks at 25.9 and 32.0 2θ (°) for Bioglass may be associated with (▲) ICDD-PDF 00-004-0697 Carbonate Apatite $Ca_{10}(PO_4CO_3OH)_6(OH)_2$ and ICDD-PDF-00-019-0272 Carbonate HA $Ca_{10}(PO_4)_3(CO_3)_3(OH)$. (✚) Halite NaCl ICDD-PDF-01-075-0306. (✖) Titanium Ti ICDD-PDF-00-001-1197. C6T: Si50 showed no significant diffraction associated with apatite formation.

4.6.4 FTIR

No signs of structural changes via FTIR were observed for any of the PBG or PBG/Ceramic compositions over the 28 d SBF submersion period when comparing pre and post submersion IR (not shown). However it is clear that all coatings remained post dissolution as shown by EDX (*Table 4.19*).

From the IR analysis C6T: Si50 and MQ BG 45S5 pre degradation showed IR peaks between 500-540 cm^{-1}, and broad absorption at 955 and 1055 cm^{-1} which were associated with Si-O-Si bonding (*Figure 4.57*) [178]. The proximity of the peak positions may have inhibited definitive analysis whilst positions of the phosphate bonds were overlapped by silicate bonds to prevent analysis of the phosphates in the sample.

Following submersion in SBF, by 3 d, emerging IR absorption peaks were associated with CHA formation, whilst no noticeable changes existed up to 28 d. In support of CO_3, peaks were found at 680 and 1430 cm^{-1} indicating formation of CHA [238]. The peaks associated with Si-O-Si absorption at 955 and 1045 cm^{-1} disappeared following submersion of both the MQ BG 45S5 and C6T: Si50 sample which is supportive of a precipitation and dissolution of the soluble silicate structure. A band positioned at 816 cm^{-1} associated with the potential formation of a silica gel could not be identified [178]. No hydroxyl groups were observed for any samples between 3000-3500 cm^{-1} (not shown).

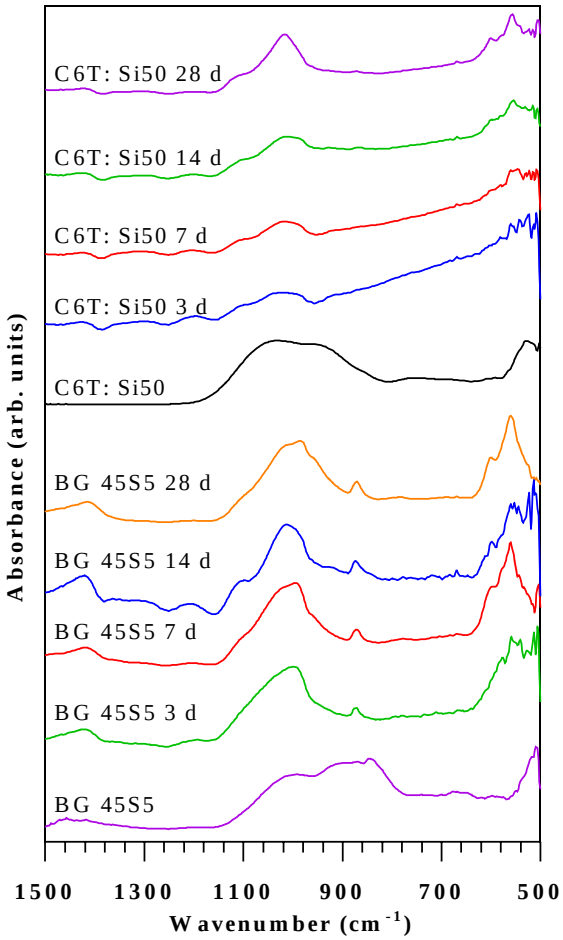

Wave-number cm^{-1}	IR Vibrational Mode
500	PO_4 O-P-O bending [239, 240]
570	Si-O-Si rocking [174] P-O symmetric bending [172, 174, 221]
610	$P-O^-$ asymmetric bending [221]
680	$C-O^-$ stretching vibration [221]
900	HPO_4 [174] $Si-O^-$ stretching vibration (Q^1) [239]
955	$Si-O^-$ stretching vibration (Q^2) [239]
1000	Si-O-Si asymmetric stretching [221]
1020	PO_4 symmetric stretching [221] and SiO_4 (Q^3 and Q^2) [174]
1045	Si-O-Si (Q^3, Q^4) combined with $P-O^-$ asymmetric stretching [174], [239]
1120	$Si-O^-$ stretching (pure silica) [174]
1430	$C-O^-$ bending vibration [221] $(CO_3)^{2-}$ asymmetric stretching [174], [172]

Figure 4.57: IR spectra of precipitated apatite from the BG 45S5 control and C6T: Si50 coating over the 28 d period. (Table) IR absorption modes for C6T: Si50 and MQ: BG 45S5 submerged in SBF for up to 28 d.

4.6.5 XPS

For C7U: P40 Fe4 only XPS O 1s and P 2p peaks were deconvoluted at all time points 1, 3, 7, 14, 21 and 28 d (*Table 4.20*). The percentage of bridging and non-bridging oxygens have been presented in the table below whilst a shift of the P 2p following 1 d in solution suggested a breakdown of the phosphate network to Q^0 and Q^1 ortho and pyro phosphates which remained as such until 28 d (*Table 4.20*). Surface compositional analysis at each time point showed a variation from the as deposited samples consistent with a cleavage of cations by 1 d. The ratio of NBO to BO also increased suggesting structural breakdown, which appeared to stabilise by day 3.

Table 4.20: Surface compositional variation of C7U: P40 Fe4 following submersion in SBF from 1-28 d. The ratio of BO to NBO was quantified whilst the majority Q structure was assessed. Orthophosphate $(PO_4)^{3-}$, Pyrophosphate $(P_2O_7)^{4-}$, Metaphosphate $(PO_3)^-$, (Q^0, Q^1 and Q^2 respectively) [48, 222, 223].

	Peak	AD at%	1 d at%	3 d at%	7 d at%	14 d at%	21 d at%	28 d at%
Na	Na 1s	14.6	2.0	1.6	2.2	1.2	1.7	1.3
P	P 2p	15.7	18.5	18.2	17.7	17.0	16.8	17.7
Ca	Ca 2p	4.1	11.4	12.5	10.9	12.5	11.5	12.4
Fe	Fe 2p	6.0	2.1	2.4	2.4	2.4	3.8	2.9
Mg	Mg 2s	1.2	0.9	0.8	1.3	1.4	1.2	0.9
O	O 1s	58.5	65.0	64.4	65.6	65.5	65.0	64.8
PO^- and P=O %*	-	-	75.6	78.7	80.5	80.0	82.0	82.0
P-O-P %*	-	-	24.4	21.3	19.5	20.0	20.0	20.0
P $2p_{3/2}$ (eV)	-	134.3	133.7	133.5	133.4	133.6	133.5	133.4
Majority Q^n Distribution	Q^2		Q^0 and Q^1					

* Normalised O 1s following subtraction of the overlapping Na KLL

4.6.6 SEM Microscopy

SEM imaging showed no surface changes associated with degradation of any of the PBG compositions over the 28 d time period (not shown). Apatite growth features were observed on the SBG C6T: Si50 (*Figure 4.58A, B, C)*, appearing by the first time point of 3 d in SBF (not shown) however, the 7, 14 and 28 d samples were electron mapped over areas of approx. 1.5, 5.0 and 3.0 mm^2 respectively (*Figure 4.58A, B, C inserts*) which showed incomplete coverage of developing apatite over the substrate disc. The areas of precipitation appeared to be oxygen rich. A BG 45S5 control was used and similarly displayed the formation of apatite for comparative purposes as shown in *Figure 4.58E,* 28 d post submersion in SBF.

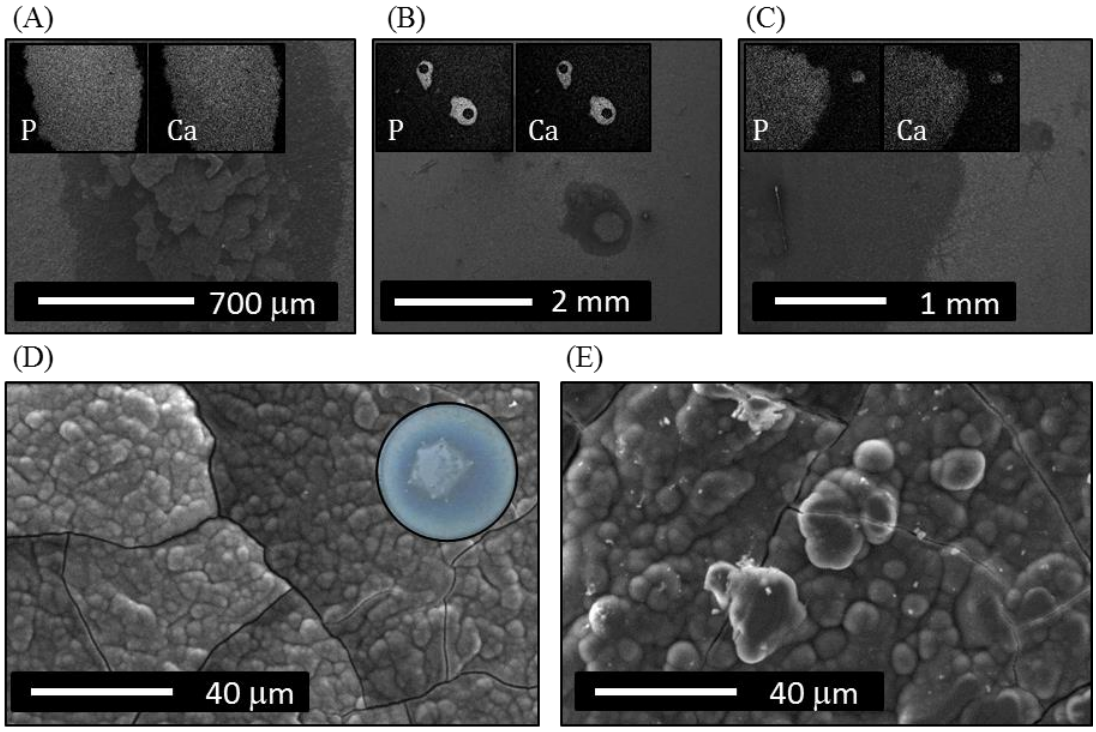

Figure 4.58: Elemental mapping of C6T: Si50 following (A) 7, (B) 14 and (C) 28 d in SBF. 28 d submerged (D) Apatite formation on C6T: Si50 (D insert) Photograph of the entire substrate surface (E) Apatite formed on MQ BG 45S5 Control.

5. Discussion

Thin-film deposition via RFMS of bio-materials such as SBG and Ca:P ceramics, notably HA have been shown to display *in vitro* and *in vivo* potential as orthopaedic coatings for soft and hard tissue repair [161, 172]. The current industrial standard utilises plasma sprayed HA, a relatively thick (>50 μm) inhomogeneous layer produced via a thermal splat method [15]. The commercial barrier is the long term clinical success of plasma sprayed HA coatings, which have been largely unchanged since the 1980's.

The hydration and hydrolysis reaction of the phosphate group enables a PBG to fully resorb in aqueous environments such as biological media, making them ideal for the delivery of therapeutic ions to the bone remodelling site. Although glass fibres have been used for composite reinforcement, the inherent brittleness of glasses restricts their use in the matrix of load bearing applications, therefore their application as a coating onto load bearing implants, enables their usage at such sites.

PBGs are amorphous, covalently bound solids, composed of a polymeric like backbone of phosphate tetrahedral PO_4 units. The inclusion of ionic species may alter the polymerisation of the network via ionic cross linking [36, 45]. The flexibility in producing controlled compositions of PBG would enable the customisation of bioactive glass coatings to accommodate for specific bone defects relevant to individual patients; a stratified approach to implant design. For example, the inclusion and subsequent release of strontium or copper may treat osteoporosis or stimulate angiogenesis [42]. Research into melt quenched PBGs has shown them to be compositionally and structurally tailorable, to control the release of a potentially vast range of ionically bound elements.

Whilst magnetron sputtering remains a wide spread technique for coating of electrical components and tooling applications [241], its usage for production of PBG in particular, has been scarce and is novel in the work presented here. Deposition of Ca:P glasses in literature is limited to amorphous deposition for the subsequent production of crystalline HA [143] whilst SBG coatings have been produced for biomineralisation of HA during dissolution [172]. Therefore the presented discussion will focus on the challenges of utilising the magnetron sputtering process for the application of customised PBG coating compositions on to implant materials.

The work discussed here commences in *Section 5.1* with the production of the melt quenched PBG formulations shaped as discs with diameter of either 75 or 57 mm, which are used for the coating process and are referred to as "targets". This is followed by the subsequent experimental deposition of coatings to formulate desired compositions and microstructures of thin films onto suitable substrates.

In *Section 5.2* a structural comparison between compositionally equivalent bulk melt quenched compositions and the novel vapour deposited coatings was made to observe potential variability due to processing.

In *Section 5.3* PBGs were assessed with cross linking elements such as iron and titanium to observe dissolution rates and degradation mechanisms with a focus on their behaviours as compared to the well documented melt derived formulations.

In *Section 5.4* the effects of heat treatment of the coatings post deposition, investigating their durability and short-range surface structures are discussed with a focus on mechanical adhesion properties to Ti6Al4V.

In *Section 5.5* the *in vitro* bioactive potential of PBGs and a SBG for comparison will be evaluated with regards to apatite forming ability in Simulated Body Fluid.

5.1 Manufacturing and Processing of Glass Targets and Deposited Coatings

Initial experimentation was conducted to gain an understanding of the sputtering behaviour of melt quenched amorphous PBG glasses relating to differential sputtering yields and deposition rates from multicomponent targets under ion bombardment. The objective behind this work was to establish the potential to tailor the deposition parameters and target compositions to obtain and predict a desired coating composition.

The intended nominal MQ targets T1U-T9U and T1T-T2T were produced amorphous (*Figure 4.1*) and differed from their as prepared compositions as measured via EDX analysis (*Table 3.2* and *Table 4.1*) by a maximum of 2.1-SiO_2 2.7-P_2O_5 1.6-MgO 3.1-CaO 2.2-Na_2O 1.3-Fe_2O_3 1.4-TiO_2 0-CuO mol%. This variation in compositions was attributed to atmospheric moisture absorption from hydrophilic P_2O_5, EDX instrumental precision, measuring precision and purity of the precursors, stated in *Table 3.1*, ranging from >97% in the case of Magnesium phosphate dibasic trihydrate. P_2O_5 absorbs moisture from the air, increasing its apparent mass when the precursors are prepared. Similar variation was recorded by Ahmed *et al.* [108] during the manufacture of ternary CaO, Na_2O, P_2O_5 glasses in which variation between nominal and prepared glasses was between (0.0-1.0), (0.3-2.8) and (0.2-3.2) mol% respectively, as determined by EDX. Furthermore, repeated n=5 spot analysis showed variability in the EDX process, on C7U: P40 Fe4 showed that composition varied by up 0.11, 0.10, 0.11, 0.53 and 0.08 mol% for P_2O_5, CaO, Na_2O, Fe_2O_3 and MgO respectively.

The target T1U: P_2O_5-40 MgO-24 CaO-16 Na_2O-20 mol% was considered the least thermally stable of T1U-T7U targets (*Table 4.2*), therefore it was utilised to establish a processing window necessary to avoid thermal target damage.

The composition T1U: P40 was tested at sputtering deposition powers of 60, 80, 100, and 120 W (*Figure 4.3*), which showed a reduction in target integrity with increasing power. The thermal properties of the target, specifically T_g and T_c increased from (435-491 °C) and (585-725 °C) respectively for T1U-T6U, signifying improved target integrity and working temperatures. Target T1U: P40 fractured upon activating the plasma at powers of 20 W. *Figure 4.2* showed an increase to 90 °C within 240 s at 5.0 ± 0.5 mm above the target surface, suggesting that thermal shock may have led to expansion and cracking.

Furthermore a differential cooling gradient present within the target from the heat sink beneath the magnetron could have contributed to differential expansion. To mitigate the risk of cracking, deposition power may be slowly ramped upon start-up and shutdown to prevent thermal shock. However throughout the length of this project all target compositions from T1U-T9U cracked as continuous ion-erosion eventually induced crack propagation. An example of extensive erosion forming a racetrack was best observed for T6U: P51.5 Fe5; used over the course of this work (*Figure 3.2B*).

T6U: P51.5 Fe5 was however shown to temporarily resist cracking following a 20 h deposition at 60 W, eventually cracking during runs thereafter. A series of heat treatments were also trailed to induce the formation of crystals within the matrix, thereby successfully lowering the TEC to mitigate the effects of thermal shock. However target structural manipulation should be avoided to prevent inconsistencies in sputtering behaviour as our studies postulate that the coating formulations

deposited depend upon short-range structural arrangement in glasses resulting from the sputtering process.

The crystallisation of T1U: P40 was observed at a deposition power of 120 W, which may have been due to plasma induced heating (*Figure 4.3* and *Appendix 9, 3.0*). The crystallisation region radiated from the centre, suggesting that the thermal radiation of the plasma was the dominant cause for temperatures increase rather than the increased energy of ion bombardment (*Figure 4.3*). Otherwise, the target damage would have been more intense along the racetrack. Ion bombardment however will result in an additional local temperature increase as the surface and subsurface atoms are involved in collisions [242].

A maximum temperature of 350 °C was recorded at 5.0 ± 0.5 mm above the PBG target T1U: P40, at 120 W deposition power (see *Figure 4.2*) The thermocouple was not in contact with the target to maintain conductivity by preventing target grounding, therefore it is expected that the actual surface temperature of the target reached beyond the crystallisation onset temperature of 560 °C for T1U: P40 (*Table 4.2*). This was evident as the combined heating effects led to the crystallisation (*Figure 4.3* and *Figure 4.4*).

Levy investigated a fused silica target which was subjected to ion beam bombardment and described the occurrence of a thermal spike within the surface and subsurface layers [242]. It was suggested that the thermal spike occurred as inelastic exchange of kinetic energy caused power to be dissipated as heat [201]. Levy *et al.* reported temperatures of 700 °C on the surface, and 400 °C 1 mm below the surface of a 1 cm^2 area, bombarded by a 10 W ion beam [242]. This was an equivalent power density of 100,000 Wm^{-2} [242]. The subsequent temperature decrease when turning off the beam

was between 200-150 °C measured over a tenth of a second [242]. Whilst this example pertained to a densely focused beam the ability to cause significant heating through surface collisions is evident. The equivalent power density applied to the targets within our sputtering rig, at 100 W was 22,640 Wm^{-2}. This was 23% of the ion beam power applied by Levy [242] and was sufficient to heat the target to above 560 °C. The addition of argon ionisation leads to plasma induced radiation of the target to above the crystallisation temperature [243]. Furthermore, power density is most concentrated over the area of the racetrack which could cause a variable heating pattern over the target.

5.1.1 Power Effects during Coating Processing and Selection

Linear relationships between deposition power and deposition rates were observed for C1U: P28 at powers from 60-120 W and for C2U: P32 at test powers of 60, 70 and 80 W (*Figure 4.14* and *Figure 4.3*). An increase in potential by varying power leads to a proportional increase in kinetic energy of the argon atoms bombarding the target. Power was held constant at 60 W for comparative analysis between coatings produced from targets T1U-T6U. This choice is discussed in the following paragraphs.

Electron penetration of the coatings during EDX analysis resulted in X-ray scattering from the substrate layer (see *Figure 4.7)*. This was particularly observed for C1U: P28 at deposition powers ranging from 60-120 W, corresponding to thicknesses as low 273 nm as compared to 1370 nm. It was found that in films below ~1 μm this distortion was observed to cause uncertainty in compositional analysis when thin and thick films were compared (data not shown). When practical, coating characterisation was assessed at thicknesses >1 μm; preferred for accurate compositional measurements here forward.

Compositional analysis for C2U: P32 suggested that as deposition rates increased from powers of 60 to 80 W, P_2O_5 content of the coating decreased by 2.9 mol%. This same effect was similarly shown for C15U: P37 compared to C13U: P32.5 deposited at 60 and 80 W respectively showing a relative decrease in P_2O_5 from 37.3 to 33.0 mol% and for C7U: P40 Fe4 compared to C11U: P32 Fe5 deposited at 60 and 90 W; a variation from 40.2 to 31.5 mol%. This suggested that temperature variation may have led to compositional changes; an effect reported by Boyd *et al.* during the heat treatment of Ca:P thin films, explained by volatility of phosphorous with temperature [158]. XPS surface analysis of C1U: P28 deposited at 60-120 W, supported volatility of phosphorous as it was found to have reduced from 21.8 to 6.6 at% respectively. The assessment of surface structures by deconvolution of the O 1s and P 2p spectra showed a proportional shift towards Q^1 $(P_2O_7)^{4-}$ pyrophosphates and Q^0 $(PO_4)^{3-}$ orthophosphate surface species from Q^2 $(PO_3)^-$ metaphosphate as the ratio of P-O-P bridges to PO^- and P=O non bridging oxygens varied from 34.8% : 65.2% to 8.5% : 91.5% [48] (*Table 4.3* and *Figure 4.8*). This variation in P-O-P surface bonding is significant as during dissolution the increased polymerisation of (C7U-C12U) led to highly soluble surfaces (see *Section 4.4*) which may have deposited stable coatings with lower surface polymerisation (*Table 4.13*). Furthermore the positioning of the Na, Mg, Ca and P peaks were consistent with formation of metal oxides.

At 100 and 120 W, C1U: P28 began to show crystal formations rich in sodium on their surface. XRD showed phases associated with $NaTiPO_4$ suggesting diffusion of deposited coating into the Ti6Al4V substrate (*Figure 4.3*, *Figure 4.4* and *Figure 4.6*). Operating at power <100 W was shown to produce amorphous coating compositions throughout the length of this work (see *Figure 4.3* and *Figure 4.16*). Substrate

temperatures were measured for C1U: P28 from 82-139 °C via a thermocouple at the coating location, however additional bombardment energy involved in the atomic collisions seemingly enabled crystallisation as low as 100 W deposition.

As target crystallisation was not observed to occur <120 W and coatings crystallisation below <100 W, all depositions within the UoN PVD rig for the purpose of comparison were conducted at <100 W to prevent thermally induced structural target damage under ion bombardment, whilst 60 W was most commonly chosen to prevent pit formations due to etching which are discussed in *Section 4.3.2*. Interestingly studies of organic PVD glasses or amorphous polymers, such as indomethacin and ethylbenzene demonstrated *in situ* molecular relaxation. Singh *et al.* devised a theoretical model, to compare melt quenched and PVD glasses and suggested that relaxation of PVD glasses required substrate temperatures 65-95% of the T_g, whilst optimal deposition occurred at the theoretical Kauzmann temperature (K_t); the temperature at which variation in entropy between liquid and solid phase was zero at the same enthalpy. K_t is a theoretical impossibility; as the entropy of a liquid will always exceed that of a solid at equal enthalpy based on the third law of thermodynamics [79, 244]. Singh *et al.* approximated optimal deposition for relaxation as 80-85% of the T_g. The model assumed a binary Lennard-Jones mixture 80:20% in relative proportion, therefore variability in the behaviour of glass systems may be expected [79]. Kearns *et al.* similarly showed experimentally by DSC that for indomethacin the optimal deposition temperature was at 85% of the T_g [82]. At the substrate temperatures ranging 82-139 °C and corresponding to 60-120 W deposition during the production of C1U: P28, molecular freezing would be expected to lead to similarly high structural enthalpy observed from melt quenched glasses.

With the current UoN PVD rig design deposition substrates temperatures were limited to plasma and bombardment induced heating effects, which cannot be increased for deposition as it was shown to lead to both target and coating crystallisation. *In situ* annealing by utilising a substrate heater may prove useful to control substrate temperatures, thereby guiding the kinetics of the condensed glass structures. See *Section 5.4* for post deposition annealing.

5.1.2 Preferential Sputtering at Constant Pressure

Sputtering yields of the multicomponent targets are governed by both cascade effects from ion penetration and momentum transfer within the surface layers of the glass target [201, 202, 242]. As dictated by the phenomena of preferential sputtering, elements within the target will sputter at varied rates according to atomic properties such as mass, density, size and relative bonding strengths [201] (*Section 2.9*). Comparative results were obtained at constant instrumental parameters for the 11 coating compositions investigated (C1U-C6U at 1.05 Pa) from (T1U-T6U) and (C7U-C11U at 1.33 Pa). T1U-T6U represented incremental compositional changes and are thus most directly comparable. T1U: P40, T2U: P45 and T3U: P50 were trialled as the target control compositions prior to introducing Fe_2O_3. The addition of Fe oxide within PBGs (as in the compositions of T4U: P50 Fe2, T5U: P50 Fe4 and T6U: P51.5 Fe5) is known to improve their durability by orders of magnitude thereby reducing the dissolution rate in solution [59].

Figure 4.16 showed an amorphous structure for all the as deposited coatings at 60 W. The short range order associated with an amorphous structure leads to broad diffraction suggested by the amorphous hump which was observed between 15 and 35 2Θ (°) [40]. These results are consistent with those found in literature for amorphous glass structures [50]. *Table 4.4* showed the variation in composition by

EDX between the targets (T1U-T6U) and the coatings (C1U-C6U) in mol%. The results showed a reduction in P_2O_5 and Fe_2O_3 of between (10.3-15.2) and (0.2-0.6) mol% respectively, and an increase in MgO, CaO, Na_2O of (4.8-6.0), (0.1-3.8), (3.0-6.9) mol% respectively.

The sputtering yield of the alkali metals was greater than the sputtering yields for the network forming phosphate, implying preferential sputtering of the network modifier ions or volatility of phosphorous as previously discussed. Berbecaru *et al.* and Stan *et al.* reported similar results whilst sputtering from silicate glass targets, with notably lower sputtering yields for Si, and P, and higher sputtering yields for Na, Mg and Ca [171, 178]. The relative changes from target to coating were reported by Berbecaru *et al.* in at%, equivalent to SiO_2-(41.4-36.1), P_2O_5-(3.2-1.1), Na_2O-(4.6-8.2), MgO-(13.9-15.3), CaO-(36.9-39.3) mol% respectively at 0.4 Pa Argon [178]. Other examples of sputtering were from targets made from HA and other Ca:P ceramics with a distinct increase in Ca:P ratio when transferred from target to coating, again indicating reduced sputtering efficiency of the phosphorous. A theory presented by numerous authors pertains to differential atomic masses leading to extraction of lighter ions by the vacuum system [143, 149, 151]. Whilst this theory may have apparent support using a simple binary Ca:P structure containing only two elements this is not supported by the results presented by Stan *et al.* [170-173, 175] or the results presented here, in which additional ions added such as Na and Mg with respective masses of 22.99 g mol^{-1} and 24.31 g mol^{-1} consistently maintained greater sputtering yields than phosphorous with a higher mass of 30.97 g mol^{-1}.

As suggested by Boyd *et al.*, volatile phosphorous products are formed during target ion bombardment which are less efficiently transferred to the coating [158].

Phosphorous deficiency in the coating has additionally been explained by its inability to form stable bonds without enough oxygen, as oxygen is readily extracted with an atomic weight of 16.00 g mol^{-1} [145]. Although this concept has been presented in the literature, supporting evidence that ions are extensively extracted in the vacuum to cause preferential sputtering has not been verified. The use of mass spectroscopy to count the proportions of ions extracted by the vacuum may be used to definitively shed light on the suggested theory.

The Effect of Iron Oxide

Sputtering of T4U: P50 Fe2, T5U: P50 Fe4, and T6U: P51.5 Fe5 showed that Fe oxide appeared to have the lowest sputtering yield of the network modifier ions with variation between 0.2-0.6 Fe_2O_3 mol% (see *Table 4.4)*. Fe oxide can exist in the glass structure as both FeO and Fe_2O_3 [58, 109, 110, 245]. Whilst the proportions of each within the glass structure are unknown it has been quantified as Fe_2O_3 by assuming stoichiometric oxide formation from the EDX analysis. The XPS results in *Section 4.5.1* suggested that Fe, at the surface exists in numerous states of at least FeO and Fe_2O_3 for the vapour deposited composition C7U: P40 Fe4. The technique of Mossbauer spectroscopy may be useful for this quantification [58].

Iron oxide maintains the highest degree of cross linking and can have an oxidation state of 2 or 3 [58]. This corresponds to the dissociation energy or bond enthalpy required to break Fe (II) or Fe (III) -O-P bonds as 818.0 or 1227.0 kJ mol^{-1} respectively [246]. The coordination of the Fe atom has been investigated in ternary and binary PBGs [58, 109]. The coordination numbers for a range of PBG compositions, containing the elements, Fe, Na, Ca, Mg, P are presented in *Table 5.1* for comparative purposes [109, 111, 245]. It has been suggested that Fe can exist in the phosphate structure as a network-modifying (i.e cross-linking) ion or can be

present in the phosphate backbone acting as a glass network former. In either case Fe can be found in either octahedral or tetrahedral coordination. This cross linking between the phosphate chains or presence within the backbone is said to be responsible for the greatly improved durability such that certain compositions of binary Fe PBGs have exhibited durability 100 times greater than soda lime glass [58, 109] and have been investigated for nuclear waste disposal. Hoppe *et al.* reported the coordination of the P-O bonds within the PO_4 tetrahedra to be 4.0, distanced at 0.155 nm apart [109]. Distortion in glasses for 4 binary proportions (see *Table 5.1*), showed Fe (II) existing in pentahedral coordination rather than the tetra or octahedral. Fe (III) was entirely formed in the octahedral coordination. Fe (II)-O and Fe (III)-O maintained distances of 0.204-0.209 nm and 0.200 nm respectively [109]. In another study the Fe-O distance in Fe containing PBGs with 5, 10 and 15 mol% Fe_2O_3 were shown to be constant as 0.200, 0.198 and 0.199 nm for Fe (III) and 0.217, 0.218 and 0.218 nm for Fe (II) [245]. The constant bond length showed consistency irrespective of Fe proportion in the glass network and supported octahedral coordination. Fe-O-P (iron present in the glass structural backbone acting as a glass former) was coordinated at a distance of 0.324 nm in all three compositions tested [245]. Based on the evidence presented, Fe in the glass compositions T3U-T6U consists of either Fe (II) and Fe (III) bonding in octahedral and tetrahedral coordination with the possibility of distorted structures. The proportion of Fe, which exists in the phosphate backbone, is unknown, however its existence leads to much stronger bonding in the structure which may affect the relative sputtering yield [58, 109]. Consequently as observed in *Table 4.4* the relative transfer of iron from the targets to coatings was significantly lower than all alkali and network modifier ions of Na, Ca, and Mg, which are more weakly bound to the structure through monovalent in the case of Na,

or divalent ionic linkages for Ca and Mg, leading to an increased proportional sputtering yield.

The Effect of Titanium Oxide

Titanium in the precursor form of TiO_2 was incorporated into the structures of T7U: P50 Ti5 and T8U: P50 Ti7 Cu5. A similarly low transfer from target to coating was observed for titanium (*Table 4.4*), again attributed to forming Ti-O-P bonds within the backbone. In addition, Ti also greatly improves the durability of glass by functioning as a quad valent Ti^{4+} network cross linker which would similarly lead to higher dissociation energies to separate Ti from its ionic linkages during ion bombardment [56]. Tang *et al.* made a structural comparison between sol gel and melt quenched glasses of the composition 70-TiO_2 30-P_2O_5 showing Ti^{4+} octahedral coordination in sol gel derived glasses compared to 4, 5 and 6 coordination in melt quenched glasses [247]. Whilst Pickup *et al.* showed that the Ti site remained octahedral for MQ compositions [248].

The Effect of Alkali Oxides

Hoppe *et al.* conducted neutron and X-ray diffraction studies in a range of binary PBGs to determine the coordination numbers of the elements present, all with molar ratios of 1. The findings revealed coordination of 6.3, 7.0 and 5.0 for Mg/P, Ca/P and Na/P glasses respectively maintaining average distances of 0.253 nm in all glass compositions [111]. The coordination for the P-O bonding in various binary glasses was constant at 4.0 with bond distances between 0.154-0.165 nm. The constant relationship in the P-O bonding was attributed to the known tetrahedral structure, which has shown to remain constant irrespective of modifying content [109, 111]. Silicate in BG 45S5 has been found to have similar coordination of 4.0 with Si-O distances of 0.161 nm whilst Ca-O and Na-O varied with respect to coordination

however showed similar neighbouring distances of 0.229 and 0.239 respectively (*Table 5.1*) [249].

The coordination and relative locations of the constituent elements leads to loose interatomic forces such as van der Waal like bonding between neighbouring atoms. The greater bond distances of the modifier ions could weaken the attraction of the atoms within the structure, again contributing to the preferential sputtering effects observed with respect to Na, Mg and Ca (*Table 4.4*). Anders *et al.* investigated simple van der Waal bonded compounds observing increased sputtering yield based on reduced bonding strength and lower atomic masses [250].

Table 5.1: Coordination numbers in a range of PBG compositions.

System (mol%)	Bonding	Coordination Number	Neighbouring Distance (nm)	References:
20-FeO, 80-P_2O_5 30-FeO, 70-P_2O_5 50-FeO, 60-P_2O_5 50-FeO, 50-P_2O_5	P-O	4.0	0.155	[109]
	Fe (III)-O	6.0	0.200	
	Fe (II)-O	6.0	0.204-0.209	
5-Fe_2O_3, 47.5-Na_2O, 47.5-P_2O_5 10-Fe_2O_3, 45-Na_2O, 45-P_2O_5 15-Fe_2O_3, 42.5-Na_2O, 42.5-P_2O_5	P-O	4.0	0.154-0.165	[245]
	Fe (III)-O	6.0	0.200, 0.198 and 0.199	
	Fe (II)-O	6.0	0.217, 0.218 and 0.218	
	Fe-P	5.0	0.324	
50-MgO, 50-P_2O_5	Mg-O	6.3	0.253	[111]
50-CaO, 50-P_2O_5	Ca-O	7.0	0.253	
50-Na_2O, 50-P_2O_5	Na-O	5.0	0.253	
30-CaO, 15-Na_2O, 45-P_2O_5, 10-CuO	Cu-O	6.0	0.198	[251]
BG 45S5	Si-O	4.0	0.161	[249]
	Ca-O	2.3	0.229	
	Na-O	6.0	0.239	

Following the dissociation of the bonded ion by impinging argon atoms the remaining energy is transferred as kinetic energy to eject the particle toward the substrate. Observation of the comparative masses of the atoms within the glass structure for (C1U-C6U) shows Fe to have the highest mass of 55.85 g mol^{-1} (see *Table 5.2*). A combination of high dissociation energy and high atomic mass would lead to the lowest sputtering yield of the network modifying ions within the structure [250] as supported by the results in *Section 4.4* (*Table 4.4*) .

Dissociation Energies, Oxidation States and Atomic Properties

Table 5.2 (below) shows the relationship between dissociation energy, oxidation state, atomic properties (mass, density and radius) and sputtering yield. The dissociation energy increases with oxidation state, correlating to a reduced sputtering yield. Variations in bond strength will exist between elements of equal oxidation states as various interatomic forces exist in addition to charge to dictate the strength of the bond. The bonds for P-O-Fe(II), Ca or Mg have oxidation states of 2 and have dissociation energies of 818.0, 928.0, 788.0 kJ mol^{-1} respectively [246].

Table 5.2: Relative sputtering yields relative to atomic properties and atomic bonding. The ranking of sputtering yield from 1-5 and 1-7 for constant pressure of 1.05 and 1.33 Pa respectively and is based on the relative variation from target to coating in at% of each element derived from Table 4.4. Dissociation energies are based on the enthalpy required to break the bond in question.

Element	Atomic Mass (g mol^{-1})	Atomic Volume (cm^3 mol^{-1})	Atomic Density (g cm^{-3}) at 300 K	Oxidation State	Dissociation Energy Per Bond (kJ mol^{-1}) [246]	Dissociation Energy based on the Number of Bonds (kJ mol^{-1}) [246]	1.05 Pa	1.33 Pa
							Relative Sputtering Lowest = 1	
Si	28.09	12.06	2.33	Covalent	798.0	3192.0	-	-
P	30.97	17.00	1.82	Covalent	596.6	2983.0	1	1
Fe	55.85	7.10	7.87	2 or 3	409.0	818.0 or 1227.0	2	3
Ca	40.08	29.90	1.55	2	464.0	928.0	3	6
Mg	24.31	14.00	1.74	2	394.0	788.0	4	5
Na	22.99	23.70	0.97	1	257.0	257.0	5	7
Ti	47.87	10.64	4.50	4	662.0	2648.0	-	4
Cu	63.55	7.11	8.94	1 or 2	343.0	343.0 or 686.0	-	2

The results for targets T1U-T6U (*Table 4.4*) show sputtering yields for the network modifier ions in the order Na > Mg > Ca > Fe, matching the relative oxidation states of 1, 2, 2 and 2/3 and more precisely relative dissociation energies of 257.0, 788.0, 928.0, (818.0 and 1227.0) kJ mol^{-1}. (C7U-C11U) were not produced from comparable target compositions, however showed preferential sputtering in the order Na > Ca > Mg > Ti > Fe > Cu; a clear distinction between alkali and transition metals and relationship between atomic densities.

Notably the low sputtering efficiency of Cu contradicted the observed trend and may have been due to its high atomic mass of 63.6 g mol^{-1} (*Table 5.2*) leading to a reduction in sputtering velocity from target to substrate. Whilst sputtering is a momentum exchange process, kinetic energy exchanges will result in greater ejection velocities for lighter elements, of equal bond strengths [201, 202]. For example, the sputtering yield of Mg is higher than Ca due to Mg being 40% less in mass relative to Ca. Additionally the dissociation energy for Mg is 15% less than the dissociation energy for Ca, requiring less energy to break the bond [84, 246].

Berg *et al.* described the ballistic cascade that occurs in the surface and subsurface layers of a target material under ion bombardment. They described particles penetrating below the surface and rebounding, amplifying the sputtering yield of lighter elements. This theory related to the mass and density of the particles and implied that the sputtering yield was additionally a product of the surrounding elements [202].

Gibbsian segregation describes a situation in which alkali metals diffuse to the surface and subsurface layers of a glass during ion bombardment [206, 207]. The argon bombardment is suggested to induce particle energies of 2-3 orders greater than those induced by thermal energy. This implied that indirect chemical bonding was responsible for preferential sputtering as the target itself changed surface composition, becoming rich in alkali metals [205]. Segregation may occur as the alkalis are removed from the glass during the sputtering process, creating a negatively charged phosphate tetrahedron. The alkali metals diffuse to neutralise the charge at the surface, therefore shielding the phosphate from sputtering [206]. Sree Harsha *et al.* presented data to support the theory that sputtering yields are correlated to the

sublimation energy of the element of structure, specifically the energy required to convert from solid to gaseous state [201, 252]. For individual elements this correlation has been presented in (*Figure 2.24*, *Section 2.8*).

5.1.3 Preferential Sputtering with Variation in Pressure

Stan *et al.* observed changes in sputtering behaviour in bioactive silicate glasses as a function of varying gas pressure [170]. Their results showed varying stoichiometry with variations in pressure. Specifically, increasing argon gas pressures up to 0.45 Pa showed closer stoichiometry of the coating relative to the target [170]. Similar results have been obtained here for the PBGs investigated (*Figure 4.17*).

As the argon pressure increased, backscattering of ions increased in accordance with a reduction in the mean free path of the argon atoms [170, 171, 173, 201]. The velocities of the ejected target ions will be reduced or may be reflected as they travel to the substrate and collide with argon atoms in their path [170, 171, 173, 201]. Pressure variation was only varied for T6U: P51.5 Fe5. As the pressure increased, the number of backscattered ions also increased at a greater rate than the increase in the number of ejected particles leading to a plateau in deposition rate. *Figure 4.17B* showed that as the pressure approached 1.87 Pa the rate of change in deposition rate diminished. Deposition rates beyond 1.87 Pa were not examined, however, it is envisaged that the number of backscattered ions would eventually exceed the number of ions to reach the substrate and the deposition rate will decline. This is a known phenomenon in which the mean free path reduces with increasing pressure to a point at which the number of backscattered ions exceeds the number of ions to reach the substrate [201]. The lighter ions experience this the most as shown by the greatest reduction in mol% with pressure on the coating as observed in *Figure 4.17*.

Figure 4.18A and B showed surface features present within the coating deposited at the lowest tested pressure of 0.28 Pa, corresponding to the lowest deposition rate of 1.23 nm min^{-1}. With reduced pressure and deposition, the energy of bombardment was expected to be lower. These cylindrical features may have developed from insufficient diffusion of the condensing particles [253].

5.1.4 Preferential Sputtering in Oxygen/Argon Environment

As the elements condense on the substrate, they form within the oxide polyhedral structure. Elemental affinity towards oxygen may lead to variable sputtering yield [172]. *Figure 4.19* shows a clear variation in coating stoichiometry at 0, 20 and 80% argon whilst no trend was found.

An apparent increase in deposition rate existed with increasing argon content as observed in *Figure 4.19B*. The reduction in deposition rate with oxygen content may be due to lower ionisation density of argon leading to fewer atoms ejecting from the target as suggested by Stan *et al.* [172]. Argon has an atomic mass 39.95 g mol^{-1} compared to oxygen's atomic mass of 15.99 g mol^{-1} thus ionised oxygen atoms would have comparatively low kinetic energy and may not reach the substrate if the mean free path of the oxygen is disrupted. There may therefore be an oxygen deficiency causing atoms to bond at lower oxidation states [146, 172]. Potential build-up of oxygen atoms on the surface of the target by "target poisoning" may also contribute to unwanted surface reactions and a decline in deposition rate [172].

5.1.5 Coating Uniformity and Reproducibility

Magnetron sputtering enables film deposition which follows the topography of the substrate, leading to enhanced adhesion [186, 253]. Such adherence was observed via FIB-SEM interfacial observation of deposited phosphate glasses on Ti6Al4V

substrates (*Section 4.4.3)*. Coating thickness variation from C7U: P40 Fe4 was recognised from light interference fringe patterns as visible light reflected off the substrate and through the sample (*Figure 4.10*). Analysis of coatings C7U: P40 Fe4 showed a thickness variation of 12.0% and 13.4%, assessed by cross sectional observation and coating mass respectively (*Figure 4.9*). Uneven vapour distribution may be expected as ion bombardment of the target varies relative to the configuration of the induced magnetic field. This variability causes an erosion racetrack to form in the target as shown in (*Figure 3.2B*). Incident ions condensing as a coating may unevenly distribute over the substrate area leading to variation in thickness and potential distribution in composition. To minimise variation the samples should ideally be rotated uniformly with respect to the plasma to maintain locational consistency between substrates and target [254]. The capabilities of the UoN PVD design do not allow for sample rotation, however in contrast it was shown (via the UDP 650) that variation in thickness over three independent batches was <1% whilst maximum variation over the sample varied by <2% . Furthermore, compositional variation particularly occurred in the TEER UDP 650 when comparing static and rotated substrates and confirmed that preferential sputtering effects may be locationally dependent such that distribution of elements varies in relation to plasma/target location. Whitacre *et al.* found that during static deposition of $LiCoO_2$ films, deposition thickness varied from ~140 to 225 nm and Li/Co ratio varied from 0.75 to 0.96 ± 0.1 over a 51 mm substrate distance. They attributed this to the variability in number of collisions resulting from mean free path, as the distance from target to substrate is not constant at each location. For substrates in rocking motion, thickness and atomic ratios were constant over the substrate area [254]. This finding suggests that during scale up of large-scale substrates such as hip stems, coating

compositions will be dependent upon the ability to uniformly maintain sputtering location with respect to the target by dynamic rotation.

Static deposition in the UDP 650 produced coating pinholes, which were eliminated during rotation. This improvement may have been due to superior adatom diffusion as deposition rates decreased and the prevention of atomic shadowing by varying the direction of deposition via sample rotation. Vick *et al.* similarly showed that by situating substrates at oblique angles to the target, atomic shadowing could be controlled [255].

The collected data highlights the potential for uniform coating distribution, improved via sample rotation to maintain consistency between substrate and target location. Regardless of this improvement, batch to batch reproducibility and compositional uniformity is superior with respect to melt quenching. Variation in melt quenched compositions was previously discussed in *Section 5.1* during the assessment of targets.

5.1.6 Summary

Multiple mechanisms affecting the transfer of a target material to its eventual deposition onto a coating have been discussed. The interactions are complex; beginning with the ionisation of the working gas, which itself can collide with transferring atoms to inhibit direct stoichiometric transfer. Once ionised argon particles begin to bombard the surface and subsurface layers, the bonding properties of that target inhibit elastic separation of ions from the target. The ability to separate modifying ions from the phosphate tetrahedral appears to be closely related to dissociation energies; however the imparting velocity of the atom will depend upon momentum transfer and therefore will be reduced at greater atomic masses. The counteracting forces culminating in the condensation of the coating layer will

inevitably lead to the non-stoichiometric transfer of atoms from the target to the coating layer. Transfer of atoms may be controllable via alteration of the working parameters, notably pressure, deposition energy and working gas.

Based on the observed reactions relating target integrity, deposition power and working atmosphere on preferential sputtering, deposition should be optimised to obtain a maximum deposition rate and coating diffusion at working pressures with the most efficient stoichiometric elemental transfer. To minimise effects of additional variables it is recommended that deposition occur in 99.99% argon and at powers approaching the thermal limit of the target under bombardment. Rotation of the samples with respect to the cathode is advised for coating reproducibility. Understanding and manipulation of the discussed forces could enable future processing to specifically tailor the formulation of the coatings deposited on the substrates, potentially enabling bioactive/fully resorbable glass coatings for improved osseointegration.

5.2 Structural Variance in Melt Quenched and Magnetron Sputtered PBG Films

In the previous section sputtering behaviour was assessed with regards to PBG composition and structure to control elemental composition of the PBG PVD coatings deposited. The next important question was whether compositional equivalence within deposited glass coatings compared with the MQ glasses would affect structure. If both the MQ and deposited coatings were similar, then the wide range of literature pertaining to structure, thermal characteristics, dissolution and bio-behaviour of countless formulations of MQ glasses could be applied to novel vapour condensed compositions of glasses. The complimentary techniques of XRD, FTIR, XPS and NMR, were used to compare the structures of three RFMS coatings and three MQ glasses. Thermal analyses by DTA and density measurements by helium pycnometry were assessed. Coating topographical features analysed by AFM were observed to vary with deposition parameters. The combined results suggested structural variability of glasses from the MQ and RFMS processing routes during the production of PBGs.

5.2.1 Coating Homogeneity and Topographical Analysis

(C13U-C15U) (*Table 4.6*) were deposited over a period of 160 h to obtain sufficient coating for ^{31}P-NMR and DTA. The deposition by RFMS generally produces coatings, which adhere to the macro-topographical features of their substrates as supported in *Figure 4.22A*. This was also observed for coatings of C7U: P40 Fe4 on sandblasted Ti6Al4V substrates by FIB-SEM cross section (*Figure 4.38*). Additionally, the atom-by-atom condensation forms structures, which demonstrate phase purity when compared to thermal splat methods [2, 144]. The EDX elemental mapping (see *Figure 4.22B-F*) showed homogenous composition throughout the cross sections of the coatings; this however was limited by the spatial resolution due to beam broadening of the EDX-SEM method, limited to ~1 μm, dependent on both

beam voltage and sample density [256]. However, such features represent improved processing precision by RFMS in contrast to conventionally plasma sprayed coatings, which exhibit lamellar crystal growth and discontinuities within the coatings due to the high temperature splat methodology during which the ejected powders can reach temperatures in excess of 2000 °C [2, 15, 21].

The topographical features of as deposited coatings varied as random distributions of pits on the coating layer surfaces were observed which resembled etching pits for C13U: P32.5, C14U: P34 and C15U: P37 *(see Figure 4.24)*. From the cross-sectional images the features appeared to be isolated to the surface (*Figure 4.23D and E*). AFM imaging (*Figure 4.24*) provided analysis of the topographical surface features. The pits grew in size as deposition power increased from 60 to 80 W, leading to a relative increases in roughness, maximum pit diameter and pit depths of (18.7 to 167.4 nm), (1240.0 to 10189.0 nm) and (228.4 to 865.5) respectively (*Figure 4.24*).

Various authors have reported the topographical matching of as deposited RFMS coatings with their substrates, whilst others show significant smoothing or roughening [201, 253, 257]. Rode *et al.* found that Al sputtered films had variable roughness's of between 0.6 and 99.6 nm by altering working pressure, and deposition powers to vary deposition rate from 0.3 to 7.7 nm s^{-1}, thus producing deposition temperatures of between 54 °C and 223 °C. Optimisation of the substrate temperature by parameter control suggested that the lower working temperatures produced the smoothest films whilst increasing pressure, deposition rate and power led to roughened samples [257]. In contrast Zhao *et al.* sputtered Alumina thin films and found that films deposited at higher power were dense and smooth which may have been attributed to bombardment by secondary electrons or negatively charged particles heating the substrate and improving diffusion through kinetic energy exchanges [253]. This could

also result from isotropic grain growth due to increased energy. Sree Harsha *et al.* emphasised the occurrence of surface roughening and void formation due to atomic shadowing from layered growth of the adatom. In order to prevent surface roughening, the diffusion of the adatom must be equal or greater than the rate of void formation such that at high deposition rates, increasing to, or exceeding a critical temperature can control the roughness via adequate diffusion of the adatom. For amorphous film formation the diffusion should be kept considerably low as shown here and presented in literature [201]. Momentum of bombarding particles varied depending on gas pressure, power and temperature; therefore the morphology of the condensed films remains a compromise. Further increasing temperature and power of the deposition may improve atomic diffusion of the coating until nucleation and crystallisation occurs. Alternatively as suggested previously this could be improved by *in situ* annealing [201]. The Thornton model is often used to assess the temperature: microstructure relationship during which argon pressure, substrate and target melting temperatures are assessed to predict adatom diffusion. Whilst the model pertains to metallic targets by evaporation methods, a similar regime may be assessed in future work to incorporate bombardment energies [258].

The range of topographical behaviour observed has been attributed to the interrelating processing factors of surface etching and diffusion of the adatom. The increase in deposition power may lead to surface diffusion and therefore smoothing however the third factor of ion etching may additionally cause pitting, of intensity relative to the momentum of the incoming particles. Surface etching could occur as atoms condense onto the substrate, to either diffuse efficiently into the growing layer or to bombard the coating surface. The observed increase in pit size as deposition power was varied

from 60-80 W indicated that surface etching might have been the overriding factor influencing the surface topography of the coating layers.

Careful consideration of deposition parameters should be undertaken to deposit at maximum deposition rates whilst optimising adatom diffusion, to avoid void formations or to prevent surface etching. Notably deposition at 1.60 Pa and 60 compared to 80 W resulted in an 80% increase in deposition rates from 1.45 - 2.61 nm min^{-1} however the pits depths and diameters increased by 313% and 722% respectively highlighting the potential trade-off. Whilst such low deposition rates are undesirable for future scale up, *insitu* substrate heating or application of a substrate bias could enhance the mobility of condensing particles for adequate diffusion of the adatom.

5.2.2 Structural characterisation of RFMS coatings compared to MQ glasses

XRD *Figure 4.25* showed no significant distinction in the positioning of the amorphous hump or variation between melt quenched and coated glasses, suggesting similar short range diffraction resulting from the phosphate tetrahedral structure. When compared to previously shown coating diffraction patterns for thin coatings (*Figure 4.16*), diffraction humps were overriding features of all coatings as no substrate signal was present due to increased coating thickness ranging from 13.9 - 25.0 μm. FTIR, XPS, and ^{31}P NMR were utilised to investigate the distribution of Q^n species and structural polymerisation in the surface and bulk material respectively. n denotes the number of bridging oxygen's per PO_4 tetrahedral to determine the ratio of Q^0 (orthophosphates), Q^1 (pyrophosphates), Q^2 (metaphosphates) and Q^3 (ultraphosphates) [48]. Coatings C13U: P32.5, C14U: P34, C15U: P37 were deposited below their T_g by PVD in vacuum conditions, whilst all MQG compositions were quenched from 1200 °C to room temperature in atmospheric

conditions. The shift in the $(P\text{-}O\text{-}P)_{asy}$ IR band to lower wavenumbers suggested that the PVD coatings produced may have longer bridging P-O-P bond lengths to their MQ counterparts. A longer P-O-P bonding is reflected by a reduction in vibrational frequency and therefore the IR shift observed (see *Figure 4.25*). Koo *et al.* postulated that greater field strength in more polymerised structures of MQ glass extends the P-O-P bond length which they observed, however did not quantify, following a shift in the Raman spectra after replacing Cu^{1+} with Cu^{2+} [75, 77].

The XPS (*Figure 4.26B P 2p*) implied the presence of PO_3 (Q^2) groups found in the coatings surface for which the P-O-P bonding was 34.7-35.1% in comparison to 11.1-17.0% for MQG (*Table 4.7*, *Figure 4.26A and B)*. MQG surfaces contained PO_4^{3-} (Q^0) and P_2O_7 (Q^1) sites (*Figure 4.26A)*, which were consistent with the relative lower percentage of P-O-P bonding. An increase in polymerisation (P-O-P bonding) in MQG as P_2O_5 content increased from P32.5 to P37 was observed, whilst in contrast, no such variations were seen for the PVD coatings. A possible presence of hydroxyl OH groups located between 532-534 eV may represent a contribution to the size of the P-O-P peaks [259]. This, whilst requiring mention was unlikely due to the production of thin-film coatings within an inert vacuum environment and the absence of hydroxyl groups in the IR spectra which was collected up to 4000 $cm^{-1.}$

The NMR spectra for all compositions (*Figure 4.27*) showed variable bulk structures of compositionally similar PVD coatings and MQG'. The data suggested increased polymerisation with an increase in P_2O_5 content from P32.5 to P37 mol%. The Q^n distributions of the MQGs found were generally in accordance with literature sources and followed the expected trends consistent with greater P_2O_5 content leading to polymerisation and Q^2 formation [48, 77]. Isotropic shifts ranged

from -0.9 to +2.5 ppm for Q^0, -9.7 to -7.9 ppm for Q^1 and -24.5 to -17.8 ppm for Q^2. These chemical shifts closely matched those found by Walter *et al*. who similarly reduced P_2O_5 content in MQ invert glasses to compare seven compositions ranging from (39.4-28.7) P_2O_5 (33.9-25.8)-CaO (26.1-20.7)-Na_2O (0.0-22.8)-MgO mol%. Their comparable compositions contained 32.7, 34.5 and 37.9 P_2O_5 mol%, which showed isotropic shifts ranging +4.0 ppm for Q^0, -6.4 to -6.5 ppm for Q^1 and -16.3 to -21.0 ppm for Q^2 [230]. During a study of sol-gel prepared quaternary Na/Ca/Ti/P glasses Foroutan *et al.* reported Q^0, Q^1 and Q^2 sites at -1.2 to -0.2 ppm, -10.3 to -10.0 ppm and -22.8 to -21.9 ppm, respectively [260].

NMR conducted by Ahmed *et al.* for ternary Ca/Na/P MQG showed that P45 compositions were made up of Q^1 and Q^2 species (20:80%) respectively whilst P50 and P55 compositions were almost entirely Q^2 species, indicating a near infinite polymer-like chain of PO_4 tetrahedra [66]. Walter *et al.* reported Q^2: Q^1: Q^0 ratios of (11.0: 87.0: 2.0), (17.0: 83.0: 0.0%), (43.0: 57.0: 0.0%) for P32.7, P34.5 and P37.9 MQGs respectively [230].

The NMR results here showed a significant presence of Q^0 (PO_4^{3-}) orthophosphates in PVD coatings whilst also showing that coatings were highly polymerised such that they contained 23.0, 30.9, 45.2% Q^2 species for C13U: P32.5, C14U: P34, C15: P37 compared with 8.6, 14.2, and 31.0 % for MQ1: P32.5, MQ2: P34, MQ3: P37 respectively. This variation could be attributed to the differences in melting/vaporisation and quenching/condensing temperatures and pressures. However the increase in Q^0 species at 80 W to 23.5% for C13U: P32.5 from 12.8% for C14U: P34 and 9.4% for C15U: P37 may additionally be the result of intensified surface etching by incoming particles, onto the deposited coating as shown previously by AFM [201].

DTA (*Figure 4.29*) revealed thermal properties supportive of glass formation in all coatings, specifically the presence of a distinct T_g for each composition, which showed further support for structural and compositional homogeneity. Variation in thermal traces between coatings and MQ glasses as T_g decreased (487.5-463.5 °C) vs. (507.6-477.2 °C) respectively from P32.5-P37, again suggested dissimilar structural properties for compositionally equivalent glasses. The observed processing windows, T_g - T_c onset dictates the suitable range for post-annealing [36, 39]. Notably this difference from P32.5 - P37 ranged 11.3 vs. 70.3 °C for coatings and MQ compositions respectively whilst the windows themselves ranged from 100.7-112.0 vs. 61.0-131.3 °C respectively suggesting the crystallisation tendency in coatings remained relatively consistent whilst process ability of in MQ compositions improved with increasing P_2O_5 content.

Walter *et al.* used NMR and DTA to conclude that the reduction in polymerisation by increased Q^0 and Q^1 components was coupled with increasing T_g and increasing durability. Additionally they showed that the less polymerised structures were denser, increasing from 2.67 to 2.80 g cm^{-3} composed of shorter P-O-P chain lengths as confirmed by neutron diffraction [230]. A similar relationship between polymerisation, T_g and P-O-P chain length, implied by IR, have been observed and suggested here as coatings maintained greater polymerisation, lower T_g and higher frequency of IR absorbance for P-O-P chains with respect to their equivalent MQ compositions.

Additionally density assessment for (C13U-C15U) vs. (MQ1-MQ3) by Helium Pycnometry conducted here in (*Table 4.8*) revealed ranges of 2.06-2.48 vs. 2.69-2.71 g cm^{-2} again supporting results by Walter *et al.* to suggest that

the less polymerised MQ glasses were also denser [230]. Ishii *et al.* investigated vapour deposited ethylbenzene at temperatures approaching the T_g showing that high molecular relaxation during deposition close to the T_g led to unconventionally dense glasses. In contrast low temperature deposition causes molecules to freeze upon condensation, leading to greater volumes and therefore the lower densities observed here [41].

5.2.3 Summary

The work presented here highlights a fundamental variation in thermal and structural properties of sputtered and melt quenched glasses. By consideration of each formation method it should be recognised that melt-quenched glasses undergo formation regimes far different to vapour condensation methods. Firstly due the inherent thickness of melt quenched composition a degree of structural reordering may occur as the cooling rate is limited by the glasses ability to dissipate heat in its environment. In contrast vapour condensation here occurred at rates 1-10 nm min^{-1}, which at low temperature would lead to instantaneous molecular freezing. However whilst not attempted, molecular mobility may be controlled by altering the substrate temperate close to the T_g as suggested by Singh *et al.* [79], thereby facilitating *in situ* relaxation. Vollmayr *et al.* suggested that a reduction in the cooling rate of glasses reduced their enthalpy and increased glass density; an effect associated with molecular relaxation [261]. Secondly, the sputtering process allows for a vast landscape of controllable vaporisation and condensation conditions, which has been shown to form conventional glass structures whilst significantly altering their specific properties compared to their melt quenched counterparts. Further in-depth structural assessment with varying deposition parameters may lead to a situation in which structural properties such as polymerisation, bond lengths and thermal properties could be

tailored, not by altering compositions, but by varying pressures, powers, or substrate temperatures in a similar way as shown for metallic crystal growth via the Thornton model [258].

PVD coatings, whilst compositionally tailored to match MQ glasses, cannot be directly compared due to variability in structure and internal enthalpy, resulting from the inherent differences in condensation regimes and environments, which are further complicated by continuous bombardment of incoming particles.

5.3 Degradation of Phosphate Glass Coatings

Resorbable PBGs can be tailored to deliver a controlled release of ions during dissolution [36, 62, 101]. This distinct advantage could potentially be extended to the production of thin-film coatings for orthopaedic implants [35, 38, 59, 60, 98, 100].

Previous analysis showed that PVD glasses are structurally unique with regards to polymerisation compared with MQ glass therefore comparison of degradation was performed. Two bulk formulations MQ4: P28 Fe6 and MQ5: P40 Fe4 (see *Table 5*) were prepared by melt quenching and compared to compositionally equivalent coatings produced by magnetron sputtering, using a single glass target deposited under varying parameters; T6U: P51.5 Fe5. EDX analyses confirmed that the compositions of the sputtered coatings C12U: P28 Fe6, C7U: P40 Fe4 were consistent with the bulk glass manufactured by melt quenching (MQ4: P28 Fe6 and MQ5: P40 Fe4) whilst XRD confirmed MQ5: P40 Fe4 and C7U: P40 Fe4 to be amorphous (see *Figure 4.30*). The FTIR results suggested structural similarities for MQ5: P40 Fe4 and C7U: P40 Fe4 containing similar IR absorption spectra (*Figure 4.31*). However, MQ4: P28 Fe6 and C12U: P28 Fe6 showed variable IR absorption behaviour which may have resulted from differences in microstructure due to crystallisation of MQ4: P28 Fe6 during the melt quenching process (*Figure 4.31*).

5.3.1 Glass Forming Limits

The ability to vary the production landscape by altering condensation energy through substrate heating allows for flexibility from instantaneous atomic freezing at lower temperatures to atomic mobility at temperatures near to the T_g [41]. Therefore structures which crystallise during melt quenching may be formed amorphous during vapour deposition.

Below a threshold limit of a network forming (P_2O_5 content), crystallisation may occur as seen in the case of MQ4: P28 Fe6, for which the melt could not be quenched fast enough to maintain its amorphous disordered structure [262]. In contrast the near instantaneous atom-by-atom condensation from magnetron sputtering to form a coating, enabled a glass/ceramic structure of C12U: P28 Fe6 composition to be formed containing two crystal phases which were attributed to FeO and $FePO_4$ (*Figure 4.30*). Ahmed *et al.* reported surface crystals of $CaMgP_2O_7$ during rapid quenching of P_2O_5-40 CaO-25 Na_2O-5, MgO-30 mol%, suggesting that the high divalent cation/phosphate ratio of 1.375 (or ratio of cross linking cations/phosphate = 2.75) was limiting the glass forming potential by conventional quenching for that glass system [50]. The calculated cross linking cation/phosphate ratio for the glasses produced here can be found in *Table 5.3*. MQ4: P28 Fe6 maintained a ratio of 4.00, considerably beyond the suggested glass-forming window, which led to crystallisation during melt quenching.

Table 5.3: Glass forming limits by cross-linking cation/phosphate ratios.

Composition (mol%)	Cross linking cation:phosphate ratio	Melt quenched structure
MQ4/C12U: P28 Mg27 Ca20 Na19 Fe6	4.00	Bulk crystallisation
MQ5/C7U: P40 Mg24 Ca16 Na16 Fe4	2.30	Amorphous
P40 Ca25 Na5 Mg30	2.75 [50]	Surface crystallisation

5.3.2 Compositionally Equivalent Coatings compared with Melt Quenched Glasses

The formed amorphous MQ5: P40 Fe4 rods were degraded in dH_2O over a period of 83 d (*Figure 4.32*). The coatings C12U: P28 Fe6 and C7U: P40 Fe4 were degraded until the entire coating was dissolved with most of the degradation occurring within 24 h (*Figure 4.34A*).

Bunker *et al.* showed degradation of PBGs to be highly pH dependent, with increased degradation at lower pH resulting from the higher level of free H^+ in solution infiltrating the polymer like P-O-P chains [34]. Subsequent release of H^+ during dissolution could also lead to autocatalysis. Ahmed *et al.* and Abou Neel *et al.* suggested that dissolution of the chains in H_2O in solution led to formation of phosphoric acid, lowering the pH of the media [98, 263].

For all coating and MQ compositions the solutions were changed periodically (twice per week) and the pH readings were obtained throughout the degradation period in PBS and dH_2O. During the degradation of MQ5: P40 Fe4, pH values remained between 7.27-7.40 and 6.77-7.02 for PBS and dH_2O respectively. The pH results for C12U: P28 Fe6 and C7U: P40 Fe4 degradation remained between 7.30 and 7.48 following precipitate formation in PBS. pH values were not obtained for degradation of coatings in dH_2O as the low conductivity due to the lack of ions in solution led to continuous drifting of measurements. This inability indicated that the solution did not at any point become saturated. In contrast, degraded MQ glasses released sufficient ions over 24 h in the solution, which enabled stable pH readings.

According to Bunker *et al.* and Gao *et al.*, the degradation of PBGs in water occurs in three stages; The acid/base reaction in which H_2O molecules react with network modifying cations to form H^+ ions and cleaved cations in solution. A resultant hydroxyl group is formed to compensate the charge of the oxygen within the tetrahedral. This hydration stage breaks down the structural chains. Secondly the hydrolysis reaction cleaves the P-O-P bonds leading to polymer like disentanglement [34, 99]. The initial exponential degradation profile was described by Bunker *et al.* as diffusion of solution or hydration of the surface layer prior to the hydrolysis reaction. The partially hydrated layer beneath is then exposed as the surface layer [34].

Initial Solubility

The dissolution of all coatings (C7U-C12U) compositions in dH_2O showed an exponential degradation profile as described by Bunker *et al.* for MQ glass compositions. This was followed by a plateau into a linear dissolution regime (*Figure 4.34A* and *Figure 4.41B*). The variation between sample solubility in the exponential phase may be attributed to chelating modifying ions and most crucially, the affinity of water penetration into the sample due to increased network polymerisation [34, 99].

Dissolution in a thin-film coating of glass or a glass surface layer may be most dependent upon the ability of the media to diffuse, increased by the concentration of P-O-P linkages in the surface and sub-surface layers. Gao *et al.* suggested that the rate of hydration was fastest during initial exposure in solution and that the diffusion of water through the layer decreased with thickness, followed by a steady state hydration and linear degradation rate [99]. To assess this theory, pertaining to hydration ability, sessile drop by measurement of contact angle was analysed for all coating compositions and for MQ: P40 Fe4, shown in *Table 4.11*. The hydrophilic nature of the deposited PBG coatings was characterised by complete wetting of the surface, compared to 24.8° for MQ5: P40 Fe4. Notably C12U: P28 Fe6 and C7U: P40 Fe4, exhibited a steeper initial exponential solubility in comparison to MQ5: P40 Fe4 (*Figure 4.32B compared with Figure 4.34A*) and continued to degrade exponentially in the first 2 h, approaching the linear profile thereafter. This suggested that the diminished contact angle, showing the super hydration ability of the coating was responsible for their enhanced initial exponential solubility. Polymerisation of the surface was assessed by XPS.

The surfaces of compositionally similar MQ and coatings analysed by XPS demonstrated significant structural variation of C7U: P40 Fe4 compared to MQ5: P40 Fe4, suggesting a ratio of P-O-P to PO^- of 34.2 : 65.8% compared with 20.5% to 78.5% respectively. Similarly all other degraded coatings (C7U-C12U) were found to have BO : NBO ratios ranging (28.5-34.2) : (71.5-65.8) %. Deconvolution of the P 2p on the surface of C7U: P40 Fe4 suggested the presence of more soluble (Q^2) $(PO_3)^-$ metaphosphate structures (*Table 4.3*) [48]; further supported by the high concentration of P-O-P bonding in the coatings. This would, therefore explain the increase in initial hydrophilicity of the coatings compared to the MQ glass surfaces, which were found to contain $(P_2O_7)^{4-}$ and $(PO_4)^{3-}$, (Q^1 and Q^0) structures respectively [48, 223, 224]. This could also explain the increased degradation rate over the initial 24 h, and the initial rapid solubility phase in the first 2 h. Abou Neel *et al.* also showed variation in polarity from contact angle measurements with water, which was suggested to be due to P-O-P bonding in the wetted surface layer [98].

Linear Degradation

Following the initial exponential solubility phase, the coating compositions exhibited linear dissolution rates between 2-24 h of 0.5 x 10^{-4} and 2.1 x 10^{-4} mg mm^{-2} h^{-1} for C12U: P28 Fe6 and C7U: P40 Fe4, respectively (*Figure 4.41A and Table 4.10*). Linear degradation profiles from 2-24h in dH_2O for compositionally equivalent MQ5: P40 Fe4 and C7U: P40 Fe4 showed dissolution rates 2.1 times faster in the coating than its MQ counterpart.

The short range bonding in the bulk of the coating structures was assessed in different compositions of C13U: P32.5, C14U: P34 and C15: P37 as shown previously in *Section 4.3*, by ^{31}P NMR, showing that coatings were more polymerised than MQ

counterparts, likely leading to their lower durability as observed in the case of C7U: P40 Fe4 compared with MQ: P40 Fe4.

The decline in dissolution rate from 2-24 h in the linear regime is reflected by XPS results collected following 16 h of degradation of C7U: P40 Fe4, which showed BO : NBO ratio for coatings of 22.5% to 77.5% and presence of $(P_2O_7)^{4-}$ Q^1 and $(PO_4)^{3-}$ Q^0 units (*Table 4.3*) similar to as manufactured MQ5: P40 Fe4 suggesting preferential resorption of the originally present Q^2 metaphosphates within the as deposited surface layer, leaving behind a less polymerised, and more durable structure than previously observed in the surface layer.

Pitting Corrosion

Due to the finite nature of the coating layer, as the hydrated layer cannot expand beyond the depth of the substrate, the liquid appeared to spread laterally, as implied by the cross sectional FIB-SEM micrograph and AFM of the degraded coatings (*Figure 4.38A-E*). This was most evident when comparing to pre dissolution FIB-SEM micrographs for coating on polished and sandblasted substrates (*Figure 4.36*). SEM observation of C7U: P40 Fe4 degraded in dH_2O at time points 4-24 h showed surface voids expanding with time, until the coating was entirely eroded after 48 h in solution (*Figure 4.37*). Similar voids were also apparent on the sandblasted substrates (*Figure 4.38C and D*). Haque *et al.* reported the peeling or "pitting corrosion" of P_2O_5-40 CaO-25 Na_2O-5, MgO-30 mol% fibres following 8 h degradation in water [102]. Abou Neel *et al.* experienced a similar peeling effect for Fe containing fibres [98]. This peeling effect in fibres was suggested to be due to the differential hydration between surface and bulk layers leading to tensile forces and subsequent cracking [103].

5.3.3 Compositionally Variable Coatings

Whilst deposition parameters were maintained for (C7U-C10U), the challenge remains in controlling condensation kinetics between compositions, as even under identical parameters, target glasses were deposited at variable deposition rates, dependent upon external factors such as electrical conductivity of the glass during sputtering. To produce coating of 2.67 μm thick, deposition times varied for (C7U-C10U) from 1165 min to 3000 min (*Table 4.9*) suggesting that formation energy varied across samples.

Literature of MQ glasses suggests that comparative dissolution rates are primarily related to the network connectivity of the glass structure and are therefore dominated by the covalently bonded (P-O-P) structure and by ionic cross linking from the inclusion of cations such as Mg, Ca, Na and Fe [34, 50, 98, 101, 106]. Iron and titanium incorporation as a Fe-O-P or Ti-O-P to form hydration resistant bridges, and their ability to link tetrahedra as trivalent and quad valent cross linkers respectively are believed to result in lower solubility [56, 58, 98]. To test this, Fe_2O_3 was increased from 4 to 8.5 mol% in C7U: P40 Fe4 and C10U: P40 Fe8. Both compositions were deposited under identical sputtering conditions and formed at identical deposition rates which would eliminate varying condensation energies as a differentiating factors (*Figure 4.41A and Table 4.10*). Dissolution rates were 2.12 ± 0.21 compared with $2.57 \pm 0.43 \times 10^{-4}$ mg mm^{-2} h^{-1} for 4 and 8.5 mol% Fe_2O_3 respectively. It is therefore interesting to note that the faster dissolution rate with 8.5 mol% Fe composition or similar rates within the calculated standard error, contradicted literary trends for melt quenched glasses. Linear dissolution rates ranged from 0.76 ± 0.11 to $2.57 \pm 0.43 \times 10^{-4}$ mg mm^{-2} h^{-1} (*Table 4.10*).

The third Fe containing coating for further comparison, C12U: P28 Fe6 appeared to be the least soluble of the three compositions containing Fe. Identification of two broad diffraction peaks was observed for coating C12U: P28 Fe6 indicating partial crystallisation with a FeO and a $FePO_4$ phases to form a glass ceramic during condensation (*Figure 4.30*). Crystalline ceramics are more thermodynamic stable due to their low entropy and low enthalpy states, leading to greater durability in solution [264]. The crystallite formations could have been the dominant factor accounting for the greater coating stability in dH_2O.

Within this work comparative assessment of all amorphous coating compositions deposited at 60 W, (C7U-C10U) showed no considerable variation in dissolution rates by expected orders of magnitude via increased proportions of Fe or reduction in P_2O_5. The ability to control dissolution rates by orders of magnitude as understood for MQ glasses was not apparent for PVD coatings. Further investigation by NMR, Neutron Diffraction, Mossbauer spectroscopy and density measurements should be undertaken to obtain complete information regarding bulk structural properties whilst diffusion of the growing coating layer and formation enthalpies should be maintained across compositions. It is however difficult to definitively assess this behaviour without detailed bulk structural properties; techniques which are not readily available for thin films at the present time given necessary sample volumes.

5.3.4 Additional Factors Influencing Dissolution

Processing route may be the overriding factor to influence structural changes in glass and therefore variable degradation rates. Magnetron sputtering at low temperature produces instantaneously condensed coatings upon a substrate, forming residual tensile stresses within the atomic layers, which may contribute to the higher degradation rates within the glass.

The potential for variation in dissolution characteristics has been suggested based on thermodynamic changes during formation. Post formation thermal annealing of melt quenched glasses has been used to reduce dissolution rates [102, 114, 115]. Cozien-Cazuc *et al.* showed annealing at 5 °C below the T_g for PBG fibres, allowing the structure to reorientate to its more thermodynamically stable position, suggesting the relief of internal stresses reduced dissolution by half [114, 115]. Ray *et al.* demonstrated the potential to vary structure via changes in the melting parameters alone by measuring Fe^{2+} and Fe^{3+} concentrations in P_2O_5-60 Fe_2O_3-40 mol% glasses as melting temperatures changed from 1150 to 1450 °C to find that this alone caused an increase from 17 to 57% in Fe^{2+} [265].

Surface structural variation analysed between melt quenched and sputtered coatings may be caused by etching during the sputtering process leading to structural changes on the surface of the coating [266]. The ion bombardment of the coating surface may manipulate the structure to form the highly soluble phosphate structure observed. Additionally surface pits appeared to be preferential sites for dissolution. Pit formations during the coating process were observed by AFM for C7U: P40 Fe4 prior to dissolution (*Figure 4.36*). Preferential pitting could also indicate nano-scale variation within the structural bonding of the coating layer, contributing to the pitting corrosion effects observed (*Figure 4.38*).

Variation in glass dissolution properties for identical compositions of glass, either formed by melt quenching or vapour deposition are dependent upon their formation conditions. Variable bulk coating structures and stress states are particularly affected by the inconsistencies in formation kinetics which can be caused by changes in deposition rates to affect atomic mobility and therefore structural properties during condensation.

5.3.5 Degradation in PBS and Precipitation Formation

Degradation of coatings in PBS formed precipitation in all cases, (C7U-C11U). Following submersion, degradation was halted and observation of the coating surface at 21 d for C12U: P28 Fe6 and 4 d for C7U: P40 Fe4 (*Figure 4.41B),* showed dispersion of precipitation over the sample area (*Figure 4.39* and *Figure 4.41E, F*). Notably certain compositions exhibited more confluent precipitation layers, adhered to the substrate surface, in particular the composition C8U: P31 Ti6 (*Figure 4.41E)*. This variability indicated that variation in ion release profiles due to composition might have led to, in some cases, the formation of a diffusion inhibiting precipitate layer above the remaining glass. In other cases only precipitation was left covering the surface of the substrate as observed by FIB-SEM section of a precipitated layer (*Figure 4.39E*). For C7U: P40 Fe4, *Figure 4.39* showed time points up to 21 d during which formation of a layer was observed on both polished and sandblasted substrates.

Particulate formation was first apparent after 4 h in PBS (*Figure 4.39A*). Pitting corrosion as seen in dH_2O was also observed. At all-time points beyond 4 h, dissolution characteristics were no longer apparent in the form of pitting, leading to the likelihood that the rate of precipitate formation exceeded the dissolution reaction between 4 and 12 h in solution (*Figure 4.39A* and *B*).

In the first 24 h either the coatings had precipitated in their entirety or a dissolution inhibiting diffusion barrier had formed. Tracking of the compositions changes as determined by EDX for C7U: P40 Fe4 showed that by 12 h the initial glass composition had changed. These compositional changes stabilised by 24 h (*Figure 4.35B*). Submersion in PBS up to 21 d indicated a fully stable coating layer covered by precipitation. XRD data for C12U: P28 Fe6 and C7U: P40 Fe4, 28 d post degradation suggested amorphous precipitation with no additional crystalline phases

beyond those detected in the substrate or in the as deposited C12U: P28 Fe6 (*Figure 4.30*). The FTIR absorption spectra 28 d post submersion showed remaining bonds associated with $(PO_3)^-$ and PO^- deformation modes which supported structural changes associated with formation of stable precipitation (*Figure 4.31*).

Furthermore, XPS deconvolution of the P 2p supported the FTIR and showed surface structural changes (*Table 4.3*) attributed to $(PO_3)^-$ [48, 222]. Quantification was conducted in at% to reflect potential changes in oxidation states associated with the precipitation. Variation from the original composition of C7U: P49 Na18 Mg15 Ca12 Fe6 at% to P41 Na22 Mg4 Ca12 Fe21 at% as analysed by EDX showed an insignificant change from 0.25 bulk Ca:P ratio to 0.29. The changes indicated a large increase in Fe from 6-21 at%, and an increase in Na from 18 to 22 at% respectively. No further signs of compositional changes were observed beyond 12 h. This stabilised layer composition suggests a partially dissolved PBG coating layer, on which a stable precipitated layer formed. Based on the XPS compositional analysis, 4 d post degradation in PBS an increase in Na from 4.1 at% pre degradation to 30.6 at% post PBS degradation and an increase in Fe from 1.3 at% to 2.9 at% suggested that the formed precipitation might been an amorphous Sodium Iron Metaphosphate.

5.3.6 Precipitation of Glasses in Literature

Ca:P apatite layers in phosphate containing saline solutions [72, 92-95] have often been reported. In particular Varila *et al.* assessed BG 45S5 and SBGs with SiO_2 content of 53 wt% and 68 wt%, submerged in SBF, TRIS, PBS and cell culture media for up to two weeks [94]. In TRIS, HA formation was observed during dissolution; however, as the layer formed, a diffusion barrier inhibited dissolution. This reaction was attributed to release of Ca in PBS, reacting with phosphorous to form HA [94].

A. Tas *et al.* proposed that Mg functions as a crystallisation inhibitor forming X-ray amorphous precipitants; a finding which could be linked to the stability of the precipitation formed from the glass C12U: P28 Fe6 and C7U: P40 Fe4, which appeared to be X-ray amorphous following XRD [92].

A review by Tas *et al.* concluded that precipitation layers could be biomimetically synthesised at (37 °C pH =7.4) in a range of aqueous saline solutions which specifically contained similar ionic concentrations as extracellular fluid [92]. The particles formed in DMEM solution were similar in morphology to ones observed here and were found to be X-ray amorphous. Coverage of precipitation on an optical glass slide submerged in media was reported to increase and stabilise by 48 h [72, 92].

5.3.7 Summary

Degradation of thin sputtered PBG coatings here exhibited unique behaviour as compared to their MQ counterparts, attributed to greater proportions of metaphosphate Q^2 species and increased P-O-P bonding in the surface structure, which consequently caused accelerated hydration and dissolution. The early solubility may require stabilisation by manipulation of condensation temperatures or by thermal annealing, which has been attempted in *Section 4.5* and discussed in *Section 5.4*.

Early indications are that sputtered coatings exhibit potential for controlled degradation at an implant site whilst showing the additional possibility of forming precipitation layers, which could show benefits for osseointegration if such a reaction occurred and proved to be bioactive *in vivo*. The desirable outcome may be the potential formation of a stable layer, similar in composition to HA or it's precursor phases. Further assessment of ion release profiles in *Section 5.4.4* for C7U: P40 Fe4 will show the linear potential to deliver ionic products. The flexibility for various ion inclusions in PBG may allow for the stratified design of bio therapeutic coatings.

5.4 Post Deposition Annealing; Mechanical, Structural and Degradation Properties

A post heat treatment stage in glasses is conventionally conducted within their processing window to allow residual stresses formed during quenching to diffuse from the glass, therefore leading to improved mechanical properties due to molecular relaxation [84]. Crystallisation may be desirable to provide thermodynamic stability to coatings which considered metastable in their amorphous state [84].

Earlier discussion showed that compositionally equivalent RFMS coatings deposited below the T_g are structurally variable to their melt quenched counterparts, showing characteristics of highly stressed structures, and increased polymerisation of the bulk material via ^{31}P NMR and of the surface layer via XPS (*Section 5.2*). This increase in polymerisation led to increased solubility of RFMS coatings over their melt quenched counter parts (*Section 5.3.2)*. Therefore the work here aims to observe the effects of post deposition annealing and crystallisation.

5.4.1 Heat Treatment

The selected heat treatment (HT) temperatures of 500, 550 and 610 °C for C7U: P40 Fe4 was based on a central position within the processing window, the onset and peak crystallisation temperatures respectively, of the compositionally equivalent melt quenched glasses MQ5: P40 Fe4. The $T_{g\ onset}$, $T_{g\ peak}$, and $T_{c\ onset}$ and $T_{c\ peak}$ were measured as 463, 485, 590 and 608 °C (not shown). Temperatures were chosen on this basis pre-emptively with the assumption of structural and thermal similarities which are now known to be incorrect following the findings of *Section 5.2*, which showed that sputtered coatings and melt quenched glasses are unique with respect to thermal properties such that T_g was 14-20 °C less than MQ compositions whilst processing windows varied from 101 - 112 °C for coatings

compared to 61-131 °C for three MQ compositions. C8U: P31 Ti6 was heat treated as Kasuga *et al.* showed a similar composition of a melt quenched and annealed glass ceramic to precipitate a bioactive apatite layer when dissolved in SBF solution therefore *Section 4.6* assessed bioactive performance [52].

5.4.2 EDX Compositional and Structural Analysis by XRD, FTIR, XPS

The composition of HT samples remained consistent within 1.5 mol% for C7UAD and C7U-500°-120, attributed to precision of the EDX method, batch reproducibility and coating variation as previously mentioned. However Significant variation showing a reduction in P_2O_5 to 38.43 and 36.85 mol% for C7U-550°-30 and C7U-610°-30 respectively may have suggested possible volatilisation of phosphorus with increasing temperature (*Table 4.14*) [158].

The coating C7U: P40 Fe4 was deposited amorphous. XRD suggested the formation and subsequent growth of hematite (Fe_2O_3) crystals within C7U-500°-30 and C7U-500°-120. A low intensity, broad hematite peak located around 32.5 2Θ (°) was observed following C7U-500°-30 and C7U-500°-120. Multiple crystalline phases emerged following C7U-550°-30, increasing in intensity at C7U-610°-30.

Phases were suggested however the occurrence of preferred orientation, significant texturing, overlapping of the diffraction angles for multiple crystals present and the low peak to noise ratio associated with grazing incidence should be considered. The identified phases were modelled by Rietveld Refinement accounting for lattice distortion (see *Appendix: Section 9*).

In addition a Calcium Phosphate β-$Ca_2P_2O_7$ phase (Ca:P = 1.0) in the C8U-500°-30 coating was present. The broad hump associated with amorphous diffraction remained, for all coatings with the exception of C7U-610°-30, suggesting the

formation a glass-ceramic structure (*Figure 4.43*). Similarly, Kasuga *et al.* formed a β-$Ca_2P_2O_7$ phase in a formulation of titanium containing melt quenched glass/ceramic which was shown to precipitate apatite in SBF solution [57].

The increased IR peak intensity in C7U-500°-30 and C7U-500°-120 in comparison to C7UAD supported the growth of Hematite crystals. IR absorption (*Figure 4.45*) revealed peaks located between 500-565 cm^{-1}; consistent with PO_4^{3-} within the phosphate structure and the possible presence of Hematite. Wang *et al.* reported vibration bands for hematite (α-Fe_2O_3) between 567-584 cm^{-1} showing variation in peak position based on crystallite shape [236]. Crystallisation of multiple phases was reflected in the IR spectra as the occurrence of peak splitting of vibrational bands suggested the presence of inhomogeneous bonding, consistent with variability in bond angles and lengths. The decline in relative intensities of the P-O-P bands at 900 and 769 cm^{-1} and of the PO_4^{3-} unit at 530 cm^{-1} following 16 h degradation may indicate cleavage of the P-O-P bond or leaching of alkali cations from the PO_4^{3-} (Q^0) units.

XPS survey spectra indicated the surface elemental compositions within the first 5-10 nm of the coating layer (*Figure 4.44A, C, E*). *Table 4.15* and *Figure 4.44* showed low peak intensity associated with phosphorus following C7U-500°-30 to C7U-610°-30 as at% varied from 21.6 to 1.6, 1.3, 2.1, 3.5 at% respectively, whilst the proportion of Fe increased in the as manufactured coatings from 1.4 to 22.4, 22.8, 18.1 and 10.6 at%. The growth of crystals and migration of alkali cations may have diffused to the surface of the glass coating. The variation in surface compositions is likely due to the competitive formation and diffusion of alkali containing crystals. Crystallisation is a thermally activated process upon which elements within the amorphous structure diffuse into the nucleated crystal. The heterogeneous nature of

the reaction and potential for recrystallisation as temperature varies, encouraged the formation of numerous phases [264].

For C7U-500°-30 and C7U-500°-120 the proportional iron increase supported the growth of hematite whilst the subsequent reduction to 10.6 at% and apparent increase in sodium to 16.1 at% for C7U-550°-30 and C7U-610°-30 respectively may be due to the prevalence of sodium containing crystals due to activation energies of modifying ions within the glass matrix favouring the diffusion of ions.

In addition the volatility of phosphorous may have led to a surface deficiency [158]. As previously mentioned Boyd *et al.* suggested that for Ca:P films which underwent post deposition annealing at 500 °C, the Ca:P was reported to increase, explained by volatile phosphorous evaporating from the surface [157].

Iron, in particular can function as a divalent or trivalent network cross linker therefore its bonding was assessed by high resolution scans. Fe 2p for C7UAD could not be deconvoluted with a sufficient level of confidence based on low signal intensity and the presence of closely spaced binding energies attributed to the multiple chemical states (*Figure 4.44B, D and F*). Gupta *et al.* showed over 20 peaks located between 708.3-713.6 eV which were attributed to FeO, F_2O_3, Fe_3O_4, FeOOH [267]. The peak positions were determined by analysis of standard reference materials. The asymmetrical peak shape towards 709.0 eV and the breath of the Fe $2p_{3/2}$ spin orbital suggested the combined presence of Fe_2O_3, Fe_3O_4, and FeOOH [267]. Gupta *et al.* suggested peak 1 positions at 709.8 eV, 710.2 eV, 710.2 eV respectively with peak 4 positions at 712.3, 713.6 and 713.2 eV respectively [267].

The defined asymmetric peak positions of 710.4 and 710.6 eV, the narrowing of the Fe $2p_{3/2}$ and Fe $2p_{1/2}$ peaks and the satellite peak locations of 7.9/7.8 and 8.7/8.0 eV

from the main spectral peaks for C7U-500°-30 and C7U-500°-120 respectively (*Figure 4.44B and D)* suggested the prominence the Fe_2O_3. Grosvenor *et al.* located satellite peaks for hematite (α-Fe_2O_3), magnetite (Υ-Fe_2O_3), lipidocrocite (Υ-FeOOH), magnetite (Fe_3O_4) to be spaced 8.3, 8.5, 8.0 and 5.9 eV from their electron spin orbital Fe $2p_{3/2}$.

Fe on the surface may have existed in the multiple oxidation states, FeO, Fe_2O_3, Fe_3O_4 and FeOOH which was the cause of broadening of the Fe 2p high resolution spectrum (see *Figure 4.44*) [234]. FeOOH however was not supported as hydroxyl groups were absent from all IR spectra (*Figure 4.45*).

Minitti *et al.* reported the formation of <1 μm thick hematite coatings on oxidised basaltic glass at 700 °C whilst showing no such formation at 350 °C [235]. The mechanism was believed to be the removal of electrons from Fe^{2+} by oxidation and re-oxidation at the surface with Fe to form Fe^{3+}. Cation vacancies within the bulk of the glass subsequently allowed metal ions to move outwards, facilitating the additional migration of Mg and Ca oxides [268]. Wisniewski *et al.* demonstrated the formation of hematite and magnetite crystals in Fe containing soda-lime glass when annealed at 480 °C (30 °C below the measured T_g of 510 °C) [269]. The complementary techniques of FTIR, XPS, and XRD confirmed Fe oxidation on the surface and the crystallisation of Fe_2O_3 as hematite. SEM imaging at 64,000 times magnification showed crystallite growths (*Figure 4.52C inset).* Hematite formation below the measured crystallisation onset of MQ5: P40 Fe4 could also be attributed to the dissimilarity in thermal properties of sputtered coatings.

5.4.3 Mechanical Properties

The scratch test and pull off adhesion tests describe the failure mechanisms of a coating under multi-axial and tensile loads respectively [217]. The scratch test is considered the more versatile method of determining mechanical adherence of the coating as it provides multiple failure modes. Failure characteristics are more representative of practical orthopaedic applications as coating failures may more often be caused by shear, rather than pure tension.

Scratch Testing

Theoretical and experimental representations of scratch failure modes have been presented in *Figure 2.14* and *Figure 4.46* or the literature review and results sections respectively. Interfacial integrity following HT on polished substrates, in the case of C7U-500°-30 and C7U-500°-120 appeared to be compromised by coating/substrate delamination; as observed in FIB-SEM cross sections (see *Figure 4.49B and C*). Scratch tests (*Figure 4.46* and *Figure 4.47*) showed variation in L_{c5} (interfacial delamination) from 5.0 to 2.3 to 4.4 N for AD, C7U-500°-30 and C7U-500°-120 respectively. The failure modes for L_{c1}-L_{c5} ranged over 4.0 N for AD, and were, in contrast, closely spaced ranging over 1.3 and 2.0 N for C7U-500°-30 and C7U-500°-120, demonstrating a decrease in ductility due to catastrophic coating failure at the point of initial indentation L_{c1}. C7U-500°-30, showed increased L_{c1} (initial scratch) to 2.0 N and L_{c5} to 4.4 N. All coatings exhibited brittle failure mechanisms however HT seemingly led to increased brittleness and hardness with prolonged dwell time of 120 min.

Sandblasting with Al_2O_3 remains the commercial standard for surface roughening of orthopaedic implants prior to plasma spraying, as topographical features assist with coating adherence to the implant and contribute to mechanical fixation to the bone

during the integration process [270]. The C7U: P40 Fe4 coatings on sandblasted substrates showed no signs of catastrophic failure, specifically the absence of spallation due to trackside delamination. The interfacial properties were improved as delamination occurred at 8.6 - 11.3 N for C7UAD, C7U-500°-30 and C7U-500°-120 respectively (*Figure 4.46B*). Toque *et al.* applied up to 2.5 N loads on 1.3-2.0 μm Ca:P sputtered films deposited onto 316L stainless steel. Results showed interfacial delamination at 800-900 mN. Post deposition annealing similarly led to a reduction in interfacial failure loads as shown here for polished substrates, in the range of 450-550 mN [186]. Additionally Cheng *et al.* compared pull off and scratch tests on sol gel HA coatings and reported scratch delamination of up to 487 mN and pull off strengths of up to 22 MPa [271].

Pull Off Testing

Cozien-cazuc *et al.* tested the tensile properties of MQ: P40 Fe4 formed as glass fibres, both as prepared and up to 3 d degradation in dH_2O and reported tensile strengths of 480 ± 150, dropping to 370 ± 60 MPa. Following annealing at 444 °C (5 °C below the T_g) a reduction in tensile strength to 290 ± 50 MPa was observed and an increase in strength following 3 d degradation to 460 ± 140 MPa [272]. For coatings on polished substrates a similar reduction in failure properties due to coating embrittlement was detected here following annealing. Sglavo *et al.* also showed ranging tensile properties of PBG optical fibres of between 200-400 MPa [273]. Given the measured failure strength of glass itself, the measurable interfacial failure strength at the coating substrate interface is considerably lower than the anticipated tensile properties of the glass itself to fail cohesively in tension.

C7UAD, C7U-500°-30 and C7U-500°-120 prepared and tested here showed sufficient minimum adhesive properties according to ISO (15.0 MPa) and FDA (50.8 MPa)

regulations on pull off testing (*Table 4.16*) and additionally superseded the strength of the epoxy in all cases. Whilst the pull off method remains the standardised quantitative assessment of coating/substrate mechanical strength, the actual failure loads may be unattainable in some cases due to the limiting factor being the tensile strength of the epoxy used, which was shown to be 76.8 ± 3.5 MPa. ISO-0-137792 Part 2 "Coatings of Hydroxyapatite" states that the minimum interfacial tensile strength should be no less than 15.0 MPa [237]. Callahan *et al.* stated in the 1994, FDA draft guidance for Ca:P coatings on medical Implants that the minimum interfacial strength for FDA commercially approved coatings was 50.8 MPa [19] (*Table 4.16*). To add perspective to the pull off results a commercial plasma sprayed HA coating on Ti6Al4V, provided by Zimmer was tested utilising the same protocols and equipment as for the PBG coatings and observed to fail at 76.7 ± 1.1 MPa by cohesive coating failure, likely resulting from through thickness defects (*Table 4.16 and Figure 4.48A-D*).

Ong *et al.* tested ion beam sputtered Ca:P films comparing the pull off strength of deposited amorphous, water quenched and furnace cooled coatings and reported pull of strengths of 38.0 ± 8.2 MPa, 17.0 ± 6.5 MPa and 9.0 ± 9.0 MPa respectively with failure either occurring at the coating interface or cohesively [139].

In similar studies, Mardare *et al.* and Stan *et al.* produced silicate bioactive glasses by RFMS and reported pull off values. Mardare *et al.* reported adhesion strength of 41.0 ± 4.5 MPa for 300 nm bioactive glass on titanium substrates. Post-deposition heat treatment of the coating layer at 900-1000 °C caused crystallisation and subsequent reduction in adhesion to 16.3 ± 1.9 MPa [169]. Mardare's work was carried out above the phase transition temperature of titanium in which the titanium

changes from Hexagonal close packing to body centred cubic structure and reduces in volume, inducing stress in the materials [169, 193].

As shown in (*Figure 4.48E, G*) silicate glass coatings were produced and tested in the case of C6T: Si50, which fully delaminated from their substrates at 14.7 ± 1 MPa (*Table 4.16*). Stan *et al.* reported interfacial strengths of as deposited silicate glass coatings of 29.2 ± 7.0 MPa and attributed the less than optimal adhesion achieved to the thermal expansion coefficient (TEC) mismatch between the deposited coatings and substrates during deposition [175]. Belluci *et al.* reported literary values for thermal expansion of a number of MQ bioactive silicate glasses suggesting a range 8.8 – 15.6 x 10^{-6} K^{-1} [274]. Improvements by Stan *et al.* in adhesion by reducing the TEC of the coating through compositional changes led to production of a glass coating with TEC of 10 x 10^{-6} K^{-1}, applied to their titanium substrates with TEC of 9.2 - 9.6 x 10^{-6} K^{-1} [174]. The adhesion strength for this glass was measured as >75 MPa (limited by the epoxy) [172]. Whilst bonding is dramatically improved by tailoring TEC by altering composition, this restricts the flexibility of coating compositions that can be applied. Further publications demonstrated improved pull off to >85.0 MPa, again limited by the strength of the epoxy, following an annealing process during which Stan *et al.* suggested that heat treatment caused a noticeable diffusion of titanium into the glass at the interface, forming chemical bonding leading to improved adhesion [173].

Unfortunately TEC could not be assessed in thin films; therefore the MQ5: P40 Fe4 was cast as rods for comparison. The TEC was assessed for T1U-T6U and MQ5: P40 Fe4, ranging from 11.6 – 16.0 (*Table 4.2*) and 13.6 ± 0.2 K^{-1} respectively. These values however are not directly comparable as it was previously shown that

structures and thermal properties varied in coatings. Elmer *et al.* cited TEC in TI6Al4V between 8.5 – 10.0 x 10^{-6} K^{-1} [275]. The higher TEC of PBG with respect to the Ti6Al4V substrate may have caused the observed ripples in of the coating shown in SEM micrographs (*Figure 4.52B, C*) and the interfacial delamination shown in FIB-SEM sections (*Figure 4.49B, C, E, F)* following C7U-500°-30 and C7U-500°-120. However without knowing the TEC of the thin film it was not possible to determine whether differential expansion was the primary cause of variation in adhesive properties.

The multi-layer composition C7T: Multilayer, failed at the blended interface at 39.6 ± 1.0 MPa between the PBG sub layer and the SBG top layer. Optimisation of the blending process was not attempted however in future might lead to improved adhesive strengths (*Table 4.16*).

5.4.4 Degradation and Ion Release of As Deposited and Heat Treated Samples

As previously discussed degradation of PBG occurs by hydration and subsequent hydrolysis during which H^+ ions interchange with cations to form P-OH^- and cleaved ions. This is followed by the subsequent disentanglement of the polymer like chains [34, 99]. Notably ion chromatography confirmed that the PBG thin films similarly to MQ glasses, linearly released ionic constituents during dissolution. The rate of ion release correlated with the rates of dissolution for C7UAD, C7U-500°-30 and C7U-500°-120 (*Figure 4.51* and *Table 4.17*).

As discussed in *Section 4.4.2*, the PBG coating composition C7UAD was highly soluble in the first 2 h, degrading exponentially, prior to stabilising to a linear regime thereafter. Reproduction of this experiment showed similar behaviour as observed in *Figure 4.50A*. The thermal annealing processes led to a reduction in initial solubility

as the comparative mass losses were 2.9, 0.3, 0.7, 0.4 and 0.3 x 10^{-3} mg mm^{-2} for AD, C7U-500°-30 to C7U-610°-30 respectively. This effect may have been due to the reduction of soluble P-O-P bonds following HT at the surface of the material as shown by XPS (*Figure 4.44B, C*).

For C7U-500°-30 and C7U-500°-120 the formation of hematite crystals led to improved durability over the 96 h time period. From 2 h to 96 h the linear degradation rates for C7U-500°-30/C7U-500°-120 and AD were 0.68 ± 0.02, 0.84 ± 0.01 and 2.05 ± 0.35 x 10^{-4} mg mm^{-2} h^{-1} respectively, showing an increase in coating durability by a factor of 2.44 - 3.01 ± 0.35. There were, however, no significant variations in the quantitative degradation properties between C7U-500°-30 and C7U-500°-120. Surface SEM micrographs of C7UAD showed randomly distributed narrow corrosion pits 16 h post degradation. Following C7U-500°-30, corrosion pits appeared to widen and following C7U-500°-120, visible pitting associated with degradation was most uniform, indicating that prolonged C7U-500°-120 led to a more diffused, homogenous bulk structure. The scatter of degradation rates as shown by the error bars for all HT samples in *Figure 4.50* also indicated improved coating stability.

Chouka *et al.* and Cozien-Cazuc *et al.* both showed pitting corrosion of Ca:P and PBG fibres following degradation in Tris-Buffered HCL and distilled water respectively, whilst also reporting improved durability of annealed fibres over their non-annealed counterparts. Chouka *et al.* suggested that durability was proportional to annealing temperature [114, 115]. Remarkably C7U-550°-30 showed only a marginal reduction in dissolution properties as compared to C7U-500°-30 and C7U-500°-120 whilst C7U-610°-30 showed considerable stability, which may suggest dissolution of only the amorphous phase. Continuation of C7U-610°-30 up to 28 d showed that the

coating fully stabilised between 14-21 d with an overall mass loss of 3.3×10^{-3} mg mm^{-2}. Furthermore SEM observation showed porosity within the coating structure, which may be due to dissolution of the soluble phases over the 28 d period (*Figure 4.54*). XRD, which followed 28 d dissolution similarly, showed the remaining crystalline structure (not shown).

5.4.5 Summary

This chapter has highlighted positive and negative aspects of post deposition annealing, regarding adhesion properties, structural changes, topographical alterations and solubility. The ability to control dissolution and ion release rates of vapour deposited coatings by formation of crystalline phases is beneficial to their application. The formation of ceramic structures may be responsible for increased hardness and greater interfacial delamination forces of the coating layer. Conversely differential expansion of the substrate and coating layers caused partial delamination and surface roughening as observed following C7U-500°-30 and 120. However the emergence of Ti containing crystalline phases following C7U-550°-30 and C7U-610°-30 are two counteracting events which may have influenced interfacial adhesion. Nonetheless the pull off adhesion strengths achieved for PBG coatings superseded FDA and ISO requirements for C7UAD and HT 500 °C samples on polished substrates.

Production of PBG thin films was shown to be a promising method for delivering a controlled release of ions at a dissolution site, whilst the ability to further control such properties through heat treatment was verified. *Section 5.5* will discuss the *in vitro* apatite forming potential of a range of as deposited PBG compositions by submersion in SBF solution.

5.5 The Bioactive Potential of Sputtered Glass Coatings

Bioactive glass, notably BG 45S5 is known to precipitate a stable bone like HA layer on its surface following *in vivo* implantation. Due to HAs compositional and structural similarity to the cortical bone surface, HA is responsible for the stimulation and attachment of osteoprogenitor cells leading to their differentiation into Human Osteoblast Cells (HOB), for bone regeneration [276]. This effect, may also be assisted following the release of therapeutic ions such as, Mg, Ca, Sr, F, P etc [42].

The common *in vitro* assessment of bioactivity relating to apatite forming ability is the submersion of the material in SBF to observe the potential nucleation and growth of a biological like apatite in solution. SBF is supersaturated with respect to HA and may form given the creation of nucleation sites, however despite this it remains the standardised method for assessing *in vitro* bioactive capabilities [86]. Secondly and perhaps of primary importance in the assessment of bioactivity is the cellular response to a material at the point of application. With respect to bone surfaces *in vitro* cellular attachment of MG63 HOB cells and their ability to subsequently proliferate, and differentiate, leading to the formation of an Extra Cellular Matrix (ECM) is considered as an indicator of cytocompatibility demonstrated by the ability of cells to function within the implantation environment.

5.5.1 Apatite Forming Ability in SBF "*in vitro* Bioactivity"

The formation of CHA from compositional variations of MQ SBG has been independently cited countless times since Larry Hench most notably formulated BG 45S5 [46]. In contrast the ability of melt quenched PBG to the same effect has been scarcely identified, whilst an extensive review of Ca:P based RFMS coatings has been so far unconvincing in demonstrating apatite forming ability of amorphous coatings in SBF [149, 161, 194]. Wolke *et al.* did however show *in vivo* precipitation

of amorphous-crystalline Ca:P layer of carbonate apatite following implantation of a Ti coated substrate within rabbits. Formation was observed as early as the one week time point [162]. This suggested that *in vitro* studies do not necessarily dictate the bioactive effectiveness *in vivo*.

Van der Wal *et al.* showed that the only situations in which apatite could be formed from immersion of Ca:P coatings was by induction of a layer by initial submersion in an overly concentrated SBF with respect to Ca and P, postulating that pre-nucleation was necessary [161]. The recent ISO 23317: 2014 "Implants for Surgery- *In vitro* evaluation for apatite-forming ability of implant materials" as formulated by Kokubo *et al.* does not suggest pre nucleation or continuous recycling of media over the dissolution period [86, 219]. All work conducted here strictly followed Kokubo's protocol as reflected in ISO 23317: 2014. However, recycling of SBF may be more representative of the situation at an *in vivo* implant cite for which dynamic flow is likely [277]. Additionally ISO 23317: 2014 does not dictate environmental conditions, lacking direction for testing. For example whether to incubate the sample in air or 5% CO_2, or to have the solutions sealed are unspecified. This inconsistency can significantly affect pH conditions or cause evaporation, leading to the possibility of spontaneous precipitation.

5.5.2 Apatite Forming Ability on Glass Coatings and MQ BG 45S5

The C6T: Si50 (*Table 4.18*) coating deposited from BG 45S5 which is composed as SiO_2-46.13 P_2O_5-2.6 CaO-26.91 Na_2O-24.35 mol%. Stan *et al.* demonstrated that ~0.5 μm thick SBG coatings could precipitate a CHA layer on a silicon substrate *in vitro* within 30 d of submersion. The comparable ability of an ion doped PBG coatings to precipitate a CHA or its prerequisite of, Ca deficient phases has not been tested *in vitro* and is of interest as a number of literary sources have shown bioactive

precipitation on melt quenched compositions. In particular Kasuga *et al.* demonstrated the composition P_2O_5-30 CaO-60 Na_2O-7 TiO_2-3 mol% to have precipitated bone-like apatite phases of β-$Ca_3(PO_4)_2$ [57], suggesting that hydration of titania was responsible for forming nucleation sites for apatite growth. They further showed that production of a glass-ceramic by heat treatment could stabilise the composition and lead to more efficient apatite formation by dissolution of the amorphous phase. Hence the coatings C8U: P31 Ti6 and its HT variants (*Table 4.18*) in particular were designed here for their compositional proximity to the bulk PBG shown to be bioactive by Kasuga *et al.* [52].

Both the silicate MQ BG 45S5 control and the RFMS C6T: Si50 demonstrated apatite-forming ability by 7 d in solution as confirmed by FTIR in *Figure 4.57*. Continuous apatite formation of the MQ BG 45S5 control appeared to be coupled with an increase in pH of the surrounding media [277].

The assessed glass coatings, notably C7U: P40 Fe4, C8U: P31 Ti6, C8U-500°-30, C5T: P40 Fe4, and C6T: Si50 were observed to degrade in the SBF solution over the first 3 d and stabilise thereafter. An initial pH increase may suggest that the release of cations during dissolution or adsorption of hydrogen from solution led to an increase in the pH and therefore apatite forming ability [277]. Dissolution of the BG 45S5 control led to an increase in pH, suggesting a continuous release of cations. Notably in contrast the glass ceramic C8U-500°-30 showed no signs of mass loss over the test period however pH values were shown to increase and subsequently decline whilst the same was true of the Ti6Al4V control in solution. This behaviour could suggest multiple effects, including the possible liberation of H^+ ions in solution to lower the local pH. Van der Wal *et al.* showed linear dissolution for 215 nm thick Ca:P amorphous compositions over a 14 h test period. They however did not report beyond

this time point to whether they observed stabilisation of the layer. In addition they similarly found that crystalline compositions remained inert as observed here [161].

The compositional variations following the 28 d time point was assessed by EDX analysis to determine variation in Ca:P to suggest precipitation of apatite. In both MQ Bioglass and C6T: Si50, increased concentrations of Ca:P to 1.4 and 1.3 respectively, over areas of the sample which may have been an indication of pre-mineralised Ca:P or amorphous Ca:P (ACP) (*Table 4.19*).

Furthermore the MQ BG 45S5 sample showed diffraction associated with formation of a CHA layer, initially observed at the 7 d time point (*Figure 4.56*). Similar peaks were identified by Kokubo *et al.* following 45S5 submersion in a pre-formulation of SBF [88]. Infrared spectroscopy showed the presence of carbonated apatite for both BG 45S5 and C6T: Si50, notably CO_3^{2-} and PO_4^{3-} peaks. The absence of Hydroxyl groups within the spectra suggests the presence of poorly crystalline apatite or ACP [240]. Low angle diffraction (2°) scans were conducted in order to isolate a surface precipitation layer. As no diffraction patterns were found associated with the coating C6T: Si50, there was visual identification via SEM (*Figure 4.57*) and suggestions of carbonate apatite via FTIR (*Figure 4.58*) suggesting that the X-rays may have either missed the locations of apatite formation, as the layer was too thin or not uniformly dispersed on the surface for analysis. It could also support the formation of ACP.

Berbecaru *et al.* at 15 d, similarly showed growth of apatite crystals of Ca:P=1.3, the XRD similarly showed no signs of crystallisation however they were able to identify CHA on their RFMS Bioactive glass coatings via XRD, similar in position to the Bioglass control here, by 30 d of submersion. Ca:P = 1.77 by 30 d [178]. ACP is a pre requisite to the crystallisation of apatite forming at Ca:P ratios ranging from 1.15-1.5 forming at acidic pH values, whilst carbonate and magnesium are crucially thought to

prevent mineralisation [278, 279]. In contrast higher, alkali pH values are believed to accelerate mineralisation towards TCP and HA. Zhao *et al.* suggested that ACP has superior function to TCP and HA for promoting osteoconductivity due to its degradable and mineralisation capabilities [279].

All PBG compositions, C7U: P40 Fe4, C8U: P31 Ti7 and C8U-500°-30 showed no signs of apatite precipitation. Since C7U: P40 Fe4 contained no stable nucleation points for such formation this was as expected. In addition precipitation requires an increase in pH, which in the case of Bioglass occurs by alkali ion leaching. As previously discussed in *Section 5.3*, during dissolution in dH_2O no such pH changes were observed due to the low ionic levels present within the thin coating layers. If pH had varied due to degradation, the formation of phosphoric acid would lower the overall pH, preventing bioactive precipitation [98]. As the pH of all samples appeared to decline following coating dissolution post 3 d it is believed that dissolution had stopped and all coating layers had stabilised.

The coating compositions showed mass loss associated with dissolution, which was observed to fluctuate as the effects of remaining ions from saline solution could result in greater apparent masses *Figure 4.55*. In combination with pH measurements it is suggested that the bulk of dissolution for all glass coating compositions occurred by 3 d, at the point of maximum pH whilst no considerable change in mass suggested coating stability up to 28 d.

The ability for apatite to nucleate and precipitate requires that the glass fulfils numerous structural requirements. For example Kasuga *et al.* suggested that apatite formation requires the creation of functional groups for the nucleation of absorbed orthophosphates $(PO_4)^{3-}$ and Ca^{2+} ions. In SBG phosphorous is assumed to fit in the structure as a network modifier as a Q^0 orthophosphate due to its low concentration,

therefore aiding precipitation [45, 178]. To fulfil this requirement the PBG itself should consist of pyro and orthophosphates upon which the Ti in the glass forms Ti-OH^- upon dissolution to exist as the nucleation points similar to the Si-OH^- silanol groups formed in SBG [57]. Therefore the coating composition C8U: P31 Ti6 contained 5.5% mol% TiO_2. However the position within the structure, whether it would function as a network former or modifier could contain clues to its apatite forming ability. From ^{31}P-NMR shown previously of sputtered thin-films it has been demonstrated that films appeared to be highly soluble whilst containing more Q^2 units than their melt quenched counterparts as opposed to Q^1 pyrophosphates in *Section 5.2*. Kasuga *et al.* observed a pre requisite to HA formation in melt quenched PBG, which was a Ca:P gel layer [57].

Berbecaru *et al.* postulated that there might be a minimum requirement of coating thickness for the formation of CHA. By the 30th day of submersion ~480 nm thick RFMS SBG layer containing boron could homogenously biomimetically synthesize CHA in SBF. This was due to the increase in local pH surrounding the coating and its ability to form nucleation sites for the formation of Ca:P crystals, leading to continuous Ca precipitation. The observed decrease in local pH shown in *Figure 4.55* would have prevented the formation or mineralisation of apatite here.

5.5.3 Summary

As Stan and Berbecaru *et al.* remain the only known authors to show apatite formation on RFMS thin films glasses, it is theorised here that whilst CHA was identified on C6T: Si50, it may have been due to the enhanced durability of their composition due to boron inclusion or structural variability. Stan and Berbecaru *et al.* did not report upon the pH changes of their solutions [178]. The fundamental variance between ISO 2007 and 2014 is that the SBF volume to surface area ratio is 1000x less than in ISO 2007 which would enable the pH of the solution over the sample to change considerably, favouring apatite precipitation [219, 220].

All PBGs tested in SBF remained inert following initial solubility whilst C8U-500°-30 was inert due to its crystallinity following an initial dissolution period. Although many have attempted to tailor PBG compositions to create apatite-forming abilities, it seems that the ultimate purpose of PBG should be their ability to fully resorb *in vitro* to release ions for bio-therapeutic purposes. In *vitro* apatite formation should be left to their proven SBG counterparts however without the organic components of the human blood plasma, and the inadequate control of pH and flow conditions to mimic an implantation site within the body, the effectiveness of Kokubo's SBF is in doubt. Confirmation of bioactivity should be confirmed by *in vitro* cell studies leading to *in vivo* testing.

6. Conclusions

6.1 Manufacturing and Processing of Glass Targets and Deposited Coatings

PBG coatings were formed via the process of magnetron sputtering, involving the ionic bombardment of the precursor MQG to be subsequently condensed as coatings. Batch reproducibility and compositional homogeneity across the sample surface was confirmed. The effects of increasing power from 60-120 W showed that targets fractured, showing the undesired potential to crystallise due to thermal shock, plasma radiation, and ion bombardment. This heating subsequently led to structural changes and crystallisation in deposited coating structures at 100 W depositions. A suitable processing power was deemed below 100 W to produce amorphous coating compositions.

The complication of preferential sputtering was observed such that transfer of atoms from target to coating was non-stoichiometric, attributed to variation in atomic bonding and atomic properties within multi component glasses. The covalently bound phosphate network had the strongest bonds and subsequently the lowest sputtering yields whilst the network modifier ions were ejected from the target in order of increasing dissociation energy. The modifier ions present were found to sputter in the order Na > Ca > Mg > Fe. Additionally, the yields varied according to relative atomic mass as kinetic energy exchanges suggested that the lighter particles would be more easily ejected and would maintain a higher relative velocity. An indication of relative sputtering yields were determined from the variation between target and coating stoichiometry's for 6 target compositions resulting in a reduction in P_2O_5 and Fe_2O_3 of between (10.3–15.2), (0.2–0.6) mol% respectively and an increase in MgO, CaO, Na_2O of (4.8–6.0), (0.1–3.8), (3.0–6.9) mol% respectively. The improved understanding of the preferential sputtering effects enabled the production of

pre-determined glass compositions. Further experimentation showed an ability to coat 3D geometries and polymers such as PLA (T_g < 66 °C).

6.2 Structural Variance in Melt Quenched and Magnetron Sputtered PBG Films

Significant differences in short-range structural variation between vapour condensed and conventional melt-quenched phosphate glasses, via ^{31}P MAS-NMR, XPS, FTIR and DTA were observed. Coating compositions of samples P32.5, P34 and P37 showed greater bulk network polymerisation based on the presence of (23% to 45% Q^2 species) versus (9% to 32% Q^2 species) in melt-quenched glasses as determined by NMR. The proportion of P-O-P bridging oxygens as suggested by XPS on the surface of coatings remained consistent at (34% to 35%) forming $(PO_3)^-$ metaphosphates (Q^2), whilst P-O-P bonding in melt-quenched glasses increased from (12% to 18%) and were found to form $(PO_4)^{3-}$ orthophosphates (Q^0) and $(P_2O_7)^{4-}$ pyrophosphates (Q^1). AFM analysis of the coating surfaces showed nano-topographical changes due to etch pitting, which led to Ra increases from 19 nm to 167 nm, which correlated to increased deposition rate and therefore bombardment energy.

This structural variability may be explained by the variation in formation enthalpy and continuous etching of the coating during deposition as ion bombardment readily leads to surface functionalisation and preferentially removal of alkali cations. Remarkably DTA results also showed variable thermal properties. The dissolution of PBG has been shown to be dependent upon P_2O_5 content within the glass structure, therefore PVD coating surface layers would be less durable than their MQG counterparts due to increased polymerisation. The structural variations observed support a remarkable experimental finding in the production of inorganic-glasses.

6.3 Degradation of Phosphate Glass Coatings

PBG coatings on Ti6Al4V substrates were observed to fully degrade in distilled water. In particular a comparison of PBG and MQ glass of the composition P40 Fe4 was undertaken. The initial solubility for C7U: P40 Fe4 exceeded that of MQG, and was attributed to variable surface chemistries such that there were 34.2% P-O-P linkages at the surface of the coatings as compared to the 20.5% in MQG as shown by XPS. Although NMR spectra were not obtained for compositions of degraded glasses the previously concluded trend in *Section 4.3.5* suggested greater polymerisation and therefore solubility of coating structures. This may have been related to continuous surface etching during the sputtering process, formation of pits leading to preferential dissolution sites. The degradation rate of coatings from 2-24 h was shown to increase by a factor of 2.06 over MQG. Coatings of 2.67 μm in C7U: P40 Fe4 showed pitting corrosion associated with preferential hydration and degradation, which led to lateral dissolution. Coatings on sandblasted substrates exhibited greater stability such that no peel off was shown, although discontinuous pitting corrosion was present. This was visually observed via FIB-SEM cross sectional milling. Most remarkably the expected trends of increased solubility due to network cross linking was not observed, whilst no significant trends were observed for 5 compositions of degraded thin films.

All coatings degraded in PBS precipitated a stable precipitant within 24 h. Initial solubility was observed until the precipitation reaction exceeded dissolution. Over a 21 d period for C7U: P40 Fe4 and a 4 d period for (C8U-C11U) no variation in the precipitant characteristics were noticed beyond stable formation. The layer entirely precipitated and partially adhered to the substrate in some cases, whilst in others may have inhibited further glass degradation as EDX analysis indicated the presence of remaining glass beneath the precipitation.

6.4 Post Deposition Annealing; Mechanical, Structural and Degradation Properties

PBG coatings were deposited amorphous onto both polished and sandblasted Ti6Al4V substrates. Coatings were subsequently heat treated at 500-610 °C to observe the effects on structure and dissolution of post deposition annealing and crystallisation. Similar structural changes were observed for 2 heat treatments at 500 °C, associated with the formation of Fe_2O_3 hematite crystals whilst XPS showed the reduction of phosphorous from (21.6-1.3) at%, coupled with an increase in iron from (1.4-22.8) at% within the surface layers. HT at 550 and 610 °C led to the formation of multiple phases and formation of bubbles within the coating topography.

Pull off adhesion tests were limited by the strength of the epoxy, therefore all PBG coatings showed average strengths in excess of 73.6 MPa, exceeding the international ISO standard and FDA requirements. Scratch adhesion tests revealed brittle failure modes for coatings on polished substrates. Although heat treatment improved the overall adhesion values, coatings failed catastrophically at the location of initial indentation, suggesting that HT led to increased hardness at the expense of coating embrittlement. Coatings applied to sandblasted substrates were mechanically durable, showing no trackside delamination or tensile cracking whilst loads associated with interfacial delamination were increased to between 8.6-11.3 N. For comparison of interfacial adhesion a SBG C6T: Si50, a blended multi-layer consisting of a PBG base layer/C6T: Si50 top layer and a plasma sprayed HA coating from Zimmer were assessed, failing at an interfacial tensile load of 14.7 MPa, at the blend interface at 39.6 MPa and cohesively in the coating layer at 76.7 MPa respectively.

C7U: P40 Fe4 as deposited and heat treated coatings at 500 °C were degraded in dH_2O for up to 96 h and assessed for ion release in ultrapure water up to 48 h. As

deposited coatings were fully resorbed beyond 24 h, HT coatings remained beyond the 96 h time point whilst coatings heat treated at 610 °C were continued to 28 d, stabilising by 21 d. HT Improved the durability of coatings by diminishing the initial exponential solubility profile in the first 2 h of submersion and ultimately reduced linear degradation rates by factors of 2.44-4.55 ± 0.35 from HT 500 °C – HT 610 °C. Furthermore HT led to a reduction in ion release rates by maximum factors of 3.9, 4.0, 4.3, 3.4 and 7.7 for P, Na, Mg, Ca and Fe respectively. Release rates ranged from 0.39 – 0.05 ppm h^{-1}, 0.10 - 0.02 ppm h^{-1} and 0.10 - 0.02 ppm h^{-1} for the as deposited, HT 500 °C, 30 min and HT 500 °C, 120 min coatings respectively.

6.5 The Bioactive Potential of Sputtered Glass Coatings

PBGs were shown to be unsuitable for use *in vitro* to form a bone like apatite layer, rendering their bio potential most suitable for therapeutic ion leaching which may be promising to enhance the osseointegration process of hydroxyapatite. A SBG coating however formed apatite *in vitro*, proving to be a potential next generation replacement for hydroxyapatite.

RF Magnetron sputtering is a promising method for the controlled deposition of adherent bio-resorbable PBGs, enabling the production of tailored compositions and coating thickness which may find application upon orthopaedic load bearing implants for their potential to leach therapeutic ions at the implant site. The versatility and low temperature capabilities of the coating procedure allowed for applications ranging from medical polymers such as PLA to metallic alloys such as Ti6Al4V.

Publications and Conferences

Stuart, B., et al., *Preferential Sputtering in Phosphate Glass Systems for the Processing of Bioactive Coatings*. Thin Solid Films, 2015.

Stuart, B.W., et al., *Degradation and Characterization of Resorbable Phosphate-Based Glass Thin-Film Coatings Applied by Radio-Frequency Magnetron Sputtering.* ACS applied materials & interfaces, 2015. 7(49): p. 27362-27372.

Stuart, B.W., et al., *Insights into Structural Characterisation and Thermal Properties of Compositionally Equivalent Vapour-condensed and Melt Quenched Glasses*. Materials & Design, 2016.

Society of Glass Technology, September 2016 – *Structural Variability and Dissolution Characteristics of RF Magnetron Sputtered Ion-Doped Phosphate Based Glass Coatings.*

World Biomaterials Congress, May 2016 – *RF Magnetron Sputtering of Bioresorbable Ion Doped Bioactive Glass Coatings.*

European and UK Society of Biomaterials, August 2014 – *RF Magnetron Sputtering of Multicomponent Ion Doped Phosphate Glasses.*

7. Future Work

Preferential Sputtering

Literary theories suggested that differential atomic masses led to proportional extraction of elements by the vacuum, leading to "preferential sputtering". Mass spectroscopy may be used to quantify the elemental proportions pumped out the chamber during glass deposition to definitively assess this belief.

Preferential sputtering of PBG within this thesis was based on the non-stoichiometric transfer of elements from target to coating compositions by assessment of the pre-use target composition and coating compositions. However, it may prove complimentary to assess the ion bombarded target surface (the racetrack) for compositional and structural variations.

Structural Analysis and *in situ* Relaxation

Whilst XPS was used to show short-range surface structures, bulk structural analysis by ^{31}P-NMR was limited to three compositions of deposited glass. ^{31}P NMR, Neutron Diffraction and Mossbauer Spectroscopy (for iron containing compositions) should be conducted for coatings in relation to deposition parameters, and to deposited compositions. Comparative studies of density, bulk polymerisation and dissolution trends should be compared to understand the structural, compositional and dissolution relationship.

Glass condensation within this thesis was limited to hyper-quenched layers, believed to be in high enthalpy stress states, therefore assisting the dissolution process. The formation enthalpy landscape may be manipulated by enhancing atomic mobility to facilitate similar structural relaxation effects to *in situ* annealing. Methods such as substrate heating or the acceleration of ions onto the substrates by utilising a substrate

bias may facilitate atomic mobility at deposition temperatures close to the T_g. Differential Scanning Calorimetry may be used to assess the endothermic recovery of the glass transition, thereby suggesting the enthalpy recovery due to structural relaxation.

Post deposition heat treatment was used to control coating dissolution through crystallisation. A heating stage capable of temperatures up to 700 °C may be adapted within UoN PVD or TEER UDP 650 Rig designs to crystallise or anneal coatings during deposition.

Process Upscaling and Elemental Blending by Co-Deposition

Preliminary investigation within the TEER UDP 650 showed enhanced reproducibility. However, due to the rotational configuration of the samples, deposition rates were limited to a maximum of 0.21 nm min^{-1}. Transition metal constituents such as TiO_2, Fe_2O_3, CuO were melt-quenched into the target structures and subsequently transferred to the condensed coatings. However by utilising the quad-cathode capabilities of the TEER UDP 650 it may prove suitable to concurrently deposit the target glass containing alkali metal components and to co-deposit the transition metal network modifiers to produce a glass blend. This approach could lead to improved reproducibility, further control of dissolution characteristics and the capability to produce layered/graded compositions.

Mechanical Properties and coating of 3D Implants

Mechanical testing was limited to uni-directional scratch testing and tensile pull off for coatings on 2D surfaces. Nano indentation and wear tests should be conducted to replicate the forces induced on a surface in operation. For example coating of a hip stem and subsequent wear analysis to replicate the implantation of the stem should be undertaken and the effects on the coating observed. Secondly, post dissolution

adhesion should be assessed to ensure that the mechanical properties are maintained in operation.

In *Vitro* Cytocompatibility

Vapour deposited coatings were manufactured for their potential to promote osteogenesis upon load bearing implants, thereby assisting in the regeneration of hard tissue and orthopaedic fixation. Coating compositions and their heat-treated variations should be assessed for cytocompatability by culturing of MG63 osteoblast cells. A preliminary cytotoxicity assay; Neutral Red should be conducted. Indicators of cellular proliferation and differentiation by Alamar Blue, Alkaline Phosphatase, and Osteocalcin may indicate an ability to stimulate cellular activity. The antimicrobial efficacy of coatings containing Cu, or Ag may be assessed for their potential to inhibit bacterial colonisation using strains such as Staphylococcus Aureus. Glass compositions may be tailored to contain more potent antimicrobial components such as Ag, or Ga.

8. References

1. *National Joint Registry*. 2013: England, Wales and Northern Ireland.
2. Zhang, S., *Biological and Biomedical Coatings Handbook Processing and Characterization*. 2011, Florida: CRC Press.
3. Pruitt, L.A. and A.M. Chakravartula, *Mechanics of Biomaterials: Fundamental Principles for Implant Design*. 2011: Cambridge University Press.
4. Navarro, M., et al., *Biomaterials in orthopaedics.* J R Soc Interface, 2008. **5**(27): p. 1137-58.
5. Charnley, J., *Anchorage of The femoral Head prothesis to the Shaft of the Femur.* The Journal of Bone and Joint Surgery, 1960. **42-B**(1): p. 28-30.
6. Jimi, E., et al., *The current and future therapies of bone regeneration to repair bone defects.* International journal of dentistry, 2012. **2012**.
7. Clarke, B., *Normal bone anatomy and physiology.* Clin J Am Soc Nephrol, 2008. **3 Suppl 3**: p. S131-9.
8. Mediaswanti, K., et al., *A review on bioactive porous metallic biomaterials.* J Biomim Biomater Tissue Eng, 2013. **18**(104): p. 2.
9. Sieniawski, J., et al., *Microstructure and mechanical properties of high strength two-phase titanium alloys.* Titanium Alloys-Advances in Properties Control, 2013: p. 69-80.
10. Gilbert, S.F., *Developmental biology: the anatomical tradition*. 2000.
11. *Bone*, in *Encyclopædia Britannica*. Encyclopædia Britannica Inc: Encyclopædia Britannica Online.
12. Le Guéhennec, L., et al., *Surface treatments of titanium dental implants for rapid osseointegration.* Dental materials, 2007. **23**(7): p. 844-854.
13. Branemark, R., et al., *Osseointegration in skeletal reconstruction and rehabilitation: a review.* J Rehabil Res Dev, 2001. **38**(2): p. 175-81.
14. Jönsson, S., K. Caine-Winterberger, and R. Brånemark, *Osseointegration amputation prostheses on the upper limbs: methods, prosthetics and rehabilitation.* Prosthetics and orthotics international, 2011. **35**(2): p. 190-200.
15. Sun, L., et al., *Material Fundamentals and Clinical Performance of Plasma-Sprayed Hydroxyapatite Coatings: a Review.* J Biomed Mater Res, 2001. **58**(5): p. 570-92.
16. Cizek, J., K.A. Khor, and Z. Prochazka, *Influence of spraying conditions on thermal and velocity properties of plasma sprayed hydroxyapatite.* Materials Science & Engineering C-Biomimetic and Supramolecular Systems, 2007. **27**(2): p. 340-344.
17. Wang, B., et al., *The shear strength and the failure mode of plasma‐sprayed hydroxyapatite coating to bone: The effect of coating thickness.* Journal of biomedical materials research, 1993. **27**(10): p. 1315-1327.
18. Administration, U.S.F.a.D., *510(K) Information Needed for Hydroxyapatite Coated Orthopedic Implants.*
19. Callahan, T.J., J.B. Gantenberg, and B.E. Sand, *Calcium phosphate (Ca-P coating) draft guidance for preparation of food and drug administration (FDA) sumbissions for orthopaedic and dental endosseuous implants* A.S. 1196, Editor. 1994, American Society for Testing and Materials: Philedelphia.
20. ASTM, *ASTM F1609-08(2014) - Standard Specification for Calcium Phosphate Coatings for Implantable Materials*, in 2014.
21. Jeong-Hoon, L., K. Su-Gwan, and L. Sung-Chul, *Histomorphometric study of bone reactions with different hydroxyapatite coating thickness on dental implants in dogs.* Thin Solid Films, 2011. **519**: p. 4618-4622.
22. Abu-Amer, Y., I. Darwech, and J.C. Clohisy, *Aseptic loosening of total joint replacements: mechanisms underlying osteolysis and potential therapies.* Arthritis Res Ther, 2007. **9 Suppl 1**: p. S6.

23. Hailer, N.P., G. Garellick, and J. Karrholm, *Uncemented and cemented primary total hip arthroplasty in the Swedish Hip Arthroplasty Register.* Acta Orthop, 2010. **81**(1): p. 34-41.
24. Bauer, T.W. and J. Schils, *The pathology of total joint arthroplasty.* Skeletal radiology, 1999. **28**(9): p. 483-497.
25. Buford, A. and T. Goswami, *Review of wear mechanisms in hip implants: Paper I - General.* Materials & Design, 2004. **25**(5): p. 385-393.
26. Amstutz, H.C., et al., *Mechanism and clinical significance of wear debris-induced osteolysis.* Clin Orthop Relat Res, 1992(276): p. 7-18.
27. Lee, J.M., et al., *Size of metallic and polyethylene debris particles in failed cemented total hip replacements.* J Bone Joint Surg Br, 1992. **74**(3): p. 380-4.
28. Bloebaum, R.D., et al., *Complications with hydroxyapatite particulate separation in total hip arthroplasty.* Clin Orthop Relat Res, 1994. **298**: p. 19-26.
29. Epinette, J.-A. and M.T. Manley, *Fifteen years of clinical experience with hydroxyapatite coatings in joint arthroplasty*. 2013: Springer.
30. Yang, Y.-C. and E. Chang, *Influence of residual stress on bonding strength and fracture of plasma-sprayed hydroxyapatite coatings on Ti–6Al–4V substrate.* Biomaterials, 2001. **22**(13): p. 1827-1836.
31. Reikerås, O. and R.B. Gunderson, *Failure of HA coating on a gritblasted acetabular cup: 155 patients followed for 7-10 years.* Acta Orthop Scand, 2002. **73**(1): p. 104-108.
32. Lee, J.J., L. Rouhfar, and O.R. Beirne, *Survival of hydroxyapatite-coated implants: a meta-analytic review.* Journal of Oral and Maxillofacial Surgery, 2000. **58**(12): p. 1372-1379.
33. Jones, J.D., et al., *Clinical evaluation of hydroxyapatite-coated titanium plasma-sprayed and titanium plasma-sprayed cylinder dental implants: a preliminary report.* Oral Surgery, Oral Medicine, Oral Pathology, Oral Radiology, and Endodontology, 1997. **84**(2): p. 137-141.
34. Bunker, B.C., G.W. Arnold, and J.A. Wilder, *Phosphate Glass Dissolution In Aqueous Solution.* Journal of Non-Crystalline Solids, 1984. **64**(3): p. 291-316.
35. Ahmed, I., et al., *Composites for Bone Repair: Phosphate Glass Fibre Reinforced PLA with Varying Fibre Architecture.* J Mater Sci Mater Med, 2011. **22**(8): p. 1825-34.
36. Knowles, J.C., *Phosphate Based Glasses for Biomedical Applications.* Journal of Materials Chemistry, 2003. **13**(10): p. 2395-2401.
37. Han, N., et al., *Influence of screw holes and gamma sterilization on properties of phosphate glass fiber-reinforced composite bone plates.* J Biomater Appl, 2013. **27**(8): p. 990-1002.
38. Liu, X.L., et al., *Magnesium Coated Bioresorbable Phosphate Glass Fibres: Investigation of the Interface Between Fibre and Polyester Matrices.* Biomed Research International, 2013. **13**.
39. *Bio-Glasses : An Introduction*, ed. J. Jones and A. Clare. 2012: John Wileys and Sons Ltd.
40. West, A.R., *Solid State Chemistry and Its Applications*. 2nd ed. 2014: John Wiley & Sons Ltd.
41. Ishii, K. and H. Nakayama, *Structural relaxation of vapor-deposited molecular glasses and supercooled liquids.* Physical Chemistry Chemical Physics (Incorporating Faraday Transactions), 2014. **16**(24): p. 12073-12092.
42. Hoppe, A., N.S. Guldal, and A.R. Boccaccini, *A review of the biological response to ionic dissolution products from bioactive glasses and glass-ceramics.* Biomaterials, 2011. **32**(11): p. 2757-74.
43. *NDT Resource Center*. [cited 2014 June 23]; Thermal Conductivity].
44. Beall, G.H. and L.R. Pinckney, *Nanophase Glass-Ceramics.* Journal of the American Ceramic Society, 1999. **82**(1): p. 5-16.
45. Jones, J.R., *Review of bioactive glass: from Hench to hybrids.* Acta biomaterialia, 2013. **9**(1): p. 4457-4486.
46. Hench, L.L., *The Story of Bioglass.* J Mater Sci Mater Med, 2006. **17**(11): p. 967-78.

47. Shaharuddin, S., *Manufacture and Characterisation of Novel Resorbable Phosphate Based Glass Fibres for Biomedical Applications*. 2012, The University of Nottingham: Nottingham.
48. Brow, R.K., *Review: the Structure of Simple Phosphate Glasses.* Journal of Non-Crystalline Solids, 2000. **263**(1-4): p. 1-28.
49. Omrani, R.O., et al., *Structural and Thermochemical Properties of Sodium Magnesium Phosphate Glasses.* Journal of Alloys and Compounds, 2015. **632**: p. 766-771.
50. Ahmed, I., et al., *Cytocompatibility and Effect of Increasing MgO Content in a Range of Quaternary Invert Phosphate-Based Glasses.* J Biomater Appl, 2010. **24**(6): p. 555-75.
51. Neel, E.A.A., et al., *Doping of a high calcium oxide metaphosphate glass with titanium dioxide.* Journal of Non-Crystalline Solids, 2009. **355**(16): p. 991-1000.
52. Kasuga, T., et al., *Calcium Phosphate Invert Glasses and Glass-Ceramics with Apatite-Forming Ability.* Bioceramics 15, 2003. **240-2**: p. 265-268.
53. Neel, E.A.A., et al., *Structure and properties of strontium-doped phosphate-based glasses.* Journal of the Royal Society Interface, 2008: p. rsif. 2008.0348.
54. Massera, J., et al., *Thermal properties and surface reactivity in simulated body fluid of new strontium ion-containing phosphate glasses.* Journal of Materials Science: Materials in Medicine, 2013. **24**(6): p. 1407-1416.
55. Brauer, D.S., et al., *Fluoride-containing bioactive glass-ceramics.* Journal of Non-Crystalline Solids, 2012. **358**(12-13): p. 1438-1442.
56. Kiani, A., et al., *Titanium-containing bioactive phosphate glasses.* Philos Trans A Math Phys Eng Sci, 2012. **370**(1963): p. 1352-75.
57. Kasuga, T., T. Hattori, and M. Niinomi, *Phosphate glasses and glass-ceramics for biomedical applications.* Phosphorus Research Bulletin, 2012. **26**(0): p. 8-15.
58. Yu, X.Y., et al., *Properties and Structure of Sodium-Iron Phosphate Glasses.* Journal of Non-Crystalline Solids, 1997. **215**(1): p. 21-31.
59. Ahmed, I., et al., *Processing, Characterisation and Biocompatibility of Iron-Phosphate Glass Fibres for Tissue Engineering.* Biomaterials, 2004. **25**(16): p. 3223-3232.
60. Neel, E.A., et al., *Characterisation of Antibacterial Copper Releasing Degradable Phosphate Glass Fibres.* Biomaterials, 2005. **26**(15): p. 2247-54.
61. Avent, A.G., et al., *The Dissolution of Silver-Sodium-Calcium-Phosphate Glasses for the Control of Urinary Tract Infections.* Journal of Non-Crystalline Solids, 2003. **328**(1-3): p. 31-39.
62. Ahmed, I., et al., *Antimicrobial Effect of Silver-Doped Phosphate-Based Glasses.* J Biomed Mater Res A, 2006. **79**(3): p. 618-26.
63. Krishnan, V. and T. Lakshmi, *Bioglass: A Novel Biocompatible Innovation.* Journal of advanced pharmaceutical technology & research, 2013. **4**(2): p. 78.
64. Fredholm, Y.C., et al., *Influence of strontium for calcium substitution in bioactive glasses on degradation, ion release and apatite formation.* J R Soc Interface, 2012. **9**(70): p. 880-9.
65. Franks, K., I. Abrahams, and J. Knowles, *Development of soluble glasses for biomedical use Part I: In vitro solubility measurement.* Journal of Materials Science: Materials in Medicine, 2000. **11**(10): p. 609-614.
66. Ahmed, I., et al., *Phosphate Glasses for Tissue Engineering: Part 1. Processing and Characterisation of a Ternary-Based P2O5–CaO–Na2O Glass System.* Biomaterials, 2004. **25**(3): p. 491-499.
67. Gentleman, E., et al., *The effects of strontium-substituted bioactive glasses on osteoblasts and osteoclasts in vitro.* Biomaterials, 2010. **31**(14): p. 3949-56.
68. Lu, Y., et al., *Synthesis and characterization of Ca–Sr–P coating on pure magnesium for biomedical application.* Ceramics International, 2014. **40**(3): p. 4559-4565.
69. Lakhkar, N., et al., *Titanium and strontium-doped phosphate glasses as vehicles for strontium ion delivery to cells.* Journal of biomaterials applications, 2011. **25**(8): p. 877-893.

70. Andersen, O.Z., et al., *Accelerated bone ingrowth by local delivery of strontium from surface functionalized titanium implants.* Biomaterials, 2013. **34**(24): p. 5883-90.
71. Boyd, A.R., et al., *Strontium-substituted hydroxyapatite coatings deposited via a co-deposition sputter technique.* Materials Science and Engineering: C, 2015. **46**: p. 290-300.
72. Cuneyt Tas, A., *X-ray-Amorphous Calcium Phosphate (ACP) Synthesis in a Simple Biomineralization Medium.* Journal of Materials Chemistry B, 2013(35): p. 4511-4520.
73. Ding, H., et al., *Toward a detailed understanding of magnesium ions on hydroxyapatite crystallization inhibition.* Crystal Growth & Design, 2014. **14**(2): p. 763-769.
74. Kasuga, T., et al., *Bioactive calcium phosphate invert glass-ceramic coating on β-type Ti–29Nb–13Ta–4.6 Zr alloy.* Biomaterials, 2003. **24**(2): p. 283-290.
75. Koo, J., B.-S. Bae, and H.-K. Na, *Raman spectroscopy of copper phosphate glasses.* Journal of non-crystalline solids, 1997. **212**(2): p. 173-179.
76. Shih, P.Y., S.W. Yung, and T.S. Chin, *FTIR and XPS Studies of P2O5-Na2O-CuO Glasses.* Journal of Non-Crystalline Solids, 1999. **244**(2-3): p. 211-222.
77. Shih, P., J. Ding, and S. Lee, *31P MAS-NMR and FTIR Analyses on the Structure of CuO-Containing Sodium Poly-and Meta-Phosphate Glasses.* Materials chemistry and physics, 2003. **80**(2): p. 391-396.
78. Ahmed, I., et al., *The structure and properties of silver-doped phosphate-based glasses.* Journal of Materials Science, 2007. **42**(23): p. 9827-9835.
79. Singh, S., M.D. Ediger, and J.J. de Pablo, *Ultrastable glasses from in silico vapour deposition.* Nat Mater, 2013. **12**(2): p. 139-144.
80. Yu, H., et al., *Suppression of β relaxation in vapor-deposited ultrastable glasses.* Physical review letters, 2015. **115**(18): p. 185501.
81. Tournier, R.F., *Formation temperature of ultra-stable glasses and application to ethylbenzene.* Chemical Physics Letters, 2015. **641**: p. 9-13.
82. Kearns, K.L., et al., *Influence of substrate temperature on the stability of glasses prepared by vapor deposition.* Journal of Chemical Physics, 2007. **127**(15): p. 154702-154702.
83. Dawson, K.J., et al., *Anisotropic structure and transformation kinetics of vapor-deposited indomethacin glasses.* The Journal of Physical Chemistry B, 2010. **115**(3): p. 455-463.
84. Rao, K.J., *Structural Chemistry of Glasses*. 2002: Elsevier.
85. Guo, Y., et al., *Ultrastable nanostructured polymer glasses.* Nature materials, 2012. **11**(4): p. 337-343.
86. Kokubo, T. and H. Takadama, *How Useful is SBF in Predicting in Vivo Bone Bioactivity?* Biomaterials, 2006. **27**(15): p. 2907-2915.
87. Drouet, C., *Apatite formation: why it may not work as planned, and how to conclusively identify apatite compounds.* BioMed research international, 2013. **2013**.
88. Kokubo, T., et al., *Solutions able to reproduce in vivo surface‐structure changes in bioactive glass‐ceramic A‐W3.* Journal of biomedical materials research, 1990. **24**(6): p. 721-734.
89. Li, Y., et al., *Early stages of calcium phosphate formation on bioactive borosilicate glass in aqueous phosphate solution.* Journal of the American Ceramic Society, 2008. **91**(5): p. 1528-1533.
90. Pourhashem, S. and A. Afshar, *Double layer bioglass-silica coatings on 316L stainless steel by sol–gel method.* Ceramics International, 2014. **40**(1): p. 993-1000.
91. Plewinski, M., et al., *The effect of crystallization of bioactive bioglass 45S5 on apatite formation and degradation.* Dental Materials, 2013. **29**(12): p. 1256-1264.
92. Tas, A.C., *The Use of Physiological Solutions or Media in Calcium Phosphate Synthesis and Processing.* Acta Biomaterialia, 2014. **10**(5): p. 1771-1792.
93. Yamamoto, S., et al., *Fundamental Study on Apatite Precipititate Ability of CaO-MgO-SiO2 Compounders Employed Pseudo Body Solution of Application for Biomaterials.* Journal of American Ceramic Society, 2012. **48**(2): p. 180-184.

94. Varila, L., et al., *Surface Reactions of Bioactive Glasses in Buffered Solutions.* Journal of the European Ceramic Society, 2012. **32**(11): p. 2757-2763.
95. Fagerlund, S., L. Hupa, and M. Hupa, *Comparison of Reactions of Bioactive Glasses in Different Aqueous Solutions.* Advances in Bioceramics and Biotechnologies, 2010. **218**: p. 101-113.
96. Han, L. and T. Okiji, *Bioactivity Evaluation of Three Calcium Silicate-Based Endodontic Materials.* Int Endod J, 2013. **46**(9): p. 808-14.
97. Niiranen, H. and P. Tormala, *Bioabsorbable polymer plates coated with bioactive glass spheres.* J Mater Sci Mater Med, 1999. **10**(12): p. 707-10.
98. Neel, E.A., et al., *Effect of Iron on the Surface, Degradation and Ion Release Properties of Phosphate-Based Glass Fibres.* Acta Biomaterialia, 2005. **1**(5): p. 553-563.
99. Gao, H., T. Tan, and D. Wang, *Dissolution Mechanism and Release Kinetics of Phosphate Controlled Release Glasses in Aqueous Medium.* J Control Release, 2004. **96**(1): p. 29-36.
100. Sharmin, N., et al., *Effect of Boron Addition on the Thermal, Degradation, and Cytocompatibility Properties of Phosphate-Based Glasses.* BioMed Research International, 2013. **2013**: p. 12.
101. Neel, E.A.A., et al., *Bioactive Functional Materials: a Perspective on Phosphate-Based Glasses.* Journal of Materials Chemistry, 2009. **19**(6): p. 690-701.
102. Haque, P., et al., *Degradation Properties and Microstructural Analysis of 40P2O5–24MgO–16CaO–16Na2O–4Fe2O3 Phosphate Glass Fibres.* Journal of Non-Crystalline Solids, 2013. **375**: p. 99-109.
103. Cozien-Cazuc, S., et al., *Effects of Aqueous Aging on the Mechanical Properties of P40Na20Ca16Mg24 Phosphate Glass Fibres.* Journal of Materials Science - Materials in Electronics, 2008. **43**(14): p. 4834-4839.
104. Parsons, A., et al., *Properties of sodium-based ternary phosphate glasses produced from readily available phosphate salts.* Journal of non-crystalline solids, 2006. **352**(50): p. 5309-5317.
105. Uo, M., et al., *Properties and cytotoxicity of water soluble Na2O-CaO-P2O5 glasses.* Biomaterials, 1998. **19**(24): p. 2277-84.
106. Christie, J.K., et al., *Nanoscale Chains Control the Solubility of Phosphate Glasses for Biomedical Applications.* J Phys Chem B, 2013. **117**(36): p. 10652-7.
107. Stahli, C., et al., *Characterization of aqueous interactions of copper-doped phosphate-based glasses by vapour sorption.* Acta Biomater, 2014. **10**(7): p. 3317-26.
108. Ahmed, I., et al., *Comparison of phosphate-based glasses in the range 50P2O5–(50−x)CaO–xNa2O prepared using different precursors.* European Journal of Glass Science and Technology Part A, 2007. **49**(2): p. 63-72.
109. Hoppe, U., et al., *The Fe-O coordination in iron phosphate glasses by X-ray diffraction with high energy photons.* Journal of Physics-Condensed Matter, 2003. **15**(36): p. 6143-6153.
110. Al-Hasni, B. and G. Mountjoy, *Structural investigation of iron phosphate glasses using molecular dynamics simulation.* Journal of Non-Crystalline Solids, 2011. **357**(15): p. 2775-2779.
111. Hoppe, U., D. Stachel, and D. Beyer, *The Oxygen Coordination of Metal Ions in Phosphate and Silicate Glasses Studied by a Combination of X-ray and Neutron Diffraction.* Physica Scripta, 1995. **T57**: p. 122-126.
112. Franks, K., et al., *The effect of MgO on the solubility behavior and cell proliferation in a quaternary soluble phosphate based glass system.* Journal of Materials Science: Materials in Medicine, 2002. **13**(6): p. 549-556.
113. Haque, *Degradation properties and microstructural analysis of 40P2O5–24MgO–16CaO–16Na2O–4Fe2O3 phosphate glass fibres.* Journal of Non Crystalline Solids, 2013.
114. Cozien-Cazuc, S., et al., *Real-Time Dissolution of P40Na20Ca16Mg24 Phosphate Glass Fibers.* Journal of Non-Crystalline Solids, 2009. **355**(50-51): p. 2514-2521.

115. Choueka, J., et al., *Effect of Annealing Temperature on the Degradation of Reinforcing Fibers for Absorbable Implants.* Journal of biomedical materials research, 1995. **29**(11): p. 1309-1315.
116. Neel, E.A. and J. Knowles, *Physical and biocompatibility studies of novel titanium dioxide doped phosphate-based glasses for bone tissue engineering applications.* Journal of Materials Science: Materials in Medicine, 2008. **19**(1): p. 377-386.
117. Mulligan, A., M. Wilson, and J. Knowles, *Effect of increasing silver content in phosphate‐based glasses on biofilms of Streptococcus sanguis.* Journal of Biomedical Materials Research Part A, 2003. **67**(2): p. 401-412.
118. Mulligan, A., M. Wilson, and J. Knowles, *The effect of increasing copper content in phosphate-based glasses on biofilms of Streptococcus sanguis.* Biomaterials, 2003. **24**(10): p. 1797-1807.
119. Rahaman, M.N., B.S. Bal, and W. Huang, *Review: emerging developments in the use of bioactive glasses for treating infected prosthetic joints.* Mater Sci Eng C Mater Biol Appl, 2014. **41**: p. 224-31.
120. Ferraris, S., et al., *Antibacterial and bioactive nanostructured titanium surfaces for bone integration.* Applied Surface Science, 2014. **311**: p. 279-291.
121. Nomura, T. and K. Masui, *Anion-Selective Field-Effect Transistor Sensor Using RF-Sputtering Film of Alkali Metal-Free Lead Phosphate Glass Containing Silver Oxide.* Bulletin of the Chemical Society of Japan, 1992. **65**(9): p. 2338-2342.
122. Lee, T., et al., *Characteristics of plasma-sprayed bioactive glass coatings on Ti-6A1-4V alloy: an in vitro study.* Surface and Coatings Technology, 1996. **79**(1): p. 170-177.
123. Gomez‐Vega, J., E. Saiz, and A. Tomsia, *Glass‐based coatings for titanium implant alloys.* Journal of biomedical materials research, 1999. **46**(4): p. 549-559.
124. Sola, A., D. Bellucci, and V. Cannillo, *Enamelled coatings produced with low-alkaline bioactive glasses.* Surface and Coatings Technology, 2014. **248**: p. 1-8.
125. Al-Noaman, A., S.C. Rawlinson, and R.G. Hill, *Bioactive glass-stoichimetric wollastonite glass alloys to reduce TEC of bioactive glass coatings for dental implants.* Materials Letters, 2013. **94**: p. 69-71.
126. Bolelli, G., et al., *Microstructural and in vitro characterisation of high-velocity suspension flame sprayed (HVSFS) bioactive glass coatings.* Journal of the European Ceramic Society, 2009. **29**(11): p. 2249-2257.
127. Boccaccini, A., et al., *Electrophoretic deposition of biomaterials.* Journal of The Royal Society Interface, 2010. **7**(Suppl 5): p. S581-S613.
128. Albayrak, O., O. El-Atwani, and S. Altintas, *Hydroxyapatite coating on titanium substrate by electrophoretic deposition method: effects of titanium dioxide inner layer on adhesion strength and hydroxyapatite decomposition.* Surface and Coatings Technology, 2008. **202**(11): p. 2482-2487.
129. Chen, F., et al., *Biocompatibility of electrophoretical deposition of nanostructured hydroxyapatite coating on roughen titanium surface: in vitro evaluation using mesenchymal stem cells.* Journal of Biomedical Materials Research Part B: Applied Biomaterials, 2007. **82**(1): p. 183-191.
130. Pishbin, F., et al., *Single-step electrochemical deposition of antimicrobial orthopaedic coatings based on a bioactive glass/chitosan/nano-silver composite system.* Acta biomaterialia, 2013. **9**(7): p. 7469-7479.
131. Ladwig, A., et al., *Atmospheric plasma deposition of glass coatings on aluminum.* Surface and Coatings Technology, 2007. **201**(14): p. 6460-6464.
132. Wang, C., Z. Chen, and M. Wang, *Fabrication and characterization of bioactive glass coatings produced by the ion beam sputter deposition technique.* Journal of Materials Science: Materials in Medicine, 2002. **13**(3): p. 247-251.
133. Hamadouche, M., et al., *Bioactivity of sol‐gel bioactive glass coated alumina implants.* Journal of biomedical materials research, 2000. **52**(2): p. 422-429.

134. Sepulveda, P., J. Jones, and L. Hench, *In vitro dissolution of melt‐derived 45S5 and sol‐gel derived 58S bioactive glasses.* Journal of biomedical materials research, 2002. **61**(2): p. 301-311.
135. Liu, D.-M., Q. Yang, and T. Troczynski, *Sol–gel hydroxyapatite coatings on stainless steel substrates.* Biomaterials, 2002. **23**(3): p. 691-698.
136. Kim, H.W., et al., *Hydroxyapatite and fluor‐hydroxyapatite layered film on titanium processed by a sol‐gel route for hard‐tissue implants.* Journal of Biomedical Materials Research Part B: Applied Biomaterials, 2004. **71**(1): p. 66-76.
137. Ren, M., et al., *Calcium phosphate glass/MgF 2 double layered composite coating for improving the corrosion resistance of magnesium alloy.* Journal of Alloys and Compounds, 2014. **591**: p. 34-40.
138. Nowling, G., et al., *Chamberless plasma deposition of glass coatings on plastic.* Plasma Sources Science and Technology, 2005. **14**(3): p. 477.
139. Ong, J.L., et al., *Structure, solubility and bond strength of thin calcium phosphate coatings produced by ion beam sputter deposition.* Biomaterials, 1992. **13**(4): p. 249-54.
140. Yang, Y., K.-H. Kim, and J.L. Ong, *A review on calcium phosphate coatings produced using a sputtering process—an alternative to plasma spraying.* Biomaterials, 2005. **26**(3): p. 327-337.
141. Nomura, T. and K. Masui, *Experimental Evidence for Anion Selective Behavior of Ion Beam Sputtered Film of Alkali Metal‐Free Phosphate Glass Deposited on MOS‐Diode.* Journal of The Electrochemical Society, 1993. **140**(5): p. 1234-1237.
142. Wolke, J.G., et al., *Study of the Surface Characteristics of Magnetron-Sputter Calcium Phosphate Coatings.* J Biomed Mater Res, 1994. **28**(12): p. 1477-84.
143. Yonggang, Y., et al., *Preparation and characterization of RF magnetron sputtered calcium pyrophosphate coatings.* Journal of Biomedical Materials Research Part A, 2006. **76A**(4): p. 744-752.
144. Shi, J.Z., et al., *Application of magnetron sputtering for producing bioactive ceramic coatings on implant materials.* Bull. Mater. Sci, 2008. **31**(6): p. 877-884.
145. Van Dijk, K., et al., *Influence of annealing temperature on RF magnetron sputtered calcium phosphate coatings.* Biomaterials, 1996. **17**(4): p. 405-10.
146. Van Dijk, K., et al., *Study of the influence of oxygen on the composition of thin films obtained by rf-sputtering from a CA4PO43 OH target.* Thin Solid Films, 1997. **304**: p. 191-195.
147. Lo, W.J. and D.M. Grant, *Hydroxyapatite thin films deposited onto uncoated and (Ti,Al, V)N-coated Ti alloys.* J Biomed Mater Res, 1999. **46**(3): p. 408-17.
148. Jansen, J., et al., *Application of magnetron sputtering for producing ceramic coatings on implant materials.* Clinical oral implants research, 1993. **4**(1): p. 28-34.
149. Ong, J.L., G.N. Raikar, and T.M. Smoot, *Properties of calcium phosphate coatings before and after exposure to simulated biological fluid.* Biomaterials, 1997. **18**(19): p. 1271-1275.
150. Ong, J.L., et al., *Bone response to radio frequency sputtered calcium phosphate implants and titanium implants in vivo.* J Biomed Mater Res, 2002. **59**(1): p. 184-90.
151. Yamashita, K., et al., *Preparation of Apatite Thin Films Through RF-Sputtering from Calcium Phosphate Glasses.* Journal of the American Ceramic Society, 1994. **77**(9): p. 2401-2407.
152. Lo, W. and D. Grant, *Hydroxyapatite Thin Films Deposited onto Uncoated and (Ti, Al, V) N‐Coated Ti Alloys.* Journal of biomedical materials research, 1999. **46**(3): p. 408-417.
153. Ding, S.J., C.P. Ju, and J.H.C. Lin, *Characterization of hydroxyapatite and titanium coatings sputtered on Ti‐6Al‐4V substrate.* Journal of biomedical materials research, 1999. **44**(3): p. 266-279.

154. Ding, S.J., C.P. Ju, and C. Lin J.-H, *Immersion behavior of RF magnetron-assisted sputtered hydroxyapatite/titanium coatings in simulated body fluid.* Journal of biomedical materials research, 1999. **47**(4): p. 551-563.
155. Lo, W., et al., *Physical, chemical, and biological characterization of pulsed laser deposited and plasma sputtered hydroxyapatite thin films on titanium alloy.* Journal of biomedical materials research, 2000. **50**(4): p. 536-545.
156. Boyd, A.R., C. O'Kane, and B.J. Meenan, *Control of Calcium Phosphate Thin Film Stoichiometry Using Multi-Target Sputter Deposition.* Surface and Coatings Technology, 2013. **233**(0): p. 131-139.
157. Boyd, A.R., et al., *Sputter deposition of calcium phosphate/titanium dioxide hybrid thin films.* Materials Science and Engineering, 2008. **C**(28): p. 228-236.
158. Boyd, A., M. Akay, and B. Meenan, *Influence of target surface degradation on the properties of rf magnetron‐sputtered calcium phosphate coatings.* Surface and interface analysis, 2003. **35**(2): p. 188-198.
159. Coe, S.C., *The deposition, characterisation and biocompatibility of hydroxyapatite and silicon doped hydroxyapatite thin film coatings for orthopaedic applications*. 2008, University of Nottingham.
160. Marriott, T., *Magnetron Sputtering of Bioceramics*. 2011, University of Nottingham.
161. van der Wal, E., et al., *Initial reactivity of rf magnetron sputtered calcium phosphate thin films in simulated body fluids.* Applied Surface Science, 2005. **246**(1-3): p. 183-192.
162. Wolke, J.G.C., et al., *In Vivo Dissolution behaviour of Various RF magnetron-sputtering Ca-P coatings on roughened titanium implants.* Biomaterials, 2003. **24**(14): p. 2623-2629.
163. Yang, Y.Z., et al., *Effect of post-deposition heating temperature and the presence of water vapor during heat treatment on crystallinity of calcium phosphate coatings.* Biomaterials, 2003. **24**(28): p. 5131-5137.
164. Wolke, J., et al., *Study of the surface characteristics of magnetron‐sputter calcium phosphate coatings.* Journal of biomedical materials research, 1994. **28**(12): p. 1477-1484.
165. Gross, K., V. Gross, and C.C. Berndt, *Thermal analysis of amorphous phases in hydroxyapatite coatings.* J. Am. Ceram. Soc., 1998. **81**(1): p. 106-112.
166. Narushima, T., et al., *Preparation of calcium phosphate films by radiofrequency magnetron sputtering.* Materials transactions, 2005. **46**(10): p. 2246-2252.
167. Srinivas, K., et al., *Effect of sputtering pressure and power on composition, surface roughness, microstructure and magnetic properties of as-deposited Co2FeSi thin films.* Thin Solid Films, 2014. **558**: p. 349-355.
168. Yoshinari, M., et al., *Influence of rapid heating with infrared radiation on RF magnetron-sputtered calcium phosphate coatings.* J Biomed Mater Res, 1997. **37**(1): p. 60-7.
169. Mardare, C.C., et al., *Deposition of Bioactive Glass-Ceramic Thin-Films by RF Magnetron Sputtering.* Journal of the European Ceramic Society, 2003. **23**(7): p. 1027-1030.
170. Stan, G.E. and D. Bojin, *Adherant Glass-Ceramic Thin Layer with Bioactive Potential Deposited by Magnetron Sputtering Techniques.* U.P.B Sci. Bull., Series B, 2010. **72**(2): p. 187-196.
171. Stan, G.E., et al., *Bioactive Glass Thin Films Deposited by Magnetron Sputtering Technique: The Role of Working Pressure.* Applied Surface Science, 2010. **256**(23): p. 7102-7110.
172. Stan, G.E., et al., *Biomineralization Capability of Adherent Bio-Glass Films Prepared by Magnetron Sputtering.* J Mater Sci Mater Med, 2010. **21**(4): p. 1047-55.
173. Stan, G.E., et al., *Effect of Anealing Upon the Structure and Adhesion Properties of Sputtered Bio-Glass/Titanium Coatings.* Applied Surface Science, 2009. **255**(22): p. 9132-9138.

174. Berbecaru, C. and G.E. Stan, *The bioactivity mechanism of magnetron sputtered bioglass thin films.* Applied Surface Science, 2012. **258**(24): p. 9840-9848.
175. Stan, G.E., et al., *On the Bioactivity of Adherent Bioglass Thin Films Synthesized by Magnetron Sputtering Techniques.* Thin Solid Films, 2010. **518**(21): p. 5955-5964.
176. Popa, A.-C., et al., *Submicrometer Hollow Bioglass Cones Deposited by Radio Frequency Magnetron Sputtering: Formation Mechanism, Properties, and Prospective Biomedical Applications.* ACS applied materials & interfaces, 2016. **8**(7): p. 4357-4367.
177. Popa, A., et al., *Superior biofunctionality of dental implant fixtures uniformly coated with durable bioglass films by magnetron sputtering.* Journal of the mechanical behavior of biomedical materials, 2015. **51**: p. 313-327.
178. Berbecaru, C., et al., *The bioactivity mechanism of magnetron sputtered bioglass thin films.* Applied Surface Science, 2012. **258**(24): p. 9840-9848.
179. Stan, G.E., *Strong Bonding between sputtered bioglass-ceramic films and Ti-substrate Implants induced by atomic inter-diffusion post deposition heat treatments.*
180. Popa, A., et al., *Nanomechanical characterization of bioglass films synthesized by magnetron sputtering.* Thin Solid Films, 2014. **51**: p. 313-327.
181. Massera, J., et al., *Crystallization mechanism of the bioactive glasses, 45S5 and S53P4.* Journal of the American Ceramic Society, 2012. **95**(2): p. 607-613.
182. Kofstad, P., *High-temperature oxidation of titanium.* Journal of the Less Common Metals, 1967. **12**(6): p. 449-464.
183. Bull, S. and E. Berasetegui, *An overview of the potential of quantitative coating adhesion measurement by scratch testing.* Tribology International, 2006. **39**(2): p. 99-114.
184. Mittal, K., *Adhesion measurement of thin films.* 1976. **3**(1): p. 21-42.
185. Bull, S.J., *Failure mode maps in the thin film scratch adhesion test.* Tribology International, 1997. **30**(7): p. 491-498.
186. Toque, J.A., et al., *Adhesion failure behavior of sputtered calcium phosphate thin film coatings evaluated using microscratch testing.* Journal of the Mechanical Behavior of Biomedical Materials, 2010. **3**(4): p. 324-330.
187. Mohseni, E., E. Zalnezhad, and A.R. Bushroa, *Comparative investigation on the adhesion of hydroxyapatite coating on Ti-6Al-4V implant: A review paper.* International Journal of Adhesion and Adhesives, 2014. **48**: p. 238-257.
188. Filiaggi, M.J., N.A. Coombs, and R.M. Pilliar, *Characterization of the interface in the plasma-sprayed HA coating/Ti-6Al-4V implant system.* J Biomed Mater Res, 1991. **25**(10): p. 1211-29.
189. Kim, H.W., et al., *On the Feasibility of Phosphate Glass and Hydroxyapatite Engineered Coating on Titanium.* Journal of Biomedical Materials Research Part A, 2005. **75**(3): p. 656-667.
190. Goller, G., *The effect of bond coat on mechanical properties of plasma sprayed bioglass-titanium coatings.* Ceramics International, 2004. **30**(3): p. 351-355.
191. Lopez-Esteban, S., et al., *Bioactive glass coatings for orthopedic metallic implants.* Journal of the European Ceramic Society, 2003. **23**(15): p. 2921-2930.
192. Wolke, J.G.C., et al., *Stability of radiofrequency magnetron sputtered calcium phosphate coatings under cyclically loaded conditions.* Biomaterials, 1997. **18**(6): p. 483-8.
193. Stan, G.E., *Strong Bonding between sputtered bioglass-ceramic films and Ti-substrate implants induced by atomic inter-diffusion post- deposition heat treatments.*
194. Takahashi, K., et al., *Characterization and in vitro evaluation of biphasic calcium pyrophosphate-tricalciumphosphate radio frequency magnetron sputter coatings.* J Biomed Mater Res A, 2008. **84**(3): p. 682-90.
195. Thian, E.S., et al., *Magnetron co-sputtered silicon-containing hydroxyapatite thin films - an in vitro study.* Biomaterials, 2005. **26**(16): p. 2947-2956.
196. Kim, H.-W., et al., *Calcium phosphates and glass composite coatings on zirconia for enhanced biocompatibility.* Biomaterials, 2004. **25**(18): p. 4203-4213.

197. Hasan, M.S., et al., *Material Characterisation and Cytocompatibility Assessment of Quinternary Phosphate Glasses.* Journal of Materials Science Materials in Medicine, 2012. **23**(10): p. 2531-2541.
198. Costa, D.O., et al., *The differential regulation of osteoblast and osteoclast activity by surface topography of hydroxyapatite coatings.* Biomaterials, 2013. **34**(30): p. 7215-7226.
199. Webster, T.J., et al., *Enhanced functions of osteoblasts on nanophase ceramics.* Biomaterials, 2000. **21**(17): p. 1803-10.
200. Aufderheide, E., *Coatings Technology Handbook: Sputtered Thin Film Coatings*. 3 ed. 2006: Taylor & Francis Group, LLC.
201. Sree Harsha, K.S., *Principles of Physical Vapor Deposition of Thin Films*. Vol. 1. 2006, Great Britain: Elsevier.
202. Berg, S. and I.V. Katardjiev, *Preferential sputtering effects in thin film processing.* Journal of Vacuum Science & Technology a-Vacuum Surfaces and Films, 1999. **17**(4): p. 1916-1925.
203. Maaloul, L. and L. Stafford, *Measurements of sputtered neutrals and ions and investigation of their roles on the plasma properties during rf magnetron sputtering of Zn and ZnO targets.* Journal of Vacuum Science & Technology A, 2013. **31**(6): p. 061306.
204. Alfonso, E., G. Cubillos, and J. Olaya, *Thin film growth through sputtering technique and its applications*. 2012: INTECH Open Access Publisher.
205. Kelly, R., *On the Role of Gibbsian Segregation in Causing Preferential Sputtering.* Surface and Interface Analysis, 1985. **7**(1): p. 1-7.
206. Miotello, A., et al., *Alkali-Metal Segregation at Glass Surfaces during Electron-Irradiation.* Physical Review B, 1991. **43**(5): p. 3831-3836.
207. Battaglin, G., et al., *Alkali Migration in Ion Irradiated Glasses.* Nuclear Instruments & Methods in Physics Research Section B-Beam Interactions with Materials and Atoms, 1984. **1**(2-3): p. 511-515.
208. Malherbe, J.B., et al., *Preferential Sputtering of GaAs.* Surface and Interface Analysis, 1992. **18**: p. 491-495.
209. Boyd, A.R., C.O. Kane, and B.J. Meenan, *Control of Calcium Phosphate Thin Film Stoichiometry Using Multi-Target Sputter Deposition.* Surface and Coatings Technology, 2013. **233**: p. 131-139.
210. Botterill, N.W., *Deposition and characterisation of thin film nickel-titanium shape memory alloys for microactuation*, in *Mechanical Engineering*. 2002, The University of Nottingham: Nottingham.
211. Zhang, S., L. Li, and A. Kumar, *Materials Characterization Techniques*. 2009, Taylor & Francis Group.
212. Smith, B.C., *Fundamentals of Fourier transform infrared spectroscopy*. 2011: CRC press.
213. Walls, J., *Methods of surface analysis: techniques and applications*. 1990, CUP Archive.
214. Brown, M.E., *Introduction to Thermal Analysis : Techniques and Applications*. 2nd ed. 2001, New York: Kluwer Academic Publishers.
215. Webb, P.A., *Volume and density determinations for particle technologists.* Micromeritics Instrument Corp, 2001. **2**(16): p. 01.
216. Yuan, Y. and T.R. Lee, *Contact angle and wetting properties*, in *Surface science techniques*. 2013, Springer. p. 3-34.
217. Mittal, K.L., *Adhesion Measurement of Films & Coatings: Volume 2*. 2001.
218. Taylor, H.E., *Inductively coupled plasma-mass spectrometry: practices and techniques*. 2001: Academic Press.
219. ISO, *ISO 23317:2014: Implants for Surgery- In Vitro evaluation for apatite-forming ability of implant materials*. 2014.
220. ISO, *ISO 23317:2007: Implants for Surgery - In Vitro evaluation for apatite-forming ability of implant materials.* 2007.

221. Stanciu, G., et al., *Investigation of the hydroxyapatite growth on bioactive glass surface.* Journal of Biomedical & Pharmaceutical Engineering, 2007. **1**(1): p. 34-39.
222. Wagner, C.D., et al., Nist Standard Reference Database.
223. Puziy, A.M., et al., *XPS and NMR Studies of Phosphoric Acid Activated Carbons.* Carbon, 2008. **46**(15): p. 2113-2123.
224. Wagner, C.D., *Handbook of x-ray photoelectron spectroscopy: a reference book of standard data for use in x-ray photoelectron spectroscopy*. 1979: Physical Electronics Division, Perkin-Elmer Corp.
225. Dementjev, A., et al., *X-ray Photoelectron Spectroscopy Reference Data for Identification of the C 3 N 4 Phase in Carbon–Nitrogen Films.* Diamond and related materials, 2000. **9**(11): p. 1904-1907.
226. Brauer, D.S., et al., *Effect of TiO2 addition on structure, solubility and crystallisation of phosphate invert glasses for biomedical applications.* Journal of Non-Crystalline Solids, 2010. **356**(44-49): p. 2626-2633.
227. Abid, M., M. Et-Tabirou, and M. Hafid, *Glass Forming Region, Ionic Conductivity and Infrared Spectroscopy of Vitreous Sodium Lead Mixed Phosphates.* Materials research bulletin, 2001. **36**(3): p. 407-421.
228. Lee, D.-B., L.-S. Hong, and Y.-J. Kim, *Effect of Ca and CaO on the high temperature oxidation of AZ91D Mg alloys.* Materials transactions, 2008. **49**(5): p. 1084-1088.
229. Ardizzone, S., et al., *Magnesium salts and oxide: an XPS overview.* Applied Surface Science, 1997. **119**(3): p. 253-259.
230. Walter, G., et al., *The structure of CaO–Na 2 O–MgO–P 2 O 5 invert glass.* Journal of non-crystalline solids, 2001. **296**(3): p. 212-223.
231. Khattak, G., A. Mekki, and L. Wenger, *X-ray Photoelectron Spectroscopy (XPS) and Magnetic Susceptibility Studies of Vanadium Phosphate Glasses.* Journal of Non-Crystalline Solids, 2009. **355**(43): p. 2148-2155.
232. Serra, J., et al., *FTIR and XPS studies of bioactive silica based glasses.* Journal of Non-Crystalline Solids, 2003. **332**(1): p. 20-27.
233. Grosvenor, A., B. Kobe, and N. McIntyre, *Studies of the oxidation of iron by water vapour using X-ray photoelectron spectroscopy and QUASES™.* Surface Science Reports. **572**(2): p. 217-227.
234. Grosvenor, A., et al., *Investigation of multiplet splitting of Fe 2p XPS spectra and bonding in iron compounds.* Surface and Interface Analysis, 2004. **36**(12): p. 1564-1574.
235. Minitti, M.E., M.D. Lane, and J.L. Bishop, *A new hematite formation mechanism for Mars.* Meteoritics & Planetary Science, 2005. **40**(1): p. 55-69.
236. Wang, Y., A. Muramatsu, and T. Sugimoto, *FTIR analysis of well-defined α-Fe 2 O 3 particles.* Colloids and Surfaces A: Physicochemical and Engineering Aspects, 1998. **134**(3): p. 281-297.
237. ISO, *ISO 13779-2:2008: Implants for surgery -- Hydroxyapatite -- Part 2: Coatings of hydroxyapatite*. 2008.
238. Agathopoulos, S., et al., *Formation of hydroxyapatite onto glasses of the CaO–MgO–SiO 2 system with B 2 O 3, Na 2 O, CaF 2 and P 2 O 5 additives.* Biomaterials, 2006. **27**(9): p. 1832-1840.
239. Slav, A., et al. *Rough bioglass films prepared by magnetron sputtering*. in *Key Engineering Materials*. 2008. Trans Tech Publ.
240. Stoch, A., et al., *FTIR monitoring of the growth of the carbonate containing apatite layers from simulated and natural body fluids.* Journal of Molecular Structure, 1999. **511**: p. 287-294.
241. Kelly, P. and R. Arnell, *Magnetron sputtering: a review of recent developments and applications.* Vacuum, 2000. **56**(3): p. 159-172.
242. Levy, P.W., *Shaping or Figuring Ceramic Surfaces by Ion-Beam Bombardment.* The Science of Ceramic Machining and Surface Finishing, 1970: p. 155-168.
243. Koike, K., *Measurement on the excitation temperature of argon plasma jet under strong magnetic field.* Vacuum, 2004. **73**(3-4): p. 352-358.

244. Speedy, R.J., *Kauzmann's paradox and the glass transition.* Biophysical chemistry, 2003. **105**(2): p. 411-420.
245. Musinu, A., G. Piccaluga, and G. Pinna, *X-ray diffraction investigation of iron in sodium phosphate glasses.* Journal of Physical Chemistry, 1996. **100**(30): p. 12462-12466.
246. Dean, J.A., *The Strengths of Chemical Bonds*. 15th ed, ed. L.s.H.o. Chemistry. 1998, United States: McGraw-Hill, INC.
247. Tang, A.J., et al., *Structure study of binary titanophosphate glasses prepared by sol-gel and melting methods.* Journal of the Ceramic Society of Japan, 2004. **112**(1309): p. 496-501.
248. Pickup, D.M., et al., *Ti K-edge XANES study of the local environment of titanium in bioresorbable TiO2–CaO–Na2O–P2O5 glasses.* Journal of Materials Science: Materials in Medicine, 2008. **19**(4): p. 1681-1685.
249. FitzGerald, V., et al., *An x-ray diffraction study of the structure of Bioglass and its sol-gel analogue as a function of composition.* Physics and Chemistry of Glasses-European Journal of Glass Science and Technology Part B, 2007. **48**(5): p. 340-344.
250. Anders, C. and H.M. Urbassek, *Effect of binding energy and mass in cluster-induced sputtering of van-der-Waals bonded systems.* Nuclear Instruments & Methods in Physics Research Section B-Beam Interactions with Materials and Atoms, 2005. **228**: p. 84-91.
251. Pickup, D.M., et al., *X-ray absorption spectroscopy and high-energy XRD study of the local environment of copper in antibacterial copper-releasing degradable phosphate glasses.* Journal of non-crystalline solids, 2006. **352**(28): p. 3080-3087.
252. Kudriavtsev, Y., et al., *Calculation of the surface binding energy for ion sputtered particles.* Applied surface science, 2005. **239**(3): p. 273-278.
253. Zhao, Y.D., et al., *Surface roughness of alumina films deposited by reactive r.f. sputtering.* Thin Solid Films, 1996. **286**(1-2): p. 45-48.
254. Whitacre, J., W. West, and B. Ratnakumar, *The influence of target history and deposition geometry on RF magnetron sputtered LiCoO 2 thin films.* Journal of power sources, 2001. **103**(1): p. 134-139.
255. Vick, D., et al., *Self-shadowing and surface diffusion effects in obliquely deposited thin films.* Thin Solid Films, 1999. **339**(1): p. 88-94.
256. Friel, J.J. and C.E. Lyman, *Tutorial review: X-ray mapping in electron-beam instruments.* Microscopy and Microanalysis, 2006. **12**(01): p. 2-25.
257. Rode, D., V. Gaddam, and J.H. Yi, *Subnanometer surface roughness of dc magnetron sputtered Al films.* Journal of Applied Physics. **102**(2): p. 024303.
258. Thornton, J.A., *Influence of apparatus geometry and deposition conditions on the structure and topography of thick sputtered coatings.* Journal of Vacuum Science & Technology, 1974. **11**(4): p. 666-670.
259. McCafferty, E. and J. Wightman, *Determination of the concentration of surface hydroxyl groups on metal oxide films by a quantitative XPS method.* Surface and Interface Analysis, 1998. **26**(8): p. 549-564.
260. Foroutan, F., et al., *Novel sol–gel preparation of (P2O5) 0.4–(CaO) 0.25–(Na2O) X–(TiO2)(0.35− X) bioresorbable glasses (X= 0.05, 0.1, and 0.15).* Journal of Sol-Gel Science and Technology, 2015. **73**(2): p. 434-442.
261. Vollmayr, K., W. Kob, and K. Binder, *How do the properties of a glass depend on the cooling rate? A computer simulation study of a Lennard‐Jones system.* The Journal of chemical physics, 1996. **105**(11): p. 4714-4728.
262. Tilley, R.J., *Understanding Solids: the Science of Materials*. 2004: John Wiley & Sons.
263. Ahmed, I., et al., *Quantification of anion and cation release from a range of ternary phosphate-based glasses with fixed 45 mol% P2O5.* Journal of biomaterials applications, 2005. **20**(1): p. 65-80.
264. Rawlings, R.D., J. Wu, and A. Boccaccini, *Glass-ceramics: their production from wastes—a review.* Journal of materials science, 2006. **41**(3): p. 733-761.

265. Ray, C., et al., *Effect of melting temperature and time on iron valence and crystallization of iron phosphate glasses.* Journal of non-crystalline solids, 1999. **249**(1): p. 1-16.
266. Kester, D.J. and R. Messier, *Micro-Effects of Resputtering Due to Negative-Ion Bombardment of Growing Thin-Films.* Journal of Materials Research, 1993. **8**(8): p. 1938-1957.
267. Gupta, R.P. and S.K. Sen, *Calculation of multiplet structure of core p-vacancy levels.* Physical Review B, 1974. **10**(1): p. 71-77.
268. Cooper, R.F., J.B. Fanselow, and D.B. Poker, *The mechanism of oxidation of a basaltic glass: Chemical diffusion of network-modifying cations.* Geochimica et Cosmochimica Acta, 1996. **60**(17): p. 3253-3265.
269. Wisniewski, W., et al., *Crystallisation of iron containing glass-ceramics and the transformation of hematite to magnetite.* CrystEngComm, 2011. **13**(12): p. 4025-4031.
270. Yeo, I.-S., *Reality of Dental Implant Surface Modification: A Short Literature.* Open Biomedical Engineering Journal, 2014. **8**: p. 114-119.
271. Cheng, K., et al., *Bonding strength of fluoridated hydroxyapatite coatings: a comparative study on pull-out and scratch analysis.* Thin Solid Films, 2009. **517**(17): p. 5361-5364.
272. Cozien-Cazuc, S., et al., *Effects of Aqueous Aging on the Mechanical Properties of P40Na20Ca16Mg24 Phosphate Glass Fibres.* Journal of Materials Science, 2008. **43**(14): p. 4834-4839.
273. Sglavo, V.M., et al., *Mechanical Properties of Phosphate Glass Optical Fibers.* International Journal of Applied Glass Science, 2014. **5**(1): p. 57-64.
274. Bellucci, D., V. Cannillo, and A. Sola, *Coefficient of thermal expansion of bioactive glasses: available literature data and analytical equation estimates.* Ceramics International, 2011. **37**(8): p. 2963-2972.
275. Elmer, J., et al., *In situ observations of lattice expansion and transformation rates of α and β phases in Ti–6Al–4V.* Materials Science and Engineering: A, 2005. **391**(1): p. 104-113.
276. Price, N., et al., *Human osteoblast‐like cells (MG63) proliferate on a bioactive glass surface.* Journal of biomedical materials research, 1997. **37**(3): p. 394-400.
277. Verné, E., et al., *Early stage reactivity and in vitro behavior of silica-based bioactive glasses and glass-ceramics.* Journal of Materials Science: Materials in Medicine, 2009. **20**(1): p. 75-87.
278. Combes, C. and C. Rey, *Amorphous calcium phosphates: synthesis, properties and uses in biomaterials.* Acta Biomaterialia, 2010. **6**(9): p. 3362-3378.
279. Zhao, J., et al., *Amorphous calcium phosphate and its application in dentistry.* Chemistry Central Journal, 2011. **5**(1): p. 1.

9. Appendices

1.0

High resolution scan of C7U-500°-120 to observe peak located at 33 2Θ (°).

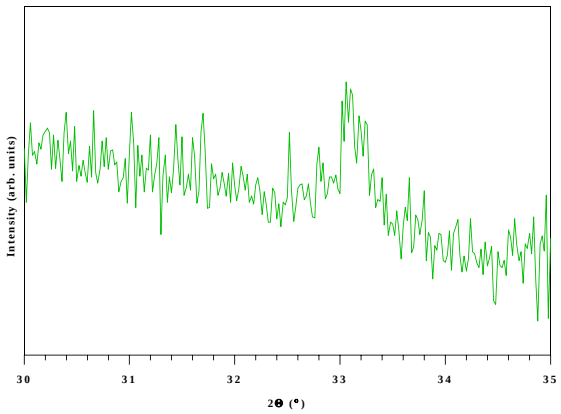

2.0

Rietveld Refinement of selected XRD spectra.

MQ4: P28 Fe6

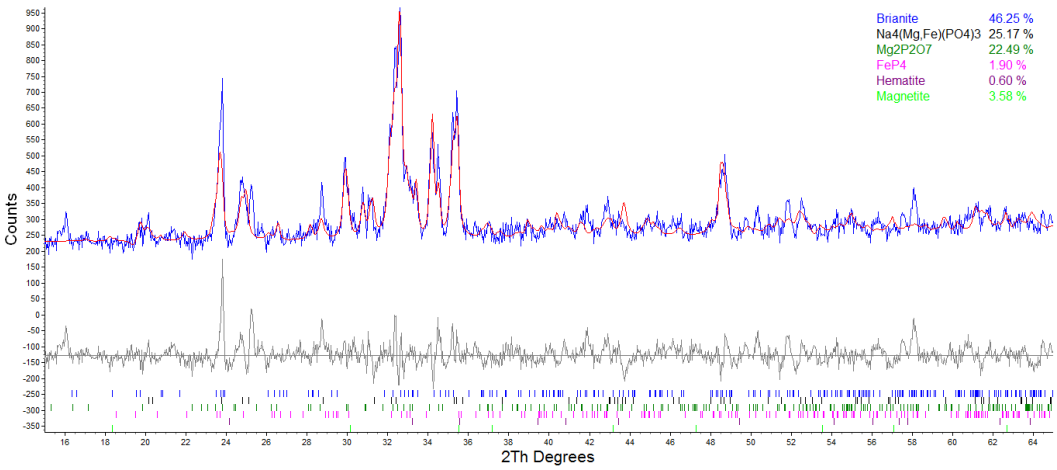

C12U: P28 Fe6

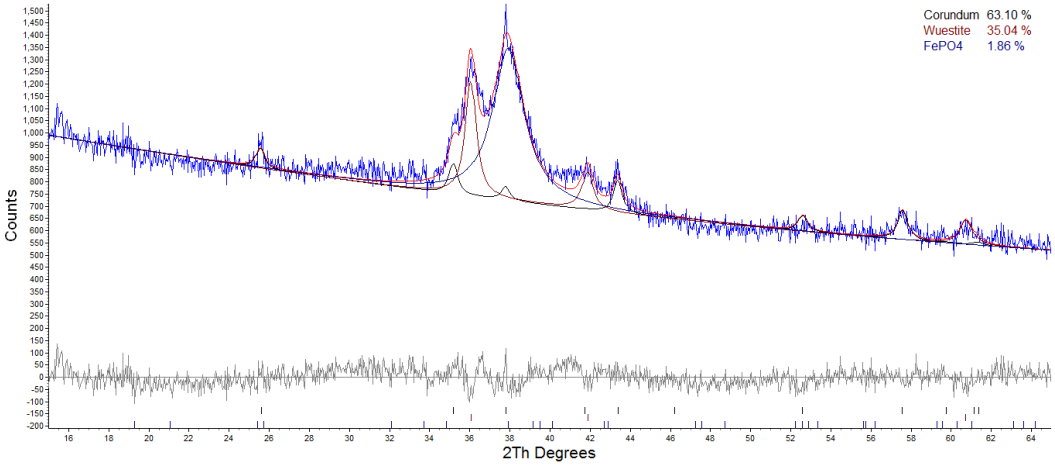

C7U-610°-30

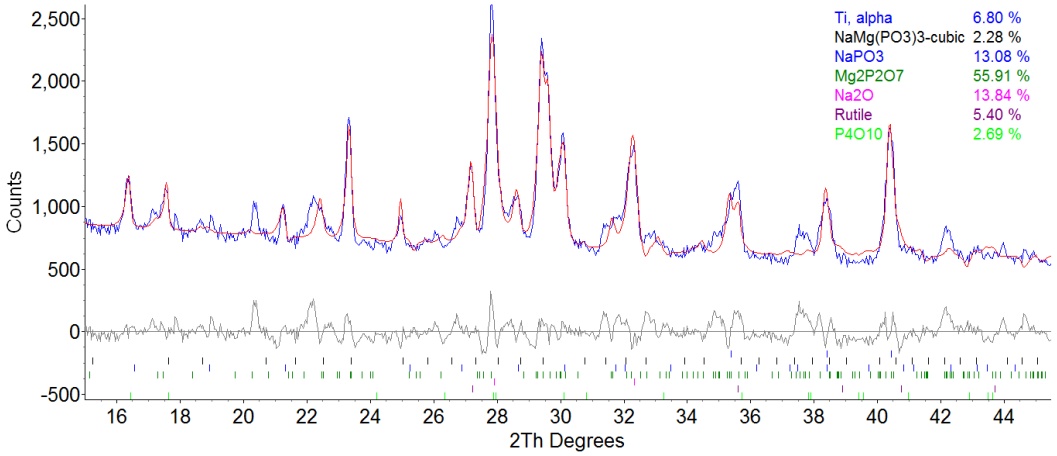

C8U-500°-30

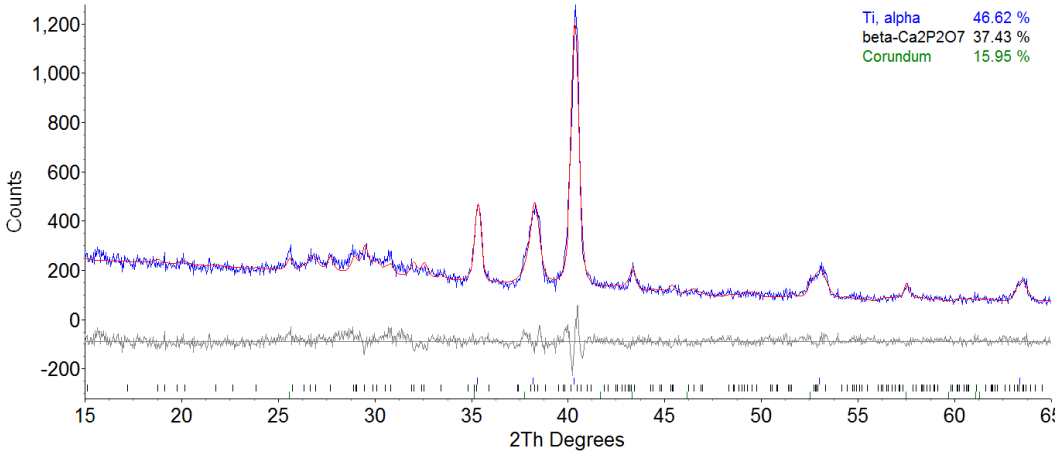

3.0

XRD of *in situ* Radiation induced heating of T1U: P40 following 120 W deposition for 600 min.

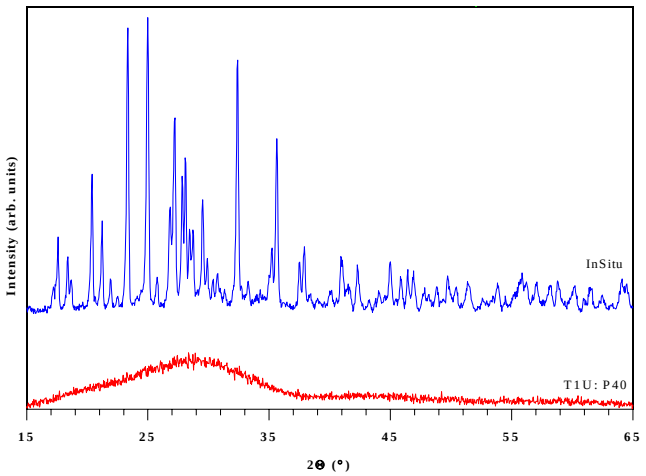

4.0

Magnified glass transitions from Figure 4.29